Chapter 2
Extended Stress Intensity Factor Concepts

D. Radaj

Abstract The stress intensity factor concept for describing the stress field at pointed crack or slit tips is well known from fracture mechanics. It is substantially extended here in two directions. One extension refers to pointed V-notches with stress intensities depending on the notch opening angle. The loading mode related notch stress intensity factors K_1, K_2 and K_3 are introduced. Another extension refers to rounded notches with crack shape or V-notch shape in two variants: parabolic, elliptic or hyperbolic notches ('blunt notches') on the one hand and root hole notches ('keyholes' when considering crack shapes) on the other hand. Here, the loading mode related generalised notch stress intensity factors $K_{1\rho}$, $K_{2\rho}$ and $K_{3\rho}$ are defined. The concepts of elastic stress intensity factor, notch stress intensity factor and generalised notch stress intensity factor are extended into the range of elastic-plastic (work-hardening) or perfectly plastic notch tip or notch root behaviour. Here, the plastic notch stress intensity factors K_{1p}, K_{2p} and K_{3p} are of relevance. The original stress intensity factor concept is also transferred from cracks or slits to rigid thin inclusions.

Contents

D. Radaj and M. Vormwald, *Advanced Methods of Fatigue Assessment*,
DOI: 10.1007/978-3-642-30740-9_2, © Springer-Verlag Berlin Heidelberg 2013

2.1 Survey of Chapter Contents

The stress intensity factor concept has originally been developed in the context of fracture mechanics. For fracture phenomena, both brittle fracture and fatigue failure, the asymptotic singular stress field at the pointed crack or slit tip is most important. The stress level around the singularity is described by the stress intensity factor (SIF), possibly superimposed by the crack-parallel non-singular T-stress. In certain cases (e.g. thin-sheet lap joints), it is necessary, also to take higher order terms of the stress field approximation into account.

The local three-dimensional stress singularity at a definite point of the crack or slit front can generally be described by superimposition of three two-dimensional stress singularities corresponding to three independent loading or opening modes of the crack tip: transverse tensile loading (mode I), in-plane shear loading (mode II) and out-of-plane shear loading (mode III). The appertaining SIFs are K_{I}, K_{II} and K_{III}. Non-singular stresses may be superimposed: crack-parallel stresses (the T-stress) as well as normal stresses and symmetric shear stresses in the crack front direction. In special cases, the separation of the elementary crack tip loading modes is not possible, coupling effects together with transverse singular effects are occurring, e.g. where the crack front butts on a free surface.

The SIF concept has been substantially extended in two directions. One extension refers to pointed V-notches with stress intensities depending on the notch opening angle. Here, the loading mode related notch stress intensity factors (NSIFs) are K_1, K_2 and K_3. Another extension refers to rounded notches with crack shape or V-notch shape in two variants: parabolic, elliptic or hyperbolic notches ('blunt notches') on the one hand and root hole notches ('keyholes' when considering crack shapes) on the other hand. The notch stresses remain finite in this case, but their angular and radial distribution is linked to that of the corresponding pointed notches. Here, the loading mode related generalised NSIFs are $K_{1\rho}$, $K_{2\rho}$ and $K_{3\rho}$. They are slightly larger than K_1, K_2 and K_3, their value increases with reduced notch severity.

The elastic SIF, NSIF and generalised NSIF concepts may be extended into the range of elastic-plastic (work-hardening) or perfectly plastic notch tip or notch root behaviour. Here, the plastic NSIFs $K_{1\mathrm{p}}$, $K_{2\mathrm{p}}$ and $K_{3\mathrm{p}}$ are of relevance.

Further extensions of the SIF concepts are documented in the literature. The original SIF concept may be transferred from cracks or slits to rigid thin inclusions, from pointed V-notches to pointed rigid inclusions with V-notch shape and from blunt V-notches to the corresponding rounded rigid inclusions. Another extension is the bimaterial wedge problem with inclusion of interface crack configurations.

In Sect. 2.2, the original stress intensity factor concept is reviewed, referring to the stress field near crack tips, with application to slit tips in welded joints.

In Sect. 2.3, the notch stress intensity factor concept is summarised, referring to the stress field near pointed V-notch tips, with application to fillet-welded joints.

In Sect. 2.4, the generalised notch stress intensity factor concept is described, referring to the stress field at blunt V-notch tips and at root hole V-notch tips, with application to round bars with shoulder fillets.

In Sect. 2.5, plastic notch stress intensity factors are introduced for describing the stress and strain field at pointed V-notch tips and at parabolic notch tips. A new version of the Neuber rule accounting for the influence of the notch opening angle is presented.

In Sect. 2.6, the stress intensity factor concept is applied to rigid thin inclusions, with one example of SIF evaluation.

The bimaterial wedge problem with inclusion of interface crack configurations cannot be presented within the available space of this book. Reference is made instead to the early basic solutions (Hein and Erdogan 1971; Bogy 1971) and to a recent comprehensive study on asymptotic near-field analyses of plane multi-material joints (Sator 2010). Typical applications are interface cracks or cracks butting on the interface, the interface itself butting on a unnotched surface, on a corner-notched surface or on a more generally V-notched surface. A well known special problem is the bearing pressure between a plane rigid stamp and a plane elastic continuum.

2.2 Original Stress Intensity Factor Concept

2.2.1 Survey of Section Contents

The basic formulation of the SIF concept is reviewed. Basic is the description of the singular and non-singular stress field in the vicinity of a crack tip or slit tip. The three-dimensional stress state at any point of the crack or slit front is separated into the three two-dimensional singular loading modes I, II and III and into three non-singular modes (*T*-stress, *S*-stress and front-parallel normal stress). A coupling of singular modes together with transverse singular effects may occur where the crack or slit front butts on a free surface.

The stress field equations in the vicinity of crack or slit tips are presented and the corresponding SIFs, *T*-stress and *S*-stress are defined. These characteristic parameters are specified for the joint face edge of seam-welded and spot-welded lap joints proceeding from the linearised structural stresses which suppress the singularity completely. Lap joints with equal and unequal plate thickness, respectively, are considered.

Equivalent SIFs are defined, referring to failure under mixed-mode loading conditions. Endurable SIFs for spot-welded lap joints are finally given, both in the form of a threshold value and in the form of a *K*–*N* curve with a defined, sufficiently low scatter range.

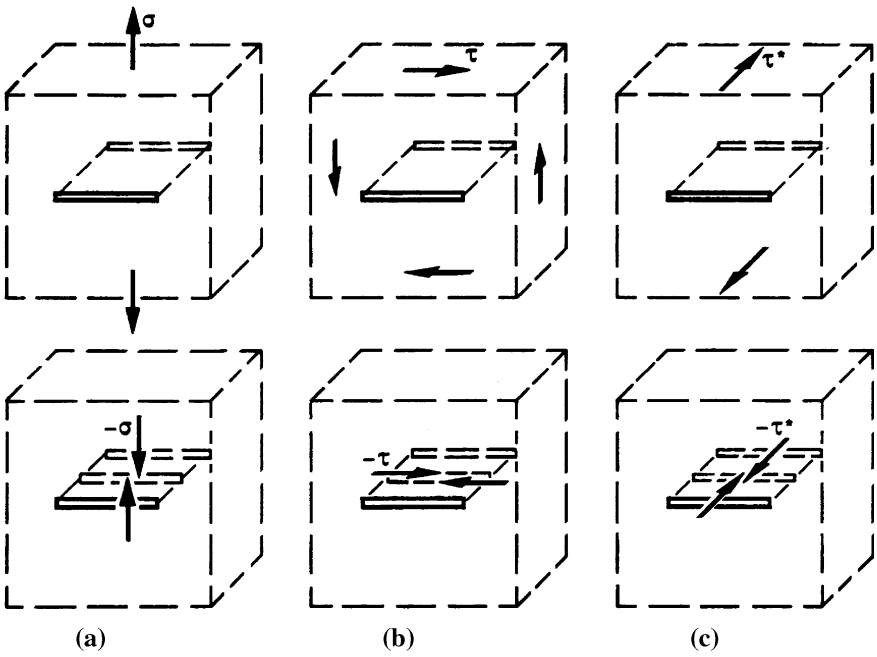

Fig. 2.1 Basic singular loading modes I (**a**), II (**b**) and III (**c**) of cracks; planar crack in the infinite plate; plane and antiplane strain fields; arrows designate remote boundary or crack flank stresses; (Radaj and Zhang 1993[1])

The expositions are based on readily available text books on fracture mechanics and on special publications. A list of symbols and a list of references are found at the end of Chap. 2.

2.2.2 Basic Crack Tip Loading Modes

The stress intensity factor concept originates from fracture mechanics. For fracture phenomena, both brittle fracture and fatigue failure, the local stress field close to the crack tip is decisive. The stresses rise to a singularity at the pointed crack tip. The intensity of this singularity is dependent on the magnitude of the relevant structural stresses.

The local three-dimensional stress field at a definite point of the crack front may generally be separated into two-dimensional stress fields which are superimposed: three loading modes with singular stresses and three loading modes with non-singular stresses. The singular loading modes comprise transverse tensile loading (mode I), in-plane shear loading (mode II) and out-of-plane shear loading (mode III), Fig. 2.1. The non-singular loading modes consist of crack-parallel tensile or compressive loading (mode 0I), crack-front-parallel tensile or

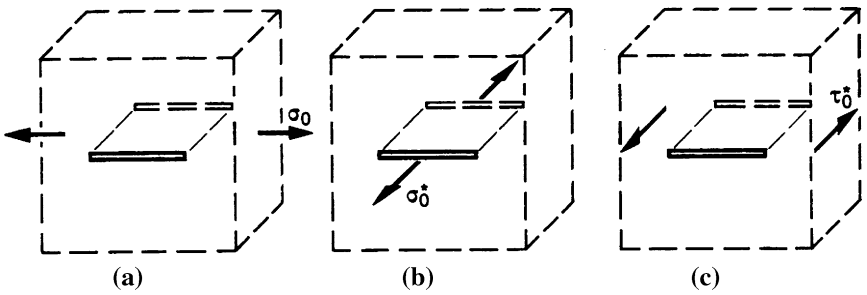

Fig. 2.2 Basic non-singular loading modes 0I (**a**), 0II (**b**) and 0III (**c**) of cracks; planar crack in the infinite plate; plane and antiplane strain fields; arrows designate remote boundary stresses; (Radaj and Zhang 1993[(1)])

compressive loading (mode 0II) and crack-front-parallel shear loading (mode 0III), Fig. 2.2.

In exceptional cases, coupling effects may occur locally between the mode-related singularities within locally three-dimensional configurations. One typical example is the crack tip in a plate of finite thickness subjected to in-plane shear loading. A transverse shear stress singularity is generated locally underneath the plate surface. Further details can be found in Sect. 2.3.3.

2.2.3 Asymptotic Stress Field near Crack Tips

The three basic loading modes with singular stresses at the crack tip produce the following asymptotic stress distribution around the crack tip (Westergaard 1939; Sneddon 1946; Irwin 1957; Williams 1957), Fig. 2.3:

$$\sigma_{ij} = \frac{1}{\sqrt{2\pi r}}\left[K_I f_{I,ij}(\theta) + K_{II} f_{II,ij}(\theta) + K_{III} f_{III,kz}(\theta)\right] \quad (2.1)$$
$$(\text{i, j} = x, y \text{ and k} = x, y \text{ or i, j} = r, \theta \text{ and k} = r, \theta)$$

The mode-related stress intensity factors (SIFs) K_I, K_{II} and K_{III} depend on the magnitude of the load, the crack length and further geometrical parameters of the considered configuration. The mode-related angle-dependent functions $f_{I,ij}$, $f_{II,ij}$, $f_{III,iz}$ describe the angular distribution of the stresses at the crack tip. The relationship above is strictly valid for $r \to 0$ and approximately valid for values of r which are small in relation to the crack length and other geometrical parameters of the configuration.

These are the asymptotic stresses in the three singular loading modes, given in polar coordinates:

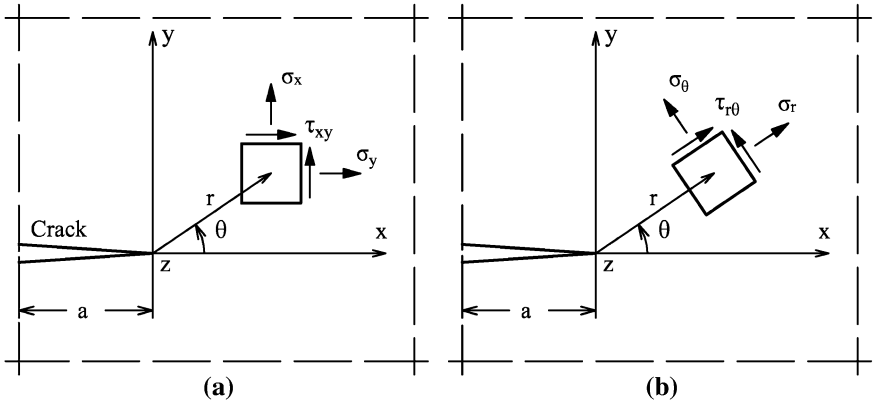

Fig. 2.3 Cartesian (**a**) and polar (**b**) coordinate systems with correspondingly defined stresses at the crack tip; (Lazzarin and Tovo 1998)

Mode I (transverse tensile loading):

$$\begin{Bmatrix} \sigma_r \\ \sigma_\theta \\ \tau_{r\theta} \end{Bmatrix} = \frac{K_{\mathrm{I}}}{4\sqrt{2\pi r}} \begin{Bmatrix} 5\cos\theta/2 - \cos 3\theta/2 \\ 3\cos\theta/2 + \cos 3\theta/2 \\ \sin\theta/2 + \sin 3\theta/2 \end{Bmatrix} \tag{2.2}$$

$$\begin{aligned} &\sigma_z = 0 \quad \text{(plane stress)} \\ &\sigma_z = \nu(\sigma_r + \sigma_\theta) = \frac{2\nu K_{\mathrm{I}}}{\sqrt{2\pi r}} \cos\frac{\theta}{2} \quad \text{(plane strain)} \end{aligned} \tag{2.3}$$

Mode II (in-plane shear loading):

$$\begin{Bmatrix} \sigma_r \\ \sigma_\theta \\ \tau_{r\theta} \end{Bmatrix} = \frac{K_{\mathrm{II}}}{4\sqrt{2\pi r}} \begin{Bmatrix} -5\sin\theta/2 + 3\sin 3\theta/2 \\ -3\sin\theta/2 - 3\sin 3\theta/2 \\ \cos\theta/2 + 3\cos 3\theta/2 \end{Bmatrix} \tag{2.4}$$

$$\begin{aligned} &\sigma_z = 0 \quad \text{(plane stress)} \\ &\sigma_z = \nu(\sigma_r + \sigma_\theta) = -\frac{2\nu K_{\mathrm{II}}}{\sqrt{2\pi r}} \sin\frac{\theta}{2} \quad \text{(plane strain)} \end{aligned} \tag{2.5}$$

Mode III (out-of-plane shear loading):

$$\begin{Bmatrix} \tau_{rz} \\ \tau_{\theta z} \end{Bmatrix} = \frac{K_{\mathrm{III}}}{\sqrt{2\pi r}} \begin{Bmatrix} \sin\theta/2 \\ \cos\theta/2 \end{Bmatrix} \tag{2.6}$$

2.2.4 Higher Order Non-Singular Stress Terms

The Eqs. (2.1–2.6) above represent asymptotic or first order approximations of the stress field around the singularity at the crack tip. They deviate from the exact solution with increasing distance from the crack tip. The complete solution for the stress field is represented by an infinite series expansion based on eigenvalues and eigenfunctions resulting in non-singular higher order stress terms (Williams 1952, 1957).

The boundary condition of load-free crack or slit flanks ($\theta = \pm\pi$), introduced into the general complex stress functions, results in a homogeneous equation system. Nontrivial solutions exist for the coefficient determinant being zero, resulting in identical eigenvalues in the three loading modes:

$$\sin 2\lambda\pi = 0 \quad \rightarrow \quad \lambda = \frac{n}{2} \quad (n = 1, 2, 3, \ldots) \tag{2.7}$$

The stresses are expressed by an infinite series of the corresponding eigenfunctions (nomenclature after Gross and Seelig 2001):

$$\sigma_{ij} = r^{-1/2}\hat{\sigma}_{ij}^{(1)}(\theta) + \hat{\sigma}_{ij}^{(2)}(\theta) + r^{1/2}\hat{\sigma}_{ij}^{(3)}(\theta) + r\hat{\sigma}_{ij}^{(4)}(\theta) + \ldots \quad (i,\ j = r, \theta) \tag{2.8}$$

$$\tau_{kz} = r^{-1/2}\hat{\tau}_{kz}^{(1)}(\theta) + \hat{\tau}_{kz}^{(2)}(\theta) + r^{1/2}\hat{\tau}_{kz}^{(3)}(\theta) + r\hat{\tau}_{kz}^{(4)}(\theta) + \ldots \quad (k = r, \theta) \tag{2.9}$$

The stress field equation σ_{ij} can be split into symmetric and antimetric parts in respect of θ, the symmetric part connected with mode I loading, the antimetric part with mode II loading. The stress field equation τ_{kz} is related to mode III loading.

The first order terms define the stress singularity at the crack tip ($r = 0$). They contain the SIFs K_I, K_{II} and K_{III}. The second order terms define a uniform non-singular stress at the crack tip, the tensile or compressive stress directed in crack direction named '*T*-stress' (Larsson and Carlsson 1973) and the symmetric shear stress in crack front direction which may be named '*S*-stress' in conformity with the *T*-stress.

These parameters control the stress field close to the crack tip (the 'near-field'), now written in the usual nomenclature up to the second term:

$$\sigma_{I,ij}^{(1,2)} = \frac{K_I}{\sqrt{2\pi r}} f_{I,ij}^{(1)}(\theta) + T f_{T,ij}^{(2)}(\theta) \tag{2.10}$$

$$\sigma_{II,ij}^{(1,2)} = \frac{K_{II}}{\sqrt{2\pi r}} f_{II,ij}^{(1)}(\theta) \tag{2.11}$$

$$\tau_{III,kz}^{(1,2)} = \frac{K_{III}}{\sqrt{2\pi r}} f_{III,kz}^{(1)}(\theta) + S f_{S,kz}^{(2)}(\theta) \tag{2.12}$$

The stress terms of higher than second order converge to zero for $r \rightarrow 0$, but may be important for larger values of r. Under certain conditions, e.g. a low sheet thickness in lap joints, the range of r, where the second order approximation is appropriate, may be very small (e.g. $r = 0.01$ mm in the tensile-shear specimen

with a plate thickness of 1 mm). Then, higher order approximations are needed. The stress equations for mode I and II loading have been derived up to the seventh term represented by $r^{5/2}$ (Berto and Lazzarin 2010).

A possible misunderstanding should immediately be removed. The higher order terms do not describe the stress field in the total structure. The series developments in Eqs. (2.8) and (2.9) are valid only within a certain distance from the slit tip, smaller than the nearest external boundary.

The T-stress σ_0 corresponds to the loading mode 0I in Fig. 2.2, the S-stress τ_0^* to the loading mode 0III. The uniform normal stress σ_0^* in the direction of the crack front produced by mode 0II loading needs no special comment.

The T-stress results in the following polar stress components:

$$\left\{ \begin{array}{c} \sigma_r \\ \sigma_\theta \\ \tau_{r\theta} \end{array} \right\}_T = T \left\{ \begin{array}{c} \cos^2\theta \\ \sin^2\theta \\ -0.5\sin 2\theta \end{array} \right\} \tag{2.13}$$

$$\sigma_z = \nu T \quad \text{(plane strain)} \tag{2.14}$$

The corresponding expression for the S-stress is:

$$\left\{ \begin{array}{c} \tau_{rz} \\ \tau_{\theta z} \end{array} \right\}_S = S \left\{ \begin{array}{c} \cos\theta \\ -\sin\theta \end{array} \right\} \tag{2.15}$$

2.2.5 Limit Value Formulae for SIFs, T-Stress and S-Stress

The SIFs K_I, K_II and K_III may be determined based on Eqs. (2.10–2.12) from the following limit value formulae which consider the predominant stresses in the ligament ($\theta = 0$):

$$K_\mathrm{I} = \lim_{r \to 0} \sqrt{2\pi r}\, \sigma_\theta \tag{2.16}$$

$$K_\mathrm{II} = \lim_{r \to 0} \sqrt{2\pi r}\, \tau_{r\theta} \tag{2.17}$$

$$K_\mathrm{III} = \lim_{r \to 0} \sqrt{2\pi r}\, \tau_{\theta z} \tag{2.18}$$

Alternatively, limit values of the predominant displacements of the crack flanks may be evaluated. Any other non-vanishing stress or displacement component for the same or other values of θ may be used in the limit value formulae.

The limit conditions above may be applied to analytical stress field solutions and their series expansion or to numerical solutions based on the finite element or boundary element method. In the latter case, the limit value evaluation is facilitated by plotting the stress or displacement components over the distance r from the crack tip in log–log scales. The first order stress approximations appear as

decreasing straight lines with the gradient corresponding to $1/r^{1/2}$. The SIFs can easily be calculated from these approximations.

T-stress and *S*-stress may also be determined from analytical solutions after series expansion of the stress field. In the case of numerical modelling, the *T*-stress is usually determined as the medium value of the tensile or compressive stresses acting in the two flank sides of the crack. In general, this crack-parallel stress is evaluated in the midsection of the (internal) crack. It has the same sign and value on both sides of the crack, whereas the corresponding stresses from mode II loading have opposite signs (Williams 1957).

Using another method, the *T*-stress results from the difference in the stresses σ_r and σ_θ acting in the ligament close to the crack tip (Lazzarin et al. 2009):

$$T = \sigma_r - \sigma_\theta \quad (\theta = 0,\ r \to 0) \tag{2.19}$$

whereas Mode II loading has no effect on these stresses.

The *S*-stress is determined as the medium of the shear stresses acting along the crack front in the plane normal to the ligament at $r \to 0$. It is the symmetric mode 0III shear stress component.

The parameters *T* and *S* are defined for $r \to 0$, but may be extended to the near field $r > 0$, $T(r)$ and $S(r)$, with a linear dependency on *r*.

2.2.6 J-Integral Expressed by SIFs and T-Stress

The line integral *J* (Rice 1968), designed for describing the fracture behaviour in nonlinear-elastic materials, can successfully be applied with certain restrictions to the elastic-plastic fracture behaviour. Rice has shown that the nonlinear energy release rate can be written as a path-independent line integral *J* around the crack tip. It has also been shown that the *J*-integral uniquely characterises the stress and strain field close to the crack tip (Hutchinson 1968; Rice and Rosengren 1968). Thus the *J*-integral is both an energy parameter and a stress intensity parameter (Anderson 1995).

In its simplified linear-elastic form, the *J*-integral may be used to determine SIFs on the basis of remote boundary conditions chosen on the integration path. Vice versa, the *J*-integral may be determined based on the available SIFs and *T*-stress.

It can be shown that, under linear-elastic conditions, the *J*-integral is equal to the energy release rate, provided coplanar crack propagation can be assumed. Then, the total *J* is the sum of the mode-related *J*-values, J_I, J_II and J_III:

$$\begin{aligned} &J = J_\mathrm{I} + J_\mathrm{II} + J_\mathrm{III} = \frac{K_\mathrm{I}^2}{E'} + \frac{K_\mathrm{II}^2}{E'} + \frac{K_\mathrm{III}^2}{2G} \\ &E' = E \quad \text{(plane stress)}, \quad E' = \frac{E}{1-\nu^2} \quad \text{(plane strain)}, \quad G = \frac{E}{2(1+\nu)} \end{aligned} \tag{2.20}$$

where *E* is the modulus of elasticity and *G* the shear modulus.

In the case of kinking crack propagation, additional terms occur in the expression for J. It is assumed that the crack propagates in the direction of the maximum energy release rate $G_{\max}$. One additional term J_K is related to mixed mode I and II loading, the other J_T to the T-stress (Erdogan and Sih 1963; Williams and Ewing 1972; Cottrell and Rice 1980; Lazzarin et al. 2009):

$$J_2 = J_K + J_T = -\frac{2K_{\mathrm{II}}}{E'}\left(K_{\mathrm{I}} + T\sqrt{\frac{8}{\pi}R}\right) \tag{2.21a}$$

In Eq. (2.21a), R is the radius of the selected circular path, i.e. J_T is path-dependent. The total J-value has the following square root form (Gdoutos 1990):

$$J_{\mathrm{tot}} = \sqrt{J^2 + J_2^2} \tag{2.21b}$$

2.2.7 General SIF Formulae

The SIFs are needed for assessing the brittle fracture or fatigue strength of structural members and specimens containing cracks, slits or flaws. The mode I SIF K_{I} is most important, because crack propagation is mainly controlled by this parameter. The crack takes a path where mode I conditions are prevailing. The mode II SIF K_{II} is important as a superimposed, mostly secondary loading effect. The mode III SIF K_{III} is of relevance to engineering problems such as torsional loaded round bars.

The SIFs depend on the geometry and position of the crack as well as on the geometrical and loading parameters of the considered structural member or specimen. Dominating parameters are the crack length and the load level. The dimension of the SIFs is $\mathrm{N/mm^{3/2}} = \mathrm{MPa\ mm^{1/2}}$, compare Eqs. (2.16–2.18).

The SIFs K_{I}, K_{II} and K_{III} in combination with the T-stress, S-stress and non-singular crack-front-parallel stress σ_0^* describe the linear-elastic stress field close to the crack tip at any point of the crack front completely. Today, the generally available numerical tools (FE and BE) allow to analyse any special crack configuration and to determine the stress field parameters just mentioned. On the other hand, formulae for SIFs are indispensable for assessing the influence of the geometrical, loading and support conditions. Any parametrical investigation and any integration into more general calculation methods is based on such formulae.

The analytical and numerical methods for determining the SIFs have been systematically reviewed (Radaj and Vormwald 2007, ibid. pp. 356–363). Formulae for SIFs are available for a large number of crack configurations in specimens and structural members (Murakami 1987; Rooke and Cartwright 1976; Sih 1973; Tada et al. 1999). Also, the T-stress solutions have been compiled (Sherry et al. 1995).

A review on the SIFs of cracks and slits in welded joints with reference to fatigue assessments is available (Radaj et al. 2006, ibid. pp. 250–259). A summary of the contents is given below.

The primary concern of the fatigue crack propagation approach applied to welded joints is directed towards surface cracks in areas of notch stress concentration such as weld toes. These cracks are assumed to be oblong and mostly continuous in the case of transverse welds or to be elliptical in the case of ends of longitudinal welds. The semi-ellipse is defined as circumscribing the more complex actual shape of several simultaneously initiated but coalescing cracks or of other planar defects.

The maximum SIF occurring at the deepest point of the semi-elliptical surface crack in a plate with superimposed notch effect is approximated by the following engineering formulae:

$$K_I = (M_{km} Y_m \sigma_m + M_{kb} Y_b \sigma_b) \frac{\sqrt{\pi a}}{\Phi} \tag{2.22}$$

with the membrane and bending structural stresses σ_m and σ_b, with the geometry factors Y_m and Y_b due to the free plate surfaces (dependent on a/t and $a/2c$, with crack depth a, crack length $2c$ and plate thickness t), with the magnification factors M_{km} and M_{kb} on membrane and bending stresses due to the notch stress concentration factor K_t (dependent on the geometrical notch parameters and the ratio a/t, $M_k = K_t$ for $a/t = 0$) and with Φ the complete elliptical integral of the second kind due to the curved crack front (dependent on the aspect ratio a/c). The factors M_k and Y may be supplemented by a factor denoting the influence of a finite plate width. The parameter $1/\Phi$ characterises the decrease in the SIF of an internal elliptical or external semi-elliptical crack relative to a crack with a straight crack front penetrating the plate thickness ($1/\Phi = 0.64$ for $a/c = 1.0$).

A large body of data characterising the dependency of $M_k Y_m$ on a/t and a/c is available for plane models of one-sided transverse attachment joints which are considered as representative for the local situation at tubular welded joints. A semi-elliptical surface crack at the toe of the one-sided fillet weld is analysed for membrane and bending stresses in the base plate. Easy-to-use formulae for the factors M_k and Y of cracks at the weld toe of various other welded joints are available.

Another application of the SIF concept is directed to the crack-like slit ends at the root of fillet welds in cruciform joints, attachment joints, lap joints and cover plate joints. Various degrees of weld penetration are analysed. Corresponding SIF formulae are available in the open literature.

The stress intensity factors referenced above presume force-controlled loading conditions, i.e. the basic structural stresses at the crack site remain unchanged while the crack propagates with increasing SIF. As far as crack growth in structural components is considered, deformation-controlled loading conditions are often more appropriate. The dependency of the SIF on crack depth is then fundamentally changed, it is decreasing. This effect is termed ‘load shedding’.

2.2.8 SIFs at Spot-Welded Lap Joints

The singular and non-singular slit tip stresses at the edge of spot welds in lap joints may be determined in a two-step analysis procedure (Radaj et al. 2006, ibid. pp. 366–512). In a first step, the structural stresses around the weld spot edge are calculated based on engineering formulae or based on a FE model consisting of plane thin-shell elements. Bernoulli's condition that plane cross sections of the thin-shell elements remain plane is valid. This results in a linear distribution over the plate thickness of superimposed membrane and bending tensile or compressive stresses and also of membrane and bending spot-edge-parallel shear stresses. The spot-edge-transverse shear stresses are defined as the medium of a parabolic distribution over the plate thickness. In a second step, these internal structural stresses which vary along the edge line of the weld spot are applied to the plane cross-sectional model of the weld spot edge containing the slit tip. Simple but accurate formulae are available for the SIFs, the *T*-stress and the *S*-stress dependent on the decomposed structural stresses and on the square-root on plate thickness t. The assumption behind the cross-sectional model of only one half of the weld spot is, that the weld spot diameter d is substantial larger than the plate thickness t, so that a direct influence of the opposed weld spot side is excluded. It has been found that in the SIF formulae for the slit tips in thin-sheet lap joints, the sheet thickness t is the dominating square-root parameter, substituting the crack length in the conventional formulae for crack tip SIFs.

The originally proposed decomposition procedure for the structural stresses at the weld spot edge in joints of equal plate thickness, Fig. 2.4, is based on symmetric and antimetric (indices ++ and +−) stresses or forces in the upper and lower plate (indices u and l) of the cross-sectional model, resulting in the different singular and non-singular loading modes (Radaj 1989). This procedure attributes primary concern to self-equilibrating force groups. The idea behind this is that forces which are transmitted from the upper to the lower plate may produce other slit tip stresses than when transmitted to a remote support within the weld spot. A stress is termed 'symmetric', if it has the same value and sign (or direction) at corresponding points above and below the slit tip. For 'antimetric' stresses, the sign is reversed.

The procedure is presented and discussed in detail in the author's book (Radaj et al. 2006, ibid. pp. 447–453), so that the presentation here can be restricted to the derived SIF formulae.

The original SIF formulae with the symmetric and antimetric stress portions in joints of equal plate thickness t read as follows:

$$K_{\mathrm{I}} = \left(\frac{1}{\sqrt{3}} \sigma_{\mathrm{b}}^{++} + 2.23 \tau_{\perp}^{+-} \right) \sqrt{t} \tag{2.23}$$

$$K_{\mathrm{II}} = \left(\frac{1}{2} \sigma_{\mathrm{m}}^{+-} + \frac{1}{2} \sigma_{\mathrm{b}}^{+-} + 0.55 \tau_{\perp}^{++} \right) \sqrt{t} \tag{2.24}$$

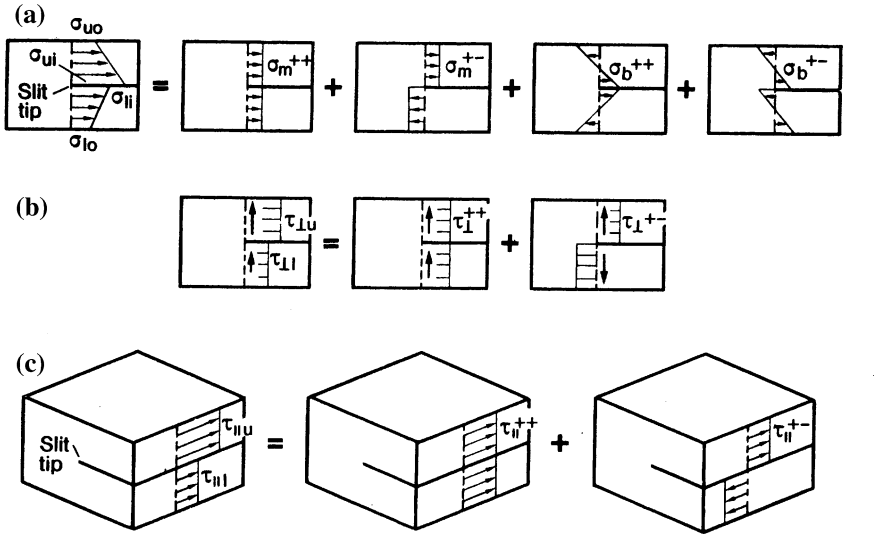

Fig. 2.4 Decomposition of the total structural stress state at the slit tip into symmetrical and antimetrical stress portions; membrane and bending stresses (**a**), transverse shear stresses (**b**) and longitudinal shear stresses (**c**); (Radaj 1989; Radaj and Zhang 1991(1), 1991(2))

$$K_{\mathrm{III}} = \sqrt{2}\tau_{\parallel}^{+-}\sqrt{t} \tag{2.25}$$

The factors 2.23 and 0.55 have been determined by an accurate boundary element analysis (Radaj 1989). Slightly different values, 2.36 and 0.60, have been derived based on a *J*-integral formulation (Zhang 1999). It is obvious from Eqs. (2.23) and (2.24) that the edge-transverse shear stresses have a remarkable influence on the SIFs K_{I} and K_{II}.

The SIFs may also be expressed in the non-decomposed stresses:

$$K_{\mathrm{I}} = [0.144(\sigma_{\mathrm{ui}} - \sigma_{\mathrm{uo}} + \sigma_{\mathrm{li}} - \sigma_{\mathrm{lo}}) + 1.115(\tau_{\perp\mathrm{u}} - \tau_{\perp\mathrm{l}})]\sqrt{t} \tag{2.26}$$

$$K_{\mathrm{II}} = [0.25(\sigma_{\mathrm{ui}} - \sigma_{\mathrm{li}}) + 0.275(\tau_{\perp\mathrm{u}} + \tau_{\perp\mathrm{l}})]\sqrt{t} \tag{2.27}$$

$$K_{\mathrm{III}} = 0.707(\tau_{\parallel\mathrm{ui}} - \tau_{\parallel\mathrm{li}})\sqrt{t} \tag{2.28}$$

By introduction of the edge-parallel shear stresses on the inner plate side (index i) in Eq. (2.28), equilibrated bending shear stresses can be assumed superimposed on the membrane shear stresses. The K_{III} value thus determined should be conservative (Radaj et al. 2006, ibid. pp. 449–450).

The original decomposition procedure above has two deficiencies. The non-singular bending stresses are not separated and the SIF K_{II} is derived from two decomposed normal stresses, Eq. (2.24), whereas one such stress should be sufficient. These deficiencies were soon realised and removed (Radaj and Zhang 1991(1), 1991(2)). A strictly mode-related decomposition was the result, with the

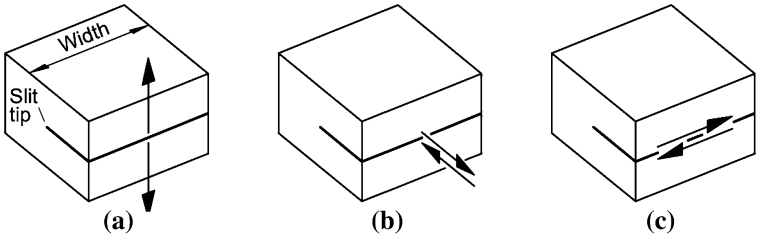

Fig. 2.5 Self-equilibrating loading states generating a stress singularity at the slit tip; pure mode I (**a**), pure mode II (**b**) and pure mode III (**c**); the pairs of resultant forces are assumed to act on the slit flanks in opposite directions in the same line each; they are evenly distributed over the specimen width; (Radaj et al. 2006)

definition that the pure modes I, II and III are produced by self-equilibrated remote boundary forces, Fig. 2.5. Non-singular modes 0 may be superimposed (in-plane membrane and bending stresses, out-of-plane membrane shear stress), which correspond to the support forces.

The characteristic stress of pure mode I loading is the counter-bending stress σ_{cb}, and that of pure mode II loading the tensile-bending stress σ_{tb}, compare Eqs. (2.26) and (2.27):

$$\sigma_{cb} = \frac{1}{4}(\sigma_{ui} - \sigma_{uo} + \sigma_{li} - \sigma_{lo}) \tag{2.29}$$

$$\sigma_{tb} = \frac{1}{2}(\sigma_{ui} - \sigma_{li}) \tag{2.30}$$

Neglecting the edge-transverse shear stress $\tau_{\perp}$, the SIFs according to Eqs. (2.26) and (2.27) have the following simple form:

$$K_I = \frac{1}{\sqrt{3}}\sigma_{cb}\sqrt{t} \tag{2.31}$$

$$K_{II} = \frac{1}{2}\sigma_{tb}\sqrt{t} \tag{2.32}$$

Other mode-related decompositions (mode I, mode II, mode 0 membrane and mode 0 bending) of the in-plane normal stresses are also possible. A principal statement is elucidating in this context (Seeger et al. 2005). The four independent normal stresses at the outer and inner plate surfaces in the cross-sectional model can always be substituted by or decomposed in four other independent stresses characterising definite linearised stress groups. It is straightforward to select the following mode-related stresses as such: the mode II related antimetric membrane stress σ_m^{II}, the mode I related symmetric bending stress σ_b^{I} and the mode 0 related membrane and bending stresses, σ_m^0 and σ_b^0. Preference is given to these decomposed stress groups, because any stress state in the cross-sectional model can thus uniquely be described by simple expressions, especially too when considering

unequal plate thickness. Self-equilibrating stress groups are not a necessary condition, because the non-equilibrated stress portions are compensated by mode 0 stress distributions. Above, the pure modes I, II and III are defined by membrane and bending stresses which are not self-equilibrated in general. Mode 0 stresses and support forces are not identical as a consequence.

Another argument supports the decomposition of the shear stresses $\tau_{\perp u}, \tau_{\perp l}$, $\tau_{\parallel u}$, $\tau_{\parallel l}$ into symmetric and antimetric stress groups without consideration of the equilibrium conditions. The resulting decomposed stresses are identical with those from a force-equilibrated decomposition also in the case of unequal plate thickness. Once more, self-equilibration is not a necessary condition.

The revised decomposition into the mode-related stresses just mentioned for joints of equal plate thickness is presented in Fig. 2.6. The SIFs are derived therefrom by the following expressions:

$$K_{\mathrm{I}} = \left(\frac{1}{\sqrt{3}}\sigma_{\mathrm{b}}^{\mathrm{I}} + 2.23\tau_{\perp}^{\mathrm{I}}\right)\sqrt{t} \tag{2.33}$$

$$K_{\mathrm{II}} = \left(\frac{1}{2}\sigma_{\mathrm{m}}^{\mathrm{II}} + 0.55\tau_{\perp}^{\mathrm{II}}\right)\sqrt{t} \tag{2.34}$$

$$K_{\mathrm{III}} = \sqrt{2}\tau_{\parallel}^{\mathrm{III}}\sqrt{t} \tag{2.35}$$

It should be noted that $\sigma_{\mathrm{b}}^{\mathrm{I}} = \sigma_{\mathrm{cb}}$ and $\sigma_{\mathrm{m}}^{\mathrm{II}} = \sigma_{\mathrm{tb}}$, which are the characteristic self-equilibrated stresses. This is an indication that self-equilibrated loading is the primary condition of the pure loading modes.

The expression for the non-singular slit tip stresses are:

$$T = \sigma_{\mathrm{m}}^{0} + \sigma_{\mathrm{b}}^{\mathrm{I}} = \frac{1}{2}(\sigma_{\mathrm{ui}} + \sigma_{\mathrm{li}}) \tag{2.36}$$

$$S = \tau_{\parallel}^{0} = \frac{1}{2}(\tau_{\parallel u} + \tau_{\parallel l}) \tag{2.37}$$

The following remark may be added. The non-singular bending stress σ_{b}^{0} characterises a third order term in the series expansion of the stress field, whereas T-stress and S-stress are second order terms.

The original decomposition procedure for the structural stresses at the weld spot edge in joints of unequal plate thickness (Radaj and Zhang 1991(1), 1991(2)) is related to the self-equilibrated pure modes I, II and III. The mode 0 bending stresses were not separated in the first version. The correspondingly amended procedure is visualised for the in-plane normal-stresses in Fig. 2.7.

At first, some notes are necessary on the status of the relevant publications, which present two slightly different versions of the method. The original version (Radaj and Zhang 1991(1)) does not separate the mode 0 bending stress. This version has been taken over into the author's book (Radaj et al. 2006), because the coefficients for the K_{I} and K_{II} expressions are available only for this deficient

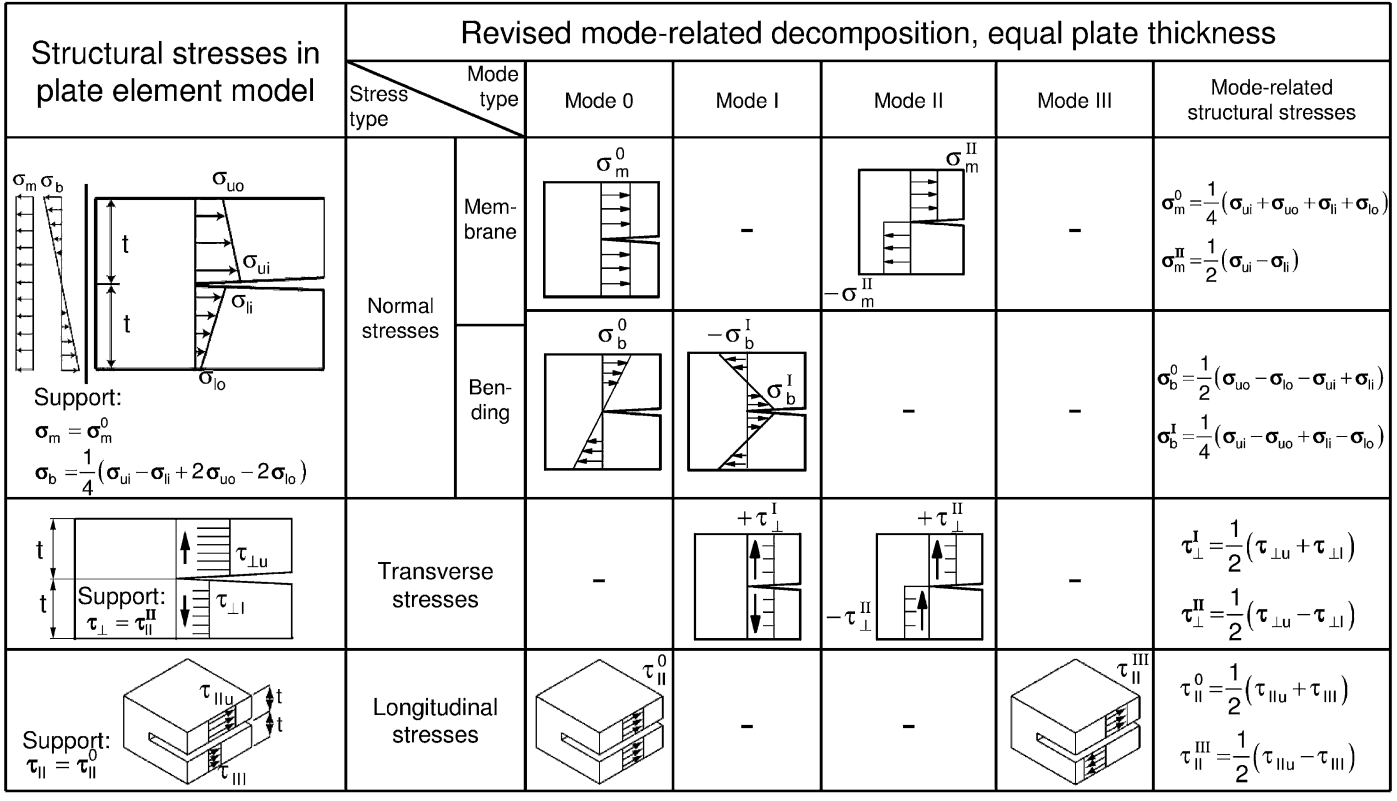

Fig. 2.6 Revised mode-related decomposition with equal plate thickness; (Seeger et al. 2005)

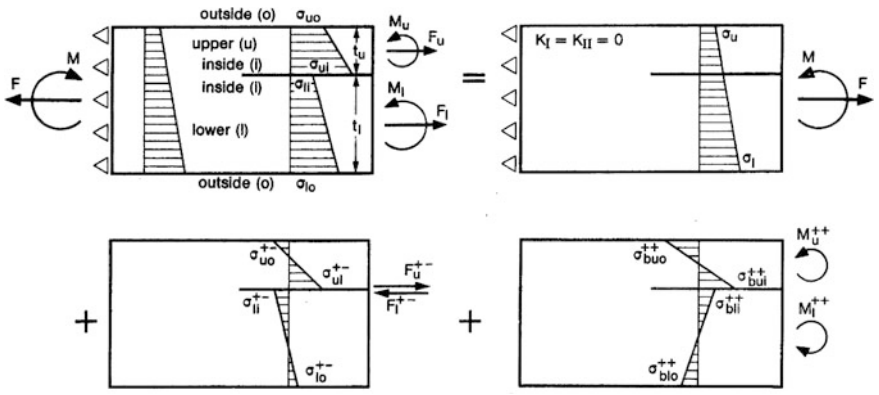

Fig. 2.7 Decomposition of the in-plane structural normal stress state at the slit tip of a lap joint cross-sectional model with unequal plate thickness into antimetrical (tension-bending) force and symmetrical moment (counterbending) portions after separation of the non-singular membrane and bending stress portion; (Radaj and Zhang 1991(2))

method (without effect on the numerical SIF results). An inconsistency in the expressions for the decomposed edge-parallel shear stresses in the book, ibid. Eqs. (10.29) and (10.30), has to be mentioned. These stresses are not self-equilibrating for thickness ratios $\delta \neq 1.0$. They should have the same form as the preceding transverse shear expressions. The coefficients K^{+-}_{IIIu} are related to the self-equilibrating stresses (Radaj and Zhang 1991(1)).

The revised decomposition into mode-related membrane and bending stresses for joints of unequal plate thickness without the condition of self-equilibration is presented in Fig. 2.8. The SIFs are derived therefrom by the following expressions:

$$K_{\mathrm{I}} = (k_{\mathrm{I,b}}\sigma_{\mathrm{b}}^{\mathrm{I+II}} + k_{\mathrm{I,m}}\sigma_{\mathrm{m}}^{\mathrm{II+I}} + k_{\mathrm{I},\perp}\tau_{\perp}^{\mathrm{I}} + k^{*}_{\mathrm{I},\perp}\tau_{\perp}^{\mathrm{II+I}})\sqrt{t_{\mathrm{u}}} \tag{2.38}$$

$$K_{\mathrm{II}} = (k_{\mathrm{II,b}}\sigma_{\mathrm{b}}^{\mathrm{I+II}} + k_{\mathrm{II,m}}\sigma_{\mathrm{m}}^{\mathrm{II+I}} + k_{\mathrm{II},\perp}\tau_{\perp}^{\mathrm{II+I}})\sqrt{t_{\mathrm{u}}} \tag{2.39}$$

$$K_{\mathrm{III}} = k_{\mathrm{III},\parallel}\tau_{\parallel}^{\mathrm{III}}\sqrt{t_{\mathrm{u}}} \tag{2.40}$$

The situation above is more complicated with unequal compared with equal plate thickness. The decomposition procedure is the same in principle, but not all decomposed stresses can be connected with a single loading mode. Some are related to two modes, but one of the two modes is dominant in general.

The stresses with a two-mode effect have an additional index related to the second mode: $\sigma_{\mathrm{b}}^{\mathrm{I}} \rightarrow \sigma_{\mathrm{b}}^{\mathrm{I+II}}$, $\sigma_{\mathrm{m}}^{\mathrm{II}} \rightarrow \sigma_{\mathrm{m}}^{\mathrm{II+I}}$, $\tau_{\perp}^{\mathrm{II}} \rightarrow \tau_{\perp}^{\mathrm{II+I}}$. The number of stress terms in the expressions for K_{I} and K_{II} is correspondingly enlarged. The coefficients of the stress terms have an index for the mode type (I, II, III), to which they contribute, and an index for the stress type (b, m, $\perp$, $\parallel$), to which they are connected. These coefficients depend on the ratio of the plate thicknesses, $\delta = t_{\mathrm{u}}/t_{\mathrm{l}}$ (indices for upper

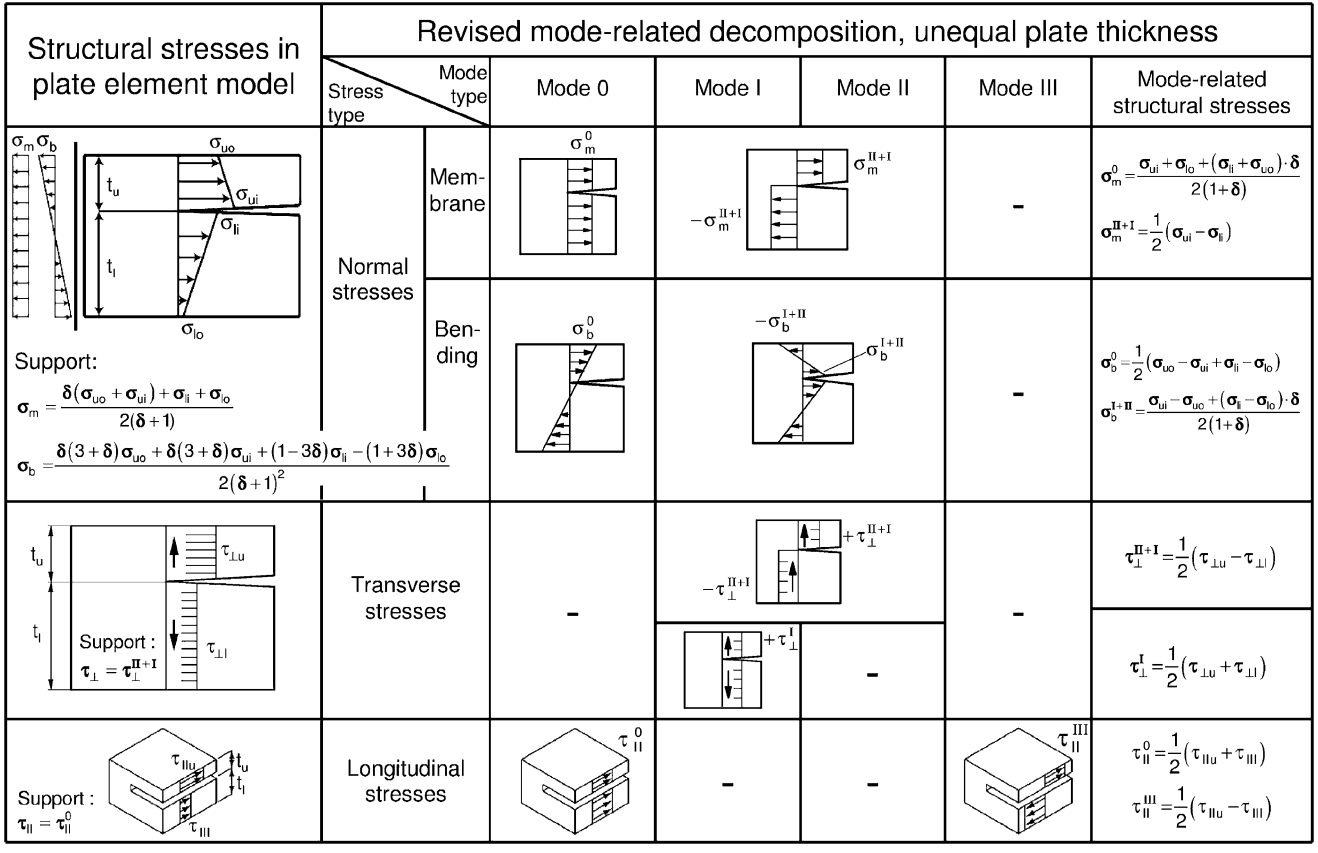

Fig. 2.8 Revised mode-related decomposition with unequal plate thickness; (Seeger et al. 2005)

Table 2.1 Coefficients of mode-related structural stresses for the SIFs K_I, K_{II} and K_{III} in joints of unequal plate thicknesses t_u (upper plate) and t_l (lower plate); (Radaj and Zhang 1999; Seeger et al. 2005)

	Mode I				Mode II			Mode III
$\delta = t_u/t_l$	$k_{I,b}$	$k_{I,m}$	$k_{I,\perp}$	$k^*_{I,\perp}$	$k_{II,b}$	$k_{II,m}$	$k_{II,\perp}$	$k_{III,\parallel}$
1.0	0.578	0	2.236	0	0	0.500	0.550	1.414
0.556	0.652	−0.218	2.025	0.876	−0.068	0.593	0.429	1.247
0.333	0.695	−0.409	1.911	1.245	−0.130	0.700	0.325	1.155
0.120	0.734	−0.671	1.794	1.656	−0.226	0.905	0.099	1.058

and lower plate). The upper plate thickness t_u is the square root parameter in the SIFs.

The coefficients of the accordingly decomposed stresses in the SIF formulae are listed in Table 2.1 for several values of δ. In the line with $\delta = 1.0$, the coefficients from Eqs. (2.23) and (2.24) appear. The coefficients $k_{I,b}$, $k_{I,m}$, $k_{II,b}$, $k_{II,m}$ for the other values of δ have been determined by application of the FE programme FRANC2D/L. The values of $k_{I,\perp}$, $k^*_{I,\perp}$, $k_{II,\perp}$, $k_{III,\parallel}$ are derived from the formulae in the original publication (Radaj and Zhang 1991(1), 1991(2)). The coefficient $k_{III,\parallel}$ is found for a membrane shear stress distribution. Bending shear stresses are not taken into account.

The coefficients of the originally decomposed stresses in the SIF formulae (inclusive of $K_{res} = (K_I^2 + K_{II}^2)^{1/2}$) are available dependent on the plate thickness ratio δ as closed form expressions and also in graphical form (Radaj and Zhang 1991(1)). They are determined based on a combination of J-integral and boundary element method. The application to the spot-welded tensile-shear and cross tension specimens is also demonstrated.

Spot-welded lap joints have also been investigated with dissimilar plate materials (Radaj and Zhang 1992, 1994). Different elastic constants are assigned to the upper and lower plate. An oscillatory stress singularity occurs at the bimaterial slit tip. It is described by special unconventional SIFs which may be substituted by the conventional SIFs in an approximative sense for engineering applications.

Only the original mode-related version of the method, which is based on self-equilibrated stress groups, is reviewed below. A revised version based on possibly simpler, non-equilibrated stress groups has been proposed, but not elaborated (Seeger et al. 2005). Any version has to come up with two complications. First, the mode 0 membrane and bending loading states have to be based on a linear distribution of the membrane and bending strains (not of the stresses), because only these produce no stress singularity at the slit tip. The corresponding membrane and bending stresses show a step and kink in gradient in the slit and interface plane. Second, the conventional SIFs K_I and K_{II} (not K_{III}) describe the stresses at the slit tip only approximately. Especially, the step in the interface-parallel normal stress values is not reproduced, but the deviations from the exact values are not too large (Radaj and Zhang 1994).

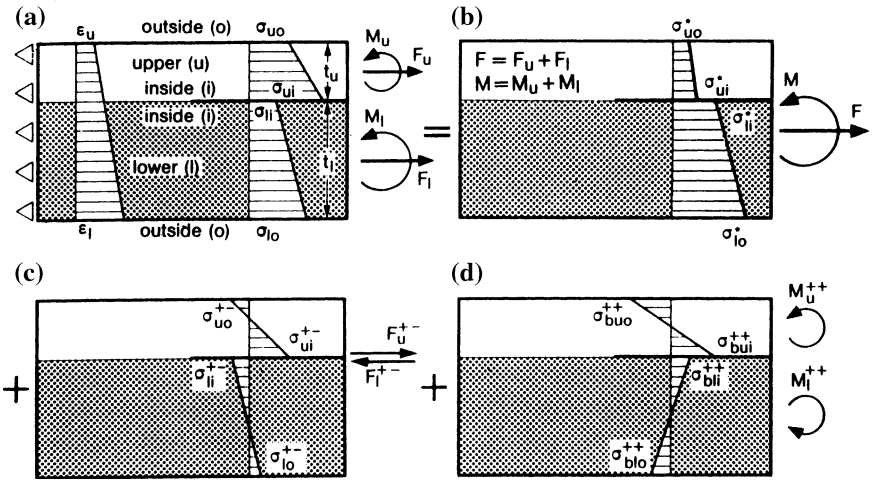

Fig. 2.9 Decomposition of the in-plane structural normal stress state at the slit tip of a bimaterial lap joint cross-sectional model (**a**), into a stress portion without singularity effect (**b**), and into tension-bending and counterbending portions with singularity effect (**c**, **d**); (Radaj and Zhang 1992)

The self-equilibrated decomposition of the membrane and bending stresses taking bimaterial conditions into account is based on Fig. 2.9. The condition of plane cross-sections is expressed by the linear distribution of the strains between ε_u and ε_l. The original plate stresses to be decomposed are σ_{uo}, σ_{ui}, σ_{li}, σ_{lo}. The mode 0 loading state is characterised by σ^*_{uo}, σ^*_{ui}, σ^*_{li}, σ^*_{lo}. The step in the stress values and in their gradient is clearly visible. Finally, the tension and counter-bending loading states are shown which are related to the stress singularity.

The SIFs K_I, K_{II} and K_{III} are given by the following expressions, all coefficients and stresses referring to the upper plate:

$$K_I = (k_{I,tb}\sigma_{tb} + k_{I,cb}\sigma_{cb} + k^{++}_{I,\perp}\tau^{++}_{\perp} + k^{+-}_{I,\perp}\tau^{+-}_{\perp})\sqrt{t_u} \tag{2.41}$$

$$K_{II} = (k_{II,tb}\sigma_{tb} + k_{II,cb}\sigma_{cb} + k^{++}_{II,\perp}\tau^{++}_{\perp} + k^{+-}_{II,\perp}\tau^{+-}_{\perp})\sqrt{t_u} \tag{2.42}$$

$$K_{III} = k_{III,\parallel}\tau^{+-}_{\parallel}\sqrt{t_u} \tag{2.43}$$

The coefficients k_μ (μ = I,tb, I,cb etc.) depend on the modulus of elasticity ratio of the two materials and on the plate thickness ratio $\delta = t_u/t_l$. They are available as closed form expressions for $\delta = 1.0$ (Radaj and Zhang 1992), gained by a combination of the boundary element and the J-integral method. The plane strain condition is appropriate when considering spot-welded joints. The linear-elastic behaviour of isotropic materials is described by two independent elastic constants, mostly the modulus of elasticity E and Poisson's ratio ν, but sometimes also the shear modulus G. The coefficients k_μ are then stated dependent on the shear modulus ratio $\beta = G_u/G_l$ supplemented by Poisson's ratios ν_u and ν_l.

The initial step in the normal stress decomposition procedure is the separation of the mode 0 non-singular membrane and bending stresses based on the condition of a linear strain distribution (plane cross-sections remaining plane). Rather complicated expressions are gained for the appertaining stresses σ^*_{uo}, σ^*_{ui}, σ^*_{li}, σ^*_{lo} (see Fig. 2.9). The characteristic stresses for mode I and mode II loading, counter-bending (index cb) and tensile-bending (index tb), are then expressed as follows:

$$\sigma_{cb,u} = \sigma^*_{ui} - \sigma_{ui} + 2(\sigma^*_{uo} - \sigma_{uo}) \tag{2.44}$$

$$\sigma_{tb,u} = 2(\sigma_{ui} - \sigma^*_{ui} + \sigma_{uo} - \sigma^*_{uo}) \tag{2.45}$$

These two equations are easily derived by considering the stresses in the upper plate after deduction of the mode 0 stresses:

$$\sigma_{ui} - \sigma^*_{ui} = \sigma_{tb,u} + \sigma_{cb,u} \tag{2.46}$$

$$\sigma_{uo} - \sigma^*_{uo} = -\frac{1}{2}\sigma_{tb,u} - \sigma_{cb,u} \tag{2.47}$$

They are valid for any plate thickness ratio and any material combination.

In the referenced publication (Radaj and Zhang 1992), ibid. Eq. (37), $\sigma_{tb,u}$ is erroneously introduced with the factor 1/2 instead of 2 in Eq. (2.45) above, but the expressions for $k_{I,tb}$ and $k_{II,tb}$ are simultaneously changed, so that K_I and K_{II} remain unchanged. Actually, $k_{I,tb} = 0$ for any modulus of elasticity ratio combined with $\delta = 1.0$ (see Fig. 6 in the referenced publication).

The decomposition of the edge-transverse and edge-parallel shear stresses based on self-equilibrated forces can be substituted, as already stated, by a decomposition into symmetric and antimetric stress groups without causing a change in the results:

$$\tau^{++}_{\perp} = \frac{1}{2}(\tau_{\perp u} + \tau_{\perp l}) \tag{2.48}$$

$$\tau^{+-}_{\perp} = \frac{1}{2}(\tau_{\perp u} - \tau_{\perp l}) \tag{2.49}$$

$$\tau^{+-}_{\parallel} = \frac{1}{2}(\tau_{\parallel u} - \tau_{\parallel l}) \tag{2.50}$$

The expression for $\tau^{+-}_{\parallel}$ is derived without considering the effect of superimposed bending shear stresses.

2.2.9 Equivalent SIFs under Mixed Mode Loading Conditions

Mixed mode loading conditions at crack or slit tips pose the question of how the SIFs of the different modes should be superimposed to give an equivalent SIF (also termed 'resultant SIF'), equivalent in respect of fatigue failure by crack initiation

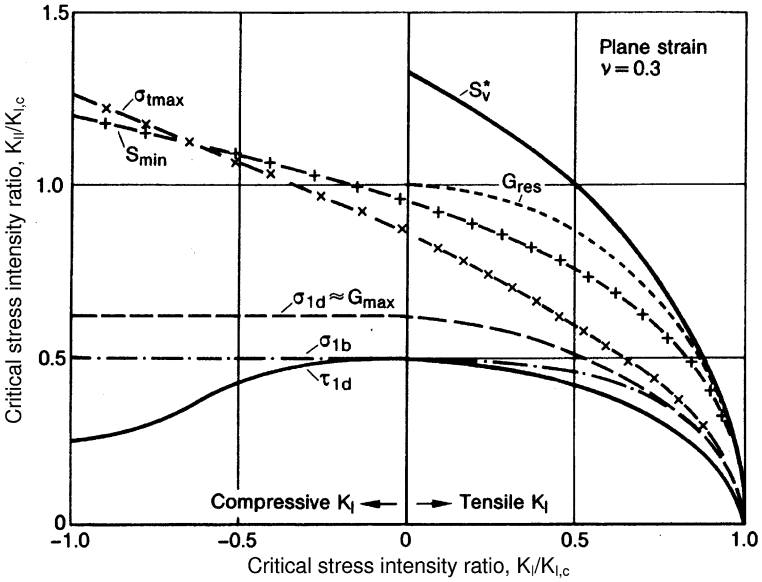

Fig. 2.10 Critical stress intensities (normalised by $K_{I,c}$) characterising crack propagation under mixed mode I and II loading conditions; various failure criteria; curve designations specified in the text; (Radaj and Zhang 1995[(1)])

and propagation. This includes the question of what critical value of K_{II} or K_{III} is equivalent to the critical value of K_I. The answer to these questions is complicated by the fact that the crack under mixed-mode loading conditions usually propagates in a non-coplanar manner, i.e. the crack changes its direction of propagation ('kinked crack'). The crack propagation angle ('kink angle') must be found first. Additional assumptions are necessary to do this. Several hypotheses and related criteria have been proposed to describe crack initiation and propagation under mixed-mode conditions. They are not generally verified by testing. It is therefore necessary to check the applicability of the criterion selected in each individual case.

The critical conditions for crack initiation and propagation under mixed mode I and II conditions, specified according to different failure criteria, are plotted in Fig. 2.10. The tensile K_I part of the diagram is mainly taken from the literature (Sih 1975). The compressive part is supplemented as far as the criteria are defined in this region. The critical SIF ratios $K_I/K_{I,c}$ and $K_{II}/K_{I,c}$ refer to the critical SIF $K_{I,c}$ in mode 1 loading: $K_{I,c} = K_{Ic}$ (fracture toughness) for brittle fractures, $K_{I,c} = K_{th}$ (threshold SIF) or $K_{I,c} = \overline{\sigma}_E(\pi\rho^*/2)^{1/2}$ (endurance limit stress $\overline{\sigma}_E$ averaged over microstructural support length ρ^*) for fatigue fractures. The following failure criteria are evaluated:

- The maximum tangential stress $\sigma_{t\ max}$ at the edge of a 'core region' around the crack tip (radius r^*) is decisive for crack propagation (Erdogan and Sih 1963).
- The minimum strain energy density at the edge of the core region expressed by the minimum strain energy density factor S_{min} is decisive for crack propagation (Sih 1973, 1974, 1975).
- The maximum dilatational strain energy density at the edge of the core region expressed by the corresponding factor S^*_{max} is decisive for crack propagation (Radaj and Heib 1978).
- The resultant energy release rate G_{max} is decisive for coplanar crack propagation (Irwin 1957).
- The maximum energy release rate G_{res} is decisive for non-coplanar crack propagation (Hussain et al. 1974).
- The process zone criteria: brittle initiation of fracture occurs at a critical value of the first principal stress σ_{1b} at distance r^* in the direction of maximum (tensile) dilatational strain energy density; 'ductile' initiation of fracture occurs at a critical value of the principal shear stress τ_{1d} (or first principal stress σ_{1d}) at distance r^* in the direction of maximum (tensile) distortional strain energy density (Radaj and Zhang 1995(1))

There are major differences in curve shape and curve position both in the tensile and the compressive range of K_I which are caused by the different formal and physical contents of the criteria. The process zone criteria differ from one another to a minor extent only. They are conservative compared with the conventional criteria. The curve for the well-known and usually preferred Erdogan–Sih criterion of maximum tangential stress, for example, runs considerably higher, especially in the compressive K_I range. The reason for this is the fact that the criterion takes only the tangential stresses around the crack tip into account and neglects the radial stresses which are rather high under mode II conditions.

The consideration above, as far as fatigue-relevant, refers to constant-amplitude loading of an ideal crack or slit tip with negligible mean stress effects. In reality further important influencing parameters have to be considered such as mean stress intensity, residual stress intensity, non-singular stresses, non-proportional loading, crack or slit tip microstructural conditions and crack closure effects among others. Whether or not a definite criterion is applicable in the special case under consideration should finally be decided on the basis of mixed mode fatigue testing results. Such data are not readily available from the literature.

The preferred criterion in the case of spot-welded or seam-welded joints is the maximum tangential stress criterion. It states that the crack or slit tip subjected to mixed mode I and II loading will propagate in the direction in which the tangential tensile stress at a small distance from the crack tip reaches its maximum. This results in the crack propagation angle $\overline{\theta}$ as a function of the SIF ratio K_{II}/K_I, Fig. 2.11. The equivalent SIF K_{eq} then follows from the condition of identical values of $\sigma_{t\ max}$ in mixed mode and pure mode I loading:

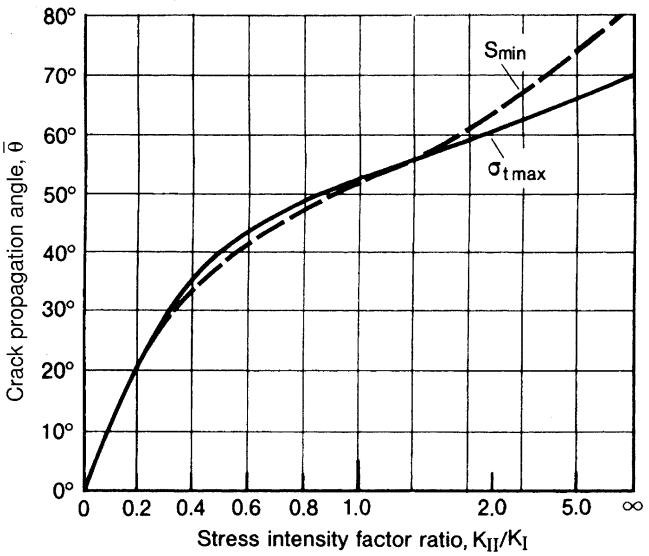

Fig. 2.11 Crack propagation angle $\overline{\theta}$ against ligament direction dependent on stress intensity factor ratio; maximum tangential stress criterion ($\sigma_{t\ max}$) compared with strain energy density criterion (S_{min}); (Yuuki et al. 1985[(1)], 1985[(2)]; Yuuki and Ohira 1986, 1989)

$$K_{eq} = \left(K_I \cos^2 \frac{\overline{\theta}}{2} - \frac{3}{2} K_{II} \sin \overline{\theta} \right) \cos \frac{\overline{\theta}}{2} \tag{2.51}$$

$$\tan \frac{\overline{\theta}}{2} = \frac{1}{4} \left(\frac{K_I}{K_{II}} \right) \pm \frac{1}{4} \sqrt{\left(\frac{K_I}{K_{II}} \right)^2 + 8} \tag{2.52}$$

where the positive root corresponds to a negative K_{II}, the negative root to a positive K_{II} (with positive K_I). Pure mode I loading results in $\overline{\theta} = 0°$ and $K_{eq} = K_I$, whereas pure mode II loading is associated with $\overline{\theta} = 70.5°$ and $K_{eq} = 1.15 K_{II}$.

The strain energy density criterion (Sih 1973, 1974, 1975) which comprises not only K_I and K_{II} but also K_{III}, is open to more varied physical interpretations and adaptable to more complex test data. The criterion states that the crack propagates in the direction of the minimum total strain energy density at the edge of the core region (approximately equal to the direction of maximum dilatational strain energy density), and that a critical value of the strain energy densities mentioned must be reached. The equivalent stress intensity factor K_{eq} follows from:

$$K_{eq} = \sqrt{A_{11} K_I^2 + A_{12} K_I K_{II} + A_{22} K_{II}^2 + A_{33} K_{III}^2} \tag{2.53}$$

The coefficients A_{11} to A_{33} are mainly dependent on the crack propagation angle (besides Poisson's ratio) which in turn is defined by the stress intensity factor ratios

K_{II}/K_I and K_{III}/K_I, respectively. The coefficients are often introduced as constant in order to simplify the procedure. The following simplified version of Eq. (2.53) follows from the application of the strain energy density criterion to the single-mode loading states of a centre crack in the infinite plate. With Poisson's ratio $\nu = 0.28$, the ratios of critical SIFs are $K_{II,c}/K_{I,c} = 0.985$ and $K_{III,c}/K_{I,c} = 0.663$, thus yielding the following formula, (Sih 1973), ibid. Eqs. (16) and (18):

$$K_{eq} = \sqrt{K_I^2 + 1.03K_{II}^2 + 2.27K_{III}^3} \tag{2.54}$$

A similar equation is obtained proceeding from the resultant energy release rate criterion (Irwin 1957) which assumes coplanar crack propagation and ignores the influence of the crack propagation angle:

$$K_{eq} = \sqrt{K_I^2 + K_{II}^2 + 1.39K_{III}^2} \tag{2.55}$$

Here, $\nu = 0.28$ is introduced, resulting in $1/(1 - \nu) = 1.39$. The same expression is derived based on the J-integral. This relationship has occasionally been applied to spot-welded lap joints (Linder et al. 1998).

The process zone criteria (Radaj and Zhang 1995(1)) also yield the general form of Eq. (2.53) partly extended by the addition of linear K_I and K_{II} terms. The corresponding curves in Fig. 2.10 (σ_{1d} and τ_{1d} for 'ductile' behaviour, σ_{1b} for brittle behaviour) result from evaluating the crack propagation angle in the different mixed-mode (inclusive of single-mode) loading states. The following more conservative form, Eq. (2.56), is proposed on the basis of the lower plotted curves in Fig. 2.10 substituting the older, less conservative form, Eq. (2.57), chosen in several comparative evaluations related to spot-welded joints (Radaj et al. 1990, 2006; Radaj and Giering 1994, 1995; Radaj and Zhang 1995(2)):

$$K_{eq} = \sqrt{K_I^2 + 3K_{II}^2 + K_{III}^2} \tag{2.56}$$

$$K_{eq} = \sqrt{K_I^2 + K_{II}^2 + K_{III}^2} \tag{2.57}$$

Kurath has found that K_{II}^2 combined with the factor 3 is valid in the case of spot welds of low-carbon steels and combined with the factor 2 in the case of spot welds of high-strength steels (Kurath 1992). The factor 4.3 has been derived from fatigue test results gained from single-spot specimens with various ratios K_I/K_{II} (Lee and Kim 2004).

Similar formulae have been derived based on the assumption of coplanar crack propagation described by a critical averaged stress over the microstructural length ρ^* (Neuber's hypothesis). Different failure criteria (Rankine's normal stress, von Mises' distortional strain energy, Beltrami's total strain energy) are combined with plane stress or plane strain multiaxiality conditions, see Sect. 1.5.2.

A diagram derived for kinked crack propagation under mixed-mode loading conditions of the crack in non-welded steels (Pook 1989) is presented in Fig. 2.12.

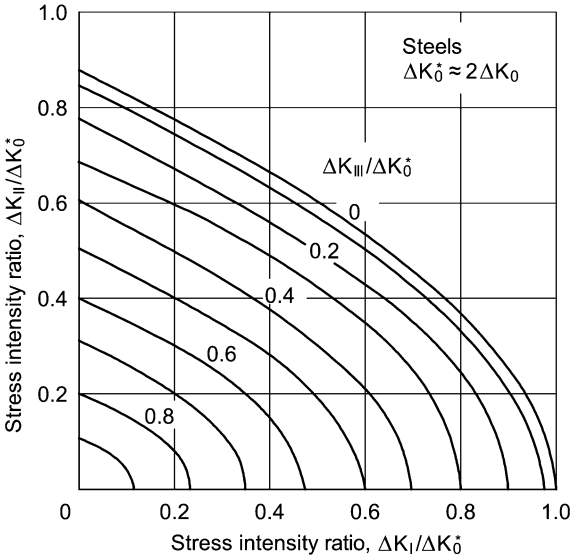

Fig. 2.12 Lower limit curves of the cyclic threshold stress intensity factors for kinked or branched macrocrack propagation under mixed mode loading conditions (modes I, II and III superimposed), based on test results for various steels; (Pook 1989)

The reference quantity ΔK_0^* is the cyclic threshold stress intensity factor for kinked or branched macro-crack propagation which may be about twice the threshold value for coplanar crack propagation in mode I.

The equivalent stress intensity factors according to Eqs. (2.51–2.57), when applied to cyclic loading, do not include the further influencing parameters governing fatigue, e.g. prestress or crack closure. Another shortcoming is the absence of the non-singular stress terms whose influence on fatigue crack initiation and propagation may be important (Haefele and Lee 1995).

2.2.10 Endurable Stress Intensity Factors

Endurable SIFs were originally defined in respect of static loading considering brittle fracture as limit condition. The fracture toughness K_{Ic} obtained in mode 1 fracture tests is the relevant material parameter. To ensure a sufficiently brittle specimen behaviour is an essential requirement on the testing procedure. Size and thickness of the specimen must be kept sufficiently large in order to maintain a predominantly elastic behaviour with three-dimensional tensile stresses ahead of the crack tip and with plastic deformations at the crack tip more or less avoided.

Endurable SIFs defined in respect of fatigue loading are the threshold SIFs ΔK_{th}, which are considered as material parameters. The parameter ΔK_{th} denotes the minimum cyclic stress range at which propagation of a (sufficiently long) crack is observed. In general, mode I testing in the high-cycle fatigue range is performed for this purpose. A typical lower bound value for structural steels is $\Delta K_{th} = 180$ MPa mm$^{1/2}$ (valid for $R = 0$).

The existence of a threshold value is explained by crack closure phenomena occurring in cyclic loading (Elber 1970, 1971). Under plane stress conditions, crack closure originating from plastic deformation at the crack tip is the predominant effect. Under plane strain conditions, other phenomena are prevailing: surface roughness, fracture particles and oxide formation.

A rough estimate of ΔK_{th} can also be gained on the basis of Neuber's microstructural support hypothesis, using the available data for structural steels (endurance limit for averaged stresses in polished surface, $\Delta\overline{\sigma}_E = 270$ MPa, microstructural length, $\rho^* = 0.1$ mm) the result is $\Delta K_{\mathrm{th}} = \Delta\overline{\sigma}_{\mathrm{E}}(\pi\rho^*/2)^{1/2} = 107\,\mathrm{MPa\,mm^{1/2}}$.

The use of endurable SIFs ΔK for the fatigue assessment of spot-welded joints is well established. Several investigations have been performed with tensile-shear loaded and peel-tension loaded specimens made of low-alloy steels, high-strength steels among them. The test results are plotted in the form of *K–N* curves (endured cycles *N* for different SIFs ΔK, interpreted as endurable SIFs ΔK over cycles *N*). These investigations and their results have been reviewed and compared (Radaj et al. 2006, ibid. pp. 471–476). The scatter of the *K–N* curve of a definite specimen type under investigation is generally small, but the deviations between the results of different authors are large and often unexplained.

Most influential on these deviations is a deficient determination of the SIFs in the spot-weld specimen under consideration. Factors 0.2–3.0 occur in the literature compared with the correct values. Thus, the corresponding *K–N* curves are by the same factors too low or too high. In the following, only one typical *K–N* curve for spot-welded joints (Yuuki et al. 1985[(1)], 1985[(2)]; Yuuki and Ohira 1986, 1989) is further discussed. The SIF ΔK_{eq} is plotted over number of cycles *N* in logarithmic scales, Fig. 2.13, representing the *K–N* curve in the following form:

$$N = A_{\mathrm{k}}(\Delta K_{\mathrm{eq}})^{-k} \tag{2.58}$$

with the inverse slope exponent *k* and the coefficient A_{k} assumed to be material parameters. Similar investigations with comparable results can be found in the literature (Mizui et al. 1988; Linder et al. 1998).

The SIF ΔK_{eq} is determined according to the maximum tangential stress criterion. The inverse slope exponent results as $k = 4.5$. The calculated SIFs are by a factor of 0.7–0.8 too low. Taking this factor into account, the endurable SIFs for $N \geq 5 \times 10^6$ cycles roughly agree with the generally accepted lower bound value for non-welded structural steels, $\Delta K_{\mathrm{th}} = 180\ \mathrm{MPa\ mm^{1/2}}$.

The width of the scatter band of the *K–N* curve is well in agreement with other local parameter curves which are used for fatigue assessment. Attributing the failure probabilities $P_{\mathrm{f}} = 2.3$ and 97.7 % to the limiting curves in the figure, the following scatter range indices are derived:

$$T_N = N_{2.3}/N_{97.7} = 0.1, \quad T_\sigma = (T_N)^{1/k} = 0.6 \tag{2.59}$$

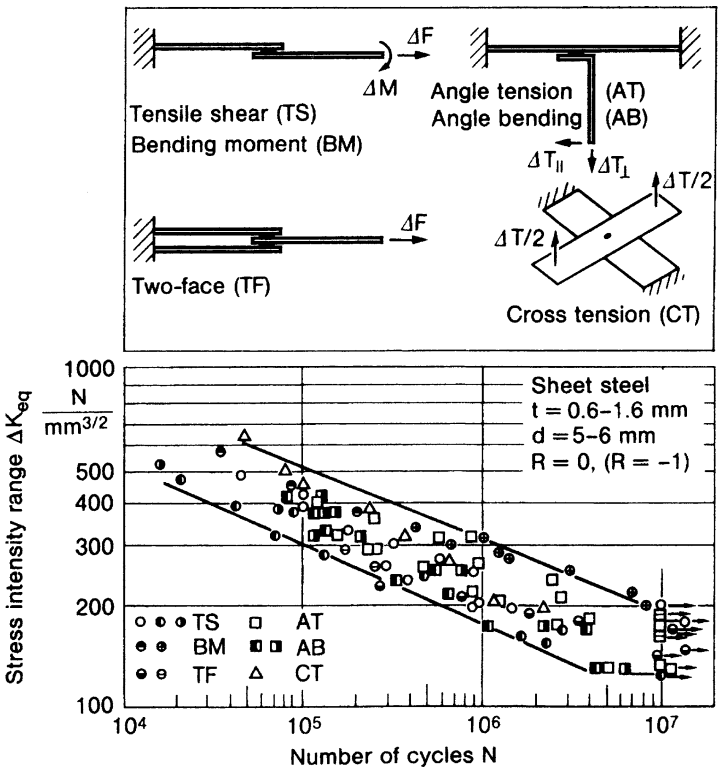

Fig. 2.13 Endurable stress intensity factor range at the weld spot of various specimens under different loading conditions according to maximum tangential stress criterion; inverse slope exponent $k = 4.5$; (Yuuki et al. 1985(1), 1985(2); Yuuki and Ohira 1986, 1989)

Several deficiencies besides too low SIFs in the investigation leading to Fig. 2.13 have to be noted: no thickness adaption of ΔK_{eq}, the non-singular or T-stress neglected, the total life evaluated instead of the crack initiation life.

2.2.11 Conclusions

The definition and use of SIFs for describing the stress field at crack tips or pointed slit tips and their application to fatigue and brittle fracture phenomena is a well established procedure for more than 50 years. Both the theoretical concepts and the application-relevant details are generally known. In this section, the SIF concept has been reviewed, giving the basic stress field equations for areas close to the crack tip or slit tip, separated in singular and non-singular parts, the singular part subdivided into the three loading modes, the non-singular part consisting of

T-stress, *S*-stress and a crack-front-parallel normal stress. Coupled singular effects may additionally occur where the crack front butts on a free surface.

The presented stress field equations and their governing parameters (SIFs K_I, K_{II} and K_{III}, *T*-stress, *S*-stress) are made available for seam-welded and spot-welded lap joints based on a structural stress analysis which avoids modelling of the singular stresses. Lap joints with equal and unequal plate thickness, respectively, are considered.

Mixed mode loading conditions are taken into account by equivalent SIF formulae representing various fracture criteria. Endurable SIFs for spot-welded joints are given in the form of a *K–N* curve with defined scatter range. These data are unreliable because the underlying SIF analysis results may be rather inaccurate. There is an urgent demand for a better substantiated and more accurate design *K–N* curve. Only relative fatigue assessments are possible based on accurate SIF analyses without a reliable *K–N* curve.

2.3 Notch Stress Intensity Factor Concept

2.3.1 Survey of Section Contents

The stress intensity factor (SIF) concept referring to crack tips or slit tips is extended to V-notch tips or re-entrant corner tips in the form of the notch stress intensity factor (NSIF) concept. The stress singularities associated with such pointed notches are less marked and expressed by a smaller negative exponent of the radial distance from the notch tip. The stress field equations for the area close to the notch tip are given for the three singular loading modes 1, 2 and 3 and for the non-singular mode characterised by the *S*-stress. A transverse singular effect coupled with mode 2 loading at free surfaces is identified and described.

The NSIF concept is applied to the re-entrant corner notches at the toe of fillet welds and butt welds. The size effect is naturally included. A link between structural stress and NSIF is established. Equivalent NSIF formulae are presented, referring to failure under mixed mode loading conditions. Endurable NSIFs dependent on number of load cycles *N* are given for non-load-carrying fillet welds of attachment joints. In parallel, the *J*-integral concept for pointed V-notches is presented and applied.

The expositions are primarily based on the pioneering analytical developments and their practical applications (mainly to welded joints) carried out by Atzori, Lazzarin, Tovo, Livieri, Meneghetti and others. A list of symbols and a list of references is available at the end of Chap. 2

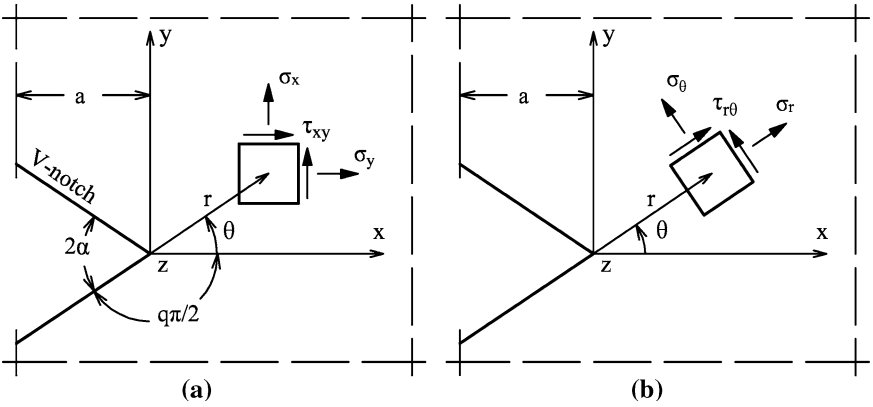

Fig. 2.14 Cartesian (**a**) and polar (**b**) coordinate systems with correspondingly defined stresses at the pointed V-notch tip; (Lazzarin and Tovo 1998)

2.3.2 Stress Field near Pointed V-Notches

The well-known concept of stress intensity factors describing the stress singularity at crack tips or slit tips under elastic material conditions can be transferred to pointed re-entrant corner notches (e.g. V-notches, stepped bars, weld toe notches). Whereas the asymptotic stress drop from the singularity at the crack tip is described by the inverse square root of the radial distance r from the crack tip (the exponent is minus 0.5), a smaller, notch angle dependent exponent occurs in the case of corner notches, which means that the degree of the singularity is reduced (Williams 1952). The stress field close to corner notches (just as the stress field close to crack tips) can be described by stress intensity factors (Gross and Mendelson 1972). These are named 'notch stress intensity factors' (NSIFs) as distinguished from the conventional stress intensity factors (SIFs) of crack tips.

The singular in-plane and out-of-plane stress fields at pointed corner notches can be specified by three notch loading modes (in analogy to the crack opening modes) related to the bisector plane of the notch: symmetric in-plane stresses (mode 1), antimetric in-plane stresses (mode 2) and out-of-plane shear stresses (mode 3). The corresponding notch loading modes are in-plane tensile loading, in-plane shear loading and out-of-plane shear loading.

The three basic loading modes with singular stresses at the notch tip produce the following asymptotic stress distribution (stress tensor σ_{ij}) around the notch tip, restricted to the first order terms (Williams 1952; Hasebe et al. 1990; Lazzarin and Tovo 1996, 1998; Quian and Hasebe 1997), Fig. 2.14:

$$\sigma_{ij} = \frac{1}{\sqrt{2\pi}}\left[K_1 r^{\lambda_1 - 1} f_{1,ij}(\theta) + K_2 r^{\lambda_2 - 1} f_{2,ij}(\theta) + K_3 r^{\lambda_3 - 1} f_{3,kz}(\theta)\right] \quad (2.60)$$

$$(\mathrm{i, j} = x, y \text{ and } \mathrm{k} = x, y \text{ or i, j} = r, \theta \text{ and k} = r, \theta)$$

The NSIFs K_1, K_2, K_3 depend on the magnitude of the load, the notch depth a, the notch opening angle 2α and further geometric parameters of the considered configuration. The angular functions $f_{1,ij}, f_{2,ij}, f_{3,kz}$ describe the angular distribution of the stress close to the notch tip. The relationship above is strictly valid for $r \to 0$ and approximately valid for values of r which are small in relation to the notch depth and other geometrical parameters of the configuration.

Just as with the crack problem ($2\alpha = 0$), the complete solution comprises non-singular higher order terms, but only a finite number for rather small values of 2α and no such terms for about $2\alpha > 45°$ (Atzori et al. 1997, ibid. Fig. 3).

The original solution for the in-plane stress field is based on the Airy stress function in polar coordinates in the following form, which comprises a symmetrical and an antimetrical component (Williams 1952; Sanford 2003):

$$F(r, \theta) = r^{\lambda+1} f(\theta) \tag{2.61}$$

where the values of λ have to be determined as part of the solution. The angular functions have to comply with the boundary conditions on the load-free faces of the V-notch (actually Williams started with the wedge, extending the solution to V-notches by considering inscribed wedge angles larger than π).

The stress can now be expressed in terms of r, λ and $f(\theta)$. Application of the boundary conditions produces a system of four simultaneous equations for four unknown constants. This system can be separated into two independent sets of equations related to the symmetrical and antimetrical stress fields. A non-trivial solution can be obtained only if the determinants of the coefficient matrices are equal to zero each. From this requirement, the condition follows:

$$\sin 2\lambda\alpha = \pm\lambda \sin 2\alpha \tag{2.62}$$

Since 2α is a fixed parameter for a specific wedge or notch, Eq. (2.62) provides the values of λ, called 'eigenvalues', necessary to ensure a nontrivial solution. Williams' solution has been widely used under the name 'eigenfunction expansion method' (Hasebe et al. 1990).

Another function-analytical approach for solving the problem of the in-plane loaded blunt V-notch comprising the pointed V-notch has been applied by Lazzarin et al. while the principal mathematical steps remained the same as in the Airy stress function method (Lazzarin and Tovo 1996, 1998; Lazzarin et al. 1998; Atzori et al. 1997). According to the Kolosov–Muskhelishvili complex stress function method, the stress fields at symmetrical V-notches subjected to mode 1 and mode 2 loading can be derived from two analytical functions defined in the following form:

$$\varphi(z) = az^{\lambda}, \quad \psi(z) = bz^{\lambda} + cz^{\mu} \tag{2.63}$$

where the coefficients a, b, c are complex and the exponents λ, μ real ($\lambda > \mu$). Williams' results would be gained with the term cz^{μ} being neglected.

In order to impose the boundary conditions, an auxiliary system of curvilinear coordinates $w = u + iv$ is introduced (Neuber 1958), which is related to the Cartesian coordinates $z = x + iy$ by the conformal mapping function

$$z = w^q \tag{2.64}$$

The condition $u = 0$ describes the pointed V-notch with notch opening angle 2α in the z-plane:

$$2\alpha = 2\pi - q\pi, \quad q = \frac{2\pi - 2\alpha}{\pi} \tag{2.65}$$

where $q = 2.0{-}1.0$ for $2\alpha = 0{-}2\pi$.

The eigenvalues in the considered method and application result from the following condition, separated into the mode 1 and mode 2 parts:

$$\sin \lambda_1 q\pi + \lambda_1 \sin q\pi = 0 \tag{2.66}$$

$$\sin \lambda_2 q\pi - \lambda_2 \sin q\pi = 0 \tag{2.67}$$

The stress field analysis for the V-notch subjected to out-of-plane shear loading (mode 3) is easier to perform, because the governing equation in terms of the out-of-plane displacements is a potential function substituting the bipotential function in the case of the in-plane stresses. Performing similar mathematical steps as before, the following eigenvalue equation is found (Quian and Hasebe 1997):

$$\sin \lambda_3(2\pi - 2\alpha) = 0 \tag{2.68}$$

The first non-zero eigenvalue is simply:

$$\lambda_3 = \frac{\pi}{2\pi - 2\alpha} \tag{2.69}$$

Actually, Quian and Hasebe have solved the more complex case of an unsymmetrical V-notch with a bimaterial interface ahead of the notch root, but with restriction to pointed notches.

The (first) eigenvalues λ_1, λ_2, λ_3 defining the degree of the stress singularity at the notch tip depend solely on the notch opening angle 2α (Williams 1952; Carpenter 1984), Fig. 2.15. The eigenvalue 0.5 is related to crack tips, $2\alpha = 0$, and the eigenvalue 1.0 (no singularity) to straight edges, $2\alpha = \pi$ (but only for mode 1 and mode 3). The eigenvalues for mode 1 loading are slightly smaller than those for mode 3 loading. They are substantially smaller in relation to mode 2 loading, thus designating severer singularities. The stress singularity in mode 2 loading is weaker and vanishes completely for $2\alpha \geq 102.6°$.

The in-plane stresses at the pointed V-notch ($\rho = 0$) are derived in the following form after introduction of the NSIFs K_1 and K_2 proposed by Gross and Mendelson (Lazzarin et al. 1998):

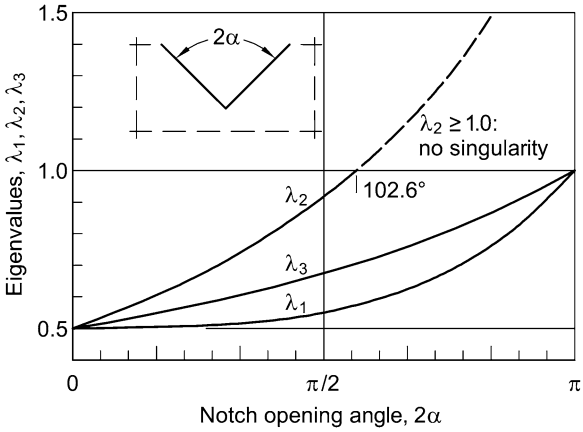

Fig. 2.15 Eigenvalues λ_1, λ_2, λ_3 defining the degree of stress singularity at pointed V-notches subjected to mode 1, 2, 3 loading conditions, dependent on notch opening angle 2α; (Lazzarin et al. 2004)

$$\left\{\begin{array}{c}\sigma_\theta\\ \sigma_r\\ \tau_{r\theta}\end{array}\right\}_1 = \frac{1}{\sqrt{2\pi}}\frac{r^{\lambda_1-1}K_1}{(1+\lambda_1)+\chi_1(1-\lambda_1)} \times\left[\left\{\begin{array}{c}(1+\lambda_1)\cos(1-\lambda_1)\theta\\ (3-\lambda_1)\cos(1-\lambda_1)\theta\\ (1-\lambda_1)\sin(1-\lambda_1)\theta\end{array}\right\}+\chi_1(1-\lambda_1)\left\{\begin{array}{c}\cos(1+\lambda_1)\theta\\ -\cos(1+\lambda_1)\theta\\ \sin(1+\lambda_1)\theta\end{array}\right\}\right]$$
$$\sigma_{z,1} = \nu(\sigma_{\theta,1}+\sigma_{r,1}) \quad \text{(plane strain)}$$
$$\chi_1 = -\frac{\sin(1-\lambda_1)q\pi/2}{\sin(1+\lambda_1)q\pi/2} \tag{2.70}$$

$$\left\{\begin{array}{c}\sigma_\theta\\ \sigma_r\\ \tau_{r\theta}\end{array}\right\}_2 = \frac{1}{\sqrt{2\pi}}\frac{r^{\lambda_2-1}K_2}{(1+\lambda_2)+\chi_2(1-\lambda_2)} \times\left[\left\{\begin{array}{c}-(1+\lambda_2)\cos(1-\lambda_2)\theta\\ -(3-\lambda_2)\cos(1-\lambda_2)\theta\\ (1-\lambda_2)\sin(1-\lambda_2)\theta\end{array}\right\}+\chi_2(1-\lambda_2)\left\{\begin{array}{c}-\sin(1+\lambda_2)\theta\\ \sin(1+\lambda_2)\theta\\ \cos(1+\lambda_2)\theta\end{array}\right\}\right]$$
$$\sigma_{z,2} = \nu(\sigma_{\theta,2}+\sigma_{r,2}) \quad \text{(plane strain)}$$
$$\chi_2 = -\frac{\sin(1-\lambda_2)q\pi/2}{\sin(1+\lambda_2)q\pi/2} \tag{2.71}$$

The antimetrical singular and symmetrical non-singular out-of-plane shear stresses have the following form (Zappalorto and Lazzarin 2011[(3)]) corresponding to Eq. (2.126):

$$\left\{ \begin{array}{c} \tau_{rz} \\ \tau_{\theta z} \end{array} \right\} = \frac{1}{\sqrt{2\pi}} K_3 r^{\lambda_3 - 1} \left\{ \begin{array}{c} \sin \lambda_3 \theta \\ \cos \lambda_3 \theta \end{array} \right\} \tag{2.72}$$

$$\left\{ \begin{array}{c} \tau_{rz} \\ \tau_{\theta z} \end{array} \right\}_S = S \left\{ \begin{array}{c} \cos \theta\pi/(\pi - \alpha) \\ -\sin \theta\pi/(\pi - \alpha) \end{array} \right\} \tag{2.73}$$

with $K_3^{(a)}$ and λ_a substituted by K_3 and λ_3, with $K_3^{(s)} r^{\lambda_s - 1}/(2\pi)^{1/2}$ substituted by the S-stress already introduced at crack tips ($2\alpha = 0$), Eq. (2.15), and with λ_s substituted by $\pi/(\pi - \alpha)$. The substitutions are introduced in order to make the equations above compatible with the hitherto used parameters.

The substitution related to the S-stress in only formally consistent with the existing analytical frame, because $S \to 0$ for $r \to 0$ according to $S = K_3^{(s)} r^{\lambda_s - 1}/(2\pi)^{1/2}$. Considering the S-stress to be a physical reality not only for $2\alpha = 0$, but also for $2\alpha > 0$ (similar to the situation with the T-stress), Eq. (2.73) is only a temporary expedient.

The characteristic stress components in the bisector plane ($\theta = 0$) have the following simple form:

$$\sigma_\theta(r, 0) = \frac{1}{\sqrt{2\pi}} K_1 r^{\lambda_1 - 1} \tag{2.74}$$

$$\tau_{r\theta}(r, 0) = \frac{1}{\sqrt{2\pi}} K_2 r^{\lambda_2 - 1} \tag{2.75}$$

$$\tau_{\theta z}(r, 0) = \frac{1}{\sqrt{2\pi}} K_3 r^{\lambda_3 - 1} \tag{2.76}$$

The NSIFs K_1, K_2, K_3 may be evaluated on the basis of the characteristic stress components above considering the limit values for $r \to 0$ (Gross and Mendelson 1972):

$$K_1 = \lim_{r \to 0} \sqrt{2\pi} r^{1 - \lambda_1} \sigma_\theta(r, 0) \tag{2.77}$$

$$K_2 = \lim_{r \to 0} \sqrt{2\pi} r^{1 - \lambda_2} \tau_{r\theta}(r, 0) \tag{2.78}$$

$$K_3 = \lim_{r \to 0} \sqrt{2\pi} r^{1 - \lambda_3} \tau_{\theta z}(r, 0) \tag{2.79}$$

The dimensions of K_1, K_2, K_3 are $\mathrm{N/mm}^{1+\lambda_1}$, $\mathrm{N/mm}^{1+\lambda_2}$, $\mathrm{N/mm}^{1+\lambda_3}$. The numerical values of K_1, K_2, K_3 can be set into comparison, e.g. as failure criteria, provided their dimension is identical, i.e. only under the condition of an identical notch angle besides an identical loading mode (for example, the stress intensity factors of crack tips are used in this way). In mode 1 loading, the stress intensity factors of crack tips are directly comparable with those of sharp notches, provided the notch opening angle is not too large ($2\alpha \leq 60°$, see Fig. 2.15), because the dimension does not change substantially. Mixed mode failure criteria must

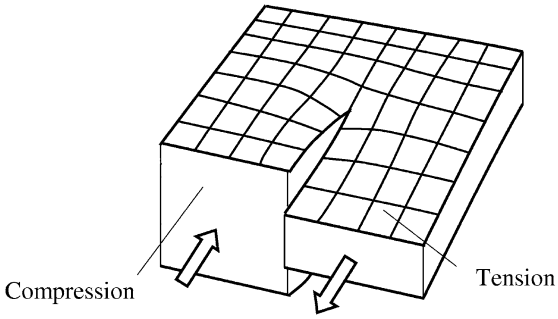

Fig. 2.16 Enlarged deformation of a mode II loaded plate specimen with a crack showing a transverse singular loading effect closely underneath the surfaces at the crack tip; (Harding et al. 2010)

therefore be based on self-normalised NSIFs (Sect. 2.3.6). Failure criteria based on averaged notch stresses (Chap. 1) or on averaged strain energy density (Chap. 3) are appropriate in other cases.

2.3.3 *Transverse Singular Effect at In-Plane Shear-Loaded V-Notches*

The elementary singularities in the loading modes 1, 2 and 3 may be locally coupled in three-dimensional configurations. One typical example is the crack front in a plate of finite thickness subjected to in-plane shear loading (mode 2), Fig. 2.16.

The exaggerated deformation plot of the crack tip region subjected to mode 2 loading shown in the figure illustrates the transverse expansion of the compressive loaded plate side and the transverse contraction of the tensile loaded plate side. At the crack front, the two opposed deformations lock each other. This produces out-of-plane shear stresses of opposite direction above and below the midplane. They vanish in the midplane and on the two plate surfaces and have a maximum closely underneath the surfaces. They constitute an out-of-plane ('transverse') shear stress singularity which resembles a mode 3 singularity, but remains symmetrical relative to the midplane. Its intensity is significantly affected by the Poisson's ratio ν. The singularity effect is largest for $\nu = 0.5$ and zero for $\nu = 0$. Simultaneously, the mode 2 intensity varies through the plate thickness, assuming Williams' original value only at a distance from the crack front of about half the plate thickness. Similar effects can be expected for non-zero notch opening angles.

The literature on coupled three-dimensional singular effects is shortly reviewed. Benthem studied these effects associated with the intersection of a wedge front of finite length with the free surface of the half space (Benthem 1977). Nakamura and Parks investigated the in-plane shear-loaded crack front intersecting a free surface as described above (Nakamura and Parks 1989). Kotousov analysed the tensile loaded V-notch in three dimensions (Kotousov and Wang 2002; Kotousov 2005;

Kotousov and Lew 2006). The following presentation refers to in-plane shear-loaded V-notches (Harding et al. 2010; Berto et al. 2011).

For describing the transverse singular effect at in-plane shear-loaded V-notches (with inclusion of cracks), the Kane and Mindlin assumptions for a flat plate of thickness $2h$ are adopted in the following form (Kane and Mindlin 1956):

$$u_x = u_x(x, y), \quad u_y = u_y(x, y), \quad u_z = \frac{z}{h} w(x, y) \tag{2.80}$$

The following two governing equations of a corresponding first order plate theory may be derived (Yang and Freund 1985):

$$\nabla^4 w - \kappa^2 \nabla^2 w = 0 \tag{2.81}$$

$$\nabla^6 \Phi - \kappa^2 \nabla^4 \Phi = 0 \tag{2.82}$$

$$\kappa^2 = \frac{6}{h^2(1 - \nu)} \tag{2.83}$$

where Φ is the stress resultant function and κ a stiffness parameter.

A further harmonic displacement function ψ is introduced for describing the in-plane and out-of-plane displacements. Assuming a general asymptotic behaviour of w, Φ and ψ at the notch tip and adopting the eigenfunction expansion method, the following eigenvalue equation is derived (Kotousov 2007; Harding et al. 2010):

$$[\sin 2\lambda_2(\pi - \alpha) - \lambda_2 \sin 2(\pi - \alpha)] \cos \lambda_O(\pi - \alpha) = 0 \tag{2.84}$$

The expression in brackets set to zero corresponds to Williams' in-plane shear stress solution, Eq. (2.62). The term $\cos \lambda_O(\pi - \alpha)$ set to zero describes an out-of-plane shear loading mode, Eq. (2.68). It has been shown that $0 < \lambda_2 < 1.0$ (singularity) occurs for $0 < 2\alpha < 102.6°$ whereas $\lambda_2 > 1.0$ (no singularity) results for $102.6° < 2\alpha < 180°$. On the other hand, $0 < \lambda_O < 1.0$ is found for $0 < 2\alpha < 180°$. The eigenvalues λ_O and λ_3 are identical because the eigenvalue equations can be presented in the same form. The expression for $\lambda_O = \lambda_3$ is given by Eq. (2.69).

However, there are major differences between mode O and mode 3. The out-of-plane singular mode O is a local mode coupled to the applied mode 2 due to a Poisson's ratio effect producing a symmetric shear stress distribution relative to the midplane of the plate. In contrast, the out-of-plane singular mode 3 is an independent loading mode associated with an antimetric shear stress distribution relative to the midplane that is totally independent of Poisson's ratio (Harding et al. 2010).

A numerical investigation using the FE method has been performed in order to study the dependence of the out-of-plane singular mode on notch opening angle and Poisson's ratio. The region near to the notch tip (radial distance $r \leq 5h$, with plate thickness $2h$) is discretised into a fine mesh of higher-order three-dimensional elements (15-node wedge-shaped and 20-node trapezoidal). The NSIFs are

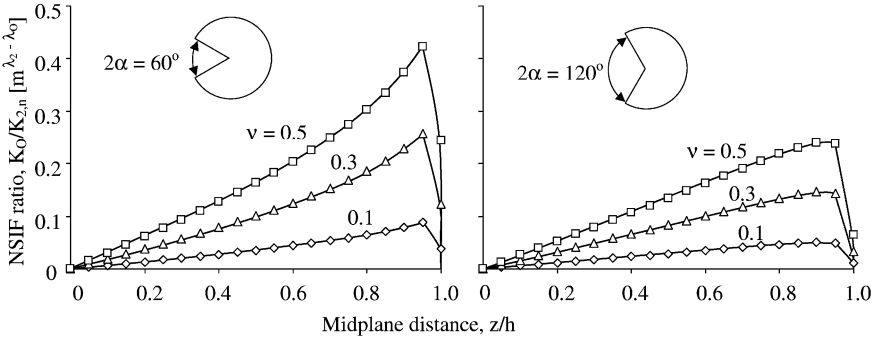

Fig. 2.17 NSIF ratio $K_O/K_{2,n}$ dependent on midplane distance z/h; out-of-plane singular mode O coupled with in-plane singular mode 2; plate thickness $2h$, Poisson's ratio ν and nominal NSIF $K_{2,n}$; (Harding et al. 2010)

found by the following limit values applied to the numerical data in the close neighbourhood of the notch tip (Seweryn and Zwolinski 1993):

$$K_2 = \lim_{r \to 0} (2\pi r)^{1-\lambda_2} \tau_{r\theta} \tag{2.85}$$

$$K_O = \lim_{r \to 0} (2\pi r)^{1-\lambda_O} \tau_{\theta z} \tag{2.86}$$

In the vicinity of the notch tip, the stress state is essentially three-dimensional. It comprises the singular out-of-plane loading mode O as well as the variability of the NSIF K_2 in the plate thickness direction. As a reference value, the nominal NSIF $K_{2,n}$ is introduced which corresponds to Williams' two-dimensional stress field solution.

Typical results of the investigation are shown in Fig. 2.17 where the NSIF ratio $K_O/K_{2,n}$ is plotted over the midplane distance z/h for three Poisson's ratios ν. The out-of-plane NSIF K_O is continuously rising to a maximum closely underneath the free surfaces of the plate. The rise is steeper for small notch opening angles. The largest values of K_O occur for $\nu = 0.5$, and K_O vanishes for $\nu = 0$. The NSIF K_2 is also much larger close to the free surface in comparison to its midplane value. Since the degree of the mode O singularity is greater than that of the mode 2 singularity (for $2\alpha = 0$), the effect of transverse mode O loading increases with the plate thickness.

The transverse singular effect in mode 2 loading is of relevance for application. Some interesting results are presented by Lazzarin and Berto (Harding et al. 2010; Berto et al. 2011). The welded lap joint models investigated using the FE method are shown in Fig. 2.18. The transverse singular effect is initiated at the stress-free lateral surface of the three-dimensional models and decreases in the direction of the midplane.

Based on the strain energy density approach, it is shown that the critical area in fatigue loading of slits ($2\alpha = 0$) is at the lateral surfaces for plate thicknesses greater than approximately 10 mm. It is shifted to the midplane for smaller thicknesses. The effect would be more pronounced if the ligament width were

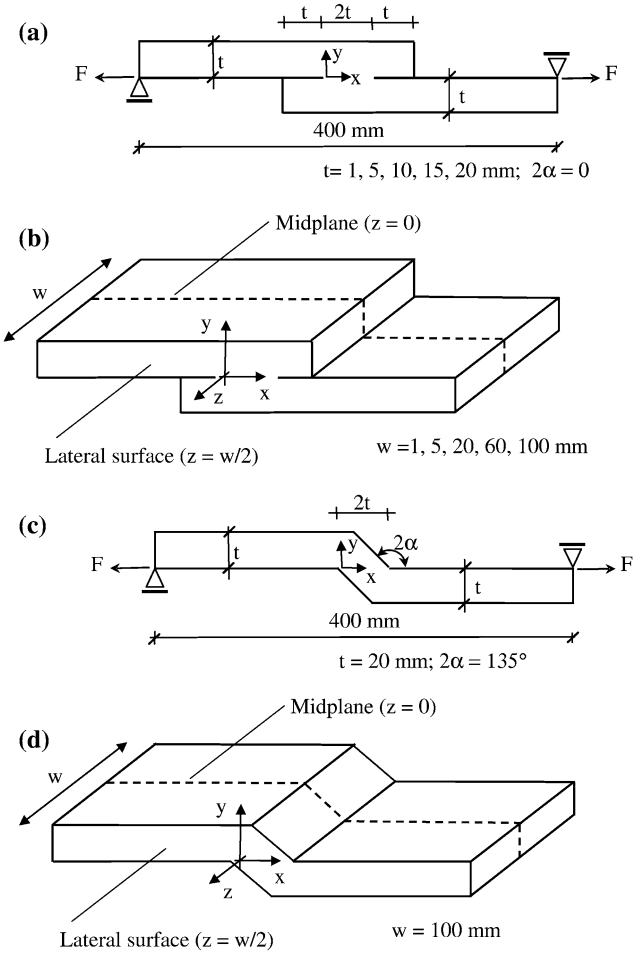

Fig. 2.18 Welded lap joint models subjected to tensile-shear loading: two-dimensional model with slit opening angle $2\alpha = 0°$ (**a**) and corresponding three-dimensional model (**b**); two-dimensional model with notch opening angle $2\alpha = 135°$ (**c**) and corresponding three-dimensional model (**d**); (Harding et al. 2010)

reduced relative to the plate thickness, resulting in an increase of mode 2 relative to mode 1 loading.

It is shown for notch opening angles $2\alpha \geq 102.6°$, where the in-plane shear stress singularity disappears, that the associated out-of-plane shear stress singularity still exists and may be dominant in the failure initiation phase.

2.3.4 NSIF Values of V-Notches and Weld Toe Notches

The NSIF values of V-notches and weld toe notches have been determined by a major number of authors. The weld toe notches are treated as a special case of V-notches ($2\alpha \approx 135°$) mainly by Italian researchers (Atzori et al. 1999(2); Lazzarin et al. 1998). Different methods are involved. The most general and convenient method is the eigenvalue expansion of the notch stress field according to Williams (also named 'asymptotic solution'), mostly combined with conventional FE analysis.

Asymptotic stress distributions at weld toe notches have been derived as early as 1985/86 without defining the NSIF parameter and without separating the mode 1 and mode 2 contributions (Atzori 1985; Lazzarin 1986). The clear analytical frame was established 1998 by Lazzarin and Tovo in the publication referenced above.

Various other methods have been used. Originally, the boundary collocation method was preferred (Gross and Mendelson 1972). Later on, special notch tip finite elements have been designed which incorporate the stress singularity: hybrid finite elements (Lin and Tong 1980), degenerate asymptotic finite elements (Akin 1976) and finite elements with constraints (Seweryn 2002). Three approaches are available for evaluating the NSIFs: direct evaluation at the singularity point, asymptotic evaluation outside the singularity point (comparison of numerical and analytical solutions) and energy methods (J-integral and strain energy density averaged over a control volume). The boundary element method is applicable with or without special singularity elements. Singular integral equations have also been successfully used (Theocaris and Ioakimidis 1979; Noda et al. 1996; Noda and Takase 2003; Savruk and Kazberuk 2006, 2007, 2010).

Useful NSIF data can be found in several publications (Gross and Mendelson 1972; Chen 1995; Seweryn and Molski 1996; Dunn et al. 1997(1), 1997(2); Lazzarin et al. 1998; Atzori et al. 1999(1); Noda and Takase 2003; Savruk and Kazberuk 2010). An extensive parametric investigation has been performed on the NSIFs at torsional loaded round bars with a circumferential hyperbolic notch of different notch opening angles 2α and different ratios of notch depth a to net cross-section radius R (Zappalorto et al. 2009). The closed form solution for the deep hyperbolic notch is combined with FE analysis results for notches of finite depth. The evaluated dimensionless NSIF is $k_3 = K_3/\tau_n^* R^{1-\lambda_3}$.

The main area of application of the NSIFs are fillet-welded joints showing any degree of penetration, but also butt-welded joints with the typical weld reinforcement are analysed in this way. The weld toe may be considered as a re-entrant corner notch of opening angle $2\alpha = 135°$ resulting in a bisector plane inclination of 112.5° against the plate surface. The stress field at the weld toe may then be described by the NSIFs K_1, K_2 and K_3, possibly supplemented by non-singular stress components (the out-of-plane S-stress and a superimposed normal stress in the direction of the toe line). Based on the NSIFs, fatigue test data may be evaluated in a form which includes the size effect. Geometries scaled in geometrical proportion and subjected to the same nominal stress are characterised by different

NSIF values. The NSIFs are used independent of whether the weld notch is really pointed or only sharply rounded. Only excessively large toe notch radii (shape-optimised welds) must be excluded. The assumption of pointed toe notches corresponds to the worst-case procedure in the fatigue assessment codes.

Considering a cross-section of finite width ahead of the notch, this width may be set equal to the plate thickness t of fillet-welded joints, the NSIFs can be expressed in the following form (Lazzarin et al. 1998):

$$K_1 = k_1 \sigma_n t^{1-\lambda_1} \tag{2.87}$$

$$K_2 = k_2 \sigma_n t^{1-\lambda_2} \tag{2.88}$$

$$K_3 = k_3 \tau_n^* t^{1-\lambda_3} \tag{2.89}$$

where σ_n and τ_n^* are the nominal stresses over the plate thickness t and k_1, k_2, k_3 are the geometry coefficients quantified further below. With regard to the application to fillet-welded joints, the reference stress of K_2 in Eq. (2.88) is not the nominal shear stress τ_n but the nominal tensile stress σ_n.

The NSIFs for fillet-welded joints (notch opening angle $2\alpha = 135°$) have the following form:

$$K_1 = k_1 \sigma_n t^{0.326} \tag{2.90}$$

$$K_2 = k_2 \sigma_n t^{-0.302} \tag{2.91}$$

$$K_3 = k_3 \tau_n^* t^{0.200} \tag{2.92}$$

The negative exponent of t in the expression for K_2, Eq. (2.91), designates non-singular stresses at the pointed notch. These can be neglected in strength predictions in comparison to the singular stresses described by K_1 and K_3, but they have to be taken into account when evaluating the stresses in front of the weld toe, Eq. (2.95), where strain gauges may be applied.

The Eqs. (2.87–2.89) are well suited to catch the size effect on the static or fatigue strength of corner-notched members, fillet-welded joints among them, provided the strength can be characterised by the NSIF (identical notch opening angles are a precondition). The following relationship is derived from Eq. (2.87) for the ratio of endurable nominal stresses σ_{n1} and σ_{n2} acting on the plate thicknesses t_1 and t_2:

$$\frac{\sigma_{n2}}{\sigma_{n1}} = \frac{k_{11}}{k_{12}} \left(\frac{t_1}{t_2} \right)^{1-\lambda_1} \tag{2.93}$$

where k_{11} and k_{12} are the geometry coefficients k_1 of the members 1 and 2.

In cases of a large net cross-sectional width between the notch tips, the notch depth a is the governing parameter instead of the plate thickness t, leading to the following relationship (Dunn et al. 1997(1), 1997(2)):

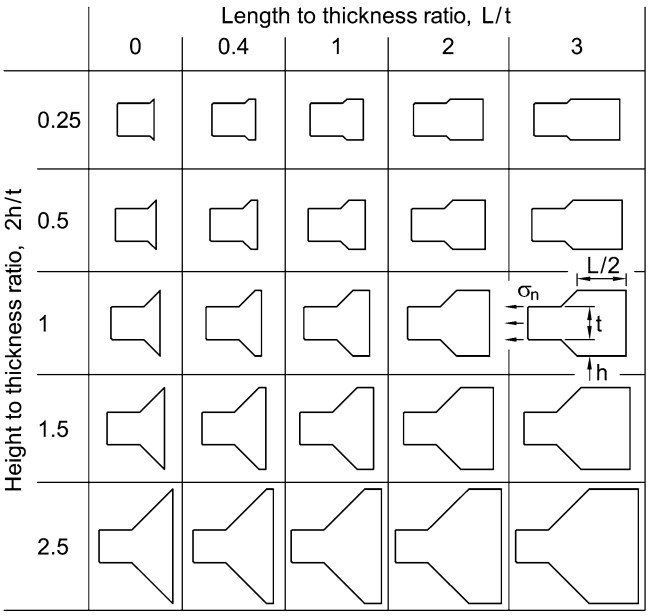

Fig. 2.19 Plane models with weld-like outer geometries (i.e. without the inner slits) subjected to tensile loading, investigated numerically using the FE method; (Lazzarin et al. 1998)

$$\frac{\sigma_{n2}}{\sigma_{n1}} = \frac{Y_1}{Y_2}\left(\frac{a_1}{a_2}\right)^{1-\lambda_1} \tag{2.94}$$

where Y_1 and Y_2 are the geometry coefficients of the members 1 and 2.

The dimensionless geometry coefficients k_1, k_2, k_3 in Eqs. (2.87–2.89) are determined based on extremely fine-meshed cross-sectional FE models of the considered welded joints evaluating the stresses in the bisector plane where they are decoupled for the three loading modes. Any stress value along the bisector plane, but sufficiently close to the notch tip, can be used to determine the NSIF by applying Eqs. (2.77), (2.78) or (2.79) and therefrom the geometry coefficient by evaluating Eqs. (2.90), (2.91) or (2.92). Systematic numerical investigations related to fillet-welded joints have been conducted (Lazzarin et al. 1998; Tovo and Lazzarin 1999).

A first investigation was related to plane models of weld-like outer geometries without the inner slits, Fig. 2.19. The geometry coefficients k_1 and k_2 dependent on the geometrical parameters (dimension ratios) are shown in Fig. 2.20. The numerical results are approximated by polynomials applying the least square method. The coefficient k_1 rises with L/t and $2h/t$, the coefficient k_2 does the opposite. Plastic notch stress intensity factors with appertaining stress distributions have also been determined for the considered joint-similar models (Lazzarin et al. 2001).

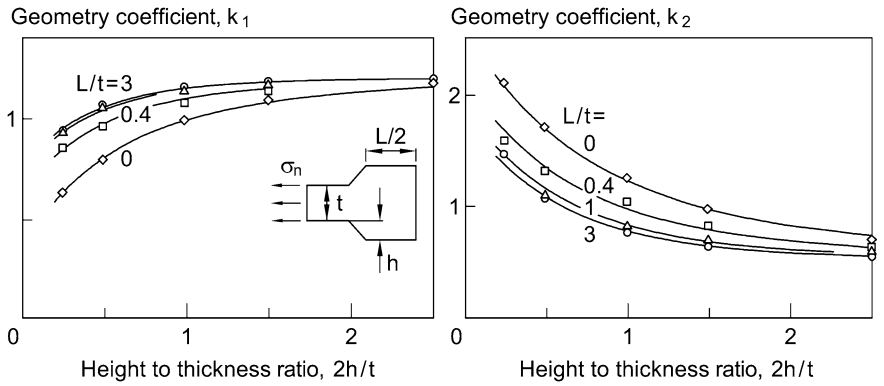

Fig. 2.20 Geometry coefficients k_1 and k_2 dependent on geometrical parameters for plane models with weld-like geometry subjected to tensile loading; FE analysis results; (Lazzarin et al. 1998)

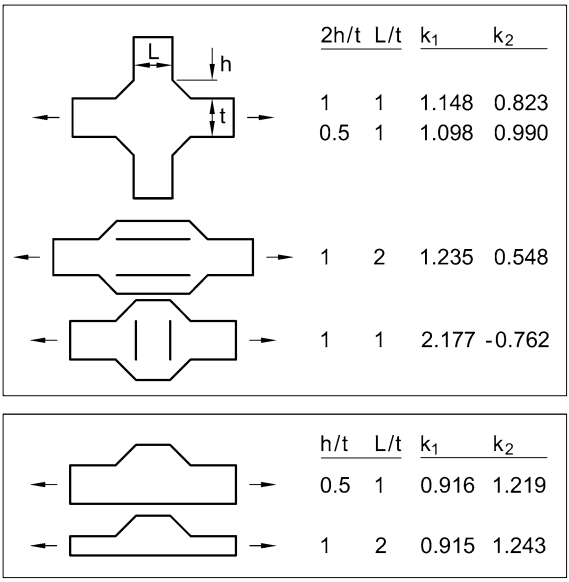

Fig. 2.21 Geometry coefficients k_1 and k_2 relating to cross-sectional models of various fillet-welded joints subjected to tensile loading; FE analysis results; (Lazzarin et al. 1998)

A second investigation was related to more realistic cross-sectional models of fillet-welded joints (through-welded cruciform joint, cover plate joint, top-cut cruciform joint) subjected to tensile loading, Fig. 2.21. Parametrical variations were considered for the cruciform attachment joint with non-load-carrying fillet welds resulting in the values of k_1 and k_2 plotted in Fig. 2.22. The curve shapes are similar to those referring to the weld-like plane models (Fig. 2.20). This means that the non-bevelled height of the transverse stiffener plate is of secondary influence.

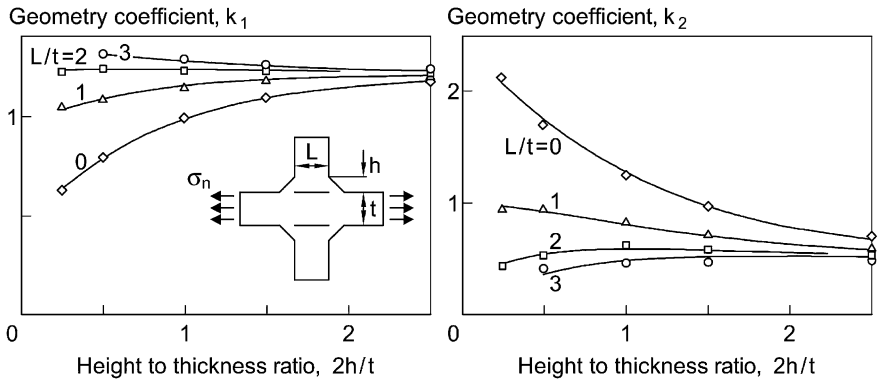

Fig. 2.22 Geometry coefficients k_1 and k_2 dependent on geometrical parameters for cruciform joint with non-load-carrying fillet welds (transverse attachment joint) subjected to tensile loading; FE analysis results; (Lazzarin et al. 1998)

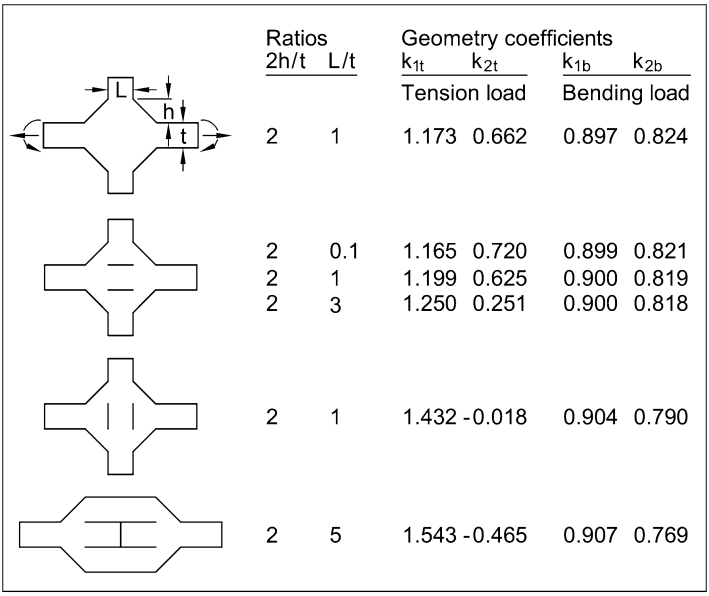

Ratios 2h/t	Ratios L/t	Geometry coefficients k_{1t} (Tension load)	k_{2t} (Tension load)	k_{1b} (Bending load)	k_{2b} (Bending load)
2	1	1.173	0.662	0.897	0.824
2	0.1	1.165	0.720	0.899	0.821
2	1	1.199	0.625	0.900	0.819
2	3	1.250	0.251	0.900	0.818
2	1	1.432	-0.018	0.904	0.790
2	5	1.543	-0.465	0.907	0.769

Fig. 2.23 Geometry coefficients k_{1t}, k_{2t} and k_{1b}, k_{2b} relating to typical cruciform and lap joints subjected to tensile force and bending moment, respectively; FE analysis results; (Tovo and Lazzarin 1999)

The plots in Fig. 2.22 refer to tensile loaded cruciform joints. Different diagrams are reported for cruciform attachment joints subjected to a bending load (Atzori et al. 1997). In the latter case, the values of k_1 and k_2 are lower, in general, explaining the higher fatigue strength of these joints under bending loading in comparison to tensile loading.

A third investigation with comparisons to the hot spot structural stress approach was related to typical cruciform and lap joints subjected to tension force or bending moment, respectively, Fig. 2.23. The values of k_1 are always higher for tensile than for bending loading. The opposite holds for the values of k_2 which are less influential on fatigue. A substantial rise in the values of k_1 occurs for the cruciform and lap joints with load-carrying fillet welds.

The coefficients k_1, k_2 and k_3 have also been determined for a fillet-welded circular tube penetrating a tensile loaded plate strip and for comparable cylindrical attachments (Susmel and Tovo 2004). Curve plots over peripheral angle indicate various crack initiation sites.

There remains an open demand for the notch stress intensity factors of butt-welded joints with different degrees of reinforcement height and width, comprising laser beam welds and gas metal-arc welds and referring to the top and root sides of the welds. The notch opening angles may vary between 90 and 180° in these cases. A tentative investigation of such joints has been presented (Lazzarin et al. 2006).

2.3.5 *Relationship between Structural Stress and NSIF for Welded Joints*

The stress rise in front of fillet welds is of major concern in respect of the hot spot structural stress approach which is widely used for the fatigue assessment of welded joints. This approach proceeds from the local structural stresses determined at the weld toe or closely in front of it by means of the FE method, of engineering formulae or of strain gauge measurements. The structural stress *S*–*N* curve can approximately be set equal to the nominal stress *S*–*N* curve of a locally comparable welded joint specimen.

The assumption behind the structural stress approach is that the fatigue-effective local parameter is correctly and generally described by the maximum structural stress. As far as the NSIF K_1 can also be considered to be fatigue-effective, the link between maximum structural stress and NSIF is of interest. Two application examples demonstrate this link in the following.

The stress rise in front of fillet welds has been determined based on the NSIFs in order to validate this approach in general by comparison with FE analysis results (Lazzarin et al. 1998). The radial stress along the free edge of the cross-sectional model, which corresponds to the surface stress in the base plate in a line normal to the fillet weld, is calculated by introducing the notch opening angle $2\alpha = 135°$ and the polar angle $\theta = 112.5°$ against the bisector plane into the general equation of stress, Eq. (2.70) and (2.71), thus yielding:

$$\sigma_r = 0.423 K_1 r^{-0.326} - 0.553 K_2 r^{0.302} \tag{2.95}$$

with the distance r from the pointed notch tip. In this equation, the sign of K_2, positive or negative, is chosen according to Williams' analytical frame. In the case

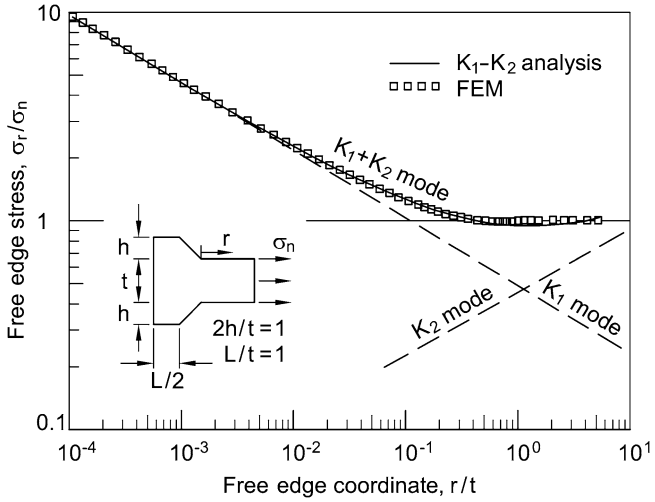

Fig. 2.24 Stress rise close to the pointed notch tip for weld-like model subjected to tensile loading; contribution of mode 1 and mode 2 loading to the free edge stress; K_1 and K_2 analysis results compared with FE analysis results; (Lazzarin et al. 1998)

considered below, K_2 is negative, so that the contribution due to mode 2 increases the contribution due to mode 1.

The stress rise close to the pointed notch tip according to Eq. (2.95) with FE-based values of K_1 and K_2 for a weld-like plane model subjected to tensile loading in comparison to the direct FE analysis results is plotted in Fig. 2.24. The logarithmic scale of the r/t axis is a means to illustrate the details of stress superposition (stresses related to K_1 and K_2) and to avoid plotting the stress singularity at $r = 0$. The stress values gained from the two methods are more or less identical up to the second crossing of the nominal stress level.

Another validation of the NSIF approach has been conducted for the same weld-like model as before, but with a blunt notch instead of a pointed notch. The NSIF stress equations extended by the notch radius term or its equivalent, Eqs. (2.116) and (2.117) reveal the basic structure, are used, Fig. 2.25. Once more, satisfactory agreement with the two methods (FE-based K_1 and K_2 as well as FE directly) is achieved.

Strain gauges applied to determine a fatigue-relevant local parameter at welds are generally placed on the free surface of the joint at a convenient distance from the notch tip of the weld toe. At this position, the effect of mode 2 loading is always present. Then, if the fatigue strength is thought of as mainly controlled by the mode 1 stress distribution, the contribution of mode 2 loading to the measured strains should be disregarded. This is possible only if one knows both NSIFs, K_1 and K_2, for a given geometry and remote loading condition. The greater the distance x from the notch tip is, the greater will be the perturbing effect due to mode 2 loading.

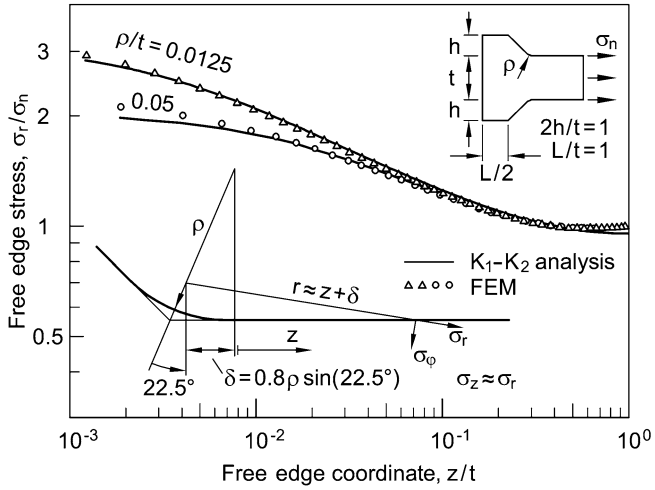

Fig. 2.25 Stress rise close to the rounded notch tip for weld-like model subjected to tensile loading; 'radial' stress σ_r along the straight free edge; K_1 and K_2 analysis results compared with FE analysis results; (Lazzarin et al. 1998)

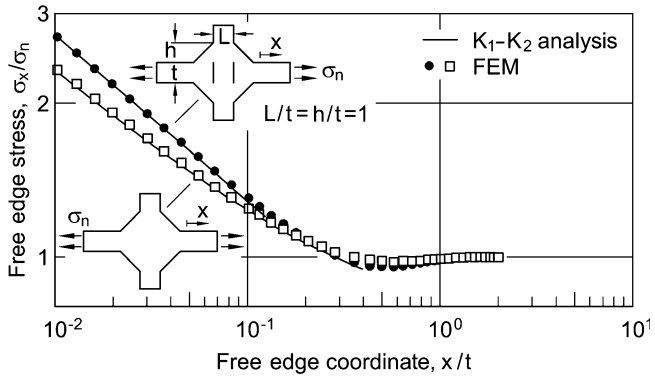

Fig. 2.26 Local stress rise above the structural stress level ($\sigma_s = \sigma_n$) plotted over distance from the pointed notch tip for the cross-sectional model of cruciform joints subjected to tensile loading; joint with slits in comparison to joint without slits; FE-based K_1 and K_2 analysis results compared with direct FE analysis results; (Tovo and Lazzarin 1999)

Two application examples are given which demonstrate deficiencies of the conventional structural stress approach and draw attention to the advantages of combining the NSIF approach with the structural stress approach (Tovo and Lazzarin 1999).

The first example refers to the different K_1 and K_2 values of the cruciform joint with full penetration welds compared with fillet welds without penetration (joint with internal slits), Fig. 2.26. The structural stresses are identical ($\sigma_x/\sigma_n = 1$), but the notch stress intensity factors, expressed by the gradients of the stress rise

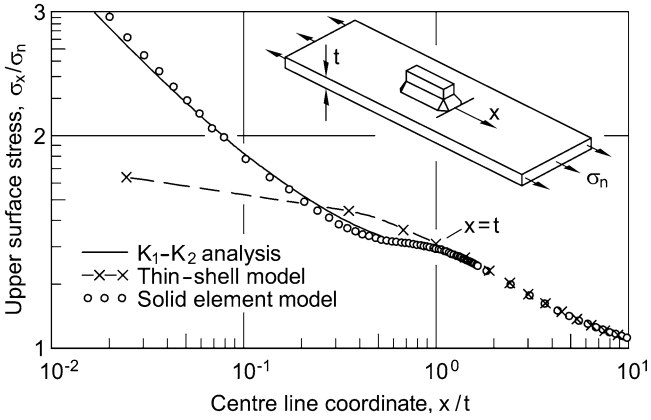

Fig. 2.27 Local stress rise plotted over distance from the weld toe for single-sided longitudinal attachment joint subjected to tensile loading; FE-based K_1 and K_2 analysis results based on structural stresses on thin-shell element model (coarse mesh) at distance $x = t$ from the weld toe (special extrapolation formula) compared with direct FE analysis results from solid element model (fine mesh); (Tovo and Lazzarin 1999)

towards the corner notch, are not. The K_1 factor ratio 1.432/1.173 = 1.221 is not too far from the IIW design recommendation, FAT class ratio 71/63 = 1.127 (Hobbacher 2009). Another conclusion from the stress plot is that direct measurement or calculation of the asymptotic stress rise towards the corner notch tip (for determining the fatigue-relevant NSIF) must be performed close to the notch tip, $x/t \leq 0.1$ (Atzori and Meneghetti 2001).

The second example of a longitudinal attachment joint refers to the fact that the conventional structural stress extrapolation to the hot spot at the weld toe may be rather inaccurate when using the FE analysis results from a thin-shell element model, Fig. 2.27. The stress rise to the weld toe in front of the attachment is well described by the NSIFs K_1 and K_2 determined on the basis of the relevant structural stresses in the thin-shell element model at distance $x = t$ from the weld toe (special extrapolation formula), as can be seen from the comparison with the FE analysis results using a fine-meshed three-dimensional solid element model. On the other hand, the structural stresses in the thin-shell element model in the region in front of the weld toe, where the conventional extrapolation to the hot spot is performed ($0.4 \leq x/t \leq 1.0$), are not sufficiently accurate, at least not with the applied element mesh.

Another link between structural stress FE analysis methods and the NSIF K_1 concept has been established (Meneghetti and Lazzarin 2007), see Sect. 3.7.3. The NSIF K_1 can be approximated by the 'peak stress' σ_p at the V-notch tip in a rather coarse globally even finite element mesh (element size typically $d = 1$ mm). The non-dimensional ratio $K_1/(\sigma_p d^{1-\lambda_1})$ is found to be independent of the notch opening angle. Once, the ratio has been determined for a definite configuration, it can be applied within a wide range of notch depths and notch angles.

2.3.6 Empirical Mixed-Mode Failure Criterion for Welded Joints

An empirical mixed-mode failure criterion for welded joints in terms of the NSIFs has been conceived in analogy to a conventional formulation in terms of the nominal stresses. The formula is based on test results for unnotched round bar specimens (ductile materials: unalloyed and alloyed steels) subjected to superimposed tensile and torsional in-phase high-cycle fatigue loading (Gough and Pollard 1935, 1937; Gough 1950). The endurable (nominal) stress ranges $\Delta\sigma$ and $\Delta\tau$ under the condition of combined loading follow an elliptical curve:

$$\left(\frac{\Delta\sigma}{\Delta\sigma_{\mathrm{E}}}\right)^2+\left(\frac{\Delta\tau}{\Delta\tau_{\mathrm{E}}}\right)^2=1 \quad (R=-1) \tag{2.96}$$

where $\Delta\sigma_{\mathrm{E}}$ and $\Delta\tau_{\mathrm{E}}$ are the endurance limit values under the condition of single mode loading, with stress ratio $R=-1$ characterising reversed stressing. The relationship between $\Delta\tau_{\mathrm{E}}$ and $\Delta\sigma_{\mathrm{E}}$ may be chosen according to conventional failure criteria (Rankine: $\Delta\tau_{\mathrm{E}}=\Delta\sigma_{\mathrm{E}}$; von Mises: $\Delta\tau_{\mathrm{E}}=\Delta\sigma_{\mathrm{E}}/3^{1/2}$; Tresca: $\Delta\tau_{\mathrm{E}}=\Delta\sigma_{\mathrm{E}}/2$). For cast iron materials and for the round bar specimens with a sharp notch (brittle material behaviour), the curve shape deviates to some extent from the elliptical shape, necessitating a slightly more complex functional representation.

An elliptical failure curve has also been found for pointed V-notches evaluating averaged notch stresses in the most critical direction (Seweryn and Mróz 1995).

Converting the nominal stress based expression due to Gough, Eq. (2.96), into a NSIF based expression, neglecting the influence of mode 2 loading (actually the mode 2 singularity is weak and vanishes for $2\alpha > 102.6°$), the following relationship is gained (Lazzarin et al. 2004):

$$\left(\frac{\Delta K_1}{\Delta K_{1,\mathrm{E}}}\right)^2+\left(\frac{\Delta K_3}{\Delta K_{3,\mathrm{E}}}\right)^2=1 \quad (R=-1) \tag{2.97}$$

where ΔK_1 and ΔK_3 are the endurable NSIFs in mixed mode loading compared with their endurance limit values $\Delta K_{1,\mathrm{E}}$ and $\Delta K_{3,\mathrm{E}}$ in single mode loading ($N_{\mathrm{E}}=1\times10^5$ up to 2×10^6 cycles). It can be shown that Eq. (2.97) is substantiated by the criterion of strain energy density averaged over the circle section volume surrounding the V-notch tip.

In order to define an equivalent NSIF, Eq. (2.97) is rewritten in the following form (Lazzarin et al. 2004):

$$\left(\frac{\Delta K_1}{\Delta K_{1,\mathrm{E}}}\right)^2+k_{1/3}^2\left(\frac{\Delta K_3}{\Delta K_{1,\mathrm{E}}}\right)^2=1 \tag{2.98}$$

$$k_{1/3} = \frac{\Delta K_{1,\mathrm{E}}}{\Delta K_{3,\mathrm{E}}} \tag{2.99}$$

The coefficient $k_{1/3}$ is the ratio of the fatigue strength in pure tensile (or bending) loading and pure torsional (or out-of-plane shear) loading, expressed by the endurable NSIF ranges at the endurance limit N_{E}. The coefficient is not a dimensionless parameter. The dimension depends via λ_1 and λ_3 on the notch opening angle 2α.

The equivalent NSIF can now be written in the following form:

$$\Delta K_{1,\mathrm{eq}} = \sqrt{(\Delta K_1)^2 + k_{1/3}^2 (\Delta K_3)^2} \tag{2.100}$$

where the units of $\Delta K_{1,\mathrm{eq}}$ coincide with those of ΔK_1, that is MPa $\mathrm{m}^{1-\lambda_1}$. Alternatively, the equivalent NSIF can be defined in units of ΔK_3, that is MPa $\mathrm{m}^{1-\lambda_3}$:

$$\Delta K_{3,\mathrm{eq}} = \sqrt{(\Delta K_3)^2 + k_{1/3}^{-2} (\Delta K_1)^2} \tag{2.101}$$

The coefficient $k_{1/3}$ has been determined based on the local strain energy density approach (see Sect. 3.2.1), evaluating the distortional strain energy density averaged in a sector volume with control radius R_0 around the notch tip (Lazzarin et al. 2004). The same radius R_0 is introduced for mode 1 and mode 3 loading conditions. The high-cycle fatigue data for a V-notch with $2\alpha = 135°$ (weld toe) made of fine-grained high-strength steel FeE460 resulted in $R_0 = 0.36$ mm, or when made of the age-hardened aluminium alloy AlSi1MgMn in $R_0 = 0.11$ mm. The following expression is then derived:

$$k_{1/3} = \sqrt{\frac{e_{\mathrm{d3}}}{e_{\mathrm{d1}}}} R_0^{\lambda_3 - \lambda_1} \tag{2.102}$$

where e_{d1} and e_{d3} are distortional strain energy density coefficients depending on the notch opening angle 2α (besides on Poisson's ratio ν).

The derivations up to here refer to high-cycle fatigue conditions ($N_{\mathrm{E}} = 1 \times 10^5$ up to 2×10^6 cycles) where the plastic deformations at the notch tip can be neglected. In the low-cycle and medium-cycle fatigue range, plastic deformations are an important effect and an accurate determination of R_0 would require an elastic-plastic analysis. The latter is avoided by considering the *S–N* curves in terms of the endurable nominal stresses $\Delta\sigma_{\mathrm{E}}$ and $\Delta\tau_{\mathrm{E}}$:

$$\Delta\sigma(N) = \Delta\sigma_{\mathrm{E}} \left(\frac{N_{\mathrm{E}}}{N}\right)^{1/k_\sigma} \tag{2.103}$$

$$\Delta\tau(N) = \Delta\tau_{\mathrm{E}} \left(\frac{N_{\mathrm{E}}}{N}\right)^{1/k_\tau} \tag{2.104}$$

where k_σ and k_τ are the inverse slope exponents of the *S–N* curves for tensile and shear loading.

In the case of identical values of k_σ and k_τ (same slope of the *S–N* curves), the coefficient $k_{1/3}$ is independent of the considered endurable number of cycles N_E. Then, the Eqs. (2.100) and 2.101) are also valid in the low-cycle and medium-cycle fatigue range.

In the conventional codes for the fatigue assessment of structural members, especially welded joints, different values of k_σ and k_τ are introduced, e.g. $k_\sigma = 3.0$ and $k_\tau = 5.0$ (Eurocode 3, 2005). In analogy to Eqs. (2.103) and (2.104), the *K–N* curves of the endurable NSIFs have the following form:

$$\Delta K_1(N) = \Delta K_{1,E}\left(\frac{N_E}{N}\right)^{1/k_\sigma} \tag{2.105}$$

$$\Delta K_3(N) = \Delta K_{3,E}\left(\frac{N_E}{N}\right)^{1/k_\tau} \tag{2.106}$$

and the mixed mode relationship in Eq. (2.97) is now formulated for the number of cycles $N_C < N_E$ in the low-cycle or medium-cycle fatigue range:

$$\left(\frac{\Delta K_1}{\Delta K_{1,C}}\right)^2 + \left(\frac{\Delta K_3}{\Delta K_{3,C}}\right)^2 = 1 \quad (R = -1) \tag{2.107}$$

In order to define an equivalent NSIF, Eq. (2.107) is rewritten in the following form:

$$\left(\frac{\Delta K_1}{\Delta K_{1,C}}\right)^2 + k_{1/3,C}^2\left(\frac{\Delta K_3}{\Delta K_{1,C}}\right)^2 = 1 \tag{2.108}$$

The coefficient $k_{1/3,C}$ is the ratio of the fatigue strength in pure tensile (or bending) loading and pure torsional (or out-of-plane shear) loading, expressed by the endurable NSIF ranges at the number of cycles, $N_C < N_E$:

$$k_{1/3,C} = \frac{\Delta K_{1,C}}{\Delta K_{3,C}} \tag{2.109}$$

Based on the *K–N* curve relationships according to Eqs. (2.105) and (2.106), introducing $N = N_C$, one gets:

$$k_{1/3,C} = \frac{\Delta K_{1,E}(N_E/N_C)^{1/k_\sigma}}{\Delta K_{3,E}(N_E/N_C)^{1/k_\tau}} = k_{1/3}\left(\frac{N_E}{N_C}\right)^{1/k_\sigma - 1/k_\tau} \tag{2.110}$$

where $k_{1/3}$ is given by Eq. (2.99).

The equivalent NSIFs can now be written in analogy to Eqs. (2.100) and (2.101) in the following form:

$$\Delta K_{1,\mathrm{eq}} = \sqrt{(\Delta K_1)^2 + k_{1/3}^2 (\Delta K_3)^2 \left(\frac{N_\mathrm{E}}{N_\mathrm{C}}\right)^{2(1/k_\sigma - 1/k_\tau)}} \tag{2.111}$$

$$\Delta K_{3,\mathrm{eq}} = \sqrt{(\Delta K_3)^2 + k_{1/3}^{-2} (\Delta K_1)^2 \left(\frac{N_\mathrm{E}}{N_\mathrm{C}}\right)^{2(1/k_\sigma - 1/k_\tau)}} \tag{2.112}$$

These relationships presume that the Gough ellipse is valid also in the low-cycle and medium-cycle fatigue range. An experimental proof of this presumption is not available.

2.3.7 Endurable NSIFs of Fatigue-Loaded Welded Joints

The fatigue strength or life of fillet-welded joints in the medium-cycle to high-cycle fatigue range ($N \geq 10^4$) can advantageously be described by endurable (elastic) NSIFs (Boukharouba et al. 1995; Verreman and Nie 1996, 1997). In contrast to the endurable nominal stresses, the endurable NSIFs are independent of the plate thickness, i.e. the size effect is already included. Fatigue test data from the literature referring to non-load-carrying fillet welds at tensile loaded transverse attachment joints of steel (mainly cruciform joints) in the as-welded condition have been evaluated to demonstrate this, Fig. 2.28 (Lazzarin and Tovo 1998). Large variations in the geometrical data are covered by the fatigue test data: plate thickness t = 13–100 mm, fillet weld leg length h = 5–16 mm, attachment length L = 3–220 mm. Only the NSIF K_1 is used to summarise the fatigue data, whereas the effect of K_2 is considered negligible in this type of joint ($2\alpha = 135°$), because no stress singularity occurs in the latter case. The large scatter range of the original nominal stress S–N curve is substantially reduced to conventional values experienced with geometrically uniform specimens.

An explanation for the fact that not only the crack initiation life but actually the evaluated total life is correctly described by endurable values of ΔK_1 is given in the following form (Atzori et al. 1999(1)): The crack initiation life (initiated crack length $a_\mathrm{i} = 0.3$ mm) and the residual crack propagation life (critical crack length $a_\mathrm{cr} = t/3$), occurring in the ratio approximately 2:1 in the investigation just quoted, are both controlled by the NSIF ΔK_1 as the dominant parameter. The SIF ΔK_I for a developing crack in the bisector plane is proportional to the NSIF ΔK_1.

The evaluation above based on ΔK_1 has been extended to tensile and bending loaded fillet-welded joints of further steels as well as of aluminium alloys (thickness t = 3–24 mm), Fig. 2.29 (Lazzarin and Livieri 2001). Different relationships are used to correlate ΔK_1 and $\Delta\sigma_\mathrm{n}$ in the tension and bending load cases. In the high-cycle range, the fatigue strength of the steel joints is about twice the

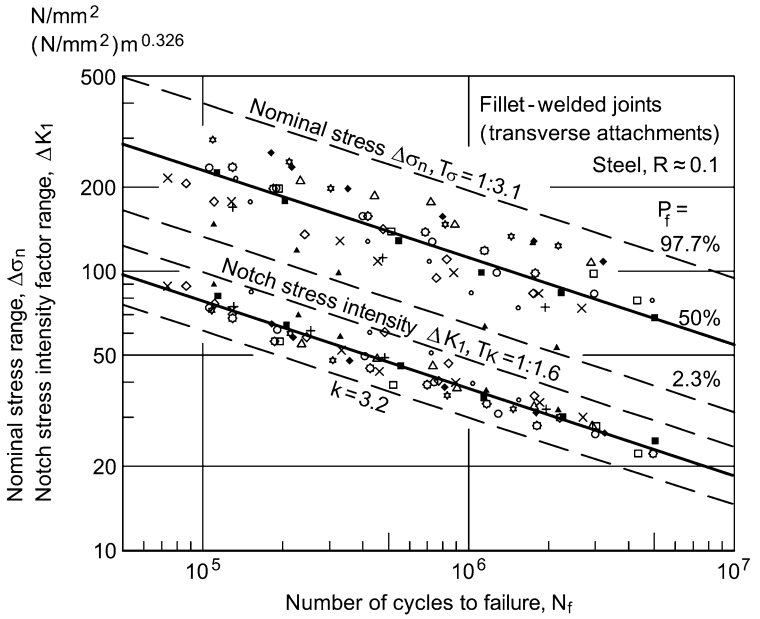

Fig. 2.28 Fatigue test data (toe failures) for fillet-welded transverse attachment joints of steel subjected to tensile loading; *S–N* curves contrasted with *K–N* curves; T_σ and T_K refer to $P_f = 2.3$ and 97.7 %; (Lazzarin and Tovo 1998)

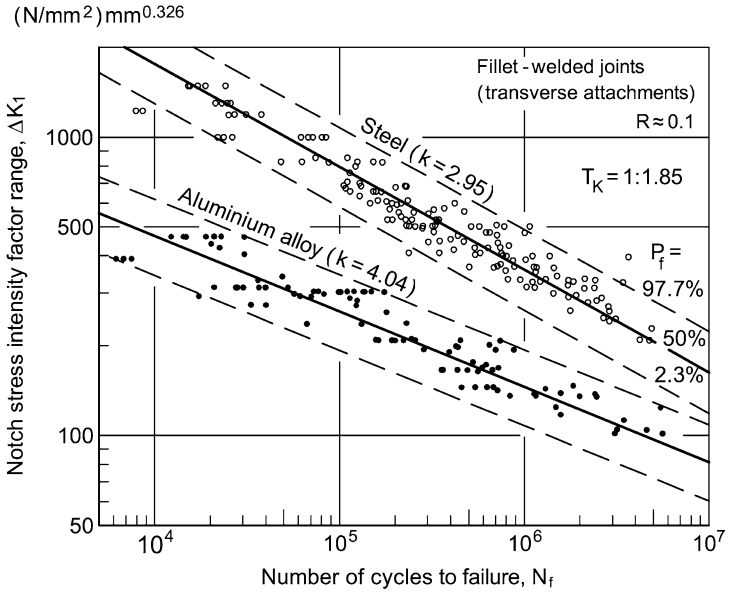

Fig. 2.29 Fatigue test data (toe failures) for fillet-welded transverse attachment joints of steel and aluminium alloy subjected to tensile and bending loads in terms of *K–N* curves; T_K refers to $P_f = 2.3$ and 97.7 %; (Lazzarin and Livieri 2001)

fatigue strength of the aluminium alloy joints. The size effect on the endurable nominal stresses is characterised by Eq. (2.93), leading to an exponent $(1 - \lambda_1) = 0.326$ of the thickness ratio. The exponent 0.25 is recommended in the Eurocode 3 (2005), exponents 0.1–0.3 dependent on joint type are found in the IIW design recommendations (Hobbacher 2009).

It has also been proposed to use the cyclic plastic zone radius R_p at the notch tip, approximated based on the elastic NSIF, for assessing the fatigue strength of fillet-welded joints. The *S–N* curves for different types of fillet-welded specimens are then replaced by a uniform R_p–N or R_p/t–N curve (Lazzarin and Livieri 2000; Koibuchi et al. 1999; Tanaka et al. 2002).

2.3.8 Endurable J-Integral for Fatigue-Loaded Welded Joints

The path-independent line integral around crack tips, usually named '*J*-integral', is a well-defined parameter characterising the fracture behaviour of crack tips (Rice 1968), compare Sect. 2.2.6. It was originally derived for linear-elastic material behaviour, but later on extended to nonlinear-elastic or elastic-plastic material behaviour, provided the loading curve is monotonic in the latter case.

The *J*-integral concept has been extended to pointed V-notches, at first under linear-elastic and then under elastic-plastic conditions (Lazzarin et al. 2002). The integral is path-dependent for corner notches subjected to mode 1 and mode 2 loading.

The J_V-integral of V-notches in linear-elastic materials can be given in the following form:

$$J_V = 2(A_{11}K_1^2 + A_{22}K_2^2) \tag{2.113}$$

where A_{11} and A_{22} depend on the notch opening angle 2α and the path around the notch tip. The dimension of J_V is MPa mm. The above integral can be made path-independent under the restriction of pure mode 1 (or pure mode 2) loading conditions, leading to the parameter

$$J_L = \frac{J_V}{R^{2\lambda_1 - 1}} \tag{2.114}$$

where R is the radius of the circular integration path. The parameter J_L remains dependent on the notch opening angle 2α.

The integrals J_V and J_L can also be defined for elastic-plastic material behaviour under the restriction of pure mode 1 loading. Using the elastic J_V-integral approach, the contributions of mode 1 and mode 2 loading can be superimposed, i.e. a well-founded failure criterion for mixed-mode loading can be established.

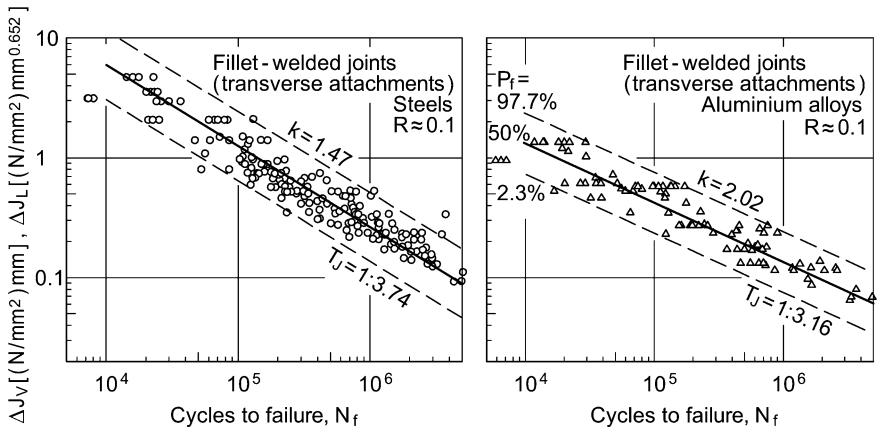

Fig. 2.30 Fatigue test data (toe failures) for fillet-welded transverse attachment joints of steels and aluminium alloys under tensile and bending loads in terms of *J*–*N* curves; scatter band characterises mean values plus minus two standard deviations; T_J refers to $P_f = 2.3$ and 97.7 %; (Lazzarin et al. 2002)

The integrals J_V and J_L have also been defined for pure mode 3 loading with inclusion of elastic-plastic material behaviour (Lazzarin and Zappalorto 2008). A different line integral around elastic corner notches subjected to mode 3 loading has independently been derived (Quian and Hasebe 1997). It evolves to be path-independent provided the notch flanks are free of loads.

The *J*-integral, defined above for V-notches, can be used as a fatigue-relevant parameter applicable to corner notches under mixed mode loading conditions, to varying notch opening angles (defined by the toe angle of the considered butt-welded or fillet-welded joints) and under conditions of local yielding at the notch tip. Evaluating the published fatigue test results for non-load-carrying transverse stiffener joints using a uniform circular path radius $R = 1$ mm, so that the values of J_V and J_L are identical, resulted in the J_V–N curves or J_L–N curves, respectively, plotted in Fig. 2.30 for fillet-welded-joints made of steels and aluminium alloys. The contribution of ΔK_2 is neglected with reference to the missing stress singularity in the case of large notch opening angles. When comparing the scatter range indices T_J and T_K, it has to be noted that a quadratic increase occurs solely by substituting a stress parameter by an energy parameter. The presented curves do not yet prove the applicability of the ΔJ-concept with regard to varying notch opening angles and marked mixed mode conditions.

More recently, J_V evaluations for welded joints have been performed based on a substantially extended data base of fatigue test results with failures proceeding from the weld toe and weld root (Livieri and Tovo 2009). The data base is almost identical with that previously used for local SED evaluations (Fig. 3.12).

2.3.9 Conclusions

The NSIFs K_1, K_2 and K_3 together with the non-singular stress components describe the stress field in the close vicinity of pointed V-notches or re-entrant corners. A transverse singular effect coupled with mode 2 loading at free surfaces is additionally identified. The numerical basis of NSIF evaluations in configurations with finite boundaries is the FE analysis method performed with extremely fine meshes.

The NSIF concept is well suited to describe the fatigue strength of fillet-welded and butt-welded joints with failure initiation at the weld toe. A uniform *K–N* curve with sufficiently low scatter range is derived which includes the size or plate thickness effect. Alternatively, a presentation in terms of the endurable *J*-integral is possible. Equivalent NSIFs are derived for cases of mixed mode loading conditions.

The NSIF parameters are well suited to constitute the basis of the endurable average strain energy density at weld notch tips which is under discussion to be implemented in the IIW recommendations for fatigue assessment.

2.4 Generalised Notch Stress Intensity Factor Concept

2.4.1 Survey of Section Contents

The notch stress intensity factor (NSIF) concept referring to pointed V-notch tips with inclusion of the conventional stress intensity factor (SIF) approach referring to pointed crack tips is extended to the generalised notch stress intensity factor concept referring to sharply rounded (blunt) or root-holed V-notches or crack tips. Notch rounding changes the stresses at the V-notch or crack tip substantially insofar as the stress singularity is removed. But the stress distribution connected with the singularity remains widely unchanged at distances from the notch root larger than one half of the notch radius ρ, provided the radius is sufficiently small in relation to the notch depth or crack length (sharp notches).

It is shown that the stress distribution at sharply rounded notches subjected to the loading modes 1, 2, 3 can be described by the generalised NSIFs $K_{1\rho}$, $K_{2\rho}$, $K_{3\rho}$ as the governing field parameters. These NSIFs are related to the maximum notch stresses σ_{max}, τ_{max}, τ^*_{max} which constitute the conventional stress concentration factors (SCFs) in engineering science. In contrast to the SCFs, the generalised NSIFs describe not only the maximum stress but the whole stress field in the vicinity of the notch root. The field information is needed for assessing failure processes such as crack initiation and propagation or microstructural damaging phenomena.

In the following, the stress field equations for blunt V-notches subjected to the three basic loading modes are given. The corresponding generalised NSIFs are

defined and evaluation procedures described. Examples for notch stress distributions determined on the basis of generalised NSIFs are given. Furthermore, V-notches with root hole are analysed under the three loading modes, the stress field being likewise described by generalised NSIFs. The NSIFs of parabolic and keyhole notches are set into comparison. The *T*-stress effect at rounded notch configurations is clarified. The generalised NSIF concept is finally applied to a round bar with shoulder fillets. The fatigue limit of sharply rounded notches can only exceptionally be directly expressed by critical NSIF values.

The expositions are mainly based on the analytical development of the generalised NSIF concept by Lazzarin, Zappalorto, Filippi and Tovo. A list of symbols and a list of references are found at the end of Chap. 2.

2.4.2 Stress Field at Blunt V-Notches Subjected to Tensile and In-Plane Shear Loading

A general solution for the stress field at sharply rounded (blunt) V-notches, subjected to tensile and in-plane shear loading is available (Lazzarin and Tovo 1996; Filippi et al. 2002(1), 2002(2); Lazzarin and Filippi 2006). The nomenclature is shown in Fig. 2.31. The theoretical frame, Kolsov–Muskhelishvili's complex stress function method combined with Neuber's auxiliary system of curvilinear coordinates, has been reviewed in Sect. 2.3.2 with application to pointed V-notches. Now, the improved solution by Filippi is evaluated in respect to blunt V-notches. The solution is not exact, but represents the first term in a series perturbating the pointed notch solution.

The auxiliary system of curvilinear coordinates is shown in Fig. 2.32. The parametric curves $u = \text{const.}$ and $v = \text{const.}$ are plotted in the $x{-}y$ plane using the conformal mapping function $z = w^q$ with $z = x + \mathrm{i}y$ and $w = u + \mathrm{i}v$. The factor q is related to the notch opening angle 2α of the pointed notch, curve $u = 0$, Eq. (2.65) and Fig. 2.31. The curve $u = u_0$ is assumed to describe the blunt notch. Its radius of curvature ρ at the intersection with the x-axis, where $r_0 = u_0^q$, is equal to

$$\rho = \frac{q r_0}{(q-1)} \tag{2.115}$$

This radius of curvature corresponds to the notch root radius. The distance r_0 between the origin of the $x{-}y$ coordinate system and the notch root depends (via q) on the notch opening angle 2α. Only for the parabolic notch ($2\alpha = 0$, $q = 2$), the relationship $r_0 = \rho/2$ is valid.

The stress field equations for blunt V-notches subjected to tensile and in-plane shear loading (mode 1 and mode 2) are presented in extension of the equations for pointed V-notches, Eqs. (2.70) and (2.71):

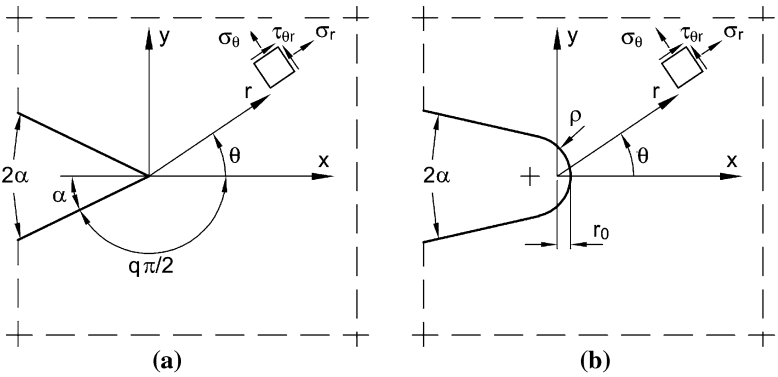

Fig. 2.31 Coordinate systems, symbols and in-plane notch stress components at pointed V-notch (**a**) and at the corresponding rounded V-notch (**b**); with $r_0 = \rho(q-1)/q$; (Lazzarin and Tovo 1998)

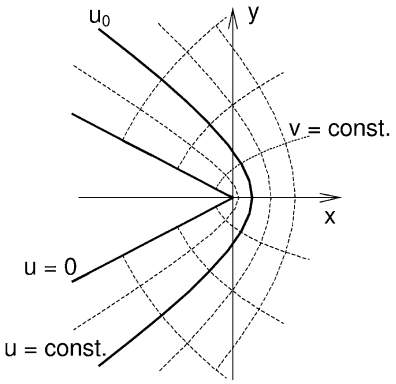

Fig. 2.32 Auxiliary system of curvilinear coordinates applied to solve the stress field problem at V-notches or hyperbolic notches; (Lazzarin and Tovo 1996)

$$\left\{\begin{array}{c}\sigma_\theta\\ \sigma_r\\ \tau_{r\theta}\end{array}\right\}_1 = \frac{1}{\sqrt{2\pi}}\frac{r^{\lambda_1-1}K_1}{(1+\lambda_1)+\chi_1(1-\lambda_1)} \times \left[\left\{\begin{array}{c}(1+\lambda_1)\cos(1-\lambda_1)\theta\\ (3-\lambda_1)\cos(1-\lambda_1)\theta\\ (1-\lambda_1)\sin(1-\lambda_1)\theta\end{array}\right\} + \chi_1(1-\lambda_1)\left\{\begin{array}{c}\cos(1+\lambda_1)\theta\\ -\cos(1+\lambda_1)\theta\\ \sin(1+\lambda_1)\theta\end{array}\right\} + \left(\frac{r}{r_0}\right)^{\mu_1-\lambda_1}[(3-\lambda_1)-\chi_1(1-\lambda_1)]\left\{\begin{array}{c}\cos(1+\mu_1)\theta\\ -\cos(1+\mu_1)\theta\\ \sin(1+\mu_1)\theta\end{array}\right\}\right] \tag{2.116}$$

$$\left\{\begin{array}{c}\sigma_\theta\\ \sigma_r\\ \tau_{r\theta}\end{array}\right\}_2 = \frac{1}{\sqrt{2\pi}}\frac{r^{\lambda_2-1}K_2}{(1+\lambda_2)+\chi_2(1-\lambda_2)} \times\left[\left\{\begin{array}{c}-(1+\lambda_2)\cos(1-\lambda_2)\theta\\ -(3-\lambda_2)\cos(1-\lambda_2)\theta\\ (1-\lambda_2)\sin(1-\lambda_2)\theta\end{array}\right\}+\chi_2(1-\lambda_2)\left\{\begin{array}{c}-\sin(1+\lambda_2)\theta\\ \sin(1+\lambda_2)\theta\\ \cos(1+\lambda_2)\theta\end{array}\right\}\right] -\left(\frac{r}{r_0}\right)^{\mu_2-\lambda_2}[(1-\lambda_2)+\chi_2(1+\lambda_2)]\left\{\begin{array}{c}\sin(1+\mu_2)\theta\\ -\sin(1+\mu_2)\theta\\ \cos(1+\mu_2)\theta\end{array}\right\}\Bigg] \tag{2.117}$$

The NSIFs K_1 and K_2 are determined for $r \to 0$ according to Gross–Mendelson's limit value definition, Eqs. (2.77) and (2.78). Several well known solutions for crack or notch configurations (Williams 1952; Irwin 1957; Creager and Paris 1967; Glinka and Newport 1987) can be considered as special cases of the above general solution, in which the NSIFs K_1 and K_2 may be substituted by the parameters a_1 and a_2 or by the maximum stresses σ_{max} at the notch tip and τ_{max} ahead of the notch tip.

Williams' solution for pointed V-notches results with $r_0 = 0$ (because $\rho = 0$), compare Eqs. (2.70) and (2.71). Westergaard–Sneddon–Irwin's solution for crack tips is derived with $r_0 = 0$, $q = 2$ and $\lambda_1 = \lambda_2 = 0.5$ (because $2\alpha = 0$), compare Eqs. (2.2) and (2.4). Creager's blunt crack (or parabolic notch) solution is obtained by imposing $r_0 = \rho/2$, $q = 2$, $\lambda_1 = \lambda_2 = 0.5$ and $\mu_1 = \mu_2 = -0.5$ (Creager and Paris 1967):

$$\left\{\begin{array}{c}\sigma_\theta\\ \sigma_r\\ \tau_{r\theta}\end{array}\right\}_1 = \frac{K_\mathrm{I}}{\sqrt{2\pi r}}\left(\frac{1}{4}\left[\left\{\begin{array}{c}3\cos\theta/2\\ 5\cos\theta/2\\ \sin\theta/2\end{array}\right\}+\left\{\begin{array}{c}\cos 3\theta/2\\ -\cos 3\theta/2\\ \sin 3\theta/2\end{array}\right\}\right]+\frac{\rho}{2r}\left\{\begin{array}{c}\cos\theta/2\\ -\cos\theta/2\\ \sin\theta/2\end{array}\right\}\right) \tag{2.118}$$

$$\left\{\begin{array}{c}\sigma_\theta\\ \sigma_r\\ \tau_{r\theta}\end{array}\right\}_2 = \frac{K_\mathrm{II}}{\sqrt{2\pi r}}\left(\frac{1}{4}\left[\left\{\begin{array}{c}3\sin\theta/2\\ 5\sin\theta/2\\ \cos\theta/2\end{array}\right\}+\left\{\begin{array}{c}3\sin 3\theta/2\\ -3\sin 3\theta/2\\ 3\cos 3\theta/2\end{array}\right\}\right]+\frac{\rho}{2r}\left\{\begin{array}{c}\sin\theta/2\\ -\sin\theta/2\\ \cos\theta/2\end{array}\right\}\right) \tag{2.119}$$

It can also be shown that Neuber's solution for the stress distribution along the notch bisector for tensile loaded V-notches is in agreement with Eq. (2.116) to a wide extent (Lazzarin and Tovo 1996).

The general stress field equations above, Eqs. (2.116) and (2.117), are approximations. They are deficient in accuracy, when applied to blunt V-notches with a large notch opening angle, e.g. $2\alpha = 135°$ referring to weld toes. With the aim of improving the accuracy of the analytical solution, the part of the equations

with the exponent μ is extended. This is achieved by adding a second analytical function to the first expression in Eq. (2.63), in order to provide further free parameters for adjustment to the boundary conditions (Filippi et al. 2002[(2)]):

$$\varphi(z) = az^{\lambda} + dz^{\mu}, \quad \psi(z) = bz^{\lambda} + cz^{\mu} \tag{2.120}$$

The resulting stress field equations are more complex than before in the second order terms which contain the exponent μ, but the accuracy of the solution is substantially enhanced, especially for large notch opening angles. An additional improvement of the exponent μ_2 for mode 2 loading has been introduced (Lazzarin et al. 2011).

2.4.3 Stress Field at Blunt V-Notches Subjected to Out-of-Plane Shear Loading

A general solution for the stress field at sharply rounded (blunt) V-notches subjected to out-of-plane shear loading has been derived on a similar analytical basis as before in the case of tensile and in-plane shear loading (Smith 2004; Zappalorto and Lazzarin 2011[(3)]). Pointed V-notches are included.

Only one analytical function (consisting of two terms) is needed for the mathematical description of the shear stress field:

$$H(z) = az^{\lambda} + bz^{\mu} \tag{2.121}$$

where the coefficients a and b are complex whereas the exponents λ and μ are real. The coefficients are introduced as real if only the antimetric part of the solution is requested. The pointed notch problem is described by neglecting the second term with the exponent μ. The reason for one analytical function being sufficient is, that the out-of-plane stress field is governed by a potential function whereas the in-plane stress fields must obey a bipotential function.

The out-of-plane shear stresses are derived in the following form, separated into antimetrical (subscript a) and symmetrical (subscript s) parts in the $r-\theta$ coordinate system:

$$\begin{Bmatrix} \tau_{rz} \\ \tau_{\theta z} \end{Bmatrix} = \frac{K_{3\rho}^{(a)}}{\sqrt{2\pi}} r^{\lambda_a - 1} \begin{Bmatrix} \sin\lambda_a\theta \\ \cos\lambda_a\theta \end{Bmatrix} + \frac{K_{3\rho}^{(s)}}{\sqrt{2\pi}} r^{\lambda_s - 1} \begin{Bmatrix} \cos\lambda_s\theta - (r/r_0)^{\mu_s - \lambda_s}\cos\mu_s\theta \\ -\sin\lambda_s\theta + (r/r_0)^{\mu_s - \lambda_s}\sin\mu_s\theta \end{Bmatrix} \tag{2.122}$$

where the antimetric and symmetric eigenvalues are dependent on the notch opening angle 2α expressed by the parameter q ranging between 2.0 and 1.0, Eq. (2.65):

$$\lambda_a = \frac{1}{q}, \quad \lambda_s = \frac{2}{q}, \quad \mu_s = \frac{1}{q}, \quad q = \frac{2\pi - 2\alpha}{\pi} \tag{2.123}$$

The generalised NSIFs $K_{3\rho}^{(a)}$ and $K_{3\rho}^{(s)}$ are determined from the stresses in the bisector plane ($\theta = 0$) of the blunt V-notch (with $r_{0+} > r_0$ in the logarithmic plot):

$$K_{3\rho}^{(a)} = \lim_{r \to r_{0+}} \sqrt{2\pi} \left[r^{1-\lambda_a} \tau_{\theta z}(r, 0) \right] \tag{2.124}$$

$$K_{3\rho}^{(s)} = \lim_{r \to r_{0+}} \sqrt{2\pi} \left[\frac{r^{1-\lambda_s} \tau_{rz}(r, 0)}{1 - (r/r_0)^{\mu_s - \lambda_s}} \right] \tag{2.125}$$

The above NSIF $K_{3\rho}^{(a)}$ can be substituted by the maximum notch stress, $K_{3\rho}^{(a)} = \tau_{max}^{(a)} r_0^{1-\lambda_a} (2\pi)^{1/2}$ with $r_0 = (1 - 1/q)\rho$ (Zappalorto et al. 2009), whereas this is not possible with the NSIF $K_{3\rho}^{(s)}$.

For the pointed V-notch, notch radius ρ and distance r_0 are equal to zero, so that the terms with r/r_0 disappear (the exponent, $\mu_s - \lambda_s$, is negative):

$$\left\{ \begin{matrix} \tau_{rz} \\ \tau_{\theta z} \end{matrix} \right\} = \frac{K_3^{(a)}}{\sqrt{2\pi}} r^{\lambda_a - 1} \left\{ \begin{matrix} \sin \lambda_a \theta \\ \cos \lambda_a \theta \end{matrix} \right\} + \frac{K_3^{(s)}}{\sqrt{2\pi}} r^{\lambda_s - 1} \left\{ \begin{matrix} \cos \lambda_s \theta \\ -\sin \lambda_s \theta \end{matrix} \right\} \tag{2.126}$$

The exponent $(\lambda_a - 1)$ is negative, thus characterising a singular stress distribution. The other exponent $(\lambda_s - 1)$ is positive, thus denoting a non-singular distribution. In the case of a crack or slit ($2\alpha = 0$), the eigenvalues are $\lambda_a = 1/2$ and $\lambda_s = 1.0$, the exponents being $(\lambda_a - 1) = -1/2$ and $(\lambda_s - 1) = 0$, Eq. (2.123) with $q = 2$. Comparison with Eq. (2.73) gives the non-singular S-stress, $S = K_3^{(s)} r^{\lambda_s - 1} / (2\pi)^{1/2}$.

In order to improve the solution for U-notches and blunt V-notches subjected to out-of-plane shear loading, a modified mapping function has been introduced which complies better with the actual notch shape consisting of a circular arc tapering off into the rectilinear flanks of the V-notch (Zappalorto et al. 2010). The resulting, more complex stress field equations have been derived. It is found that the notch stresses are markedly influenced by the details of the notch root shape. A solution for semi-elliptical notches is also available (Lazzarin et al. 2007). In both investigations the NSIFs are found by FE analysis.

2.4.4 Generalised Notch Stress Intensity Factors

For evaluating the stress fields at blunt V-notches, generalised notch stress intensity factors have to be introduced which may be differently defined depending on the type of notch geometry. Also, the simple SIFs or NSIFs may be used. For example, in Eqs. (2.116) and (2.117) the NSIFs K_1 and K_2 of the corresponding pointed notch are introduced, or in Eqs. (2.118) and (2.119) the SIFs K_I and K_{II} of the corresponding pointed crack tip. It has to be noted, that the distance r_0 is measured between the origin of r and the pointed or rounded notch or crack tip.

In Eq. (2.122), the generalised NSIF $K_{3\rho}$ is introduced, which characterises the stress field at rounded V-notches directly. There are three different limit value procedures available for determining the SIFs, NSIFs or generalised NSIFs.

The first procedure evaluates the stresses in the bisector plane of the pointed notch or crack for determining K_1, K_2, K_3 according to Eqs. (2.77–2.79) or K_I, K_II, K_III according to Eqs. (2.16–2.19) as limit values for $r \to 0$ (Gross and Mendelson 1972).

The second procedure evaluates the maximum notch stresses in the bisector plane of the rounded crack or notch (in mode 2 loading also outside the bisector plane) for determining K_I, K_II, K_III or K_1, K_2, K_3 as limit values for $\rho \to 0$. The following formulae are available, first for cracks under mode I loading based on $\sigma_\mathrm{max} = \sigma_{\theta\ \mathrm{max}}$ in the bisector plane (Irwin 1957, 1958),

$$K_\mathrm{I} = \lim_{\rho \to 0} \frac{1}{2} \sigma_\mathrm{max} \sqrt{\pi\rho} \qquad (T = 0) \tag{2.127}$$

further for cracks under mode II loading based on $\tau_\mathrm{max} = \tau_{r\theta\ \mathrm{max}}$ in the bisector plane (Cheng 1988; Radaj and Zhang 1993[(3)]) or based on $\sigma_\mathrm{max} = \sigma_{\mathrm{t\ max}}$ outside the bisector plane (Sih and Liebowitz 1968),

$$K_\mathrm{II} = \lim_{\rho \to 0} \frac{3\sqrt{3}}{2} \tau_\mathrm{max} \sqrt{\pi\rho} \tag{2.128}$$

$$K_\mathrm{II} = \lim_{\rho \to 0} \sigma_\mathrm{max} \sqrt{\pi\rho} \qquad (K_\mathrm{I} = 0,\ T = 0) \tag{2.129}$$

and finally for cracks under mode III loading based on $\tau^*_\mathrm{max} = \tau_{\theta z\ \mathrm{max}}$ (Hahn 1976; Hasebe and Kutanda 1978):

$$K_\mathrm{III} = \lim_{\rho \to 0} \tau^*_\mathrm{max} \sqrt{\pi\rho} \tag{2.130}$$

The limit value for K_I, Eq. (2.127), presumes that the crack-parallel or slit-parallel stress $\sigma_\parallel$ (or T-stress in the limit $\rho = 0$) is zero. This is further elaborated in Sect. 2.4.8.

Similar formulae are available for V-notches under mode 1 loading (Benthem 1987; Hasebe et al. 1990; Nui et al. 1994),

$$K_1 = \lim_{\rho \to 0} \frac{\sqrt{\pi}}{2} \sigma_\mathrm{max} \rho^{1-\lambda_1} \tag{2.131}$$

and also for hyperbolic V-notches under mode 2 loading (Benthem 1987), $a_{2\tau}$ and $a_{2\sigma}$ according to Table 2.2 (using a special mapping function):

$$K_2 = \lim_{\rho \to 0} \frac{\sqrt{\pi}}{a_{2\tau}} \tau_\mathrm{max} \rho^{1-\lambda_2} \tag{2.132}$$

$$K_2 = \lim_{\rho \to 0} \frac{\sqrt{\pi}}{a_{2\sigma}} \sigma_\mathrm{max} \rho^{1-\lambda_2} \tag{2.133}$$

Table 2.2 Parameter values for Benthem's NSIF K_2 of pointed V-notches, Eqs. (2.132) and (2.133); (Benthem 1987)

2α	λ_2	$a_{2\tau}$	$a_{2\sigma}$	2α	$\lambda_{2\perp}$	$a_{2\tau}$	$a_{2\sigma}$
0°	0.500	0.385	1.000	90°	0.909	0.620	1.213
30°	0.598	0.492	1.242	102.54°	1.000	0.707	1.179
60°	0.731	0.550	1.275				

Table 2.3 Parameter values for evaluation of $K_{1\rho}$ and $K_{2\rho}$ according to Eqs. (2.135) and (2.136); (Lazzarin and Filippi 2006)

2α	q	λ_1	λ_2	μ_1	μ_2	$\tilde{\omega}_1$	$\tilde{\omega}_2$
0°	2.0	0.500	0.500	−0.500	−0.500	1.000	−1.0
30°	1.833	0.501	0.598	−0.456	−0.447	1.034	−1.0
45°	1.750	0.505	0.660	−0.432	−0.412	1.014	−1.0
60°	1.667	0.512	0.731	−0.406	−0.373	0.970	−1.0
90°	1.500	0.545	0.909	−0.345	−0.288	0.810	−1.0
120°	1.333	0.616	1.149	−0.268	−0.198	0.570	−1.0
135°	1.250	0.674	1.302	−0.220	−0.151	0.432	−1.0

and finally for V-notches under mode 3 loading in analogy to Eq. (2.130):

$$K_3 = \lim_{\rho \to 0} \sqrt{\pi} \tau^*_{\max} \rho^{1-\lambda_3} \tag{2.134}$$

The Eqs. (2.127–2.134) above may be used without the limes with distinct finite values of ρ in an approximative manner, but the convergence behaviour must be checked (compare Figs. 1.32 and 1.33).

The third procedure evaluates the stresses in the bisector plane of the rounded notch or crack for determining $K_{1\rho}$, $K_{2\rho}$, $K_{3\rho}$ as the limit values for $r \to r_0$ (or $r \to r_{0+}$, the position of $\tau_{r\theta\ \max}$ in mode 2 loading) which may be combined with averaging these NSIFs over a small distance ahead of the notch root. The following formulae are derived for V-notches inclusive of cracks (Lazzarin and Filippi 2006; Zappalorto et al. 2008), Table 2.3:

$$K_{1\rho} = \lim_{r \to r_0} \frac{\sqrt{2\pi} r^{1-\lambda_1} \sigma_\theta(r, 0)}{1 + \tilde{\omega}_1 (r/r_0)^{\mu_1 - \lambda_1}} = \frac{\sqrt{2\pi} r_0^{1-\lambda_1} \sigma_\theta(r_0, 0)}{1 + \tilde{\omega}_1} \tag{2.135}$$

$$K_{2\rho} = \lim_{r \to r_{0+}} \frac{\sqrt{2\pi} r^{1-\lambda_2} \tau_{r\theta}(r, 0)}{1 + \tilde{\omega}_2 (r/r_0)^{\mu_2 - \lambda_2}} = \frac{\sqrt{2\pi} r_0^{1-\lambda_2} \tau_{r\theta}(r_{0+}, 0)}{1 - (r_{0+}/r_0)^{\mu_2 - \lambda_2}} \tag{2.136}$$

$$K_{3\rho} = \lim_{r \to r_0} \sqrt{2\pi} r^{1-\lambda_3} \tau_{\theta z}(r, 0) = \sqrt{2\pi} r_0^{1-\lambda_3} \tau_{\theta z}(r_0, 0) \tag{2.137}$$

The value $\tilde{\omega}_2 = -1$ in Eq. (2.136) is part of the stress field solution. The limit value $r \to r_{0+}$ instead of $r \to r_0$ in mode 2 loading is proposed here in order to avoid numerical problems when introducing $r = r_0$. An 'equivalent V-notch' may be defined for other notch types (e.g. semicircular) based on Eq. (2.135); (Filippi and Lazzarin 2004).

The NSIFs $K_{1\rho}$, $K_{2\rho}$, $K_{3\rho}$ differ from K_1, K_2, K_3 for finite values of ρ. They are generally enlarged for increasing values of ρ. The following relationship should be valid, because $r_0 \propto \rho$:

$$K_\mathrm{i} = \lim_{\rho \to 0} K_{\mathrm{i}\rho} \quad (\mathrm{i} = 1,\ 2,\ 3) \tag{2.138}$$

The condition according to Lazzarin, that the enlarged values of $K_{1\rho}$, $K_{2\rho}$, $K_{3\rho}$ can be used as characteristic stress field parameters at rounded notches ($\rho > 0$), is the constancy of $K_{1\rho}$, $K_{2\rho}$, $K_{3\rho}$ over a certain distance from the notch root. If this condition is met, the NSIF concept is applicable also to notches with a substantially increased notch radius.

In cases of a slightly (oscillating) dependence of $K_{1\rho}$, $K_{2\rho}$, $K_{3\rho}$ on $(r - r_0)$, the distance from the notch root, the following averaging procedure is proposed (Lazzarin and Filippi 2006):

$$\overline{K}_{\mathrm{i}\rho} = \frac{1}{\eta\rho} \int_{r_0}^{r_0+\eta\rho} K_{\mathrm{i}\rho} dr \quad (\mathrm{i} = 1,\ 2,\ 3) \tag{2.139}$$

where $\eta = 0.4$ is a recommended choice. The averaging procedure is also preferred in cases of a very small notch radius where sufficiently fine FE meshing at the notch root is difficult to achieve.

Now the question arises, to what extent the stress field equations expressed by K_1, K_2, K_3 or K_I, K_II, K_III can be used with the generally enlarged values of $K_{1\rho}$, $K_{2\rho}$, $K_{3\rho}$. The answer depends on the considered case. As far as possible, the stress field equations should be used, from which the relationships for $K_{1\rho}$, $K_{2\rho}$, $K_{3\rho}$ were derived.

These relationships depend on the notch shape. Those mentioned above refer to V-notches or hyperbolic notches with the parabolic notch as a special case. The comparison of hyperbolic with circular arc V-notches reveals a slight difference even in mode 1 loading (Savruk and Kazberuk 2010). The formulae for elliptical notches are also different to some extent. The relationships for V-notches with root hole, the keyhole notch among them, deviate even more. They will be presented in Sect. 2.4.6.

Not only the notch shape exerts an influence on the values of $K_{1\rho}$, $K_{2\rho}$, $K_{3\rho}$, but also the geometrical and dimensional parameters of the notched members as well as its loading and support conditions. Cross-sectional weakening and notch-parallel loading (or T-stress) are especially influential.

The generalised NSIFs $K_{1\rho}$, $K_{2\rho}$, $K_{3\rho}$ have potential for application insofar as they define the stress field over a finite area (or volume), just as the simple NSIFs or SIFs do. The widely used stress concentration factors (SCFs) give only the maximum stress at one point. Additional information on the stress field is needed, in order to characterise the fatigue life or brittle fracture strength, e.g. notch stress averaging, notch stress gradient, critical distance among others. In contrast, the NSIFs (possibly supplemented by the T-stress and S-stress terms) represent the complete notch stress field without additional information being necessary. Whereas the SCFs are not applicable to pointed notches, the NSIFs proceed from pointed notches.

The NSIFs in contrast to the SCFs also include the scale or size effect on brittle fracture or fatigue strength. Considering a small notched component, the notch with radius ρ_1, in comparison to a self-similar enlarged notched component, the notch with radius ρ_2, both components subjected to the same nominal stresses, then the SCFs K_t are identical, but the NSIFs are related by $(\rho_2/\rho_1)^{1-\lambda}$ according to Eqs. (2.131–2.134). They define two stress profiles of different level ahead of the notch root starting with the same value of the maximum stress. One method to determine failure-effective notch stresses is to average the notch stresses over a definite, material-dependent microstructural support length. These averaged notch stresses will be higher for the larger component. Thus, in comparison with a constant endurable averaged notch stress, the larger component with the higher NSIF will come off worse.

2.4.5 Evaluation Examples for Stresses at Blunt V-Notches

Some typical evaluation examples for the stresses at sharply rounded (blunt) V-notches subjected to tensile and in-plane shear loading are reviewed in the following in order to achieve further clarity on the generalised NSIF concept.

In the first four figures, the determination of the NSIFs $K_{1\rho}$ and $K_{2\rho}$ (as far as relevant) according to Eqs. (2.135) and (2.136) is exemplified. The tensile loaded flat bar with two-sided U-notch is considered in Fig. 2.33. A slight oscillation of $K_{1\rho}$ over $(r - r_0)$ occurs for $\rho \neq 0$ in the evaluation range up to $(r - r_0) = 1$ mm. The value of $K_{1\rho}$ rises with the ratio ρ/a (with notch depth a), as specified further below. The oscillation is enlarged for the V-notch with $2\alpha = 135°$, while the influence of ρ/a is reduced, Fig. 2.34. Mixed mode loading conditions occur in the bisector plane of the shoulder fillet flat bar in Fig. 2.35 and of the weld-like flat bar in Fig. 2.36. Once more, some variability of $K_{1\rho}$ or $K_{2\rho}$ is detected in the evaluation range.

The stress distribution in the notch bisector ahead of the notch root in a tensile loaded V-notched flat bar is plotted in Fig. 2.37 for three notch opening angles. Original and $K_{1\rho}$-based analysis results are compared. A first curve segment up to 0.1 mm is mainly controlled by the maximum notch stress. A second segment up to 5 mm presents the gradient of the corresponding pointed notch configuration. The third segment correlates with the nominal stress, actually in the net cross-section. Another similar diagram, where the notch radius is varied, is shown in Fig. 2.38. The averaged solution for $K_{1\rho}$ is evaluated. The first curve segment is limited by $(r - r_0)/\rho \approx 0.1$. The nominal stress is related to the net cross-section.

The linearised rise of $K_{1\rho}/K_1$ over the ratio of notch radius to notch depth, ρ/a, is shown in Fig. 2.39 and also by Table 2.4. Actually, the curves should start at $K_{1\rho}/K_{1\rho} = 1.0$ for $\rho/a = 0$, which is suppressed by the linearisation, compare Eq. (2.138). The result is independent on b/a for sufficiently large values of this ratio.

Corresponding results for in-plane shear loading are recorded in subsequent graphs. The analysed configuration is a rectangular plate with a two-sided internal parabolic, hyperbolic, U-shaped or V-shaped notch, the plate subjected to

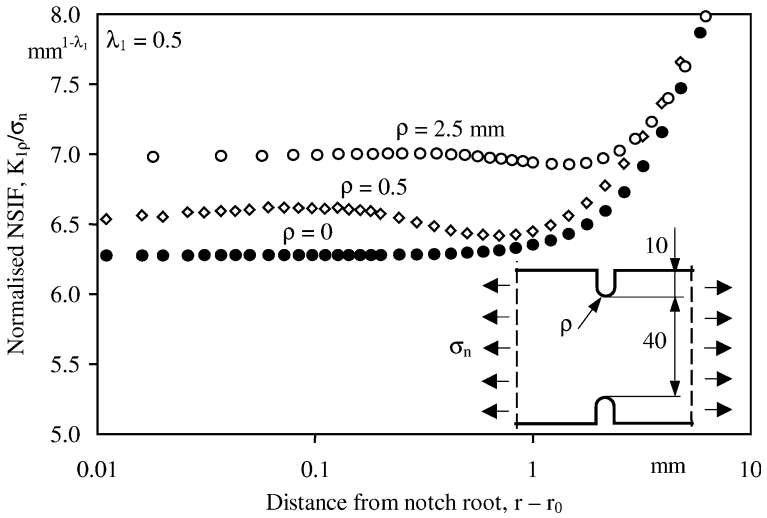

Fig. 2.33 Normalised NSIF $K_{1\rho}$ dependent on distance from U-notch root, $(r - r_0)$, Eq. (2.135) for $2\alpha = 0°$; evaluation of FE analysis results; (Lazzarin and Filippi 2006)

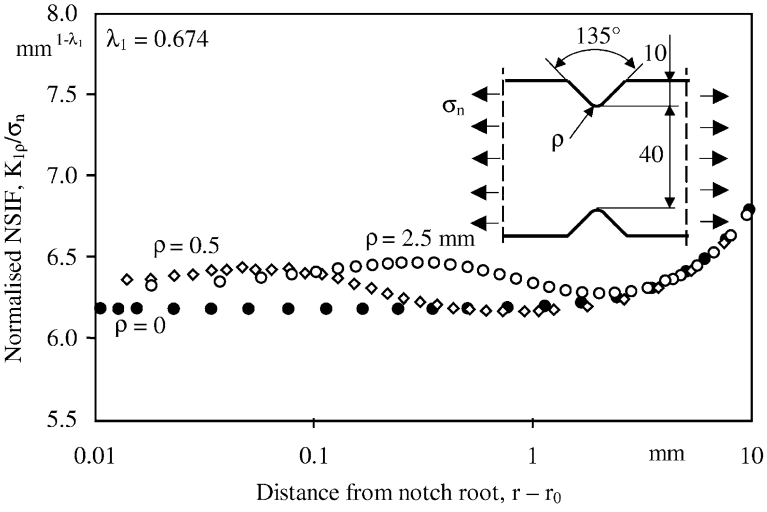

Fig. 2.34 Normalised NSIF $K_{1\rho}$ dependent on distance from V-notch root, $(r - r_0)$, Eq. (2.135) for $2\alpha = 135°$; evaluation of FE analysis results; (Lazzarin and Filippi 2006)

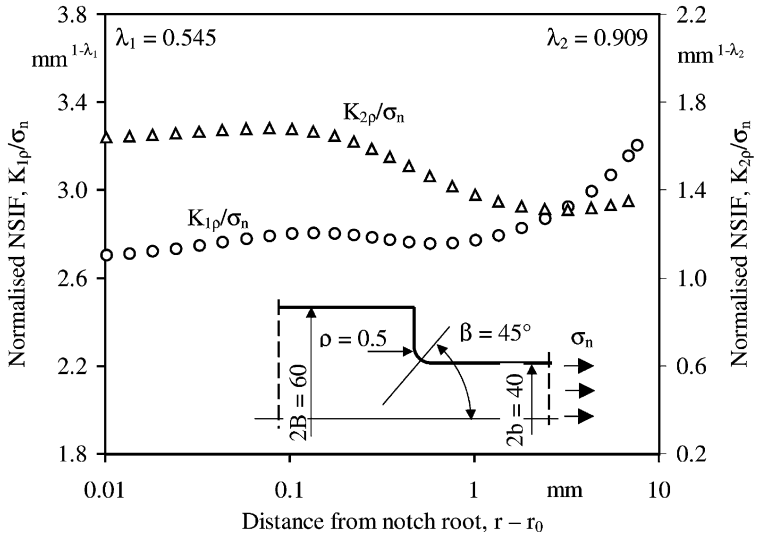

Fig. 2.35 Normalised NSIFs $K_{1\rho}$ and $K_{2\rho}$ dependent on distance from corner notch root, $(r - r_0)$, Eqs. (2.135) and (2.136) for $2\alpha = 90°$; evaluation of FE analysis results; (Lazzarin and Filippi 2006)

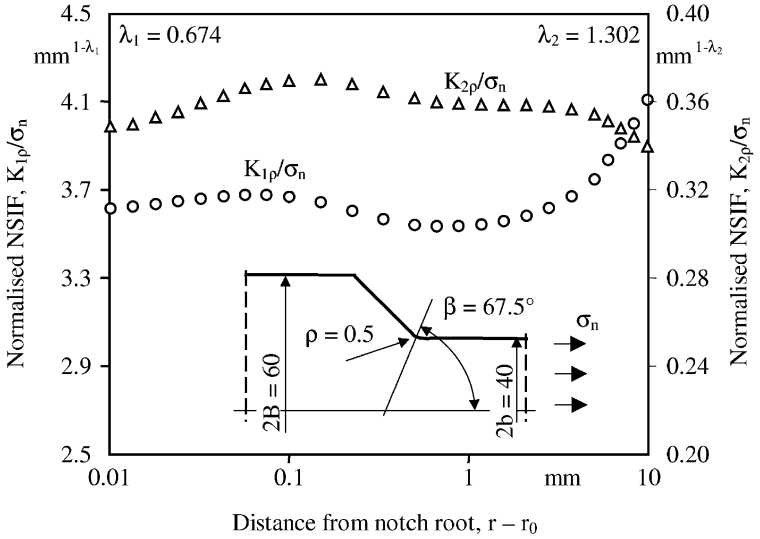

Fig. 2.36 Normalised NSIFs $K_{1\rho}$ and $K_{2\rho}$ dependent on distance from corner notch root, $(r - r_0)$, Eqs. (2.135) and (2.136) for $2\alpha = 135°$; evaluation of FE analysis results; (Lazzarin and Filippi 2006[(1)])

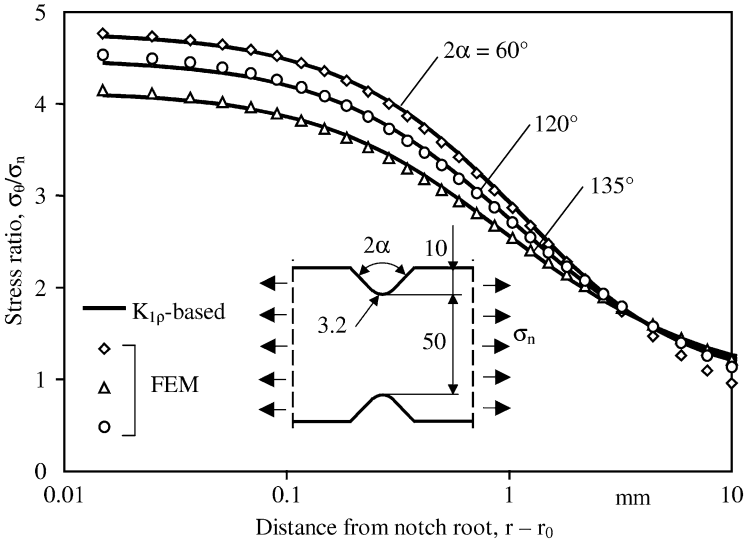

Fig. 2.37 Stress σ_θ in notch bisector ahead of the V-notch root, notch radius $\rho = 3.2$ mm, for three notch opening angles 2α; original compared with $K_{1\rho}$-based FE analysis results; $K_{1\rho}/K_1$ approximated according to Eq. (2.139) and Table 2.4; (Lazzarin and Filippi 2006)

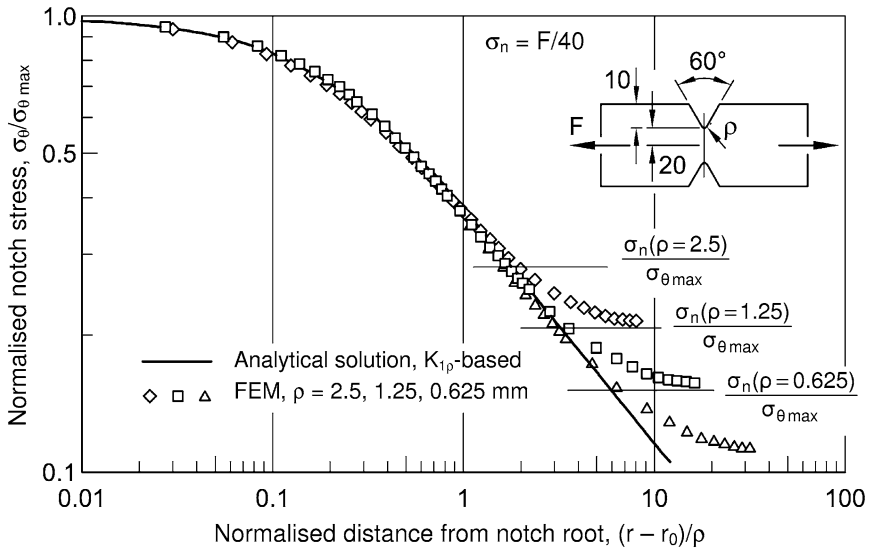

Fig. 2.38 Stress σ_θ in notch bisector over distance from V-notch root, $(r - r_0)$; direct compared with $K_{1\rho}$-based FE analysis results; $K_{1\rho}$ according to Eq. (2.139) with finite values of ρ; (Lazzarin and Tovo 1996)

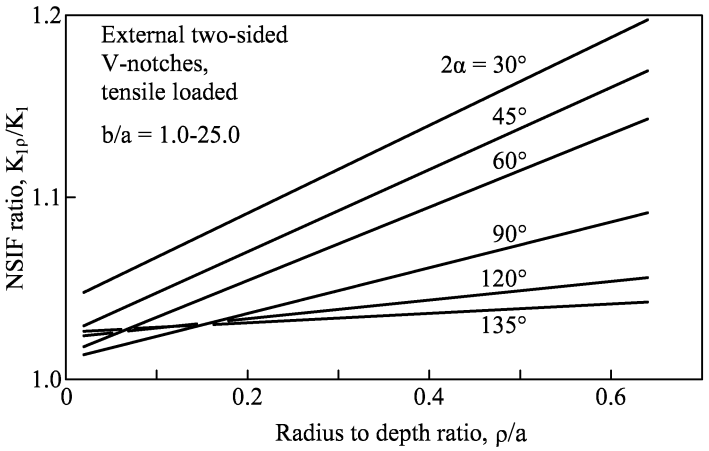

Fig. 2.39 NSIF ratio $K_{1\rho}/K_1$ dependent on the ratio of V-notch radius to V-notch depth, ρ/a, based on FE analysis results; various notch opening angles 2α; (Lazzarin and Filippi 2006)

Table 2.4 Parameter values for the approximation of $K_{1\rho}/K_1 = \varphi + \psi(\rho/a)$ for V-notched flat bar; different notch opening angles 2α; net cross-sectional width $2b$ to notch depth a ratios $2b/a = 2, 5, 10, 50$ (Lazzarin and Filippi 2006)

2α	30°	45°	60°	90°	120°	135°
φ	1.043	1.025	1.014	1.011	1.023	1.026
ψ	0.241	0.226	0.200	0.127	0.051	0.025

prescribed remote edge displacements u_0 and v_0 together with shear-compatible support conditions in the two geometrical symmetry planes, Fig. 2.40. The reference stress τ_0 is produced in the rectangular plate without the notch. It is smaller than the nominal stress in the gross cross-section of the plate with the internal notch.

At first, parabolic and hyperbolic notches are considered. The curves of $K_{2\rho}/\tau_0$ over distance from the notch root for the hyperbolic notch ($2\alpha = 60°$), Fig. 2.41, show that $K_{2\rho}$ is substantially enlarged even for small values of ρ, e.g. $\rho = 0.1$ mm. The corresponding shear stresses in the bisector are plotted in Fig. 2.42. The curves run asymptotically to the straight line of the pointed notch. The FE analysis results of the parabolic and hyperbolic notches have also been evaluated using $\overline{K}_{2\rho}$ according to Eq. (2.139). The parabolic notch results are set in comparison to $K_{2\rho}(\tau_{max})$ according to Eq. (2.128) with K_{II} substituted by $K_{2\rho}$ (Cheng 1988). Additionally, the maximum principal stresses at the notch edge corresponding to the maximum tangential stress are compared, Table 2.5. The correspondence is satisfactory.

The rise of $K_{1\rho}/K_2$ over the ratio of notch radius to notch depth, ρ/a, is shown in Fig. 2.43 for parabolic and hyperbolic notches. All the curves converge to $K_{2\rho}/K_2 = 1.0$ for $\rho/a = 0$, as demanded by Eq. (2.138). The rise is strongest for the parabolic notch.

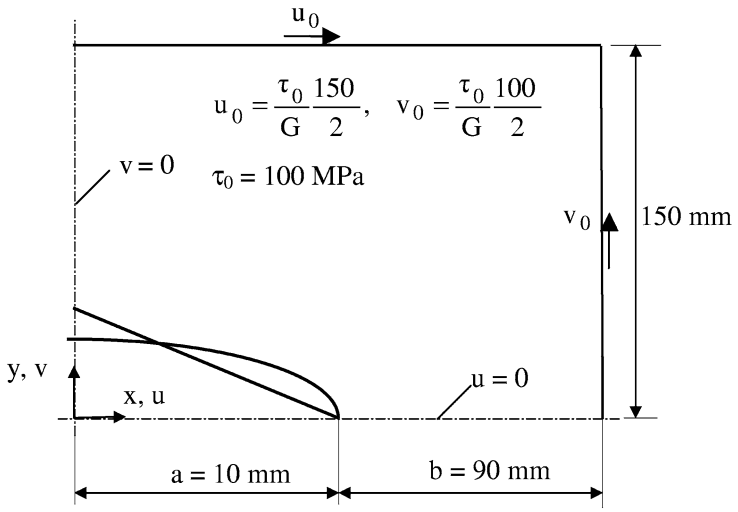

Fig. 2.40 One symmetry quarter of rectangular plate with parabolic or hyperbolic internal two-sided V-notch subjected to prescribed displacements at the remote plate edges producing in-plane shear loading conditions; same edge displacements applied to the plate with central crack or pointed V-notch of semidepth $a = 10$ mm; (Lazzarin et al. 2011)

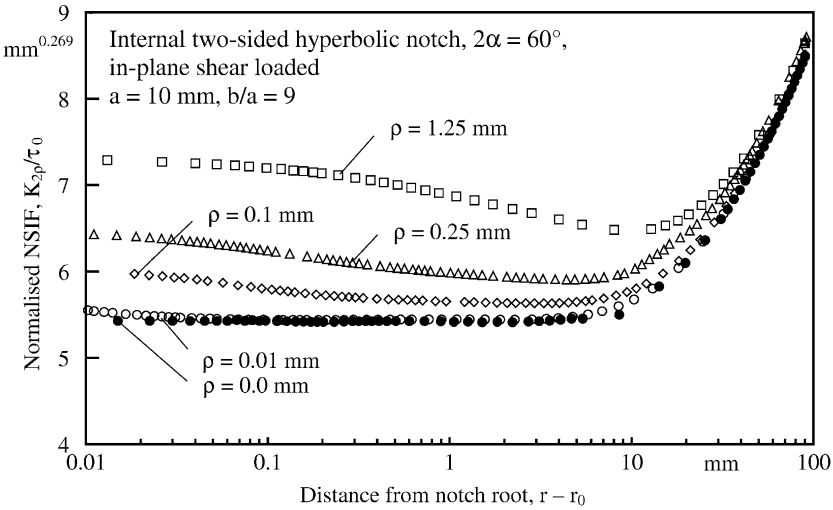

Fig. 2.41 Normalised NSIF $K_{2\rho}$ of internal two-sided hyperbolic notch ($2\alpha = 60°$, different notch radii) dependent on distance from notch root, $(r - r_0)$, $K_{2\rho}$ according to Eq. (2.136); evaluation of FE analysis results; (Lazzarin et al. 2011)

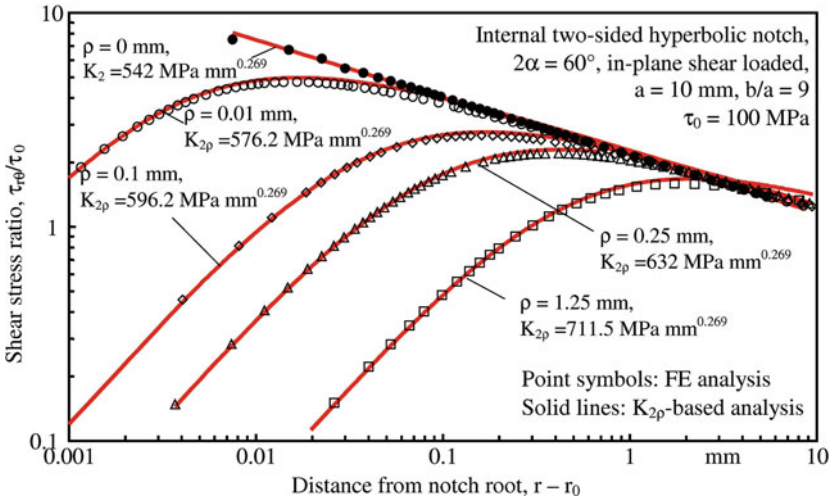

Fig. 2.42 Shear stress $\tau_{r\theta}$ in notch bisector over distance from notch root, $(r - r_0)$; internal two-sided hyperbolic notch ($2\alpha = 60°$, different notch radii), in-plane shear loaded; direct compared with $K_{2\rho}$-based FE analysis results; $K_{2\rho}$ according to Eq. (2.136) averaged by Eq. (2.139); (Lazzarin et al. 2011)

Table 2.5 Generalised NSIFs of two-sided parabolic notch ($\lambda_2 = 0.5$) in rectangular plate subjected to in-plane shear loading; $\overline{K}_{2\rho}$ averaged over 0.4ρ, Eq. (2.139), or based on τ_{max}, Eq. (2.128); additionally maximum principal (or tangential) stresses at notch edge; deviations $\Delta_K = (K_{2\rho,\tau}/\overline{K}_{2\rho} - 1) \times 100$ and $\Delta_\sigma = (\sigma_{1\,max,\overline{K}}/\sigma_{1\,max,FE} - 1) \times 100$; (Lazzarin et al. 2011)

ρ [mm]	$\tau_{r\theta\ max,FE}$ [MPa]	$\overline{K}_{2\rho}$ [MPa mm$^{0.5}$]	$K_{2\rho,\tau}$ [MPa mm$^{0.5}$]	Δ_K [%]	$\sigma_{1max,FE}$ [MPa]	$\sigma_{1\,max,\overline{K}}$ [MPa]	Δ_σ [%]
0.01	1306.1	596.0	601.5	0.92	3204.0	3211.0	0.22
0.10	465.8	677.0	678.2	0.18	1204.5	1207.9	0.28
0.50	249.3	809.6	811.8	0.27	639.2	646.0	1.05
1.25	190.3	977.7	979.8	0.21	477.8	493.4	3.26
2.50	159.5	1177.5	1161.3	−1.37	405.6	420.2	3.59
4.00	145.8	1376.2	1342.8	−2.43	370.6	388.2	4.75

At second, the U-notch and V-notches are analysed, using the $K_{2\rho}$ formula of root holes, Eq. (2.144). It was found that this formula is more accurate than the corresponding formula for hyperbolic (and parabolic) notches, Eq. (2.136), which shifts the position of $\tau_{r\theta\ max}$ closer to the notch root. The curves $K_{2\rho}/\tau_0$ over distance $(r - r_0)$ from the notch root for the U-notch, Fig. 2.44, show that $K_{2\rho}$ is substantially enlarged only for larger values of ρ ($\rho/a \geq 0.1$). The corresponding shear stresses in the bisector are plotted in Fig. 2.45. The curves are identical up to the maximum stress and then deviate in approximation of the nominal stress in the net cross-section with the exception of the $K_{2\rho}$-based solid line which presumes an infinitely wide cross-section.

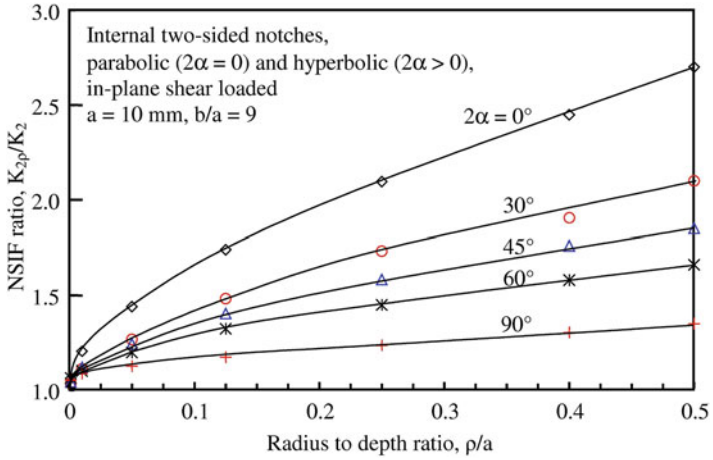

Fig. 2.43 Parabolic and hyperbolic notches: NSIF ratio $K_{2\rho}/K_2$ dependent on the ratio of notch radius to notch depth, ρ/a, based on FE analysis results; various notch opening angles 2α; (Lazzarin et al. 2011)

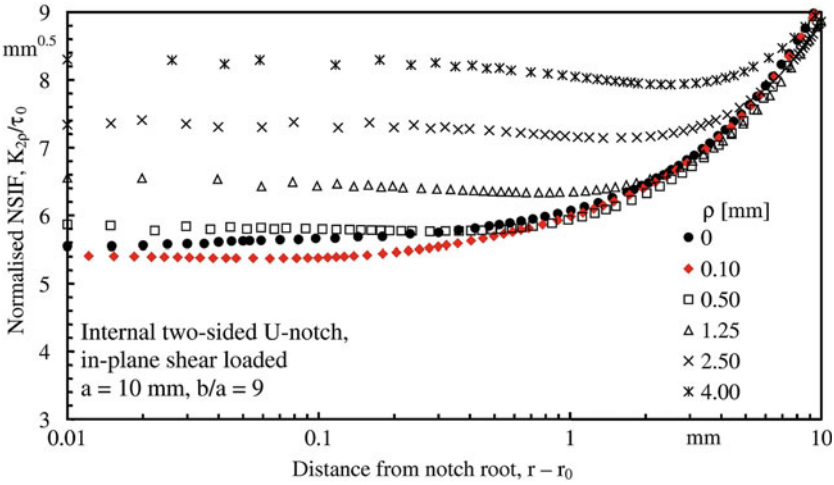

Fig. 2.44 Normalised NSIF $K_{2\rho}$ of internal two-sided U-notch (different notch radii) dependent on distance from notch root, $K_{2\rho}$ according to Eq. (2.144); evaluation of FE analysis results; (Lazzarin et al. 2011)

The rise of $K_{2\rho}/K_2$ over the ratio of notch radius to notch depth, ρ/a, is plotted in Fig. 2.46 for U-notch and V-notches. The deviation between actual and analytical notch shape has the effect that the limes condition, Eq. (2.138), is violated for larger values of 2α ($K_{2\rho}/K_2$ does not converge to 1.0 for $\rho \rightarrow 0$).

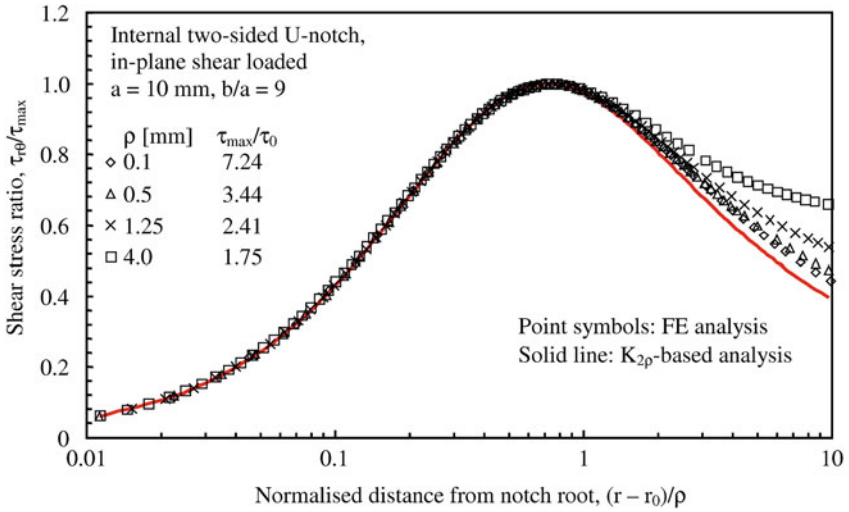

Fig. 2.45 Shear stress $\tau_{r\theta}$ in notch bisector over distance from notch root, $(r - r_0)$; internal two-sided U-notch (different notch radii), in-plane shear loaded; direct compared with $K_{2\rho}$-based FE analysis results; $K_{2\rho}$ according to Eq. (2.144); (Lazzarin et al. 2011)

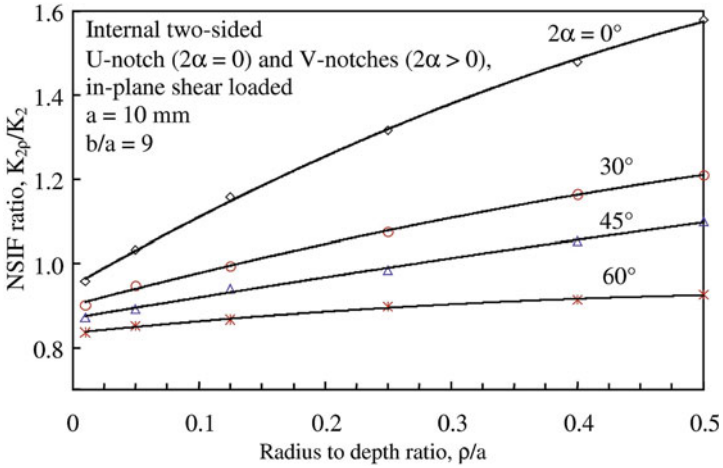

Fig. 2.46 U-notch and V-notches: NSIF ratio $K_{2\rho}/K_2$ dependent on the ratio of notch radius to notch depth, ρ/a, based on FE analysis results evaluated by Eq. (2.144); various notch opening angles 2α; (Lazzarin et al. 2011)

Finally, the notch stress curves for a quadratic plate specimen with one-sided V-notch, used for brittle fracture testing of brittle materials, are drawn in Fig. 2.47. The notch opening angle $2\alpha = 45°$ is fixed, the V-notch radius ρ is varied between 0 and 1 mm. The tensile forces F produce superimposed nominal tensile and

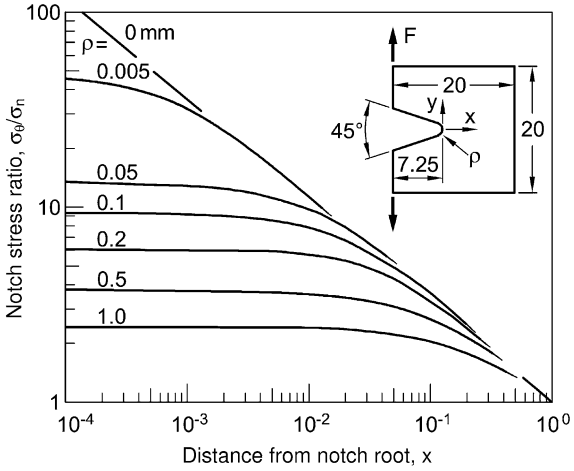

Fig. 2.47 Stress σ_θ in notch bisector over distance from notch root, x; one-sided rounded V-notches in comparison to pointed V-notch in square plate; notch opening angle $2\alpha = 45°$; (Nui et al. 1994)

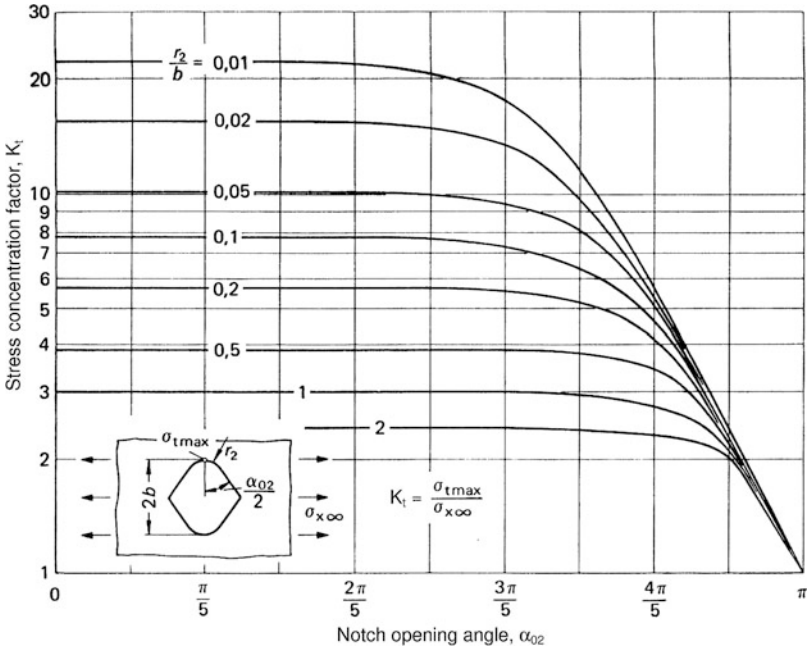

Fig. 2.48 SFCs of internal two-sided rounded V-notches ('rhombic cutouts') dependent on notch opening angle α_{02} for various ratios r_2/b of notch radius to notch depth; infinite plate subjected to remote tensile loading; results by functional analysis; (Radaj and Schilberth 1977)

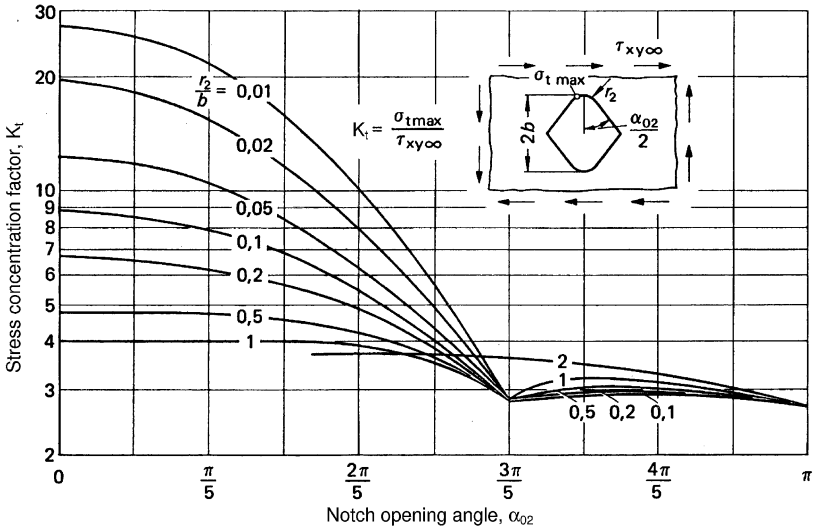

Fig. 2.49 SFCs of internal two-sided rounded V-notches ('rhombic cutouts') dependent on notch opening angle α_{02} for various ratios r_2/b of notch radius to notch depth; infinite plate subjected to remote in-plane shear loading; results by functional analysis; (Radaj and Schilberth 1977)

bending stresses in the net cross-section. The solution of the stress field problem has been achieved based on Kolosov–Muskhelishvili's complex stress function method combined with conformal mapping of the polygonal plate area onto the unit circle by applying the Schwartz–Christoffel transformation (Nui et al. 1994). For evaluating the notch stress at the pointed notch, Williams' singularity exponents are introduced. It is demonstrated that the maximum notch stresses in the close neighbourhood of the notch root, $(r - r_0)/\rho \leq 0.2$, depend predominantly on the notch radius, whereas outside this region, the notch opening angle is decisive, as given by the pointed notch solution. It is visible from the graph, that the rounded notch curves run slightly above the pointed notch curve, which indicates $K_{1\rho} > K_1$.

It is also shown more generally and in quantitative terms that the intermediate NSIF-governed stress field may be used to characterise the yielding or strength behaviour of sharply rounded notches (Nui et al. 1994; Dini and Hills 2004). This field is intermediate between the maximum notch stress governed near-field and the nominal stress governed far-field.

This subsection with the evaluation examples for the notch stresses at rounded V-notches is closed with two diagrams showing the SCFs of internal two-sided V-notches ('rhombic cutouts') in the infinite plate subjected to remote in-plane tensile and shear loading, Figs. 2.48 and 2.49; (Radaj and Schilberth 1977).

These SCFs have been determined very accurately based on complex analytical stress functions according to Kolosov–Muskhelishvili, combined with conformal mapping of the rhombic cutout with rounded V-notches according to Schwartz–Christoffel. A polygonal shape is considered, consisting of straight lines and

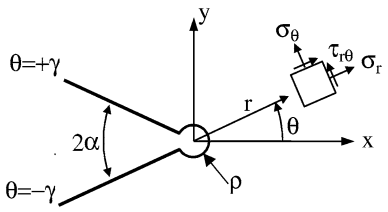

Fig. 2.50 V-notch with root hole, polar in-plane coordinate system with origin in centre of hole; (Zappalorto and Lazzarin 2011[(1)])

circular arcs. The circular arcs are approximated by multi-corner polygons. Their series expansion as a mapping function is truncated, so that the corners are smoothed. The NSIF concept is not applied.

The SCFs are primarily dependent on the ratio r_2/b of notch radius to notch depth. They may additionally depend on the notch opening angle α_{02}. In tensile loading, the latter dependency is marked only for $\alpha_{02} \geq 90°$. In shear loading, the SCFs decrease rapidly with increasing values of $\alpha_{02} > 0°$. They reach their maximum at $\alpha_{02} = 108°$. This angle corresponds to the limit value for singular stresses in mode 2 loading of pointed V-notches, $2\alpha = 102.6°$. Actually, the curve points were calculated in steps of $\Delta\alpha_{02} = 18°$, so that $\alpha_{02} = 108°$ is the curve point nearest to the no-singularity angle.

The NSIF concept needs the FE analysis as basis for evaluations in engineering applications. Parametric investigations, as just considered above, would necessitate variation of the geometrical parameters in the FE model before addressing the NSIF behaviour. To the author's knowledge, no such investigations have been performed up to now. Deviations from the SCF behaviour will predominantly be caused by a varying stress gradient normal to the notch root. This gradient is primarily dependent on the reciprocal value of ρ and only occasionally on the notch opening angle to a larger extent.

2.4.6 Stress Field at V-Notches with Root Hole

V-notches with root hole and the special case of the keyhole are rarely used in engineering designs. Here, blunt notches with a smooth transition from the rectilinear to the circular notch edge are preferred, because they produce lower notch stresses and are easier to produce. On the other hand, they are an important design within the theoretical frame of stress analysis. They allow an easier handling of solutions and they simulate the circular notch shape accurately, which is important in those cases where the maximum notch stress occurs outside the bisector. The advantage of their use in NSIF considerations is, that the variation of the notch radius does not affect the other geometrical parameters of the notch. This is not the case with elliptical, parabolic or hyperbolic notches.

First, tensile and in-plane shear loading is dealt with, then out-of-plane shear loading and finally the transverse (out-of-plane) shear loading effect produced by in-plane shear loading at load-free surfaces.

Table 2.6 Parameter values for evaluation of the stresses $\sigma_\theta(r, 0)$ normal to the bisector plane under mode 1 loading dependent on notch opening angle 2α; (Zappalorto and Lazzarin 2011[(1)])

2α	0°	30°	45°	60°	90°	120°	135°
λ_1	0.5000	0.5015	0.5050	0.5122	0.5445	0.6157	0.6736
φ_1	0.5000	0.5338	0.5770	0.6401	0.8388	1.1538	1.3556
g_1	2.0000	2.0352	2.0820	2.1523	2.3833	2.7696	3.0292
g_2	1.2500	1.2705	1.3006	1.3486	1.5116	1.7638	1.9030
g_3	1.5000	1.4942	1.4800	1.4514	1.3260	1.0639	0.8659
g_4	1.2500	1.3352	1.4453	1.6081	2.1342	3.0181	3.6243

For analysing the stress field under in-plane loading conditions for the V-notch with root hole shown in Fig. 2.50, the Kolosov–Muskhelishvili method is applied (Zappalorto and Lazzarin 2011[(1)]). The following analytical functions are used, with $\varphi(z)$ and $\psi(z)$ being interchanged in the article just mentioned (Muskhelishvili 1963):

$$\varphi(z) = az^{\lambda} + bz^{-\lambda} \tag{2.140}$$

$$\psi(z) = cz^{\lambda} + dz^{-\lambda} + ez^{-\lambda-1} + fz^{-\lambda-2} \tag{2.141}$$

where λ is real and positive whereas the coefficients a, b, c, d, e and f are complex.

The eigenvalues λ_1 and λ_2 result from the boundary condition of load-free notch flanks, as before. Further boundary conditions can be stated on the circular edge of the root hole for determining the free coefficients:

$$(\sigma_r)_{r=\rho} = (\tau_{r\theta})_{r=\rho} = 0 \tag{2.142}$$

The resulting stress field is separated into a symmetric (mode 1) and antimetric (mode 2) part. In the following, only the stress σ_θ (mode 1) or $\tau_{r\theta}$ (mode 2) in the bisector as well as the stress σ_θ at the hole edge are recorded and compared with FE analysis results for external or internal two-sided V-notches in a rectangular plate specimen. The nominal notch depth is $a = 10$ mm, the nominal semiwidth of the net cross-section is $b = 9a$. Taking the root hole into account, the actual notch depth is $(a + \rho)$ and the actual semiwidth $(b - \rho)$.

In the case of mode 1 loading, the stresses $\sigma_\theta(r, 0)$ normal to the bisector plane have the following form:

$$\sigma_\theta(r, 0) = \frac{K_{1\rho}}{\sqrt{2\pi}} \frac{r^{\lambda_1 - 1}}{(1 + \lambda_1) + \phi_1(\gamma)} \left[g_1 + g_2 \left(\frac{\rho}{r}\right)^{2\lambda_1} + g_3 \left(\frac{\rho}{r}\right)^{2\lambda_1 + 1} + g_4 \left(\frac{\rho}{r}\right)^{2\lambda_1 + 2} \right] \tag{2.143}$$

with the coefficients g_1 to g_4 and ϕ_1 depending on the notch opening angle 2α (or $2\gamma = 2\pi - 2\alpha$) according to Table 2.6. The NSIF $K_{1\rho}$ may be determined by evaluation of $\sigma_\theta(r, 0)$ from a FE analysis of the considered V-notch with root hole, solving Eq. (2.143) for $K_{1\rho}$ dependent on the distance from the notch root.

Table 2.7 Parameter values for evaluation of the stresses $\tau_{r\theta}(r, 0)$ in the bisector plane under mode 2 loading dependent on notch opening angle 2α; (Zappalorto and Lazzarin 2011[(1)])

2α	0°	30°	45°	60°	90°	120°	135°
λ_2	0.5000	0.5982	0.6597	0.7309	0.9085	1.1489	1.3021
h_1	1.6250	1.6422	1.6639	1.6941	1.7782	1.8873	1.9451
h_2	−0.7500	−0.6011	−0.5393	−0.4849	−0.3921	−0.3079	−0.2614
h_3	−1.8750	−2.0411	−2.1246	−2.2092	−2.3861	−2.5794	−2.6837

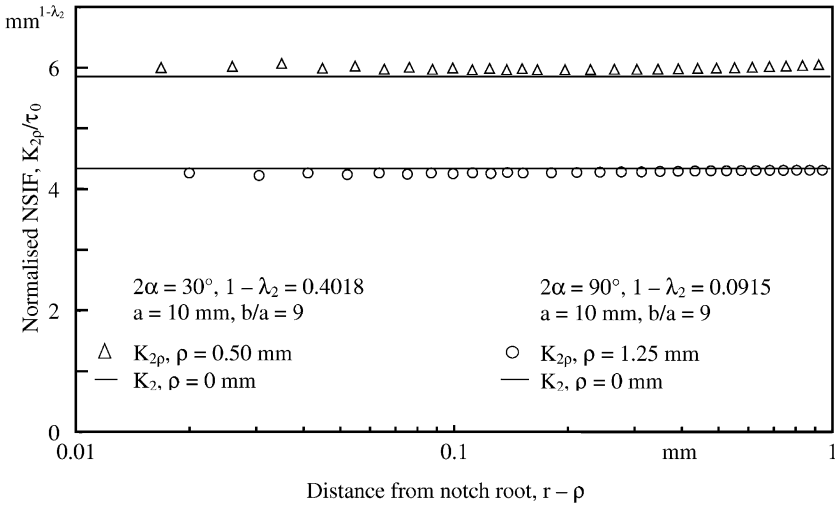

Fig. 2.51 V-notches with root hole: NSIFs $K_{2\rho}$ and K_2 dependent on distance from notch root; evaluation based on Eq. (2.144); (Lazzarin et al. 2011)

In the case of mode 2 loading, the stresses $\tau_{r\theta}(r, 0)$ in the bisector plane are given as follows:

$$\tau_{r\theta}(r, 0) = \frac{K_{2\rho}}{\sqrt{2\pi}} r^{\lambda_2 - 1} \left[1 + h_1 \left(\frac{\rho}{r} \right)^{2\lambda_2} + h_2 \left(\frac{\rho}{r} \right)^{2\lambda_2 + 1} + h_3 \left(\frac{\rho}{r} \right)^{2\lambda_2 + 2} \right] \tag{2.144}$$

with the coefficients h_1 to h_3 depending on the notch opening angle 2α according to Table 2.7. The NSIF $K_{2\rho}$ may be determined by evaluation of $\tau_{r\theta}(r, 0)$ from a FE analysis of the considered V-notch with root hole, solving Eq. (2.144) for $K_{2\rho}$ dependent on the distance from the notch root. Such an evaluation is shown in Fig. 2.51. Identical values of $K_{2\rho}$ and K_2 are found, evaluating Eq. (2.144) for $\rho > 0$ in comparison to $\rho = 0$. The values are constant over a distance from the notch root, where, with the evaluations for blunt V-notches hitherto considered, substantial variations and oscillations occur.

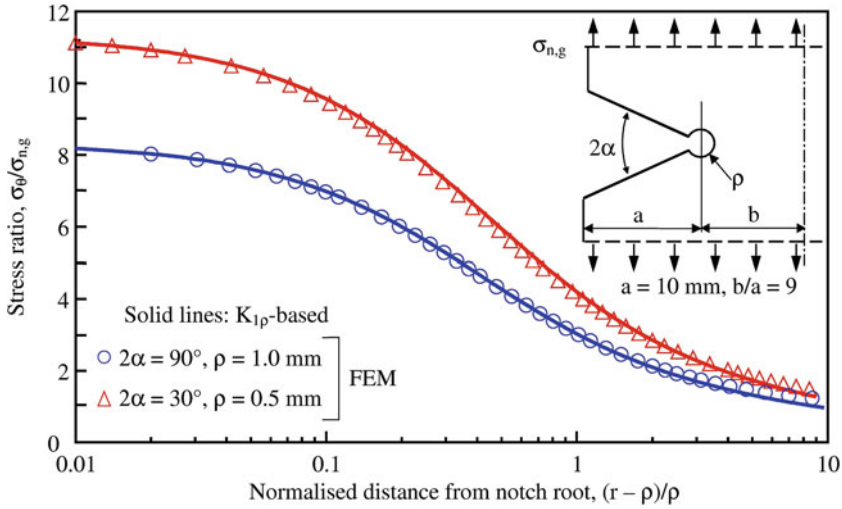

Fig. 2.52 Tensile loaded V-notch with root hole: stress σ_θ in notch bisector ahead of the notch root; two notch opening angles 2α combined with different notch radii ρ; direct compared with $K_{1\rho}$-based FE analysis results; (Zappalorto and Lazzarin 2011[(1)])

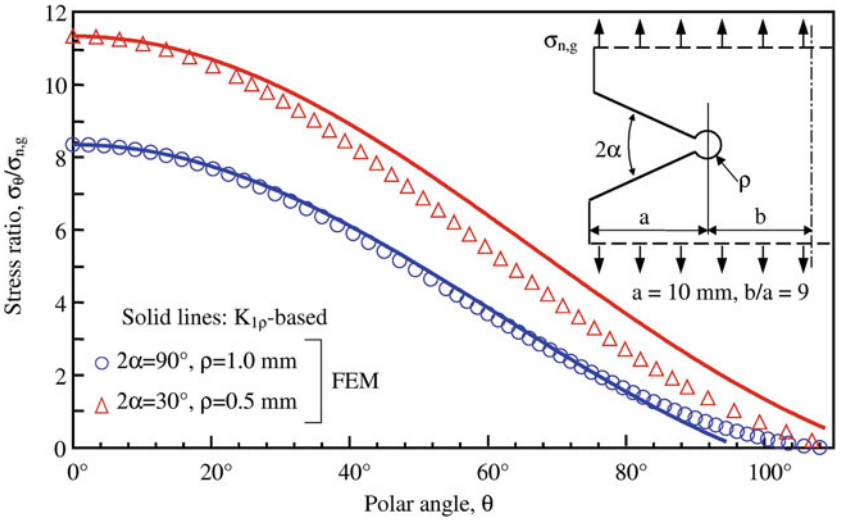

Fig. 2.53 Tensile loaded V-notch with root hole: stress σ_θ at hole edge; two notch opening angles 2α combined with different notch radii ρ; direct compared with $K_{1\rho}$-based FE analysis results; (Zappalorto and Lazzarin 2011[(1)])

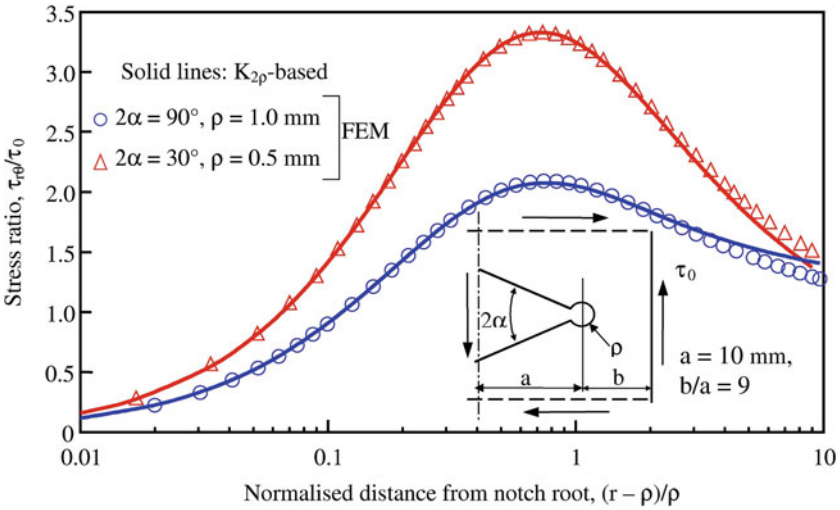

Fig. 2.54 In-plane shear-loaded V-notch with root hole: stress $\tau_{r\theta}$ in notch bisector ahead of the notch root; two notch opening angles 2α combined with different notch radii ρ; direct compared with $K_{2\rho}$-based FE analysis results; (Zappalorto and Lazzarin 2011[(1)])

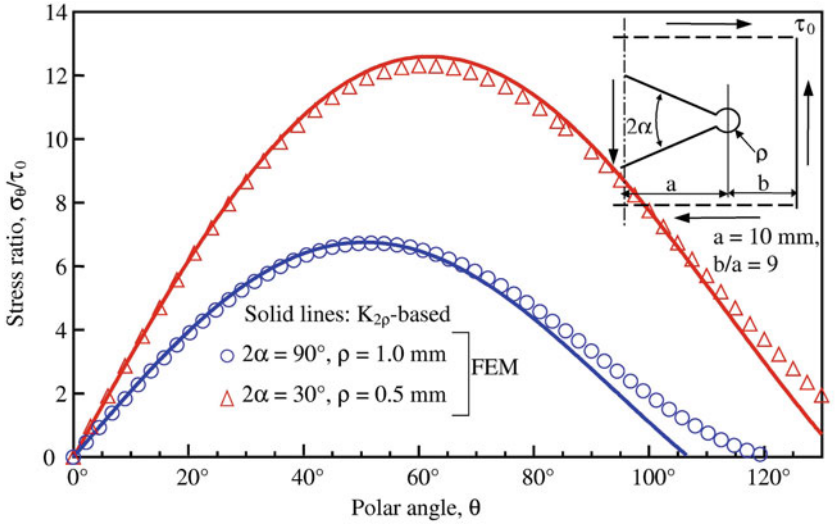

Fig. 2.55 In-plane shear-loaded V-notch with root hole: stress σ_θ at hole edge; two notch opening angles 2α combined with different notch radii ρ; direct compared with $K_{2\rho}$-based FE analysis results; (Zappalorto and Lazzarin 2011[(1)])

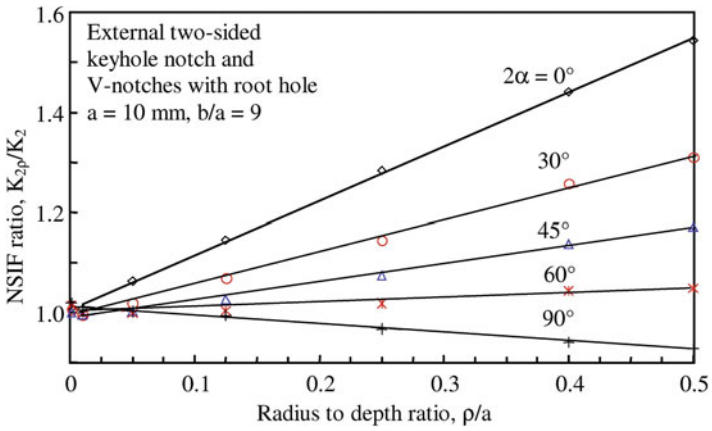

Fig. 2.56 V-notches with root hole: NSIF ratio $K_{2\rho}/K_2$ dependent on the ratio ρ/a of notch radius to notch depth, based on FE analysis results; various notch opening angles 2α; (Lazzarin et al. 2011(1))

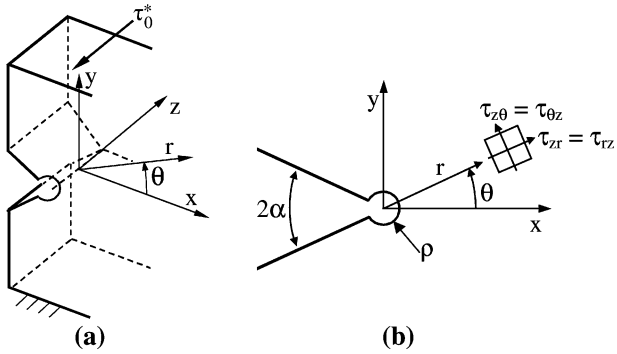

Fig. 2.57 V-notch with root hole subjected to out-of-plane shear loading (only the antiplane shear load component τ_0^* is shown); 3d view (**a**) and cross-sectional view (**b**); polar coordinate system with its origin in the centre of the hole; out-of-plane shear stress components; (Zappalorto and Lazzarin 2011(1))

For $\rho = 0$ (pointed notches), $K_{1\rho} \to K_1$ and $K_{2\rho} \to K_2$, as demanded by Eq. (1.138). The Eqs. (2.143) and (2.144) in the case of the keyhole ($2\alpha = 0$) are identical with those given in the literature (Kullmer 1992; Radaj et al. 2001).

The stresses σ_θ in mode 1 loading evaluated from the FE model mentioned above (converted to external notches) in the bisector plane ($\theta = 0$) and at the hole edge ($r = \rho$) are shown in Figs. 2.52 and 2.53. Direct FEM evaluation results are compared with the analytical stress distributions based on identical values of $\sigma_{\max}$ or $K_{1\rho}$. Some deviations are visible in the edge stress diagram, indicating the approximative character of the analytical solution.

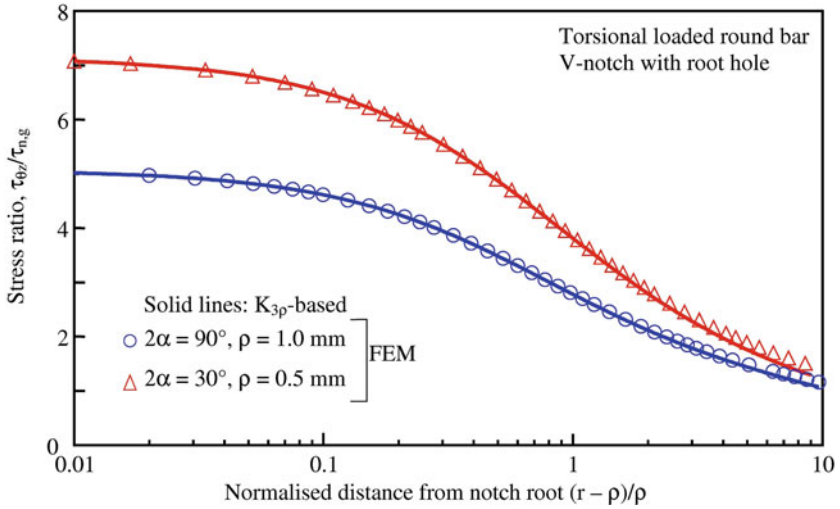

Fig. 2.58 Torsional-loaded round bar (mode 3), circumferential V-notch with root hole: shear stress $\tau_{\theta z}$ in notch bisector ahead of the notch root; two notch opening angles 2α combined with different notch radii ρ; original compared with $K_{3\rho}$-based FE analysis results; (Zappalorto and Lazzarin 2011[(1)])

The stresses $\tau_{r\theta}$ in mode 2 loading from the FE model mentioned above (with internal notches) in the bisector plane ($\theta = 0$) are plotted in Fig. 2.54. The stresses σ_θ at the hole edge ($r = \rho$) are compared in Fig. 2.55. Once more, some minor deviations occur for large values of θ.

The rise of $K_{2\rho}/K_2$ with the ratio of notch radius to notch depth, ρ/a, is shown in Fig. 2.56 for V-notches with root hole characterised by different values of the notch opening angle, 2α. All curves are linear and converge to $K_{2\rho}/K_2 = 1.0$ for $\rho/a = 0$, as demanded by Eq. (2.138). The rise is strongest for $2\alpha = 0°$ (keyhole). It is inverted to a decrease for $2\alpha \geq 70°$.

For analysing the stress field under out-of-plane shear loading conditions for the V-notch with root hole, Fig. 2.57, the following analytic function has been used (Zappalorto and Lazzarin 2011[(1)]; Zappalorto et al. 2010):

$$H(z) = \mathrm{i}az^{\lambda} + \mathrm{i}bz^{-\lambda} \tag{2.145}$$

where λ, a and b are real coefficients. Only the antimetric stress field associated with mode 3 loading is considered, compare Eq. (2.122).

The following shear stress in the bisector plane ($\theta = 0$) is derived:

$$\tau_{\theta z} = \frac{K_{3\rho}}{\sqrt{2\pi}} r^{\lambda_3 - 1}\left[1 + \left(\frac{\rho}{r}\right)^{2\lambda_3}\right] \tag{2.146}$$

In the case of torsional loading of a round bar with circumferential V-notch with root hole, the linear increase of the nominal shear stress over the radial

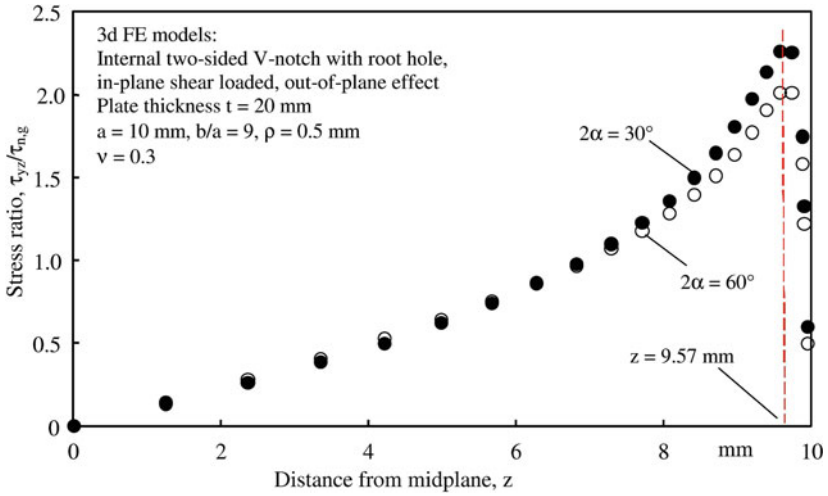

Fig. 2.59 Transverse (out-of-plane) loading effect produced by in-plane shear loading of V-notch with root hole in plate of finite thickness; out-of-plane shear stress plotted over thickness direction; FE analysis results; (Lazzarin et al. 2011)

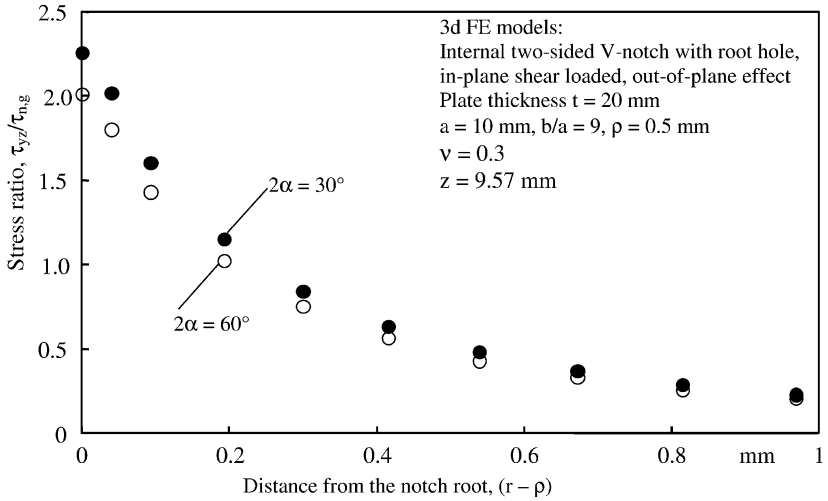

Fig. 2.60 Transverse (out-of-plane) loading effect produced by in-plane shear loading of V-notch with root hole in plate of finite thickness; decrease of maximum shear stress at $z = 9.57$ mm plotted over bisector direction; FE analysis results; (Lazzarin et al. 2011)

distance from the centre of the bar must be taken into account. This can be done by the following approximation (Zappalorto et al. 2008):

$$\tau_{\theta z} = \frac{K_{3\rho}}{\sqrt{2\pi}} r^{\lambda_3 - 1} \left[1 + \left(\frac{\rho}{r} \right)^{2\lambda_3} \right] \left(1 - \frac{r - \rho}{R_\mathrm{n}} \right) \tag{2.147}$$

where the radius R_n denotes the net cross-section of the round bar at the notch root. An evaluation example based on FE modelling with axisymmetric elements is shown in Fig. 2.58.

Finally, the transverse (out-of-plane) shear loading effect produced by in-plane shear loading at load-free surfaces is considered. The transverse singular effects in mode 2 loaded pointed V-notches have been described in Sect. 2.3.3 with the relevant literature being quoted. Here, the corresponding transverse non-singular effect associated with rounded V-notches is considered.

The effect can only be detected using three-dimensional FE models. It produces an out-of-plane shear stress which has its maximum in the close vicinity of the plate surfaces. The effect is documented by Figs. 2.59 and 2.60 (Lazzarin et al. 2011). The rectangular plate specimen shown in Fig. 2.40 is analysed, with a plate thickness of 20 mm, containing a two-sided V-notch with root hole ($\rho = 0.5$ mm). The semiwidth of the plate is 100 mm, the notch semidepth $a = 10$ mm and the notch opening angle $2\alpha = 30°$ or 60°. The plane model hitherto used is simply extended into the thickness direction z. The out-of-plane shear stress τ_{yz}, plotted over the distance z from the midplane of the plate specimen has its maximum at short distance from the plate surface and is zero in the midplane ($z = 0$) and at the two plate surfaces ($z = \pm 10$ mm), Fig. 2.59. The maximum out-of-plane shear stress is in the range of the original maximum in-plane shear stress (Fig. 2.54), but it is substantially smaller than the original maximum tangential stress at the hole edge (Fig. 2.55). The decrease of the out-of-plane stresses (maximum at $z = 9.57$ mm) with the distance $(r - \rho)$ from the notch root is shown in Fig. 2.60.

2.4.7 *Generalised NSIFs of Parabolic and Keyhole Notches in Comparison*

The stress field levels in the vicinity of pointed slit tips ('near field'), where the stresses are singular, are described by the SIFs K_I, K_II, K_III, which are related to the loading modes I, II, III:

$$K_\mathrm{I} = \sigma_\mathrm{n} \sqrt{\pi a}\, Y_\mathrm{I} \tag{2.148}$$

$$K_\mathrm{II} = \tau_\mathrm{n} \sqrt{\pi a}\, Y_\mathrm{II} \tag{2.149}$$

$$K_\mathrm{III} = \tau_\mathrm{n}^* \sqrt{\pi a}\, Y_\mathrm{III} \tag{2.150}$$

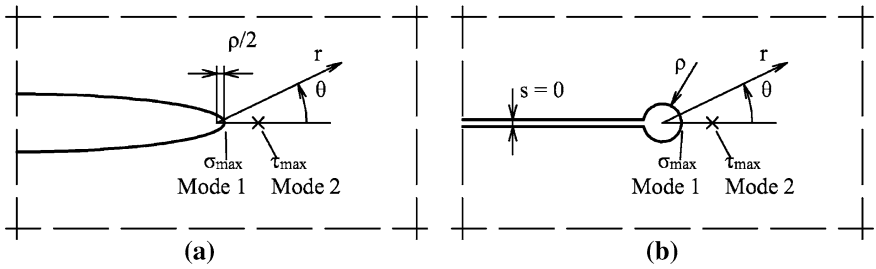

Fig. 2.61 Slender parabolic notch (**a**) and keyhole (**b**) with polar coordinate systems and indication of the position of σ_{max} in mode 1 loading and τ_{max} in mode 2 loading; (Radaj 2010)

with σ_n, τ_n, τ_n^* being the nominal or basic normal and shear stresses at the slit tip, with a being the slit length or semilength and Y_I, Y_{II}, Y_{III} being geometry factors describing the influence of finite boundaries by dimensional ratios of geometry and load position.

The SIFs quantify the first (singular) terms of a series expansion of the stress field for radial distances $r/a \ll 1.0$. The second order terms, T-stress and S-stress, may be superimposed. Any mixed mode loading state at the slit tip can be evaluated in respect of K_I, K_{II}, K_{III}, T and S, primarily by numerical methods (finite element or boundary element). Compilations of K_I, K_{II}, K_{III} formulae for basic geometric and loading cases gained by function-analytical and other methods are available (Murakami 1987). A compendium of T-stress solutions has also been published (Sherry et al. 1995).

In the following, the NSIFs $K_{1\rho}$ and $K_{2\rho}$ of slender parabolic and keyhole notches in comparison are considered, Fig. 2.61, supplemented by $K_{3\rho}$. These NSIFs describe the stress field level in the vicinity of the rounded slit ends. The maximum notch stresses σ_{max} (mode 1) and τ_{max} (mode 2) occur in the bisector plane, the former at the notch root, the latter ahead of the notch root. The maximum stress τ_{max}^* (mode 3) occurs also at the notch root. The three loading modes and their characteristic maximum stresses appear as decoupled under mixed mode loading conditions. The influence of the slit-parallel basic stress $\sigma_\parallel$ (the T-stress effect) is neglected below.

The slit, considered as the limit case $\rho \to 0$ of a slender parabolic notch or keyhole notch, provides the means to establish the relationships between the SIFs K_I, K_{II}, K_{III} and the maximum stresses σ_{max}, τ_{max}, τ_{max}^* for $\rho \to 0$ first, and then the relationships between the NSIFs $K_{1\rho}$, $K_{2\rho}$, $K_{3\rho}$ and σ_{max}, τ_{max}, τ_{max}^* for finite values of ρ. These relationships depend on the notch shape (elliptic, parabolic, keyhole or U-shaped). Once more, the relationships for mode 1, mode 2 and mode 3 are decoupled by considering σ_{max}, τ_{max} and τ_{max}^* in the bisector plane. The resulting 'defining equations' for $K_{1\rho}$, $K_{2\rho}$ and $K_{3\rho}$ are given below. The bisector direction is associated with $\theta = 0°$, and the radial distance r is measured from the origin of the polar coordinate system, whose distance from the notch root is $r_0 = \rho/2$ for the parabolic notch and $r_0 = \rho$ for the keyhole.

Converting the limit value equations for K_{I}, K_{II}, K_{III}, Eqs. (2.127), (2.128), (2.130), to the equations for $K_{1\rho}$, $K_{2\rho}$, $K_{3\rho}$ (Lazzarin et al. 2009), the following relationships are derived for slender parabolic notches:

$$K_{1\rho} = \frac{\sqrt{\pi\rho}}{2}\sigma_{\max} \quad (\theta = 0,\ r = 0.5\rho,\ T = 0) \tag{2.151}$$

$$K_{2\rho} = \frac{\sqrt{\pi\rho}}{0.3849}\tau_{\max} \quad (\theta = 0,\ r = 1.5\rho) \tag{2.152}$$

$$K_{3\rho} = \sqrt{\pi\rho}\,\tau^{*}_{\max} \quad (\theta = 0,\ r = 0.5\rho) \tag{2.153}$$

The corresponding relationships for the keyhole notch in Lazzarin's terminology are the following (Kullmer 1992; Radaj et al. 2001; Smith 2006):

$$K_{1\rho} = \frac{\sqrt{\pi\rho}}{2.1213}\sigma_{\max} \quad (\theta = 0,\ r = \rho,\ T = 0) \tag{2.154}$$

$$K_{2\rho} = \frac{\sqrt{\pi\rho}}{0.7132}\tau_{\max} \quad (\theta = 0,\ r = 1.723\rho) \tag{2.155}$$

$$K_{3\rho} = \frac{\sqrt{\pi\rho}}{1.4142}\tau^{*}_{\max} \quad (\theta = 0,\ r = \rho) \tag{2.156}$$

Obviously, $K_{1\rho}$, $K_{2\rho}$ and $K_{3\rho}$ are smaller for the keyhole notch than for the parabolic notch when $\sigma_{\max}$, $\tau_{\max}$ or $\tau^{*}_{\max}$ have the same value but using the same remote loading stresses results in identical NSIF values for the two notch shapes.

Some general questions arise in respect of a potential use of the NSIFs in engineering applications where structural boundaries may occur close to the considered notches, e.g. when applying the reference notch concept to welded joint models. Analytical expressions for the NSIFs are difficult to derive in such cases. Also, compiled data are not available. Therefore, the NSIF must be determined individually, using the FE or boundary element method and evaluating $\sigma_{\max}$, $\tau_{\max}$ or $\tau^{*}_{\max}$ for the preset notch radius ρ. Provided the notch shape in the model and in the derivation of the NSIF formula is identical (the normal choice), the evaluated NSIF value will be unambiguous and accurate. This means that the notch shape should be chosen in correspondence to the actual modelling requirements. Mostly, a keyhole or a U-shaped notch will be appropriate. In any case, the applied notch shape should be specified when presenting NSIF values. Only then, these can be used to reconstruct the notch stress field from given $K_{1\rho}$, $K_{2\rho}$, $K_{3\rho}$ and ρ values on the basis of the resulting $\sigma_{\max}$, $\tau_{\max}$ and $\tau^{*}_{\max}$ values. In the case of superimposed mode 1 and mode 2 stress fields, the resulting $\sigma_{\theta\ \max}$ value at the notch edge outside the bisector plane can easily be determined. In the case of a non-zero slit-parallel basic stress $\sigma_{\parallel}$, the appertaining notch stress field can additionally be superimposed, so that the stress field near the rounded slit tip is completely and accurately determined.

The necessary theoretical limit conditions already mentioned, Eq. (2.138), are the following:

$$K_{\mathrm{I}} = \lim_{\rho \to 0} K_{1\rho} \quad (\sigma_{\parallel} = 0) \tag{2.157}$$

$$K_{\mathrm{II}} = \lim_{\rho \to 0} K_{2\rho} \tag{2.158}$$

$$K_{\mathrm{III}} = \lim_{\rho \to 0} K_{3\rho} \tag{2.159}$$

The above considerations show that the values of $K_{1\rho}$, $K_{2\rho}$, $K_{3\rho}$ can be approximated by the values of K_{I}, K_{II}, K_{III} in the case of a microkeyhole or a slit-like U-shaped notch. The designation 'micro' means that the keyhole radius ρ is substantially smaller than the structural dimensions which control the basic stresses in the slit tip area so that major cross-sectional weakening effects are avoided. Inversely, the K_{I} and K_{II} values may be determined by the limit value procedure expressed by Eqs. (2.157–2.159). This was the original usage in the historical development. In strength assessments by engineers, the micronotch is applied as a means to quantify the near-field stress level. Because cross-sectional weakening is not at all occurring, the SIFs K_{I}, K_{II}, K_{III} are better suited for strength assessments than the NSIFs $K_{1\rho}$, $K_{2\rho}$, $K_{3\rho}$.

2.4.8 The T-Stress Effect in Rounded Notch Configurations

As already stated, the SIFs, NSIFs and generalised NSIFs are comprehensive parameters characterising not only the maximum stress at a point, but the whole stress field in the vicinity of the crack tip, notch tip or notch root. They are supplemented by the non-singular stress field components, described by the *T*-stress and *S*-stress where appropriate, Eqs. (2.13), (2.15), (2.73). A necessary condition on all these parameters is that they are approximately constant in the considered near field of the notch. This constancy has been proven by the diagrams showing the simple or generalised NSIF values over the distance from the notch tip or notch root. Higher order stress field terms may be added in unconventional cases such as application to thin-sheet lap joints.

In summary, there is no problem in using these parameters for defining the stress fields near pointed or sharply rounded notches as far as these can be approximated and superimposed by the considered singular and non-singular stress fields. Substantially three-dimensional configurations must be excluded.

The situation may become complicated when determining the SIF parameters from FE analysis models in cases of application to specimens and structural members. Here, the correct separation of the parameters is important: the separation of the mode 1 and mode 2 related constituents and the separation of the equivalent to the *T*-stress in rounded notch configurations.

The separation of mode 1 and mode 2 related constituents is not possible when evaluating the out-of-bisector maximum notch stresses, whereas the separation is no problem when evaluating the in-bisector stresses σ_θ and $\tau_{r\theta}$, as shown in the

preceding subsections. The separation of the T-stress equivalent in rounded notch configurations is dealt with below, followed by a glance at the corresponding S-stress problem.

The T-stress is defined for pointed crack or slit tips ($2\alpha = 0$) subjected to in-plane loading. The term 'slit' (comprising the crack) is preferred in the following paragraphs of this subsection. The eigenvalue-based series expansion of the in-plane stress field at the slit tip, Eq. (2.9), is truncated in general after the second term. The resulting stress field equation can be split into an even and an odd part in respect of the polar angle θ, the even part connected with the parameters K_I and T, the odd part with the parameter K_II (Sneddon 1946; Irwin 1957). The first order term defines the stress singularity at the pointed slit tip ($r = 0$), resulting in the SIFs K_I and K_II. The second order term defines a uniform slit-parallel tensile or compressive stress named 'T-stress' (Larsson and Carlsson 1973). These parameters control the stress field near to the slit tip, the 'near field', now written with the usual nomenclature, compare Eqs. (2.10) and (2.11):

$$\sigma_{\mathrm{I,ij}}^{(1,2)} = \frac{K_I}{\sqrt{2\pi r}} f_{\mathrm{I,ij}}^{(1)}(\theta) + T f_{\mathrm{T,ij}}^{(2)}(\theta) \quad (\mathrm{i,j} = r,\ \theta) \tag{2.160}$$

$$\sigma_{\mathrm{II,ij}}^{(1,2)} = \frac{K_\mathrm{II}}{\sqrt{2\pi r}} f_{\mathrm{II,ij}}^{(1)}(\theta) \quad (\mathrm{i,j} = r,\ \theta) \tag{2.161}$$

The T-stress may be determined from analytical solutions after series expansion of the stress field. In the case of FE modelling, it is usually determined from the medium stress in the two flank sides of the slit, evaluating the midsection values in case of internal slits (Williams 1957). Also, it may result from the difference in the stresses σ_r and σ_θ acting in the ligament close to the slit tip, Eq. (2.19); (Lazzarin et al. 2009).

When the pointed slit tip with occurrence of a T-stress is substituted by a rounded slit notch (e.g. a keyhole), the T-stress may deteriorate the usual evaluation procedures for $K_{1\rho}$. The reason is, that the $K_{1\rho}$ related notch stresses are superimposed by the T-stress related notch stresses. Evaluations of K_I and $K_{1\rho}$ based on the total notch stresses may thus be affected, Eqs. (2.127) and (2.129). If the T-stress effect is included in $K_{1\rho}$, the limit value relationship, Eq. (2.138), is not applicable, because non-singular stress field components are now wrongly allotted to the singular stress parameter. It is desirable, to separate the T-stress effect in order to ensure the correct application of the limit value relationship (Radaj 2010).

A problem of language is first addressed. Just as K_I and K_II do not occur at rounded slit tips, the same is true for the T-stress. The in-bisector slit-parallel stress $\sigma_r(r, 0)$ representing the T-stress at the pointed slit tip, is decreasing to zero at the rounded slit tip. So, the T-stress in a rounded slit tip model is always that slit-parallel stress which would occur without slit tip rounding in the midsection of the relevant internal slit model. This T-stress can be used to approximate the T-stress related notch stresses. The accuracy of the solution will be all the better, the smaller the notch radius in relation to the characteristic dimensions of the problem is.

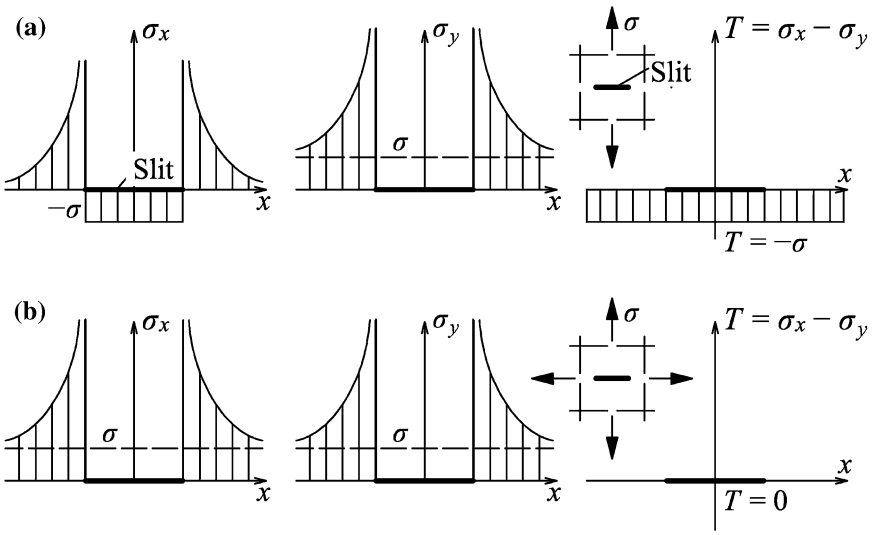

Fig. 2.62 Infinite plate with internal slit subjected to uniaxial (**a**) and biaxial (**b**) tension load; remote tensile stress σ; stresses σ_x, σ_y and T in ligament and slit line; (Radaj 2010)

The reference model of the slit is the already considered keyhole or slender elliptical notch subjected to tensile loading in slit-parallel direction. The notch stresses at the keyhole under a uniform slit-parallel tensile or compressive stress $\sigma_\parallel$ are given by (Radaj et al. 2001):

$$\sigma_\theta = \sigma_\parallel (1 - 2\cos 2\theta) \tag{2.162}$$

The solution is identical with Kirsch's solution for a single hole, with $\sigma_{\theta\ \max} = 3\sigma_\parallel$ at $\theta = 90°$ and $\sigma_{\theta\ \min} = -\sigma_\parallel$ at $\theta = 0°$ (Kirsch 1898). A more accurate solution for the keyhole gives $\sigma_{\theta\ \max} = 3.06\sigma_\parallel$ and $\sigma_{\theta\ \min} = -\sigma_\parallel$. The U-shaped notch results in $\sigma_{\theta\ \max} = 2\sigma_\parallel$ at $\theta = 69°$ (Radaj and Schilberth 1977, ibid. Fig. 5, $r/b = 1$, $r/a = 0.01$), whereas $\sigma_{\theta\ \min}$ remains unchanged. Considering the elliptical (or parabolic) slender notch, no pronounced stress maximum occurs at the notch edge, whereas $\sigma_{\theta\ \min} = -\sigma_\parallel$ at $\theta = 0°$. The latter value is confirmed by Neuber's formulae for uniaxial and biaxial tensile loading in comparison (Neuber 1985). One application-relevant conclusion from the above is that the value of the original T-stress is expressed by the notch stress at $\theta = 0°$ with opposite sign. This has to be taken into account when evaluating the $K_{1\rho}$ parameter from FE models using the notch stress at $\theta = 0°$.

Before doing so, the difference between the T-stresses at mode 1 loaded internal and external slits is demonstrated. At external slits (with an unloaded external boundary), no T-stress occurs whereas at internal slits it generally does. In order to clarify the situation in the latter case, the slit-parallel and slit-normal stresses σ_x and σ_y in the slit and ligament line $y = 0$ is discussed based on Westergaard's

closed-form solution, Fig. 2.62 (Westergaard 1939; Hahn 1976). The infinite plate, subjected to uniaxial or biaxial remote tensile stress σ is considered.

The solution for uniaxial tension gives:

$$\sigma_x = \begin{cases} -\sigma & \\ \sigma x/\sqrt{x^2 - a^2} \ -\sigma & \end{cases} \quad \sigma_y = \begin{cases} 0 & (x < a) \\ \sigma x/\sqrt{x^2 - a^2} & (x > a) \end{cases} \tag{2.163}$$

The solution for biaxial tension gives:

$$\sigma_x = \sigma_y = \begin{cases} 0 & (x < a) \\ \sigma x/\sqrt{x^2 - a^2} & (x > a) \end{cases} \tag{2.164}$$

The T-stress can be determined from the difference in the stresses σ_x and σ_y on the ligament close to the slit tip (Lazzarin et al. 2009). The expression for the T-stress is reformulated here as a limit value using the stress components σ_x and σ_y instead of σ_r and σ_θ:

$$T = \lim_{x \to a} (\sigma_x - \sigma_y) \quad (x > a) \tag{2.165}$$

Considering the above mentioned Westergaard solution, one gets $T = -\sigma$ in uniaxial tension and $T = 0$ in biaxial tension. Comparing this result with the plots in the figure, it is obvious that the T-stress in the two loading cases can be identified from the slit-parallel stress σ_x in the midsection of the internal slit, but not from the remote stress at the outside boundary of the plate. On the other hand, any superimposed loading $\sigma_{x\infty}$ at infinity will directly change the T-stress by $T = \sigma_{x\infty}$. Then, the T-stress consists of two parts, the one component connected with $\sigma = \sigma_{y\infty}$, the other with $\sigma_{x\infty}$. When considering external notches, these correspond to the condition $\sigma_{x\infty} = 0$, in general, for example the keyhole notch solution (Kullmer 1992; Radaj et al. 2001). Therefore, the solution for uniform slit-parallel tension loading is separately given by the latter authors. Altogether, it is concluded that, under uniaxial tension loading of internal rounded slit tips, the slit-parallel basic stress $\sigma_\parallel$ is equal in size and opposite in sign to the remote slit-transverse tensile stress, provided the notch radius is small in relation to the outer dimensions of the structural member.

Evaluating $K_{1\rho}$ in cases of $\sigma_\parallel \neq 0$ from FE analysis results, it is necessary to determine $K^*_{1\rho}$ without the T-stress effect and to register the T-stress or the corresponding slit-parallel basic stress $\sigma_\parallel$ separately, because different stress fields are connected with the two parameters. The equations corresponding to Eqs. (2.151) and (2.154) for the parabolic and keyhole notch types, respectively, then read as follows:

$$K^*_{1\rho} = \frac{\sqrt{\pi\rho}}{2}(\sigma_{\max} + \sigma_\parallel) \quad (\theta = 0,\ r = 0.5\rho) \tag{2.166}$$

$$K^*_{1\rho} = \frac{\sqrt{\pi\rho}}{2.1213}(\sigma_{\max} + \sigma_\parallel) \quad (\theta = 0,\ r = \rho) \tag{2.167}$$

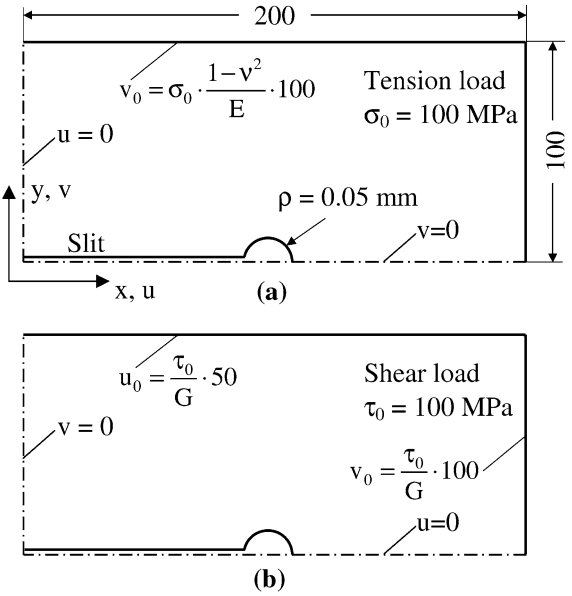

Fig. 2.63 Symmetry quarter of rectangular plate with two-sided keyhole slit, subjected to tensile loading by prescribed displacement v_0 (**a**) and to in-plane shear loading by prescribed displacements u_0 and v_0 (**b**) of the external boundary; (Radaj et al. 2009)

The necessary limit value of Eq. (2.157) is substituted as follows:

$$K_1 = \lim_{\rho \to 0} K_{1\rho}^* \tag{2.168}$$

Considering $K_{1\rho}^*$ with $\rho \to 0$ as indicated by Eq. (2.168), the slit-parallel stress $\sigma_\parallel$ in Eqs. (2.166) and (2.167) can be substituted by T. Therefore, the designation 'T-stress-corrected NSIF $K_{1\rho}^*$' is introduced. In cases of rounded slit tips, this correction is an approximation.

As an example for the T-stress correction, the plots of the K_I, $K_{1\rho}$ and K_II, $K_{2\rho}$ values for the two-sided keyhole slit in a rectangular plate with outer dimensions substantially larger than the notch radius, Fig. 2.63, has been reconsidered (Radaj 2010). The plate is subjected to uniaxial tensile and pure shear loading by prescribed remote boundary displacements with a reference stress of $\sigma_0 = 100$ MPa and $\tau_0 = 100$ MPa, respectively (Lazzarin et al. 2009). The $K_{1\rho}$ and $K_{2\rho}$ values were evaluated from FE models using Eqs. (2.154) and (2.155) not only at $r = \rho$ or $r = 1.723\rho$, but also at other distances $(r - \rho)$ close to the slit tip without considering the T-stress effect. The K_I and K_II values were also evaluated from FE models. Actually, the T-stress was found to be $T = -60$ MPa. Therefore, the $K_{1\rho}$ values are exactly 1.09 % too large at $(r - \rho) = 0.001$ mm, upper graph of Fig. 2.64. The difference decreases for $(r - \rho) > 0.001$ mm. The well known maximum notch stress gradient $-2/\rho$ perpendicular to the hole edge results in a full cancellation of the enlargement at $(r - \rho) = \rho/2 = 0.025$ mm. Obviously, the T-stress corrected $K_{1\rho}^*$ curve is then identical with the K_I curve within the plotting accuracy. The limit condition of Eq. (2.168) is precisely met, which means that the hole is sufficiently small to possess the same geometry factor Y_I as the pointed slit tip, or, in other words, that the cross-sectional weakening by the hole is negligibly small.

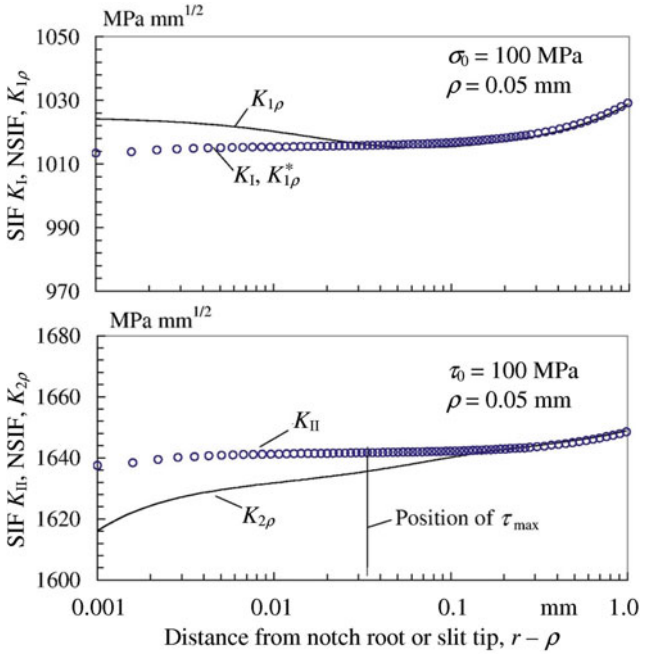

Fig. 2.64 Generalised NSIFs $K_{1\rho}$, $K^*_{1\rho}$, $K_{2\rho}$ in comparison to SIFs K_{I}, K_{II}, evaluated along bisector or ligament dependent on distance from notch root or slit tip, FE model of rectangular plate with two-sided keyhole or slit subjected to tensile and in-plane shear loading; (Lazzarin et al. 2009)

The deviations between the $K_{2\rho}$ and K_{II} curves in the lower graph of Fig. 2.64 have another reason. They occur for distances smaller than the $\tau_{\max}$ position at $(r - \rho) = 0.723\rho = 0.0362$ mm. They mirror the fact that the correct $K_{2\rho}$ value is determined from $\tau_{\max}$ at the above distance from the notch edge, with no convergence for evaluations at distances closer to the notch edge. The necessary convergence condition is $K_{2\rho} \to K_{\mathrm{II}}$ for $\rho \to 0$, but not for $(r - \rho) \to 0$. The deviations are not a T-stress effect, because the evaluated shear stresses are independent of any T-stress.

Another, more convincing proof of the necessity to apply the T-stress correction has been given by re-analysing Lazzarin's tensile-shear loaded lap joint model (Radaj 2010).

The second order term in mode 1 loading which constitutes the T-stress at slit tips may also occur with V-notches (Ayatollahi and Dehghany 2010; Ayatollahi and Nejati 2011). An effect on $K_{1\rho}$ similar to the T-stress effect above can be expected, but has not yet been investigated. The second order term in mode 3 loading which has been named S-stress, does not affect the limit value $K_{3\rho} \to K_{\mathrm{III}}$ because it does not contribute to the shear stresses $\tau_{\theta z}(r, 0)$ in the bisector plane which are related to $K_{3\rho}$.

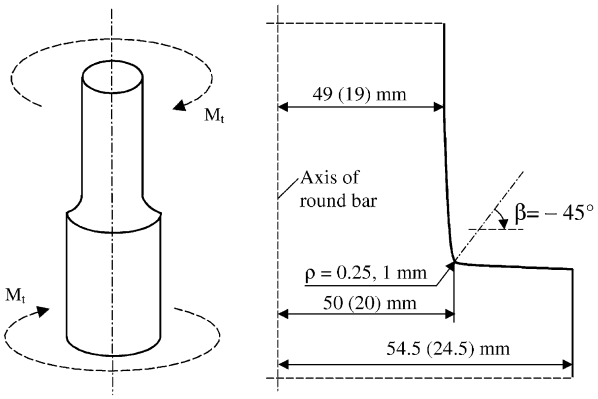

Fig. 2.65 Round bar with hyperbolic shoulder fillet subjected to torsional loading; (Zappalorto and Lazzarin 2011[3])

2.4.9 Application of the Generalised NSIF Concept to Round Bars with Shoulder Fillet

The generalised NSIF concept allows to describe the stress field at rounded notches, especially at sharply rounded notches, by a single parameter per loading mode. The intensity of the stress field, for which the NSIF is determined, must be available from other sources, in engineering applications from a FE analysis of the considered notch configuration.

The NSIFs thus found do not allow to perform a strength assessment directly. On the other hand, incorporation of the FE analysis results into the analytical frame of the NSIF concept allows fundamental insights in the setting of the model and its behaviour under modified conditions. This may be illustrated by the following example (Zappalorto and Lazzarin 2011[3]).

A round bar with shoulder fillet subjected to torsional loading is considered, Fig. 2.65. The shoulder fillet is approximated by a hyperbolic notch with notch opening angle $2\alpha = 90°$, inclined by $\beta = 45°$ against the bar axis. The notch radius is $\rho = 0.25$ or 1.0 mm. The radius up to the gross cross-section amounts to $R_g = 54.5$ or 25.5 mm, the radius up to the notch root thus being $R_n = 50$ or 20 mm.

The notch stress field (out-of-plane shear) is separated into two parts, one part antimetric, the other part symmetric, Eq. (2.122). Engineers are not always aware of the symmetric part, which corresponds to the *S*-stress originally defined at slit tips ($2\alpha = 0°$). The two parts are controlled by the antimetric and symmetric NSIFs, $K_{3\rho}^{(a)}$ and $K_{3\rho}^{(s)}$. They are determined according to Eqs. (2.124) and (2.125) and are related to the nominal torsional stress $\tau_{n,g}$ in the gross cross-section,

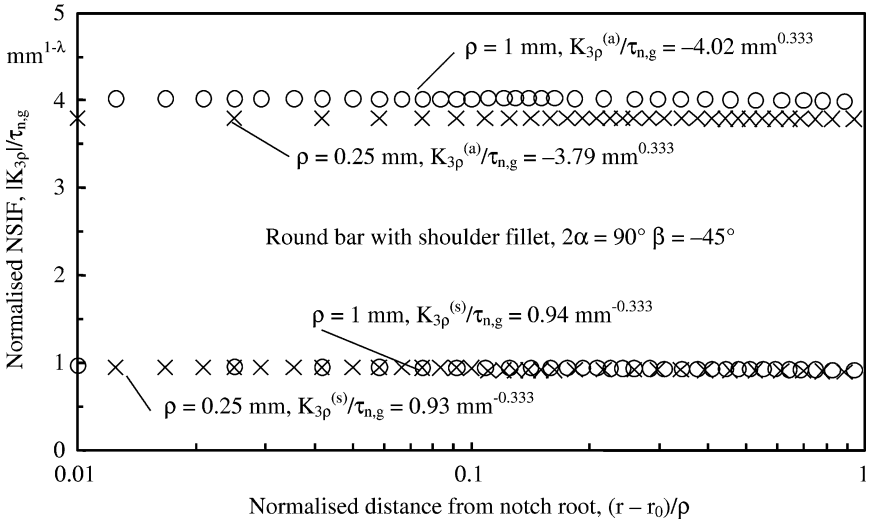

Fig. 2.66 Generalised NSIFs $K_{3\rho}^{(a)}$ and $K_{3\rho}^{(s)}$ of torsional-loaded round bar with hyperbolic shoulder fillet ($2\alpha = 90°$, two notch radii ρ) dependent on distance from notch root; evaluation of FE analysis results; nominal stress $\tau_{n,g}$ in gross cross-section; (Zappalorto and Lazzarin 2011[3])

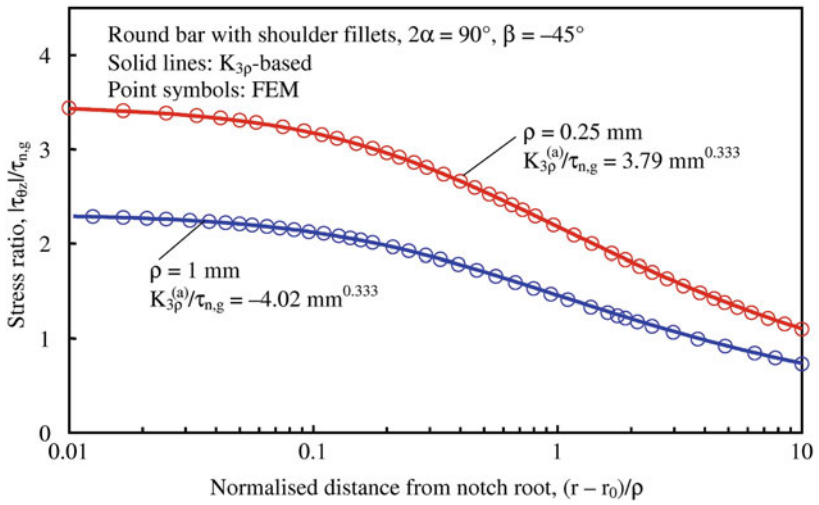

Fig. 2.67 Stress $\tau_{\theta z}$ in notch bisection over distance form notch root; torsional-loaded round bar with hyperbolic shoulder fillet; original compared with $K_{3\rho}$-based FE analysis results; nominal stress $\tau_{n,g}$ in gross cross-section; (Zappalorto and Lazzarin 2011[3])

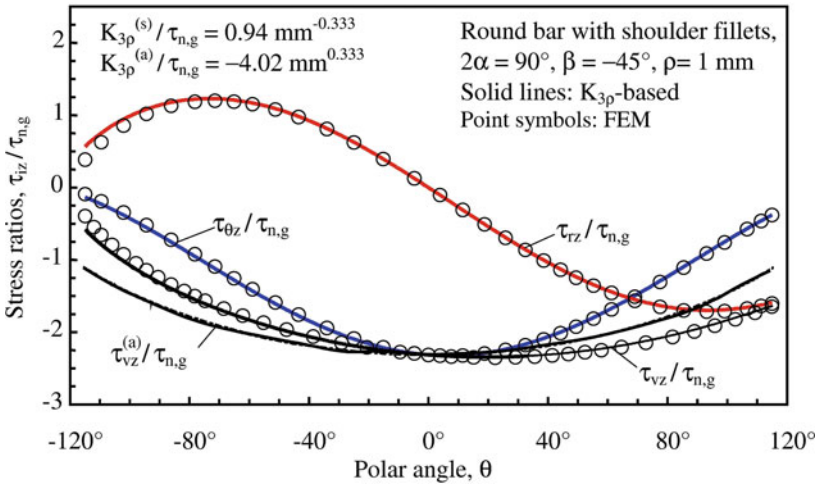

Fig. 2.68 Stresses $\tau_{\theta z}$, τ_{rz}, τ_{vz} and $\tau_{vz}^{(a)}$ at notch edge over polar angle θ; torsional-loaded round bar with hyperbolic shoulder fillet; original compared with $K_{3\rho}$-based FE analysis results; nominal stress $\tau_{n,g}$ in gross cross-section; (Zappalorto and Lazzarin 2011[3])

Fig. 2.66. Obviously, the notch radius $\rho \leq 1$ mm has no major influence on the NSIFs. The values of $K_{3\rho}^{(a)}$ and $K_{3\rho}^{(s)}$ should not directly be set into comparison, because they are different in their dimension. The NSIF $K_{3\rho}^{(a)}$ defines a stress field which is singular for $\rho \to 0$, whereas $K_{3\rho}^{(s)}$ is associated with non-singular stresses under the limit condition.

The out-of-plane shear stresses $\tau_{\theta z}/\tau_{n,g}$ in the bisector plane are plotted over the distance from the notch root for $\rho = 0.25$ and 1.0 mm, Fig. 2.67. FE analysis results and $K_{3\rho}$-based analytical curves are compared. There is no conceivable difference up to 10 mm ahead of the notch root with $R_g = 54.5$ mm. For $R_g = 24.5$ mm, this range is reduced to 1.0 mm. The stresses $\tau_{\theta z}$, τ_{rz} and τ_{vz} at the (hyperbolic) notch edge are plotted over the polar angle θ, Fig. 2.68. The shear stress τ_{vz} acts in planes normal to the notch edge, whereas the shear stresses $\tau_{\theta z}$ and τ_{rz} are related to the planes in the r–θ system before being converted to the u–v system. The curve of τ_{vz} deviates from the antimetric part $\tau_{vz}^{(a)}$ of the analytic solution outside the bisector plane. Rather confusing but correctly, the antimetric shear stresses in the r–θ system appear as symmetric in the u–v system following the notch edge in the positive direction of v.

In the same investigation, also the torsional loaded round bar with an inclined parabolic notch is considered. Further solutions are available for U-notches and blunt V-notches with an accurate mapping of the circular notch edge (Lazzarin et al. 2007). In both cases, the NSIFs are not defined.

2.4.10 Fatigue Limit Expressed by Notch Stress Intensity Factors

The generalised NSIF approach is closely related to the simple NSIF approach in respect of fatigue assessment. Both approaches can be used to assess the crack initiation life of notched members inclusive of fillet-welded joints (Boukharouba et al. 1995; Verreman and Nie 1996, 1997). The fatigue assessment of notched members comprises first the determination of the high-cycle fatigue limit (e.g. the technical endurance limit), second the extension of this limit value to the medium-cycle and low-cycle fatigue range (e.g. via the notch stress or strain *S*–*N* curve) and third the formulation of the multiaxial failure criterion (e.g. the von Mises equivalent stress in ductile materials). The fatigue process is understood as crack nucleation, short-crack growth and long-crack propagation. Crack nucleation is induced by repeated plastic notch tip deformation. Short cracks initiated at sharp notches may be arrested, provided the notch stress gradient is sufficiently steep and the basic stress level sufficiently low (non-propagating short cracks). The high-cycle fatigue limit may be described on the basis of elastic material behaviour.

The high-cycle fatigue limit for notched members has been mainly considered in relation to the fatigue limit of the unnotched material. This is expressed by the fatigue notch factor K_f which turns out to be smaller than the elastic notch stress concentration factor K_t. The relation between the fatigue strengths of rounded compared with pointed notches (inclusive of cracks) has only exceptionally been investigated. Stress intensity factors are basic for such investigations. They allow an assessment without a detailed short-crack propagation analysis, which may be too complicated for engineering purposes. Instead, the stress field in the damaging zone near the notch tip or notch root characterised by the simple or generalised NSIFs is evaluated. This 'near field' produces the driving force for crack initiation and propagation. Widely used are average stress criteria (notch stresses averaged over a material-characteristic microstructural length, area or volume at the notch tip or notch root) or, alternatively, critical distance criteria (notch stress at a material-characteristic microstructural distance from the notch tip).

The basic idea behind the approach presented in the following is the consideration of two different fatigue limits in the case of sharp notches (the notch tip radius is zero or very small, the notch stress concentration factor is correspondingly high). One fatigue limit is related to the nucleation of cracks that do not propagate, governed by the stress concentration factor K_t. The other fatigue limit is related to cracks that nucleate and then propagate, the threshold stress intensity factor ΔK_{th} applied to crack length plus notch depth being relevant.

It is straightforward with regard to the crack propagation fatigue limit of notches to introduce a crack-propagation-relevant microstructural length derived from the threshold stress intensity factor ΔK_{th} of long cracks and from the relevant crack propagation fatigue limit $\Delta\sigma_{th}$. Such a length parameter a_0 has been defined in the following form (El Haddad et al. 1979):

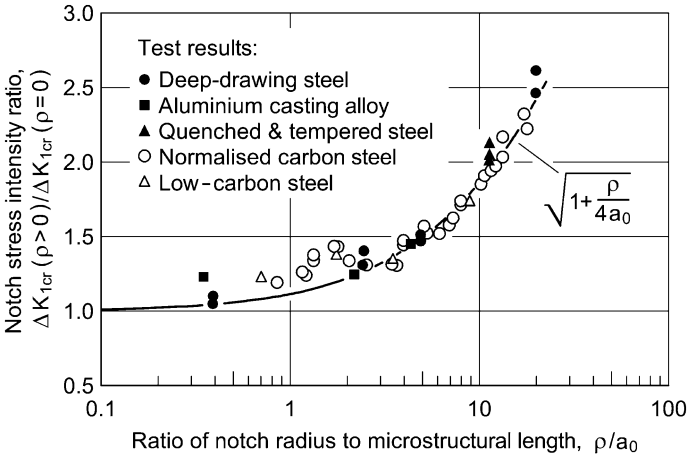

Fig. 2.69 Ratio of critical ranges of $K_{1\rho}$ and K_1, for rounded compared with pointed V-notches in different materials dependent on ratio of notch radius ρ to microstructural length a_0; analytical curve in comparison to test results; (Atzori et al. 1999[1])

$$a_0 = \frac{1}{\pi}\left(\frac{\Delta K_{\text{th}}}{\Delta \sigma_{\text{th}}}\right)^2 \tag{2.169}$$

It has been shown that the proper integration length for fatigue-effective stresses at crack and notch tips is $2a_0$, independent of the notch tip radius and the notch opening angle (Lazzarin et al. 1997).

The following relationships for mode 1 loading conditions have been derived based on the concept just mentioned (Atzori et al. 1999[1], 2001):

$$K_{\text{f}} = \frac{K_{\text{t}}}{\sqrt{1+4a_0/\rho}} = \frac{2\Delta K_1}{\Delta \sigma_{\text{n,g}}}\frac{1}{\sqrt{\pi(\rho+4a_0)}} \tag{2.170}$$

$$\Delta K_{1\text{cr}}(\rho>0) = \Delta K_{1\text{cr}}(\rho=0)\sqrt{1+\rho/4a_0} \tag{2.171}$$

with the gross area nominal stress range $\Delta\sigma_{\text{n,g}}$, the critical NSIF range $\Delta K_{1\rho\ \text{cr}} = \Delta K_{1\text{cr}}(\rho>0)$ and the critical NSIF range $\Delta K_{1\text{cr}} = \Delta K_{1\text{cr}}(\rho=0)$ beyond which initiated cracks will propagate. The derivation above uses the approximation $(1-\lambda_1) \approx 0.5$ which is justified for $2\alpha \leq 60°$. Obviously, the expression on the right-hand side of Eq. (2.170) is thus only approximately dimensionless. The prediction of fatigue strength according to Eq. (2.171) for different notch radii and materials is plotted in Fig. 2.69 and compared with various experimental results taken from the literature (Lazzarin et al. 1997; Noda et al. 1995; Yao et al. 1995). The degree of correspondence seems to be satisfactory.

The simple or generalised NSIF may directly characterise the fatigue limit as shown above or as shown for welded joints in Sect. 2.3.7. These parameters can

also indirectly be relevant for fatigue as can be seen from the *J*-integral criterion (see Sect. 2.3.8) or from the local strain energy density criterion (see Sect. 3.2.3).

Proceeding from the high-cycle fatigue limit, especially at the branching point between the crack nucleation and crack propagation curves in Frost's endurance limit over SCF diagram, $\sigma_{nE} = f(K_t)$, the medium-cycle *S*–*N* curve can be empirically approximated using an inverse slope exponent *k* which depends on the amount of elastic-plastic notch support during crack initiation and subsequent crack propagation. A more rational approach consists in using crack initiation criteria based on elastic or plastic NSIFs in the medium-cycle and low-cycle fatigue range, respectively, allowing extensions into the crack propagation range.

Multiaxial failure criteria are needed for the fatigue assessment under mixed mode loading conditions. These can be based on superposition of the effects of the individual loading modes as far as elastic NSIFs are applicable. An elliptical curve relationship has been used for fillet-welded joints in analogy to the Gough ellipse (see Sect. 2.3.6).

2.4.11 Conclusions

The stress distribution at sharply rounded notches can be described by the loading mode related generalised NSIFs $K_{1\rho}$, $K_{2\rho}$, $K_{3\rho}$ as the governing field parameters. These NSIFs are linked not only to the maximum notch stresses σ_{max}, τ_{max}, τ^*_{max}, which constitute the conventional SCFs in engineering science, but to the whole notch stress field. The field information is needed for assessing failure processes such as crack initiation and propagation or microstructural damaging phenomena. The size effect on the endurable nominal stresses is already included in the endurable NSIFs.

The generalised NSIFs can also be applied to notches with a substantially increased notch radius, provided a proper evaluation over some distance from the notch root in the bisector plane is performed, proving a sufficiently constant value of the NSIF. This value may depend on the notch radius. A substantial increase with the notch radius may be observed, especially under mode 2 loading conditions where the maximum notch stress occurs outside the bisector plane. The generalised NSIFs and the appertaining stress equations depend on the notch shape (parabolic, hyperbolic, elliptical, blunt V-notch, V-notch with circular root arc or V-notch with root hole) and on the applied analytical frame. The internal or external setting of the notch may include a minor influence of loading in the bisector direction. Structural boundary, loading and support conditions have an influence, especially if they act close to the notch. Only the effect of a finite notch depth relative to the notch radius has been systematically investigated to some extent.

The numerical basis of generalised NSIF evaluations in configurations with finite boundaries is the FE analysis method, performed with sufficiently fine

meshes. The theoretical frame of the NSIFs allows interpretations and generalisations of the FE analysis results.

Fatigue assessments are possible on the basis of the generalised NSIFs, but this access has not yet been elaborated. One reason may be, that the NSIFs depend on the overall notch shape, on the geometrical details at the notch root and on the applied analytical frame. So, their generality is restricted. As far as the stress distribution of the sharply rounded notch expressed by the generalised NSIF remains close to that of the pointed notch, expressed by the simple NSIF, failure criteria and data are transferable to some extent.

2.5 Plastic Notch Stress Intensity Factor Concept

2.5.1 Survey of Section Contents

The preceding sections refer to the stress fields and NSIFs of pointed and rounded notches under the condition of linear-elastic material behaviour. Now, the presentations are extended to nonlinear-elastic and thus approximated elastic-plastic material behaviour. The stress singularity at pointed notches continues to exist, provided strain hardening is taken into account. Plastic NSIFs are defined as distinguished from the elastic NSIFs. They include plastic strain intensity factors, which exist also for a non-hardening material behaviour.

Plastic stress intensity factors were first proposed for cracked plates under nonlinear conditions of material behaviour (Hilton and Hutchinson 1971; Hilton 1973) and later on extended to pointed V-notches with arbitrary notch opening angle (Lazzarin et al. 2001). Plastic NSIFs can be stated in terms of the elastic NSIFs, provided the local elastic and elastic-plastic strain energy densities averaged over a circle sector volume around the pointed V-notch are set equal, which is appropriate under small scale yielding conditions (Lazzarin and Zambardi 2002).

Basic information is given on the deformation theory of plasticity which leads to the HRR elastic-plastic stress and strain fields at the notch tip, named after Hutchinson, Rice and Rosengren. The elastic-plastic fields at V-notches subjected to tensile loading inclusive of the definition of the plastic NSIF are presented. The corresponding fields in out-of-plane shear loading are easier to describe analytically. The parabolic notch is treated first, followed by V-notches in general. A uniform analytical frame based on the Neuber nonlinear material law is presented. The Neuber rule linking the maximum elastic-plastic stresses and strains at rounded notch tips and Glinka's alternative concept are contrasted with findings by Zappalorto and Lazzarin, who identified an influence of the notch opening angle and of the hardening exponent on the Neuber rule. A final subsection is devoted to the analytical description of the elastic-plastic material laws.

When reviewing the available publications on the plastic NSIF concept, a lack of conceptual clarity in respect of the yield limit parameters has to be overcome in

some cases. As explained in more detail in Sect. 2.5.10, the real (engineering) yield limit parameters ε_Y, σ_Y or γ_Y, τ_Y (marked or offset yield limit) are not identical with the substitute (analytical) yield limit parameters ε_0, σ_0 or γ_0, τ_0 resulting from the intersection point of the linear-elastic and the asymptotic plastic limit curves. On the other hand, there is no general relationship available for relating the two types of yield parameters. The real yield limit is sometimes introduced in comparative investigations based on the FE method, when using the Ramberg–Osgood material law. It was not possible to remove any possible confusion in the following. The choice of the original authors had to be respected.

The expositions are mainly based on the analytical development of the plastic NSIF concept by Lazzarin and Zappalorto in a set of excellent publications which can be found in the list of references at the end of Chap. 2. A list of symbols is also available there.

2.5.2 Deformation Theory of Plasticity Founding the HRR Fields

When loading of the material exceeds a certain level, plastic deformation (yielding) occurs immediately (i.e. independently of time). The usual assumption is, that the elastic and plastic strains or strain increments add up to their total values:

$$\varepsilon_{ij} = \varepsilon_{ij,e} + \varepsilon_{ij,p}, \quad d\varepsilon_{ij} = d\varepsilon_{ij,e} + d\varepsilon_{ij,p} \tag{2.172}$$

The elastic strains are connected with the stresses according to Hooke's law. The plastic strains are conforming to the multiaxial yield condition, mostly according to von Mises. Two different formulations of the relationships between plastic strains and (elastic) stresses are in use. The 'incremental theory' refers to plastic strain increments in relation to the analytical yield surface. It is not used in the following. The 'deformation theory' founding the HRR fields considers the total strains. Both theories assume in general that no plastic volume change occurs, $\varepsilon_{p,kk} = 0$.

In the deformation theory leading to the HRR fields described below, a hardening material is considered whose uniaxial stress–strain curve is represented by the Ramberg–Osgood material law in the following normalised form related to ε_0, σ_0 which deviates from the original form related to E and H, Eq. (2.264) (Gross and Seelig 2001), Fig. 2.70a:

$$\frac{\varepsilon}{\varepsilon_0} = \frac{\sigma}{\sigma_0} + \alpha \left(\frac{\sigma}{\sigma_0}\right)^n \quad (1 < n < \infty) \tag{2.173}$$

where the terms on the right-hand side of the equation denote the elastic and plastic strain ratios. The quantities ε_0, σ_0 refer to the initiation of yielding, $\varepsilon_0 \approx \varepsilon_Y$, $\sigma_0 \approx \sigma_Y$, provided the factor α is sufficiently small. Under this special condition, the factor α results approximately from $\sigma_Y^{n-1} E/H^n$ with the yield limit $\sigma_Y = E\varepsilon_Y$, the modulus of elasticity E and the hardening (or strength) coefficient

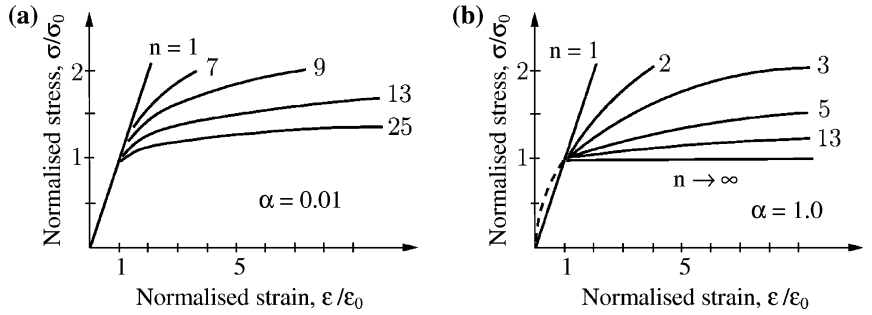

Fig. 2.70 Uniaxial stress–strain curves according to the Ramberg–Osgood material law (**a**) and according to a combination of linear-elastic and total strain power law (**b**); different factors α in the two graphs; (Gross and Seelig 2001)

H (where H is equal to σ at $\varepsilon_p = 1$). The 'strain hardening exponent' n is limited by $n = 1$ for linear-elastic and $n \to \infty$ for elastic-perfectly-plastic behaviour. It has to be noted that many authors prefer the reciprocal value $1/n$ instead of n.

At pointed notch tips, the plastic strains are found to be singular, so that the non-singular elastic strains are negligible in relation to the plastic strains, and Eq. (2.173) can be reduced to the total strain power law, in which the originally plastic strains are now interpreted as total strains:

$$\frac{\varepsilon}{\varepsilon_0} = \alpha \left(\frac{\sigma}{\sigma_0} \right)^n \tag{2.174}$$

The total strain power law, Eq. (2.174), when generalised to multiaxial stress states based on the invariant J_2 of the deviatoric stress state, can be written as follows:

$$\frac{\varepsilon_{ij}}{\varepsilon_0} = \frac{3\alpha}{2} \left(\frac{\sigma_e}{\sigma_0} \right)^{n-1} \frac{s_{ij}}{\sigma_0}, \quad \sigma_e = \sqrt{\frac{3}{2} s_{ij} s_{ij}} \tag{2.175}$$

with the effective stress σ_e according to the von Mises criterion and the deviatoric stress component s_{ij}.

The material law, Eq. (2.175), is also considered valid for a stress–strain relationship consisting of a linear-elastic rise up to the intersection point ε_0, σ_0 followed by the total strain power law in the plastic range, Fig. 2.70b:

$$\begin{aligned} \frac{\varepsilon}{\varepsilon_0} &= \frac{\sigma}{\sigma_0} \quad (\varepsilon \le \varepsilon_0) \\ \frac{\varepsilon}{\varepsilon_0} &= \left(\frac{\sigma}{\sigma_0} \right)^n \quad (\varepsilon \ge \varepsilon_0) \end{aligned} \tag{2.176}$$

Obviously, $\alpha = 1.0$ when comparing Eq. (2.173), i.e. α is not small so that the approximations $\varepsilon_0 \approx \varepsilon_Y$ and $\sigma_0 \approx \sigma_Y$ are not anymore valid. In the following, the

quantities ε_0, σ_0 are termed 'substitute yield limit' in order to distinguish them from the real yield limit ε_Y, σ_Y.

In the deformation theory, the plastic material behaviour is specified as nonlinear-elastic. For nonlinear-elastic solid bodies with a crack undergoing monotonic, small-strain deformation, Hutchinson, Rice and Rosengren have shown that the intensity of the near-tip field is expressed by the J-integral and that the stresses, strains and displacements exhibit a singularity described by $r^{-1/(n+1)}$, $r^{-n/(n+1)}$ and $r^{-1/(n+1)}$, respectively (Hutchinson 1968; Rice and Rosengren 1968). These 'HRR fields' close to the crack tip are written as follows:

$$\sigma_{ij} = \sigma_0 \left(\frac{J}{\alpha \sigma_0 \varepsilon_0 I r} \right)^{1/(n+1)} \tilde{\sigma}_{ij}(\theta, n) \tag{2.177}$$

$$\varepsilon_{ij} = \alpha \varepsilon_0 \left(\frac{J}{\alpha \sigma_0 \varepsilon_0 I r} \right)^{n/(n+1)} \tilde{\varepsilon}_{ij}(\theta, n) \tag{2.178}$$

$$u_i = \alpha \varepsilon_0 r \left(\frac{J}{\alpha \sigma_0 \varepsilon_0 I r} \right)^{n/(n+1)} \tilde{u}_i(\theta, n) \tag{2.179}$$

with the 'universal functions' $\tilde{\sigma}_{ij}(\theta, n)$, $\tilde{\varepsilon}_{ij}(\theta, n)$ and $\tilde{u}_i(\theta, n)$ dependent on the polar angle θ, the strain hardening exponent n and the state of stress (plane stress or plane strain), with the J-integral and with the Integral I depending mildly on n. Deviations occur with large-scale yielding under plane strain conditions, which may be expressed by a 'constraint factor' (Shlyannikov et al. 2011).

In the equations above, the J-integral does not separate the mode 1 and mode 2 loading components. Evaluated HRR-fields refer to pure mode 1 loading in general. Such evaluations show, that the HRR-dominated region at the crack tip is substantially reduced with increasing values of n. Simultaneously, the deformed crack tip gets more and more blunted.

Even in the considered case of crack tips ($2\alpha = 0$), it has not been possible to find a complete numerical solution. Only modelling the material as perfectly-plastic has allowed substantial progress (Unger 2001, 2005, 2007). Moving to the more general case of pointed V-notches in strain-hardening materials, the problem becomes much more demanding. Not only the 'universal functions' require numerical solution techniques, but also the exponent s characterising the degree of the singularity. Nonlinear differential equations and nonlinear eigenvalue problems have to be solved, and the superposition principle, facilitating solutions in the linear range, is not anymore applicable.

2.5.3 Elastic-Plastic Fields at Tensile Loaded V-Notches

A partial solution of the problem of elastic-plastic stress and strain fields at tensile loaded V-notches is available, originally referring to large-angle V-notches

simulating weld-like geometries (Lazzarin et al. 2001) and later on to pointed V-notches in general (Filippi et al. 2002(1)). Lazzarin proposed plastic notch stress intensity factors as parameters which combine the effects of member size, nominal stress level and constitutive material law on the notch stress and strain fields at pointed V-notches. Considering weld-like pointed corner notches subjected to a combination of mode 1 and mode 2 loading in the bisector plane, the notch stresses in the HRR field follow a series expansion:

$$\sigma_{ij}(r, \theta) = K_{1p} r^{-s} \tilde{\sigma}_{ij}^{(1)}(\theta) + K_{2p} r^{-z} \tilde{\sigma}_{ij}^{(2)}(\theta) + \ldots \tag{2.180}$$

where K_{1p} and K_{2p} are the plastic notch stress intensity factors in mode 1 and mode 2 loading, representing the symmetric singular stress field (first term) and the antimetric non-singular stress field (second term) for $2\alpha > 102°$. This equation does not express the superposition principle, because K_{1p} and K_{2p} are assumed as interconnected. Their unambiguous definition requires $\tilde{\sigma}_{e,\max}^{(1)} = \tilde{\sigma}_{e,\max}^{(2)}$ (absolute values), appertaining to the effective (or equivalent) stress σ_e according to von Mises.

The plastic NSIF K_{1p} is defined in analogy to the elastic NSIF K_1 as follows:

$$K_{1p} = \lim_{r \to 0} \sqrt{2\pi} r^s \sigma_\theta(r, 0) \tag{2.181}$$

with the exponent s depending on the hardening exponent and the notch opening angle, Eq. (2.187).

The plastic NSIFs K_{1p} and K_{2p} depend on the notch opening angle 2α, the nominal stress σ_n, the plate thickness t, the reference stress σ_0 and the hardening exponent n. The third material parameter in the Ramberg–Osgood law (besides E and n), the hardening (or strength) coefficient H, is dependent on σ_0, ε_0.

The FE analysis for K_{1p} of a weld-like corner notch model, $2\alpha = 120°$, $t = 20$ mm and $n = 4.0$, using the Ramberg–Osgood law, is presented in Fig. 2.71. The linearised approximation of K_{1p} in the range $\sigma_n = 100$–500 MPa has the following general form:

$$K_{1p} = (k_1 \sigma_n + k_{10} \sigma_0) t^s \tag{2.182}$$

Actually, the K_{1p} curves are nonlinear and start from the origin of the diagram. This relationship is found tentatively based on the analytical assumption for K_{1p}. Deviations of the analytical HRR solution (power law) from the FE solution (Ramberg–Osgood law) are not explicitly visible.

The result of the nonlinear eigenvalue analysis in respect of the exponent s is plotted in Fig. 2.72. The dependency on 2α is weak for not too large angles 2α, but the dependency on n is generally strong. The exponent z in Eq. (2.180) is negative in the considered range of large values of 2α, which means, that no singularity occurs. An example for the universal function $\tilde{\sigma}_{ij}(\theta)$ is given in Fig. 2.73, with exact values and approximations in comparison.

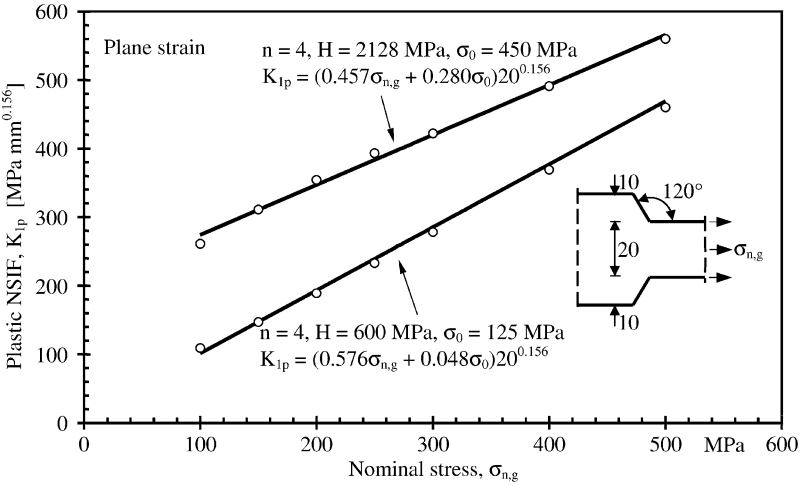

Fig. 2.71 Weld-like corner notch: plastic stress intensity factor K_{1p} dependent on nominal stress $\sigma_{n,g}$ with material parameters n, H, σ_0; linearised approximation in the range $\sigma_{n,g} = 100$ to 500 MPa; plate thickness $t = 20$ mm (Lazzarin et al. 2001)

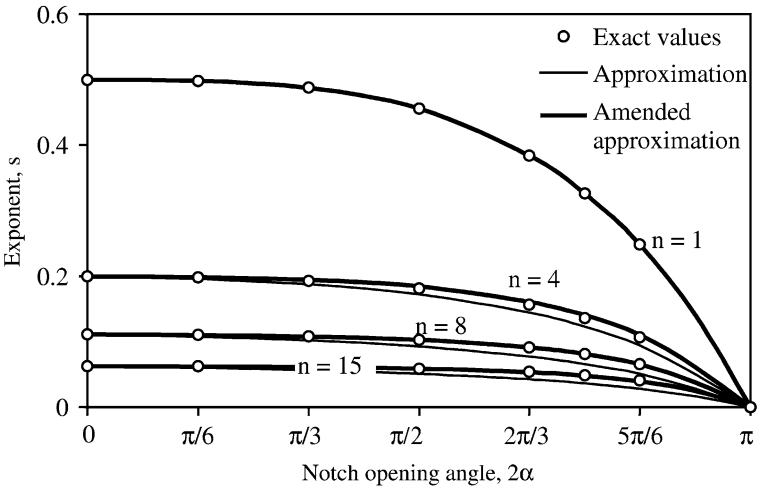

Fig. 2.72 Exponent s of the nonlinear-elastic V-notch subjected to mode 1 (symmetric) loading; exact values (Runge-Kutta) and approximations; (Filippi et al. 2002[(1)])

A more concise derivation and definition of the plastic NSIF under mode 1 loading conditions is possible based on the equivalent strain energy density approach (Lazzarin and Zambardi 2002). In this approach, the elastic-plastic strain energy density at the notch tip is found coincident with that determined under linear-elastic conditions (Glinka and Molski 1981). The approach is not directly applicable to pointed V-notches, since the strain energy density at the notch tip

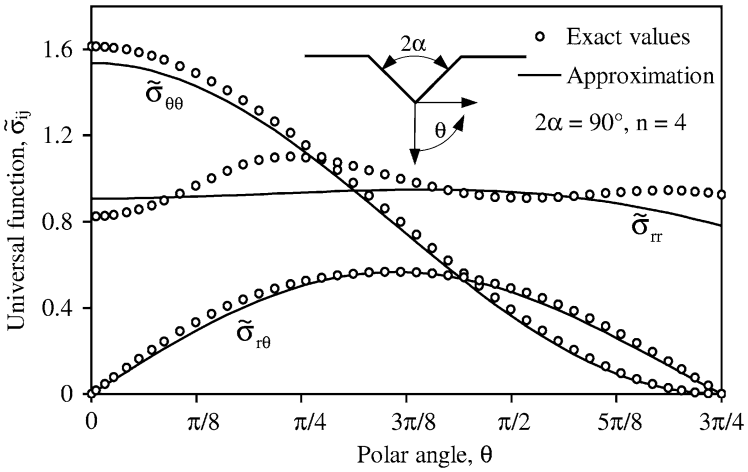

Fig. 2.73 Universal functions $\tilde{\sigma}_{ij}(\theta)$ for $2\alpha = 90°$ and $n = 4$, mode 1 (symmetric) loading; exact values (Runge-Kutta) and approximations; (Filippi et al. 2002[(1)])

tends toward infinity both for the linear-elastic and the power law hardening material. But a reformulation is possible, when applying elastic and plastic NSIFs to a finite size circle sector around the notch tip. The hypothesis is introduced that, under plane strain conditions, the value of the energy concentration due to the notch is equal for the two material laws. Under small-scale yielding conditions, this results in an identical value of the strain energy averaged over the considered circle sector. As a consequence, the plastic NSIFs of pointed V-notches can be predicted on the basis of the linear-elastic NSIFs. The essential steps of the derivation by Lazzarin and Zambardi are reviewed below.

The Ramberg–Osgood material law is the basis in the following form, generalised for multiaxial stress conditions according to the von Mises criterion:

$$\varepsilon_{ij} = \frac{1+\nu}{E} s_{ij} + \frac{1-2\nu}{E} \sigma_h \delta_{ij} + \frac{3}{2} \frac{\sigma_e^{n-1}}{C^n} s_{ij} \tag{2.183}$$

where s_{ij} is the deviatoric stress tensor, σ_h is the hydrostatic stress, δ_{ij} the Kronecker delta and σ_e the von Mises equivalent stress. Actually, the asymptotic approximation by the total strain power law is used in the analytic derivations. The material characteristic constants are the hardening exponent n and the hardening coefficient C (better known as K or H). The multiaxiality condition (plane stress or plane strain) comes in via the equivalent stress σ_e.

Based on Eq. (2.183), the plastic component W_p of the strain energy density can be calculated for monotonic loading:

$$W_p = \frac{n}{(n+1)C^n} \sigma_e^{n+1} \tag{2.184}$$

The first term of the elastic-plastic stress series expansion in the close neighbourhood of a pointed V-notch under mode 1 loading conditions, compare Eq. (2.180), turns out to be:

$$\sigma_{ij}(r,\,\theta) = K_{1p}\, r^{-s}\tilde{\sigma}_{ij}(\theta), \quad \sigma_e(r,\,\theta) = K_{1p} r^{-s}\tilde{\sigma}_e(\theta) \tag{2.185}$$

where K_{1p} is the plastic NSIF quantifying the intensity of the local stress field. The determination of the universal functions $\tilde{\sigma}_{ij}$ and $\tilde{\sigma}_e$ requires a numerical solution. They are normalised in the same manner by setting the maximum value of $\tilde{\sigma}_e(\theta)$ over the considered domain to unity.

Inserting Eq. (2.185) into Eq. (2.184), the elastic-plastic strain energy density close to the notch tip is given by:

$$W_p(r,\,\theta) = \frac{n}{(n+1)C^n}(K_{1p})^{n+1} r^{-s(n+1)}\tilde{\sigma}_e(\theta)^{n+1} \tag{2.186}$$

In the plastic zone very close to the notch tip (small-scale yielding), the elastic contribution to the total strain energy is very small. Therefore, the total energy density W can be set equal to the elastic-plastic energy density W_p which, on the other hand, is equal to the original linear-elastic energy density W_e. This should apply to any value of r within the considered notch tip region. Therefore, comparing the linear-elastic and elastic-plastic singularities, an expression for the exponent s can be gained:

$$W_e(r,\theta) \propto r^{2(\lambda_1-1)}, \quad W_p(r,\theta) \propto r^{-s(n+1)}, \quad s = \frac{2(1-\lambda_1)}{n+1} \tag{2.187}$$

The expression for $s(\lambda_1,\, n)$ has also been derived by other authors (Kuang and Xu 1987; Chen and Ushijima 2000). It is independent of the applied load value. For the crack, $\lambda_1 = 0.5$ and therefore $s = 1/(n+1)$ are valid.

The equivalent strain energy density approach (Glinka and Molski 1981) is based on the well-founded hypothesis that different constitutive models (elastic-plastic compared with linear-elastic) affect the relationship between stresses and strains but leave the value of the averaged energy density at the notch tip (sector radius R) compared with the same in the nominal stress region (energy concentration factors $K_{W,p}$ and $K_{W,e}$) unchanged:

$$K_{W,p}(R) \;=\; K_{W,e}(R) \tag{2.188}$$

This allows to express the plastic by the elastic stress intensity factor which can easily be determined by FE analysis:

$$K_{1p} = \left[\frac{n+1}{n}\frac{I_e(\gamma)}{I_p(\gamma,\,n)}K_{1e}^2\left(\frac{C^n}{2E} + \frac{n}{n+1}\sigma_n^{n-1}\right)\right]^{1/(n+1)} \quad (\gamma = \pi - \alpha) \tag{2.189}$$

where $I_e(\gamma)$ and $I_p(\gamma)$ are integrals of the elastic and plastic universal functions, the first evaluated analytically, the second numerically. The sector radius R should be

within the range of validity of the asymptotic one-term expansion of the notch tip stress field.

Under conditions of local yielding, the second term in the parenthesis is substantially smaller than the first term, so that the following simplified formula is applicable:

$$K_{1p} = AK_{1e}^{2/(n+1)} \tag{2.190}$$

$$A = \left(\frac{n+1}{n}\frac{C^n}{2E}\frac{I_e(\gamma)}{I_p(\gamma, n)}\right)^{1/(n+1)} \tag{2.191}$$

These relationships are dependent on the notch opening angle and the material parameters but do not depend on the applied load value.

The introduced hypothesis of identical energy concentration factors, Eq. (2.188), is only a well-conceived approximation. It neglects any redistribution of the stresses from the higher stressed towards the lower stressed areas. Such redistributions vary with the considered special case. Several numerical tests using the FE method have therefore been performed by Lazzarin and Zambardi with the aim to mark the range of applicability and the degree of accuracy of the approximate solutions.

The FE analyses were carried out on a flat bar specimen with two-sided V-notch subjected to a tensile load or, alternatively, on a flat bar specimen with one-sided V-notch subjected to a bending load. Plane strain conditions are assumed. The nominal stress refers to the gross cross-section. The material parameters correspond to the following two low-carbon and medium-carbon steels:

- AISI 1008: $E = 2.06 \times 10^5$ MPa, $C = 600$ MPa, $n = 4.00$, $\sigma_Y = 125$ MPa, $\nu = 0.3$
- AISI 1045: $E = 2.06 \times 10^5$ MPa, $C = 950$ MPa, $n = 8.33$, $\sigma_Y = 450$ MPa, $\nu = 0.3$

Actually, the total strain power law is applied with the substitute yield limit according to Eq. (2.283), $\sigma_0 = (H^n/E)^{1/(n-1)}$. Thus, $\sigma_0 = 85.7$ MPa for the AISI 1008 steel, and $\sigma_0 = 456.1$ MPa for the AISI 1045 steel. Only tensile loading, the notch opening angle $2\alpha = 60°$ and the AISI 1008 steel are referenced in the two figures below. The FE analysis is carried out with the Ramberg–Osgood material law which is identical with the total strain power law for the very large strain values which define the plastic NSIF.

The stresses σ_θ normal to the bisector plane are plotted over the distance from the notch tip for various (increasing) nominal stress values in Fig. 2.74. Direct FEM results are compared with the K_{1p} analysis results. Deviations from the analytical curves (linear in logarithmic scales) occur for larger distances from the notch tip.

The plastic NSIF K_{1p} is plotted over the nominal stress $\sigma_{n,g}$ in Fig. 2.75. Analysis results according to the unreduced Eq. (2.189) and the simplified Eq. (2.190) are compared with the direct FEM results. The simplified formula may not

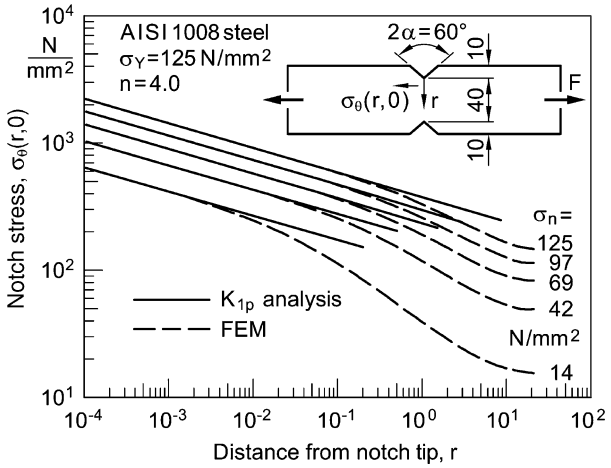

Fig. 2.74 Notch stress $\sigma_\theta(r,0)$ in the bisector plane over distance r from the V-notch tip for various nominal stresses σ_n in the gross cross-sectional area; direct FEM results compared with K_{1p} analysis results; (Lazzarin and Zambardi 2002)

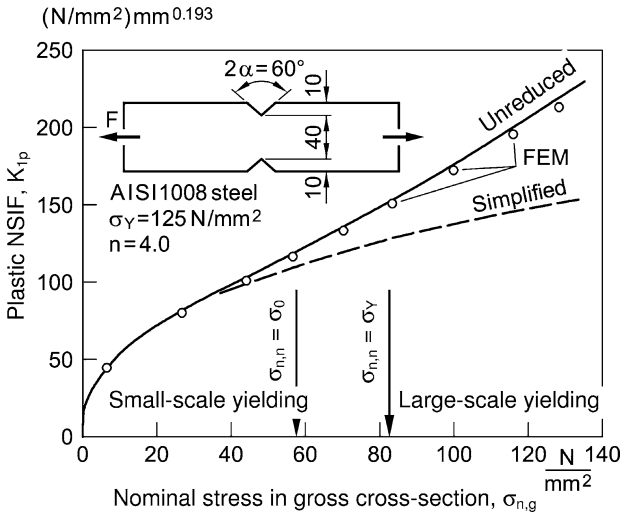

Fig. 2.75 Plastic NSIF K_{1p} over nominal stress $\sigma_{n,g}$ in the gross cross-sectional area; unreduced and simplified analytical solution compared with FEM results; ranges of small-scale and large-scale yielding; divergence point at $\sigma_{n,n} = 1.5\sigma_{n,g} = \sigma_0$; (Lazzarin and Zambardi 2002)

be used in the range of large-scale yielding, defined by $\sigma_{n,n} > \sigma_0$. The divergence point of the two curves is indicated by σ_0 and not by σ_Y, because the total strain power law is relevant. Under bending load conditions, the local yielding range, where the simplified formula is applicable, is extended to substantially larger

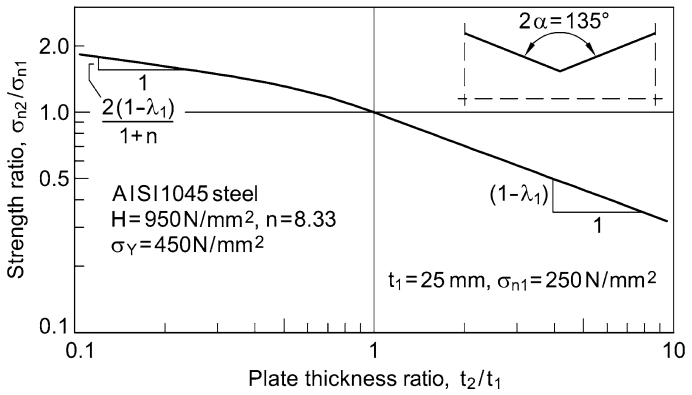

Fig. 2.76 Strength ratio σ_{n2}/σ_{n1} over gross plate thickness ratio t_2/t_1 for tensile loaded weld-like V-notched members ($2\alpha = 135°$) in medium-carbon steel AISI 1045; the fully plastic condition on the left hand side in contrast to the purely elastic condition on the right-hand side; reference values $t_1 = 25$ mm, $\sigma_{n1} = 250$ N/mm^2 in fatigue assessments according to Eurocode 3; (Lazzarin and Zambardi 2002)

nominal (bending) stress values because of the elastic bending support, characterised by the factor 1.5.

Finally, the size effect on strength is considered when varying all geometrical dimensions of the notched member in a self-similar manner, member 2 compared with member 1. The gross cross-sectional width, interpreted as plate thickness t in the weld-like models, is taken as the characteristic parameter. Based on the elastic NSIF, $K_1 = k_1 \sigma_n t^{1-\lambda_1}$, Eq. (2.87), the following relationship for the endurable nominal stresses σ_{n2} and σ_{n1} is derived:

$$\frac{\sigma_{n2}}{\sigma_{n1}} = \left(\frac{t_1}{t_2}\right)^{1-\lambda_1} \tag{2.192}$$

The corresponding formula for the plastic NSIF, $K_{1p} = AK_1^{2/(n+1)}$, Eq. (2.190), results in:

$$\frac{\sigma_{n2}}{\sigma_{n1}} = \left(\frac{t_1}{t_2}\right)^{2(1-\lambda_1)/(n+1)} \tag{2.193}$$

The ratio σ_{n2}/σ_{n1} may be interpreted as a strength ratio (fatigue or brittle fracture). The size effect on strength is thus reduced by $2/(1 + n)$ in the exponent of the plate thickness ratio t_1/t_2. The strength ratio σ_{n2}/σ_{n1} over plate thickness ratio t_2/t_1 for weld-like corner-notched members ($2\alpha = 135°$) is plotted in Fig. 2.76, using the material parameters of the AISI 1045 high-strength steel. The fully plastic condition approximated in thin-sheet material on the left-hand side contrasts with the purely elastic condition approximated in very thick plates on the right-hand side.

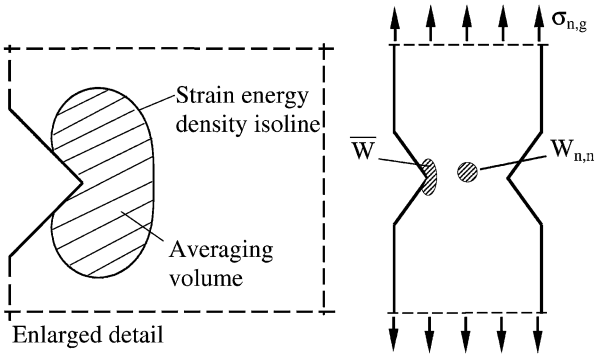

Fig. 2.77 Local volume for averaging the strain energy density W at the notch tip (resulting in $\overline{W}$) in comparison to its nominal value $W_{n,n}$ in the net cross-section; (Zappalorto and Lazzarin 2011[(2)])

2.5.4 *Elastic-Plastic Fields at Tensile Loaded V-Notches, SED-Based Approach*

It can be concluded from the expositions on tensile loaded V-notches above in comparison to the analytical work on out-of-plane shear loaded V-notches reviewed in the following subsections, that the governing equations in the former loading case (mode 1) are more complex so that they cannot be solved in a closed form as it is possible within the mode 3 approach (Unger 2001). A strain energy based approach to the mode 1 loading case is reviewed below (Zappalorto and Lazzarin 2011[(2)]). The basic idea of the approach is, to determine the strain energy density isolines around the notch tip and to compare the elastic and plastic NSIF strain energy densities averaged within a volume or area bordered by the relevant isolines, Fig. 2.77.

The averaging volume or area has to be fully contained in the near-field, where the elastic and plastic singularity, respectively, is fully valid. The isolines of the linear-elastic strain energy density for two notch opening angles under plane stress and plane strain conditions are plotted in Fig. 2.78. Normalised coordinates $\overline{x}$, $\overline{y}$ are introduced which refer to the linear-elastic condition (complex analytical expressions). The isolines of the elastic-plastic strain energy density for different hardening exponents are also given in the quoted article.

Under plane stress conditions for in-plane loading (mode 1), the positioning of the strain energy density isolines, ranging from the linear-elastic to the perfectly plastic behaviour, is similar to that under out-of-plane shear loading (mode 3). Therefore, the following relationship between $\overline{W}_p$ and $\overline{W}_e$ is transferred from the mode 3 loading case, where it is strictly valid, to the mode 1 loading case as a well founded hypothesis:

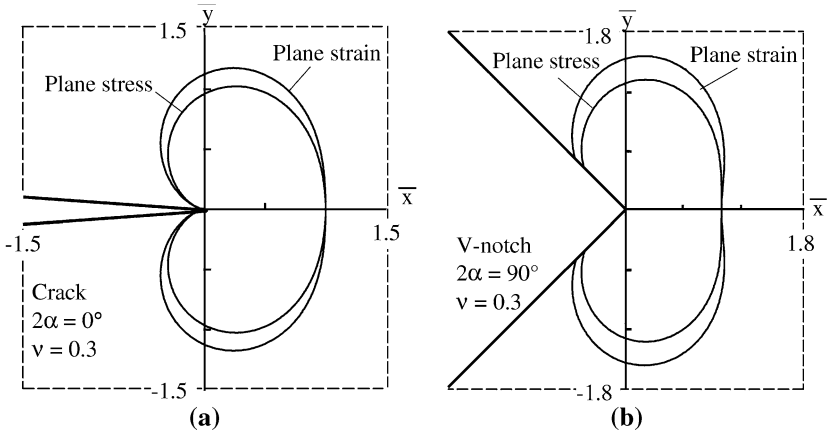

Fig. 2.78 Linear-elastic strain energy density isolines for V-notch with two different notch opening angles, $2\alpha = 0°$ (**a**) and $2\alpha = 90°$ (**b**) under plane stress and plane strain conditions in normalised coordinates $\bar{x}$, $\bar{y}$; Poisson's ratio $\nu = 0.3$; (Zappalorto and Lazzarin 2011[(2)])

$$\frac{\overline{W}_\mathrm{p}}{\overline{W}_\mathrm{e}} = \frac{2n}{n+1} \tag{2.194}$$

The following relationship is therefrom derived under the condition of small-scale yielding:

$$K_{1\mathrm{p}} = \left[K_{1\mathrm{e}}^2 \frac{H^n}{E} \left(\frac{I_\mathrm{e}}{I_\mathrm{p}} \right)^{1-\lambda_1} \right]^{1/n+1} \tag{2.195}$$

where I_e and I_p are integrals for evaluating the linear-elastic and nonlinear-elastic (named 'elastic-plastic') strain energy, respectively, within the isolines.

The analytical results are extended from the small-scale to the large-scale yielding conditions by writing Eq. (2.194) in terms of the 'energy concentration factors', $K_{W,\mathrm{p}}$ and $K_{W,\mathrm{e}}$:

$$K_{W,\mathrm{p}} = \frac{2n}{n+1} K_{W,\mathrm{e}}, \quad K_{W,\mathrm{p}} = \frac{\overline{W}_\mathrm{p}}{W_{\mathrm{n,n}}}, \quad K_{W,\mathrm{e}} = \frac{\overline{W}_\mathrm{e}}{W_{\mathrm{n,n}}} \tag{2.196}$$

Based on this relationship, the extended formula for $K_{1\mathrm{p}}$ reads:

$$K_{1\mathrm{p}} = \left[K_{1\mathrm{e}}^2 \frac{H^n}{E} \left(\frac{I_\mathrm{e}}{I_\mathrm{p}} \right)^{1-\lambda_1} \right]^{1/n+1} \times \left(1 + \frac{2n}{n+1} \frac{E}{H^n} \sigma_{\mathrm{n,n}}^{n-1} \right)^{1/n+1} \tag{2.197}$$

Under plane strain conditions for in-plane loading (mode 1), the above similarity to the out-of-plane shear behaviour (mode 3) does not exist because of the constraint effects ahead of the crack or notch tip. Therefore, the assumption

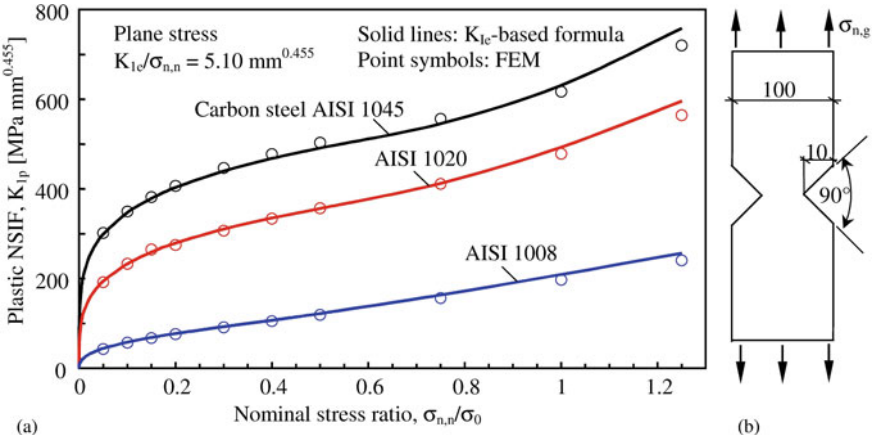

Fig. 2.79 Plastic NSIF (**a**) of V-notch ($2\alpha = 90°$) in tensile loaded flat bar (**b**) plotted over nominal stress $\sigma_{n,n}$ in net cross-section referred to substitute yield limit σ_0; plane stress conditions; (Zappalorto and Lazzarin 2011[(2)])

already used in an earlier investigation (Lazzarin and Zambardi 2002) remains valid, which referred to a circle sector of constant radius around the notch tip for averaging the strain energy density:

$$\frac{\overline{W}_p}{\overline{W}_e} = \frac{K_{W,p}}{K_{W,e}} = 1 \tag{2.198}$$

Then, applying the formal structure of Eq. (2.197), the result is:

$$K_{1p} = \left[\frac{n+1}{2n} K_{1e}^2 \frac{H^n}{E} \left(\frac{I_e}{I_p}\right)^{1-\lambda_1}\right]^{1/n+1} \times \left(1 + \frac{2n}{n+1}\frac{E}{H^n}\sigma_{n,g}^{n-1}\right)^{1/n+1} \tag{2.199}$$

One result from an investigation based on FE analysis verifying the above equations for K_{1p} as a function of K_{1e} under plane stress and plane strain conditions, respectively, is shown in Fig. 2.79. A tensile loaded flat bar with two-sided V-notch is considered. The material parameters correspond to the following three low-carbon and medium-carbon steels:

- AISI 1008: $E = 2.06 \times 10^5$ MPa, $H = 600$ MPa, $n = 4.00$, $\sigma_Y = 125$ MPa, $\nu = 0.3$
- AISI 1020: $E = 2.06 \times 10^5$ MPa, $H = 850$ MPa, $n = 6.66$, $\sigma_Y = 334$ MPa, $\nu = 0.3$
- AISI 1045: $E = 2.06 \times 10^5$ MPa, $H = 950$ MPa, $n = 8.33$, $\sigma_Y = 450$ MPa, $\nu = 0.3$

The K_{1p} curves determined according to Eq. (2.197) based on K_{1e} from a linear FE analysis are well in correspondence with the point symbols, which denote the K_{1p} values gained from nonlinear FE analysis using the total strain power law.

Based on the hypothesis for plane stress conditions, Eq. (2.194), the Neuber rule appears in terms of averaged stresses and strains corresponding to $\overline{W}_\mathrm{p}$ and $\overline{W}_\mathrm{e}$. The hypothesis for plane strain conditions, Eq. (2.198), on the other hand corresponds to the Glinka–Molski criterion in terms of averaged strain energy densities.

2.5.5 *Elastic-Plastic Fields at Out-of-Plane Shear-Loaded Parabolic Notches*

As shown in the preceding subsection, it has not been possible to solve the in-plane problem of elastic-plastic stress and strain fields at sharp notches (pointed or rounded) in a closed analytical form. The feasibility of a closed theory is substantially enhanced when considering the elastic-plastic fields in out-of-plane shear loading. Here, the governing nonlinear differential equations are easier to handle. But even here, the demands on mathematical analysis are very high.

In this subsection, an analytical study carried out by Zappalorto and Lazzarin is evaluated which is directed to the elastic-plastic field ahead of parabolic notches subjected to out-of-plane shear loading (Zappalorto and Lazzarin 2007). Small-scale yielding, but with inclusion of the stress redistribution effect, is investigated. Linear-elastic combined with perfectly plastic or power law elastic-plastic material behaviour is presumed. The analysis presents a first order ('leading term') field approximation and is therefore restricted to a small zone close to the notch tip or root. Torsional loaded round bars with a circumferential notch being the current application of out-of-plane shear field solutions, it is necessary to mention that the first order approximation must be combined with a correction term in this case, compare Eq. (2.147). The out-of-plane stress and strain symbols are used without the asterisk which was originally introduced in contrast to the in-plane shear symbols.

First, the linear-elastic followed by perfectly-plastic material behaviour is considered. The shear stresses τ_{xz} and τ_{yz} are proportional to the elastic generalised NSIF $K_{3\rho,\mathrm{e}}$. Referring to Eq. (2.153), $K_{3\rho,\mathrm{e}} = \tau_{\max}(\pi\rho)^{1/2}$ with the notch radius ρ. The shear strains γ_{xz} and γ_{yz} are proportional to $(K_{3\rho,\mathrm{e}})^2$.

Second, the linear-elastic followed by a power law elastic-plastic material behaviour, Eq. (2.281), is used as the basis of analysis. The nonlinear differential equations are transformed to a linear form by the approach described with some details in Sect. 2.5.6.

The power law of nonlinear-elastic or elastic-plastic material behaviour is written in the form of Eq. (2.286):

$$\frac{\gamma}{\gamma_0} = \left(\frac{\tau}{\tau_0}\right)^n \tag{2.200}$$

The considered resultant and simultaneously equivalent stresses and strains are:

$$\tau = \sqrt{\tau_{zx}^2 + \tau_{zy}^2} \tag{2.201}$$

$$\gamma = \sqrt{\gamma_{zx}^2 + \gamma_{zy}^2} \tag{2.202}$$

The stress and strain components follow from:

$$\left\{ \begin{matrix} \gamma_{zy} \\ \gamma_{zx} \end{matrix} \right\} = \frac{\gamma_0}{\tau_0} \left(\frac{\tau}{\tau_0} \right)^{n-1} \left\{ \begin{matrix} \tau_{zy} \\ \tau_{zx} \end{matrix} \right\} \tag{2.203}$$

The stress field in the near-tip plastic zone is controlled by the generalised elastic NSIF $K_{3\rho,\mathrm{e}}$:

$$\left\{ \begin{matrix} \tau_{zy} \\ \tau_{zx} \end{matrix} \right\} = \left[\frac{n K_{3\rho,\mathrm{e}}^2}{\pi(n+1)} \tau_0^{n-1} \right]^{1/(n+1)} \left(\frac{\tilde{F}}{r} \right)^{1/(n+1)} \left\{ \begin{matrix} \cos\overline{\theta} \\ -\sin\overline{\theta} \end{matrix} \right\} \tag{2.204}$$

where $\tilde{F} = \tilde{F}(n, \overline{\theta})$ and $\overline{\theta} = \overline{\theta}(n, \theta)$ are auxiliary functions. The corresponding strain field follows from Eq. (2.203).

The stress field equation above can be rewritten in analogy to the elastic case introducing the plastic NSIF $K_{3\rho,\mathrm{p}}$:

$$\left\{ \begin{matrix} \tau_{zy} \\ \tau_{zx} \end{matrix} \right\} = \frac{K_{3\rho,\mathrm{p}}}{\sqrt{2\pi}} \left(\frac{\tilde{F}}{r} \right)^{1/(n+1)} \left\{ \begin{matrix} \cos\overline{\theta} \\ -\sin\overline{\theta} \end{matrix} \right\} \tag{2.205}$$

With reference to the HRR field solution, the plastic NSIF is defined by the following limit value:

$$K_{3\rho,\mathrm{p}} = \lim_{r \to \rho/2} \sqrt{2\pi} r^{1/(n+1)} \tau_{zy}(r, 0) \tag{2.206}$$

Equating Eqs. (2.204) and (2.205), a relationship between plastic and elastic NSIFs under the condition of small-scale yielding (but with stress redistribution in the plastic zone) is established:

$$K_{3\rho,\mathrm{p}} = \sqrt{2\pi} \left[\frac{n}{\pi(n+1)} \tau_0^{n-1} K_{3\rho,\mathrm{e}}^2 \right]^{1/(n+1)} \tag{2.207}$$

For the crack tip ($\rho = 0$), the following special form results (Rice 1967):

$$K_{\mathrm{III,p}} = \lim_{\rho \to 0} K_{3\rho,\mathrm{p}} = \sqrt{2\pi} \left[\frac{n}{\pi(n+1)} \tau_0^{n-1} K_{\mathrm{III,e}}^2 \right]^{1/(n+1)} \tag{2.208}$$

The elastic and plastic NSIFs in terms of the maximum notch stresses are given as follows:

$$K_{3\rho,\mathrm{e}} = \tau_{\max,\mathrm{e}} \sqrt{\pi\rho} \tag{2.209}$$

$$K_{3\rho,\mathrm{p}} = \tau_{\max,\mathrm{p}}\sqrt{2\pi}\left(\frac{\rho}{2}\right)^{1/(n+1)} \tag{2.210}$$

When considering the maximum notch strains in parallel, a deviation from the original Neuber rule has been identified (compare Sect. 2.5.9).

In conclusion, an easy to survey closed form analytical solution for the elastic-plastic fields at parabolic notches (with inclusion of crack tips) subjected to out-of-plane shear loading has been derived by Zappalorto and Lazzarin. Uncertainties arise from the definition of the material law, because the Ramberg–Osgood relationship of metallic engineering materials has to be converted into the linear-elastic followed by power law elastic-plastic relationship of the analytical solution.

2.5.6 *Elastic-Plastic Fields at Out-of-Plane Shear-Loaded Pointed V-Notches*

Pointed V-notches subjected to out-of-plane shear loading are considered following the available analytical presentation (Lazzarin and Zappalorto 2008). The presumed material behaviour is linear-elastic followed by power-law strain hardening according to Eq. (2.200). Plastic and elastic NSIFs can be related under the condition of small-scale yielding. The near-tip stress and strain fields are then used to give closed-form expressions for the strain energy density averaged over a circle sector around the notch tip, as well as for the *J*-integral, both parameters as a function of the relevant plastic NSIF, these expressions being valid both for small-scale and large-scale yielding.

The basic nonlinear field equations resulting from the adoption of the nonlinear material law are converted to linear equations by introducing 'physical' coordinates as functions of stresses or of strains, similar to the hodograph transformation of fluid mechanics (Hult and McClintock 1956; Rice 1967). The resulting linear partial differential equation of second order in two parameters is solved without a series expansion (Rice 1967; Wang and Kuang 1999), based only on the 'leading order term' expressed by the nonlinear NSIF. The analysis details are passed over here, presenting the analysis results immediately.

In the near-tip plastic zone, the plastic NSIF $K_{3\mathrm{p}}$ is defined in analogy to the elastic NSIF K_3 as follows:

$$K_{3\mathrm{p}} = \lim_{r\to 0}\sqrt{2\pi}r^{1/(1-m)}\tau_{zy}(r,\,0) \tag{2.211}$$

where the parameter m in the exponent is dependent on n and 2α:

$$m = \frac{1}{2}\left(1 - n - \sqrt{(n-1)^2 + 4\omega^2 n}\right), \quad \omega = \frac{\pi}{\pi - 2\alpha} \tag{2.212}$$

Then, the elastic-plastic stress and strain fields are given dependent on $K_{3\mathrm{p}}$:

$$\left\{ \begin{matrix} \tau_{zy} \\ \tau_{zx} \end{matrix} \right\} = \frac{K_{3\mathrm{p}}}{\sqrt{2\pi}} \left(\frac{\tilde{F}}{r} \right)^{1/(1-m)} \left\{ \begin{matrix} \cos\overline{\theta} \\ -\sin\overline{\theta} \end{matrix} \right\} \tag{2.213}$$

$$\left\{ \begin{matrix} \gamma_{zy} \\ \gamma_{zx} \end{matrix} \right\} = \left(\frac{K_{3\mathrm{p}}}{\sqrt{2\pi}} \right)^{n} \frac{\gamma_0}{\tau_0^n} \left(\frac{\tilde{F}}{r} \right)^{n/(1-m)} \left\{ \begin{matrix} \cos\overline{\theta} \\ -\sin\overline{\theta} \end{matrix} \right\} \tag{2.214}$$

where τ_0 and γ_0 refer to the resultant or equivalent stresses and strains, Eq. (2.201) and (2.202), $\tilde{F} = \tilde{F}(m, \omega, \overline{\theta})$ and $\overline{\theta} = \overline{\theta}(m, \omega, \theta)$.

The relationship between plastic and elastic NSIFs under the condition of small-scale yielding (but with stress redistribution in the plastic zone) has the following form:

$$K_{3\mathrm{p}} = \sqrt{2\pi} \left[-\frac{m}{\lambda_3(1-m)} \left(\frac{K_{3\mathrm{e}}}{\sqrt{2\pi}} \right)^{1/(1-\lambda_3)} \frac{1}{\tau_0^{m+\omega}} \right]^{1/(1-m)} \tag{2.215}$$

For crack tips ($2\alpha = 0$, $\lambda_3 = 0.5$, $\omega = 1$, $m = -n$), Eq. (2.208) is confirmed.

The plastic zone considerations below refer to the reference stress τ_0 as the substitute yield limit. It is not identical with the real yield limit τ_Y. Therefore, the parameters r_p and x_p below are also substitute parameters.

The shape and size of the plastic zone is found by considering the shear stress τ_0 isolines (Tresca yield criterion). Under the condition of small-scale yielding (but with stress redistribution), the well known circular shapes at crack tips ($2\alpha = 0$) occur, but for V-notches ($2\alpha > 0$) oval shapes are typical. The oval shape gets more slender when strain hardening is weak (or the hardening exponent large).

In applications, the plastic zone size is often estimated by applying the yield criterion on the elastic stress field, resulting in the radius r_p of a circular zone around the crack or notch tip:

$$r_\mathrm{p} = \left(\frac{K_{3\mathrm{e}}}{\sqrt{2\pi}\tau_0} \right)^{1/(1-\lambda_3)} \tag{2.216}$$

According to the analysis above, the extension x_p of the plastic zone along the notch bisector line is enlarged by the stress redistribution:

$$x_\mathrm{p} = -\frac{m}{\lambda_3(1-m)} r_\mathrm{p} \tag{2.217}$$

For the crack ($2\alpha = 0$, $\lambda_3 = 0.5$, $m = -n$), this equation reproduces a result from the literature (Rice 1967):

$$x_\mathrm{p} = \frac{2n}{n+1} r_\mathrm{p} \tag{2.218}$$

The strain energy density, averaged over a small circle sector zone around the notch tip is the basis of fatigue assessment for pointed notches in engineering.

Therefore, it is appropriate to express the strain energy density by the plastic NSIF and vice versa.

Considering the power law in terms of total strains, Eq. (2.200), and assuming that the plastic strains are substantially larger than the elastic strains, the total and plastic strain energy densities can be set equal, approximated by:

$$W_{\mathrm{p}} = \int_0^{\gamma} \tau \, d\gamma = \int_0^{\gamma} \tau_0 \left(\frac{\gamma}{\gamma_0}\right)^{1/n} d\gamma \;\; = \frac{n}{n+1} \, \frac{\tau^{n+1}}{G\tau_0^{n-1}} \tag{2.219}$$

where τ and γ are the resultant or equivalent stresses and strains, Eqs. (2.201) and (2.102). Inserting the stress components τ_{zy} and τ_{zx}, Eqs. (2.213) and (2.214), the result is:

$$W_{\mathrm{p}} = \frac{n}{n+1} \frac{1}{G\tau_0^{n-1}} \left[\frac{K_{3\mathrm{p}}}{\sqrt{2\pi}} \left(\frac{\tilde{F}}{r}\right)^{1/(1-m)} \right]^{n+1} \tag{2.220}$$

The strain energy density averaged over the circle sector with radius R at the notch tip results by integration of Eq. (2.220), stating the parameter B_W:

$$\overline{W}_{\mathrm{p}} = B_W(2\alpha, \, n) \frac{K_{3\mathrm{p}}^{n+1}}{G\tau_0^{n-1}} R^{(n+1)/(m-1)} \tag{2.221}$$

For the J-integral, a similar expression is found, stating the parameter B_J:

$$J_{3\mathrm{p}} = B_J(2\alpha, \, n) \frac{K_{3\mathrm{p}}^{n+1}}{G\tau_0^{n-1}} R^{(n+m)/(m-1)} \tag{2.222}$$

Several FE analyses have been performed, in order to scale the plastic NSIFs of the investigated notched member and then to demonstrate their potential to describe the elastic-plastic field at the pointed notch tips inclusive of the average strain energy density and the J-integral. Out-of-plane shear loading is generated by a torsional moment applied to round bars with a circumferential slit ($2\alpha = 0$) or V-notch ($2\alpha = 120°$). The outer diameter is 60 mm, the inner diameter 40 mm. The two steels AISI 1008 and AISI 1045 with the material parameters specified in Sect. 2.5.3 were simulated. An important point was, to what extent the total strain power law in the theoretical analysis comes up to the well-proven Ramberg–Osgood law in the FE analysis.

The material parameters in the total strain power law in terms of the parameters in the Ramberg–Osgood law are defined as follows. It is generally accepted, not to modify the exponent n which characterises the degree of the singularity. Actually, there is no difference in the two laws when considering very large strains, which constitute the singularity. The reference values σ_0, ε_0 or τ_0, γ_0 result from the intersection point of the linear-elastic with the nonlinear power law curve (for the conversion from σ, ε to τ, γ see Sect. 2.5.10). Lazzarin and Zappalorto propose to equate the strain energy densities W_{p} resulting with the two material laws.

Integration of the plastic component in the Ramberg–Osgood law gives:

$$W_{\mathrm{p}} = \frac{n}{n+1}\,\frac{\sigma_{\mathrm{eq}}^{n+1}}{H^n} = \frac{n\,3^{(n+1)/2}}{n+1}\,\frac{\tau^{n+1}}{H^n} \quad (\sigma_{\mathrm{eq}} = \sqrt{3}\tau) \tag{2.223}$$

where σ_{eq} is the von Mises equivalent stress.

Equating this expression for W_{p} with that of the total strain power law, Eq. (2.220), the result is:

$$H = (G\tau_0^{n-1}3^{(n+1)/2})^{1/n}, \quad \tau_0 = \left(\frac{H^n}{3^{(n+1)/2}G}\right)^{1/(n-1)} \tag{2.224}$$

The combination of Eqs. (2.221) and (2.224) gives a further expression for the plastic NSIF:

$$K_{3\mathrm{p}} = \left(\frac{\overline{W}_{\mathrm{p}}H^n}{3^{(n+1)/2}B_W(2\alpha,\, n)}\right)^{1/(n+1)} R^{1/(1-m)} \tag{2.225}$$

Considering two of the carbon steels in the comparative investigation of Sect. 2.5.4, the following conversions were carried out:

- Steel AISI 1008: $\sigma_{\mathrm{Y}} = 125$ MPa, $\tau_{\mathrm{Y}} = \sigma_Y/\sqrt{3} = 72$ MPa, $\tau_0 = 47$ MPa
- Steel AISI 1045: $\sigma_{\mathrm{Y}} = 450$ MPa, $\tau_{\mathrm{Y}} = \sigma_Y/\sqrt{3} = 259$ MPa, $\tau_0 = 258$ MPa

The numerical results in the article of Lazzarin and Zappalorto are demonstrated in the following by a set of typical plots referring to the V-notch ($2\alpha = 120°$) in a round bar specimen subjected to torsional loading. All the plotted data are based on FE analysis results, because a fully analytical solution for the finite size configuration is impossible. The analytically derived relationships have been scaled by FE analysis results. What is checked by the plots is, whether or to what extent the theoretically predicted correlations are confirmed in actual configurations.

In Fig. 2.80, the determination of the plastic NSIFs $K_{3\mathrm{p}}$ from the shear stresses in the notch bisector plane (FE analysis results) according to Eq. (2.211) is shown for different nominal shear stresses $\tau_{\mathrm{n,n}}$ in the net cross-section. Horizontal curves over the distance from the notch tip are found. Their length increases with the extension of the plastic zone, i.e. with the nominal stress level. In Fig. 2.81, the shear stresses in the bisector plane are plotted, determined from the FE analysis results directly and, in comparison, from the FE-based $K_{3\mathrm{p}}$ values. The gradients in the theoretical analysis are fully confirmed by the FE analysis results.

In Fig. 2.82, the plastic NSIF $K_{3\mathrm{p}}$ is plotted over the nominal stress $\tau_{\mathrm{n,n}}$ normalised by the yield limit τ_{Y}. The $K_{3\mathrm{p}}$ values determined from the FE stresses τ_{zy} and from the average strain energy density $\overline{W}_{\mathrm{p}}$ are well in agreement, whereas the $K_{3\mathrm{p}}$ values based on the elastic $K_{3,\mathrm{e}}$ value are too low for nominal stresses above the yield limit. In Fig. 2.83, it is shown that $K_{3\mathrm{p}}$ can be approximated by a linear function of $\tau_{\mathrm{n,n}}/\tau_{\mathrm{Y}}$.

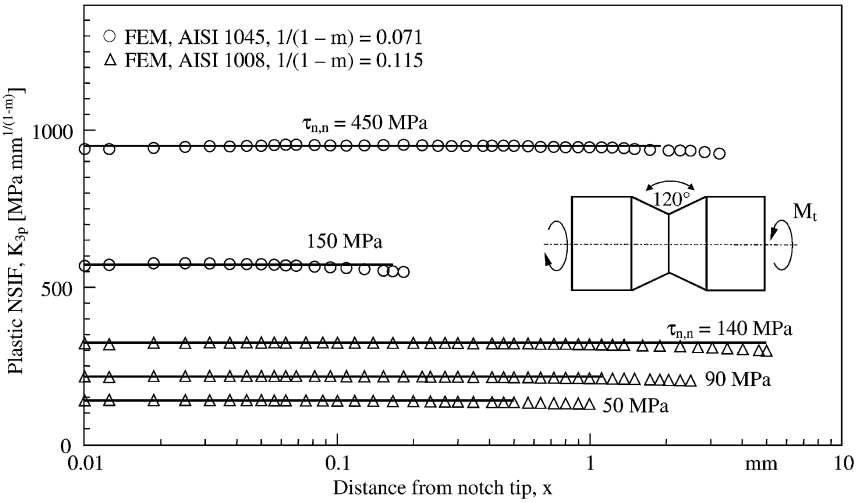

Fig. 2.80 Plastic NSIF of V-notch ($2\alpha = 120°$) in round bar subjected to torsional loading; evaluation of FE analysis results according to Eq. (2.211) (point symbols with medium lines); steels AISI 1045 and AISI 1008; nominal stress $\tau_{n,n}$ in net cross-section; (Lazzarin and Zappalorto 2008)

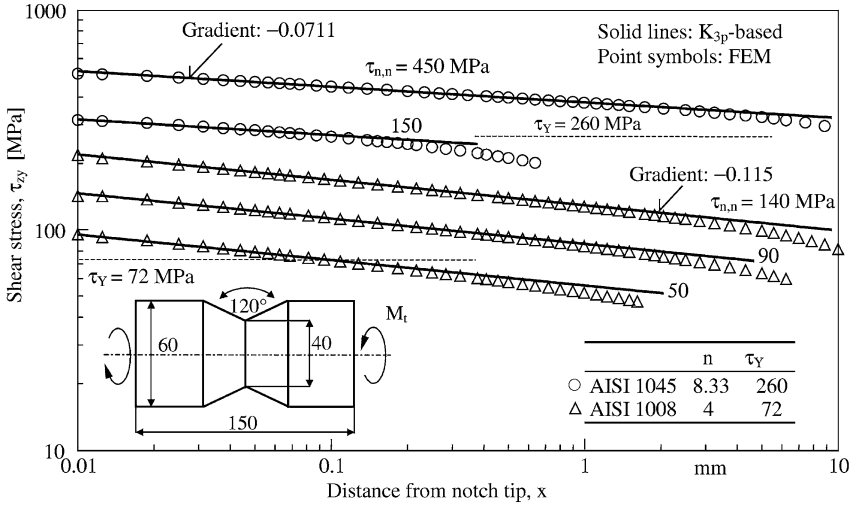

Fig. 2.81 Shear stress in bisector plane of V-notch ($2\alpha = 120°$) in round bar subjected to torsional loading; FE analysis results (point symbols) compared with K_{3p}-based values (solid lines); steels AISI 1045 and AISI 1008; nominal stress $\tau_{n,n}$ in net cross-section; (Lazzarin and Zappalorto 2008)

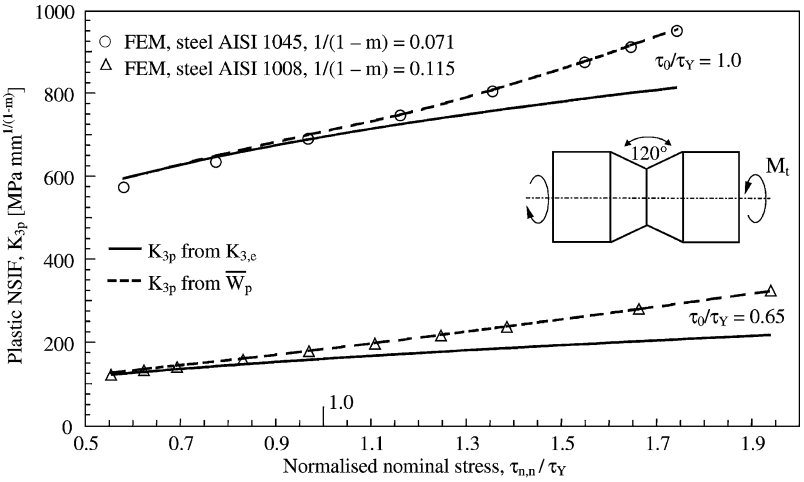

Fig. 2.82 Plastic NSIF of V-notch ($2\alpha = 120°$) in round bar subjected to torsional loading; derived from elastic NSIF (solid lines), from averaged strain energy density in circular sector of the FE model (broken lines) and from FE stresses (point symbols); steels AISI 1045 and AISI 1008; nominal stress $\tau_{n,n}$ in net cross-section; (Lazzarin and Zappalorto 2008)

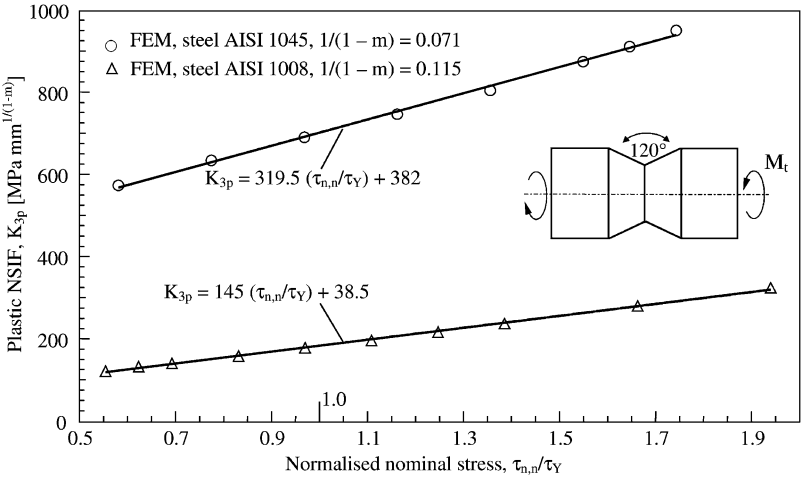

Fig. 2.83 Plastic NSIF at V-notch ($2\alpha = 120°$) in round bar subjected to torsional loading; evaluation of FE analysis results with linear medium line; steels AISI 1045 and AISI 1008; nominal stress $\tau_{n,n}$ in net cross-section; (Lazzarin and Zappalorto 2008)

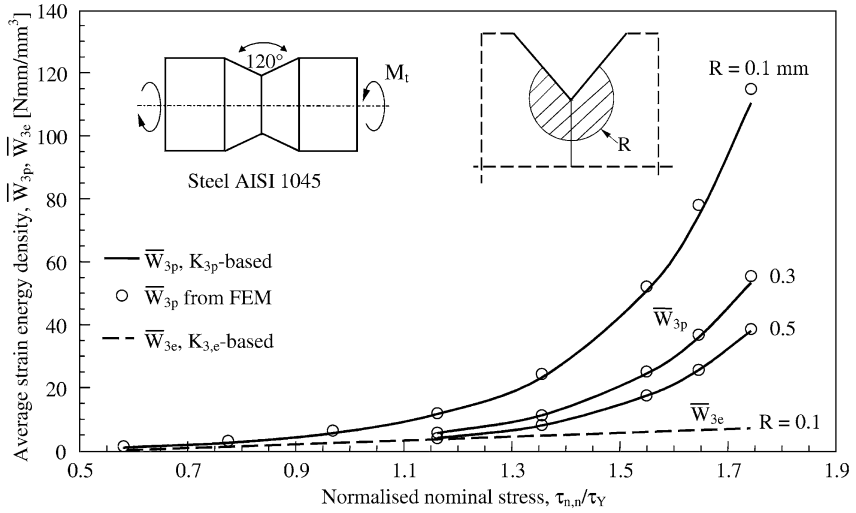

Fig. 2.84 Average plastic and elastic strain energy density at V-notch ($2\alpha = 120°$) in round bar subjected to torsional loading; direct evaluation of FE analysis results (point symbols) versus FE-based evaluation of plastic NSIFs K_{3p}, Eq. (2.221); linear-elastic behaviour in comparison; steel AISI 1045; nominal stress $\tau_{n,n}$ in net cross-section; (Lazzarin and Zappalorto 2008)

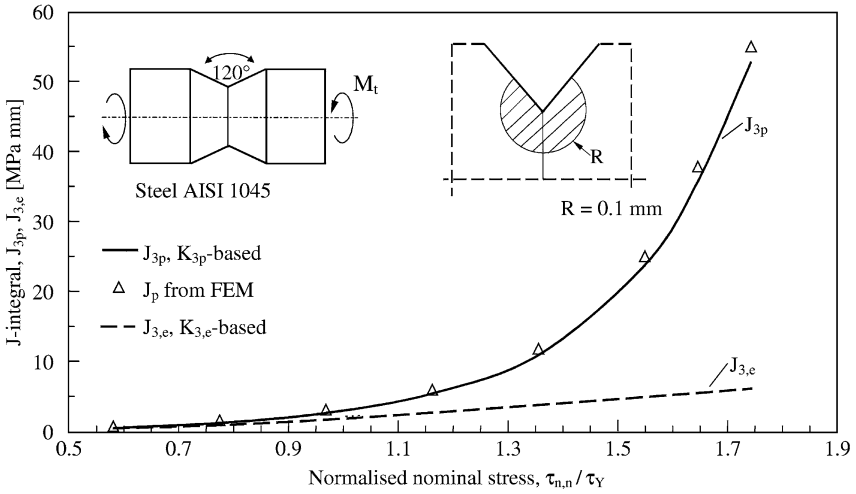

Fig. 2.85 Plastic and elastic *J*-integral at V-notch ($2\alpha = 120°$) in round bar subjected to torsional loading; direct evaluation of FE analysis results (point symbols) compared with FE-based evaluation of plastic NSIFs K_{3p}, Eq. (2.222); linear-elastic behaviour in comparison; steel AISI 1045; nominal stress $\tau_{n,n}$ in net cross-section; (Lazzarin and Zappalorto 2008)

In Fig. 2.84, the average plastic strain energy density $\overline{W}_p$ is plotted over $\tau_{n,n}/\tau_Y$, direct evaluation of FE analysis results compared with FE-based evaluation of plastic NSIFs K_{3p}, Eq. (2.215). The average elastic strain energy density $\overline{W}_e$ is shown in comparison. In Fig. 2.85, the plastic J-integral J_{3p} is drawn over $\tau_{n,n}/\tau_Y$, direct evaluation of FE analysis results contrasted with FE-based evaluation of J_{3p}, Eq. (2.222). The elastic J-integral $J_{3,e}$ is shown in comparison.

The following conclusions are drawn from the investigation reported by Lazzarin and Zappalorto: The elastic-plastic boundary assumes an oval shape for V-notches ($2\alpha > 0$) under small-scale yielding conditions. The entire stress and strain field in the plastic zone around the notch tip is unambiguously expressed by the plastic NSIF. A simple relationship exists between elastic and plastic NSIFs under the condition of small-scale yielding. The plastic NSIF can be approximated as linearly dependent on the ratio τ_n/τ_Y in the full range of small-scale and large-scale yielding. The plastic strain energy density averaged over a circle sector centred at the notch tip can be given in closed form as a function of the plastic NSIF. The same applies to the J-integral.

2.5.7 *Uniform Analysis of Nonlinear Fields at Out-of-Plane Shear-Loaded V-Notches*

In this subsection, an overview is given of the uniform approach to the analysis of nonlinear stress and strain fields at out-of-plane shear loaded V-notches (pointed or rounded) and cracks, which was presented by Zappalorto and Lazzarin in a pioneering article (Zappalorto and Lazzarin 2010). The mathematical tools were already developed in previous works (Hult and McClintock 1956; Neuber 1958; Rice 1967). Most important in respect of the uniform approach is the conversion of the governing nonlinear field equations resulting from the nonlinear material law into linear equations by introducing 'physical coordinates' as functions of stresses or strains (similar to the hodograph transformation in fluid mechanics). The appertaining series expansion can be confined to the leading order term, when the analysis is limited to the near-field at the notch or crack tip. Higher order fields have been investigated by other authors (Yuan and Yang 1994/95, Yang et al. 1996). The transformation above makes it possible to find a closed form solution of the anti-plane problem as soon as the nonlinear material law is defined. The reviewed publication is related primarily to the Neuber nonlinear material law, but comprises also the nonlinear power law and an attempt to include the Ramberg–Osgood law.

Considering the Neuber nonlinear material law according to Eqs. (2.287) and (2.288), Fig. 2.96, and taking advantage of a new polynomial form (after Legendre) of the above transformation, the closed form solution is gained under small-scale yielding conditions (Zappalorto and Lazzarin 2010). As the inversion to the r–θ plane is far from easy, the authors propose to combine two limit solutions, one for large strains close to the notch tip, the other for small strains at a certain distance from it.

For a clearer formal presentation of the results, notch strain intensity factors are introduced in analogy to the notch stress intensity factors, extending definitions used in the linear-elastic into the nonlinear-elastic range. Considering the notch bisector plane ($\theta = 0$) these elastic and plastic notch strain intensity factors are defined as follows:

$$K_{3\rho,\mathrm{e}}^{(\gamma)} = \lim_{r \to r_0} \sqrt{2\pi} r^{1-\lambda_3} \gamma(r, 0), \quad K_{3\rho,\mathrm{p}}^{(\gamma)} = \lim_{r \to r_0} \sqrt{2\pi} r^{-s_{\gamma,\mathrm{p}}} \gamma(r, 0) \tag{2.226}$$

where the subscript ρ indicates that the notch root radius may be different from zero and the exponent $s_{\gamma,\mathrm{p}}$ depends on the material law.

Considering the Neuber nonlinear material law ($s_{\gamma,\mathrm{p}} = -1$), the following relationships are derived for the linear-elastic and nonlinear-elastic (i.e. plastic) generalised notch strain and notch stress intensity factors:

$$K_{3\rho,\mathrm{e}}^{(\gamma)} = \sqrt{2\pi}(-\omega_1 C_1 \gamma_0^{\omega_1})^{1-\lambda_3}, \quad K_{3\rho,\mathrm{e}} = G\sqrt{2\pi}(-\omega_1 C_1 \gamma_0^{\omega_1})^{1-\lambda_3} \tag{2.227}$$

$$K_{3\rho,\mathrm{p}}^{(\gamma)} = -\sqrt{2\pi}\omega_1 2^{1-\omega_1}(1+\omega_1) C_1, \quad K_{3\rho,\mathrm{p}} = \sqrt{2\pi}\tau_0 \tag{2.228}$$

where $\omega_1 = \pi/(\pi - 2\alpha)$ and where C_1 is a parameter which defines the level of the strains both in the elastic and plastic zone.

The following relationship between the plastic notch strain intensity factor and the elastic NSIF has been derived:

$$K_{3\rho,\mathrm{p}}^{(\gamma)} = \sqrt{2\pi} 2^{1-\omega_1}(1+\omega_1) \left(\frac{K_{3\rho,\mathrm{e}}}{\sqrt{2\pi}\tau_0} \right)^{\omega_1+1} \gamma_0 \tag{2.229}$$

The nonlinear (elastic-plastic) strains close to the notch tip are dependent on the plastic notch strain intensity factor:

$$\begin{Bmatrix} \gamma_{zx} \\ \gamma_{zy} \end{Bmatrix} = \frac{K_{3\rho,\mathrm{p}}^{(\gamma)}}{\sqrt{2\pi}} \frac{1}{r} \begin{Bmatrix} -\cos\omega_1\theta \sin\theta \\ \cos\omega_1\theta \cos\theta \end{Bmatrix} \tag{2.230}$$

The corresponding stresses are given by:

$$\begin{Bmatrix} \tau_{zx} \\ \tau_{zy} \end{Bmatrix} = \tau_0 \begin{Bmatrix} -\sin\theta \\ \cos\theta \end{Bmatrix} \tag{2.231}$$

The linear-elastic strains and stresses at a sufficient distance from the notch tip are expressed by the elastic NSIF:

$$\begin{Bmatrix} \gamma_{zx} \\ \gamma_{zy} \end{Bmatrix} = \frac{K_{3\rho,\mathrm{e}} r^{\lambda_3 - 1}}{\sqrt{2\pi} G} \begin{Bmatrix} -\sin(1-\lambda_3)\theta \\ \cos(1-\lambda_3)\theta \end{Bmatrix} \tag{2.232}$$

$$\begin{Bmatrix} \tau_{zx} \\ \tau_{zy} \end{Bmatrix} = \frac{K_{3\rho,\mathrm{e}} r^{\lambda_3 - 1}}{\sqrt{2\pi}} \begin{Bmatrix} -\sin(1-\lambda_3)\theta \\ \cos(1-\lambda_3)\theta \end{Bmatrix} \tag{2.233}$$

When the notch root radius is different from zero, the solution can also be expressed by the maximum notch stress or strain, based on the following relationships:

$$K_{3\rho,\mathrm{p}}^{(\gamma)} = \sqrt{2\pi}\gamma_{\max,\mathrm{p}} r_0, \quad \tau_{\max,\mathrm{p}} = \tau_0, \quad K_{3\rho,\mathrm{e}} = \sqrt{2\pi}\tau_{\max,\mathrm{e}} r_0^{1-\lambda_3} \tag{2.234}$$

where r_0 is the distance of the notch root from the origin of the polar coordinate system.

The stress and strain distributions along the notch bisector plane of a pointed V-notch ($\rho = 0$, $2\alpha = 120°$) subjected to out-of-plane shear loading are plotted in Fig. 2.86. The complete solution based on Legendre polynomials and its two limit lines, both according to Zappalorto and Lazzarin, are compared with Neuber's different analytical approach (Neuber 1961). The numerical results are fully corresponding. The plot refers to the pointed notch ($\rho = 0$), but is transferable 'in principle' to cases of a small finite notch radius ($\rho > 0$), provided the coordinate x is truncated on the left hand side of the notch root.

The above theory has also been used to determine the substitute elastic-plastic boundary under small-scale yielding conditions by imposing the condition $\gamma = \gamma_0$. The complete solution is compared with the purely elastic and purely plastic solutions. The plastic zone according to the complete solution presented by Zappalorto and Lazzarin is substantially larger than according to the elastic and plastic limit solutions.

Considering the total strain power law according to Eq. (2.286), Fig. 2.95, and applying the same analytical tools as before, the following expressions for the stresses and strains in the close vicinity of the notch tip are derived from a stress-based (as opposed to strain-based) formulation of the nonlinear problem:

$$\left\{ \begin{matrix} \tau_{zx} \\ \tau_{zy} \end{matrix} \right\} = \frac{K_{3\rho}}{\sqrt{2\pi}} \left(\frac{\tilde{F}}{r} \right)^{1/(1-m)} \left\{ \begin{matrix} -\sin\overline{\theta} \\ \cos\overline{\theta} \end{matrix} \right\} \tag{2.235}$$

$$\left\{ \begin{matrix} \gamma_{zx} \\ \gamma_{zy} \end{matrix} \right\} = \left(\frac{K_{3\rho}}{\sqrt{2\pi}} \right)^{n} \frac{\gamma_0}{\tau_0^n} \left(\frac{\tilde{F}}{r} \right)^{n/(1-m)} \left\{ \begin{matrix} -\sin\overline{\theta} \\ \cos\overline{\theta} \end{matrix} \right\} \tag{2.236}$$

where $K_{3\rho}$ is the nonlinear NSIF, generalised for any value of ρ; compare Eqs. (2.213) and (2.214), where $\rho = 0$ and where 'nonlinear' is interpreted as 'plastic'. The exponent m corresponds to Eqs. (2.211) and (2.212). $\tilde{F} = \tilde{F}(m, \omega_1, \overline{\theta})$ and $\overline{\theta} = \overline{\theta}(m, \omega_1, \theta)$ are auxiliary parameters.

Finally, an attempt has been made by Zappalorto and Lazzarin to achieve a solution for the stress and strain field at the notch tip when considering the Ramberg–Osgood material law in the following special form:

$$G\gamma = \tau + \delta\tau^n \quad (1 < n < \infty) \tag{2.237}$$

where G is the shear modulus, n the hardening exponent, δ a material constant ($\delta = \tau_0^{1-n} = G/H_\tau^n$) and τ_0, γ_0 marking the intersection point of the linear-elastic

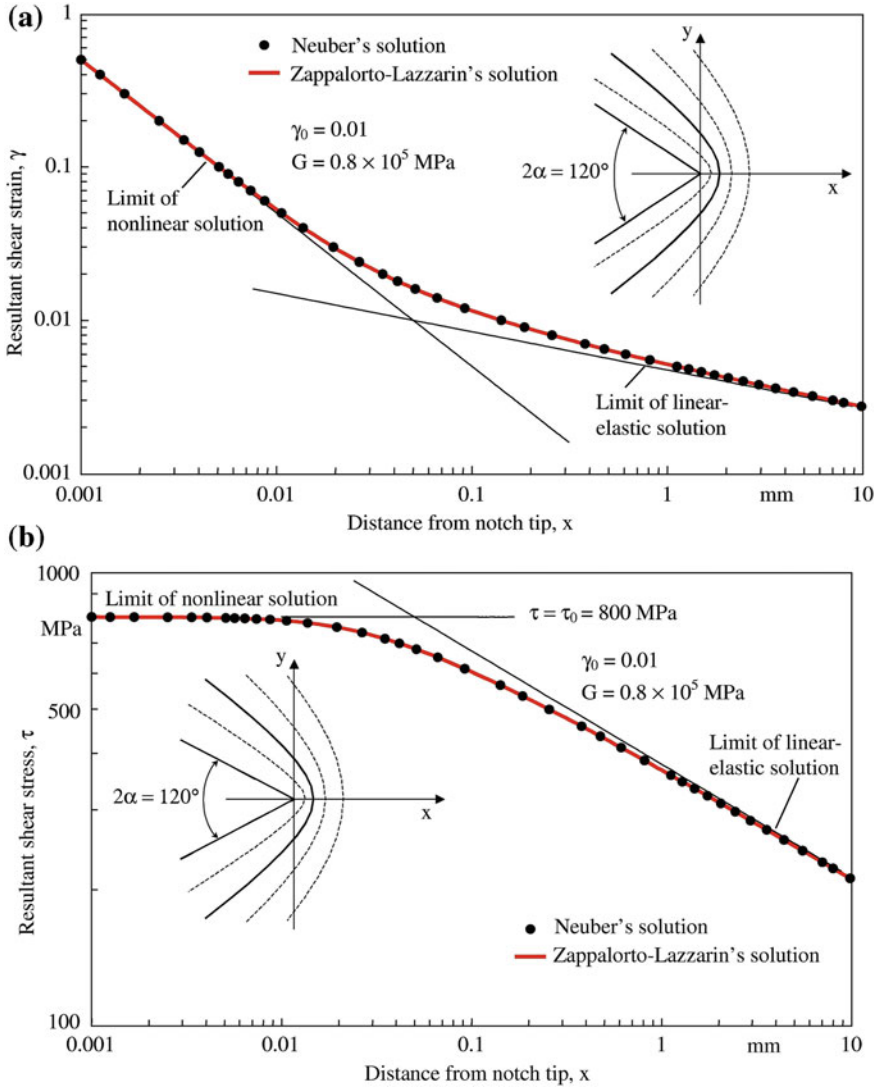

Fig. 2.86 Elastic-plastic strain distribution (**a**) and stress distribution (**b**) along the notch bisector plane of pointed V-notch ($\rho = 0$, $2\alpha = 120°$) subjected to out-of-plane shear loading; solutions based on the Neuber nonlinear material law; Neuber's compared with Zappalorto–Lazzarin's analytical approach; (Zappalorto and Lazzarin 2010)

curve and the asymptotic plastic total strain power law curve. Equation (2.237) can be derived from the normalised form of the Ramberg–Osgood relationship, Eq. (2.173), by setting $\alpha = 1.0$ there. This corresponds to the total strain power law combined with the initially linear-elastic behaviour. The Eq. (2.237) may be termed 'the asymptotic form' of the Ramberg–Osgood relationship.

A complete solution for V-notches with notch opening angle different from zero by application of the above analytical tools is not possible, but the two limit conditions for τ allow special solutions. The limit condition $\tau \to \infty$ of purely plastic behaviour at the notch tip results in the already derived Eqs. (2.235) and (2.236) with $K_{3\rho} = K_{3\rho,\mathrm{p}}$. The limit condition $\tau \to 0$ of linear-elastic behaviour results in the Eqs. (2.232) and (2.233).

For the special case of a notch opening angle equal to zero corresponding to pointed or blunt crack tips, a complete solution based on the asymptotic form of the Ramberg–Osgood relationship has been presented (Zappalorto and Lazzarin 2010).

2.5.8 Plastic Zone Related to Elastic Higher Order Singularities

The higher order singularities at crack tips and V-notch tips are generally omitted in the linear-elastic analysis with the argument that the strain energy and the displacements in the near-tip region should remain bounded. But it has been shown that the higher singular terms are significant in the elastic field outside the non-linear zone around the crack tip (Hui and Ruina 1995). Later on, it has been proven that the higher order singular terms can be included in the elastic part of the complete elastic-plastic stress and strain field solutions for out-of-plane shear loading (Zappalorto and Lazzarin 2011[(4)]). The findings of the two authors just mentioned are summarised in the following.

At crack tips, higher order singularities of the order $(1 - 2\mathrm{j})/2$ with $\mathrm{j} = 2, 3, 4, 5, \ldots$ are found which are governed by the order 1 stress intensity factor K_{III}. The Neuber material law, Eq. (2.287), is applied under small-scale yielding conditions. The higher order terms are found to be dependent, besides on K_{III}, on the substitute radius r_{p} of the plastic zone around of the crack tip. The strains in the ligament under out-of-plane shear loading conditions read as follows, whereas the stresses result from $\tau = G\gamma$:

$$\gamma = \frac{K_{\mathrm{III}}}{G\sqrt{2\pi x}}\left[1 + \frac{r_{\mathrm{p}}}{4x} + \frac{1}{32}\left(\frac{r_{\mathrm{p}}}{x}\right)^2 - \frac{1}{128}\left(\frac{r_{\mathrm{p}}}{x}\right)^3 - \frac{5}{2048}\left(\frac{r_{\mathrm{p}}}{x}\right)^4 + \ldots\right] \tag{2.238}$$

$$r_{\mathrm{p}} = \frac{K_{\mathrm{III}}^2}{2\pi\tau_0^2} \tag{2.239}$$

For crack tips, now using the Ramberg–Osgood material law in the form of Eq. (2.237), $G\gamma = \tau + \delta\tau^n$ with $\delta = \tau_0^{1-n} = G/H_\tau^n$, the following relationship is derived, with the hardening exponent $n = 4.0$ as an example, once more in the ligament under out-of-plane shear loading conditions:

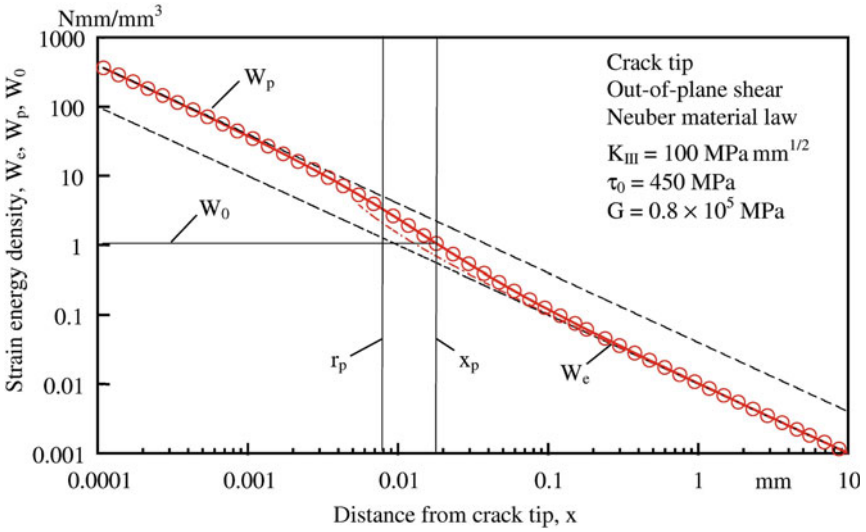

Fig. 2.87 Plastic (W_p) and elastic (W_e) strain energy density over distance x from the crack tip; substitute yield limit γ_0, γ_0 defines r_p from linear-elastic analysis and x_p from elastic-plastic analysis (Zappalorto and Lazzarin 2011[4])

$$\tau = \frac{K_{III}}{\sqrt{2\pi x}}\left[1 + \frac{2\pi}{3\sqrt{6}}\left(\frac{r_p}{x}\right) - \sqrt{2}\left(\frac{r_p}{x}\right)^{3/2} + \frac{\sqrt{2}\pi^2}{9}\left(\frac{r_p}{x}\right)^2 - \frac{8\sqrt{2}\pi}{3\sqrt{3}}\left(\frac{r_p}{x}\right)^{5/2} + \ldots\right] \tag{2.240}$$

$$\gamma = \frac{1}{G}(\tau + \delta\tau^4) = \frac{1}{G}\left[1 + \left(\frac{\tau}{\tau_0}\right)^3\right]\tau \quad (n = 4) \tag{2.241}$$

The conclusion from Eqs. (2.238) and (2.240) is, that the intensities of the higher order terms depend on the plastic zone radius r_p, which is defined by the substitute yield limit τ_0 (not identical with the real yield limit τ_Y).

The physical necessity of the higher order singular terms is proven on the basis of the strain energy density distribution. The asymptotic densities along the ligament in the elastic zone, W_e, and in the plastic zone, W_p, considering the Neuber material law are given by:

$$W_e = \frac{1}{2}G\gamma^2 = \frac{K_{III}^2}{4\pi G}\frac{1}{x} \tag{2.242}$$

$$W_p = \tau_0\gamma = \frac{K_{III}}{\pi G}\frac{1}{x} \quad (\gamma \gg \gamma_0) \tag{2.243}$$

It is obvious from the above asymptotic behaviour, that the strain energy density level in the plastic zone is four times greater than in the elastic zone with a

smooth transition according to the complete solution, Fig. 2.87. The strain energy density corresponding to the substitute yield limit $\gamma = \gamma_0$ is given by:

$$W_0 = \tau_0 \gamma_0 \left(\sqrt{2} - 1\right) \quad (\gamma = \gamma_0) \tag{2.244}$$

This strain energy density occurs on the ligament at the distance x_p:

$$x_p = \left[\sqrt{2} + \ln\left(1 + \sqrt{2}\right)\right] r_p = 2.3\, r_p \tag{2.245}$$

For V-notch tips, similar relationships for the stress and strain field have been derived by the same authors based on the Neuber material law under small-scale yielding conditions. Here, it was found that the higher order terms are governed by the first linear-elastic eigenvalues and not by higher order solutions. Once more, the higher order terms can be presented within a relationship governed by K_3 and dependent on the radius r_p of the substitute plastic zone around the V-notch tip.

The notch opening angle $2\alpha = 135°$, $\lambda_3^{(1)} = 0.8$, is considered as an example. The strains in the bisector plane under out-of-plane shear loading conditions read as follows, whereas the stresses result from $\tau = G\gamma$:

$$\gamma = \frac{K_3}{G\sqrt{2\pi}x^{1/5}}\left[1 + \frac{1}{3}\left(\frac{r_p}{x}\right)^{2/5} + \frac{1}{8}\left(\frac{r_p}{x}\right)^{4/5} + \frac{5}{54}\left(\frac{r_p}{x}\right)^{6/5} + \frac{41}{2592}\left(\frac{r_p}{x}\right)^{8/5} + \ldots\right] \tag{2.246}$$

$$r_p = \left(\frac{K_3}{\tau_0\sqrt{2\pi}}\right)^{1/(1-\lambda_3)} = \left(\frac{K_3}{\tau_0\sqrt{2\pi}}\right)^{5} \tag{2.247}$$

The conclusion is that the higher order singular terms can fully be included in the elastic part of the complete elastic-plastic stress and strain field solutions. The intensity of these additional terms depends on the elastic stress intensity factor and the substitute plastic zone radius r_p.

2.5.9 *Neuber Rule Including the Influence of the Notch Opening Angle*

The reviewed analytical developments related to elastic-plastic fields at sharp notches make it possible to include the influence of the notch opening angle in the Neuber rule where an unexpected effect in total is observed. Before presenting these results in detail, the Neuber rule is explained in general. It refers to rounded notches with exclusion of pointed notches, in contrast to the NSIF approach, which refers to pointed notches with inclusion of rounded notches.

The elastic-plastic notch stresses and strains can be approximated by predominantly uniaxial models and correspondingly simple formulae. Widely used is Neuber's 'macrosupport formula' besides an approximation by Glinka based on

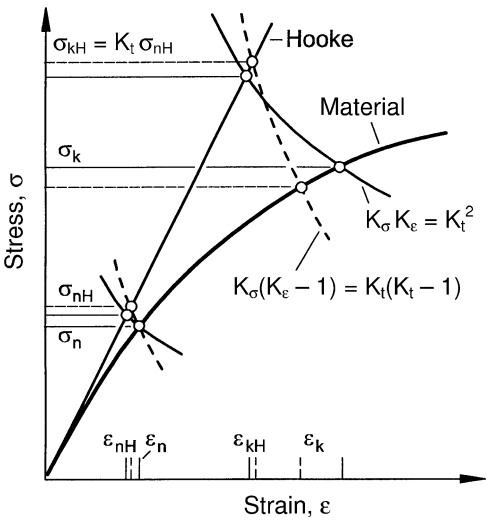

Fig. 2.88 Illustration of the analysis of elastic-plastic notch stresses and strains for sharp and mild notches; maximum notch stress σ_k, maximum notch strains ε_k, nominal stress σ_n, nominal strain ε_n, subscript H for 'Hooke' (after Neuber 1961, 1968(1), 1968(2), 1985)

the strain energy density. As soon as the yield limit is locally exceeded, the notch stresses rise underproportional and the notch strains overproportional. The relation between the elastic-plastic stress and strain concentration factors, K_σ and K_ε, on the one hand and the elastic stress concentration factor K_t on the other hand, is given by Neuber for sharp and mild notches, respectively, by the following equations (Neuber 1961, 1968(1), 1961(2), 1985):

$$K_\sigma K_\varepsilon = K_t^2 \quad (K_t \gg 1.0) \tag{2.248}$$

$$K_\sigma(K_\varepsilon - 1) = K_t(K_t - 1) \tag{2.249}$$

These equations are expressed by the maximum notch stresses $\sigma_k = \sigma_{max}$ and maximum notch strains $\varepsilon_k = \varepsilon_{max}$ (in the elastic-plastic range) as well as by the nominal stresses σ_n and nominal strains ε_n (in the elastic range) as follows:

$$\sigma_k \varepsilon_k = \sigma_n \varepsilon_n K_t^2 = \frac{\sigma_n^2}{E} K_t^2 \tag{2.250}$$

$$\sigma_k(\varepsilon_k - \varepsilon_n) = \sigma_n \varepsilon_n K_t(K_t - 1) = \frac{\sigma_n^2}{E} K_t(K_t - 1) \tag{2.251}$$

The content of Eqs. (2.248–2.251) is illustrated by Fig. 2.88, where the condition of elastic nominal stresses and strains referring to the net cross-section is deleted in favour of possibly occurring elastic-plastic conditions. Conforming to Neuber's analysis, the maximum actual notch stresses and strains on the stress–strain curve of the material are determined starting from the maximum linear-elastic notch stress $\sigma_{kH} = \sigma_{max,e}$ (with appertaining maximum notch strain ε_{kH}) on the Hooke straight line curve. The connection between appertaining points on the two curves is established by hyperbola-like curve sections, which run flatter for sharp notches,

Eq. (2.250) and steeper for mild notches, Eq. (2.251). Thus, slightly higher notch root stresses and strains are found with the former than with the latter equation.

The maximum linear-elastic notch stress σ_{kH} according to Hooke result from the Hooke nominal stress σ_{nH} (with appertaining nominal strain ε_{nH}) by multiplication with the elastic stress concentration factor K_t. The Hooke nominal stress is connected with the actual nominal stress σ_n (with appertaining nominal strain ε_n) by the hyperbola-like curve sections mentioned above. They are slightly higher than the actual nominal stress and differently high for the two curve sections. Thus, different values of σ_{kH} appear with the same value of K_t. The increase and the difference in σ_{kH} disappear if the actual nominal stress σ_n remains linear-elastic. As can be seen from Fig. 2.88, too high notch stresses and notch strains are determined, if the original Neuber rule, Eq. (2.248), is applied to mild notches.

The Neuber rule was originally proposed based on general mathematical considerations on an appropriate 'leading function' (Neuber 1961). The Neuber formulae, Eqs. (2.248) and (2.250), were subsequently analytically derived for parabola-like notches subjected to out-of-plane shear loading with an arbitrary nonlinear material law (Neuber 1985, ibid. pp. 86–87). Actually, a parabolic notch was the basis in combination with the Neuber material law in the unconventional form $G\gamma = \tau/(1 - \tau/\tau_0)$. The law does not allow for hardening under large strains. The resulting formula was then rewritten in terms of tensile stresses and strains with reference to the von Mises criterion.

As an alternative to the (original) Neuber rule, Glinka has proposed an approach based on the strain energy density in order to determine the elastic-plastic stresses and strains (Glinka 1985). The assumption is introduced that the strain energy density in the elastically supported plastic area at the notch tip (small-scale yielding) remains equal to the value of the linear-elastic solution (equivalent strain energy density concept). This assumption suggests itself for uniaxial and proportionally biaxial stress states, because the stresses and strains exceeding the yield limit deviate in opposite directions from the linear-elastic behaviour, whereas the principal directions of the stress and strain state remain unchanged. The Glinka approach offers a higher solution accuracy than the original Neuber formula. This has been proven on an experimental basis and was further substantiated by the following comparison of the two approaches.

The comparison is based on the Ramberg–Osgood material law. It is simplified by the assumption that the nominal stress remains in the linear-elastic range. The elastic strain energy density rising with the squared product of nominal stress times stress concentration factor is equated with the correspondingly rising elastic and plastic components of the elastic-plastic strain energy density at the notch tip (Glinka 1985):

$$\frac{\sigma_n^2}{2E} K_t^2 = \frac{\sigma_k^2}{2E} + \frac{\sigma_k}{n' + 1} \left(\frac{\sigma_k}{H}\right)^{1/n'} \tag{2.252}$$

where $1/n'$ is used instead on n as the hardening exponent ($0 < n' < 1.0$).

The original Neuber equation in terms of the Ramberg–Osgood material law, considered as a strain energy density equation, reads:

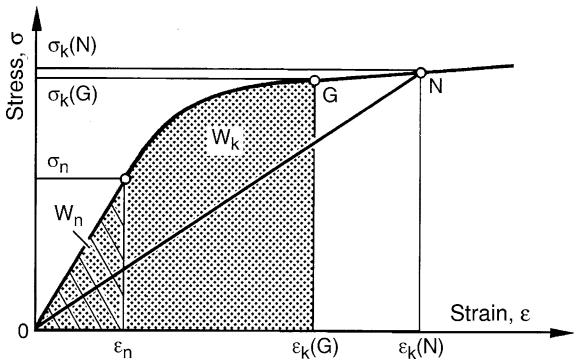

Fig. 2.89 Illustration of the elastic-plastic notch stress and strain analytical solutions by Glinka (point G) and by Neuber (point N); Glinka's solution on the basis of a constant ratio of strain energy densities W_k und W_n; (Glinka 1985)

$$\frac{\sigma_n^2}{2E}K_t^2 = \frac{\sigma_k}{2}\left[\frac{\sigma_k}{E} + \left(\frac{\sigma_k}{H}\right)^{1/n'}\right] \tag{2.253}$$

The solutions according to Glinka (curve point G) and Neuber (curve point N) are contrasted in Fig. 2.89. The strain energy density W_n of the nominal stress appears as a hatched triangular area. The corresponding strain energy density W_k of the maximum notch stress and strain is represented by the halftone area below the curve. The strain energy density according to the Neuber solution is characterised by the area below the straight line between the points 0 and N. The notch strain according to Neuber is substantially larger than according to Glinka. Experimental data confirm Glinka's result. Also, Neuber's modified solution, Eq. (2.251), reduces the notch strain.

The plastic NSIF approach by Zappalorto and Lazzarin allows further comparisons with the Neuber and Glinka results. The characteristic feature of this approach in respect of the Neuber rule is that the influence of the hardening exponent n and of the notch opening angle 2α is explicitly taken into account.

A first relationship is gained from the elastic-plastic stress and strain field analysis for parabolic notches ($2\alpha = 0$) subjected to out-of-plane shear loading (Zappalorto and Lazzarin 2007). The material law consists of linear-elastic behaviour up to the substitute yield limit τ_0 and power law behaviour in terms of the total strains above this limit. Continuing the exposition in Sect. 2.5.5, the following equation for the elastic-plastic notch stresses and strains is derived:

$$\tau_{\max,p}\gamma_{\max,p} = \tau_0\gamma_0\frac{2n}{n+1}\frac{1}{\pi\rho}\left(\frac{K_{3\rho,e}}{\tau_0}\right)^2 = \frac{2n}{n+1}\frac{(\tau_{\max,e})^2}{G} \tag{2.254}$$

By dividing both sides of the equation by $\tau_n\gamma_n = \tau_n^2 G$, one obtains the Neuber rule in the following form:

$$K_\tau K_\gamma = \frac{2n}{n+1}K_t^2 \tag{2.255}$$

This relationship is different from Neuber's original expression $K_\tau K_\gamma = K_t^2$ by a factor 1.0–2.0, identical only for the linear-elastic limit case ($n = 1$) and with the largest deviation for the elastic perfectly-plastic material ($n \to \infty$).

Based on the above analytical frame, an explicit formula for the maximum stress $\tau_{\max,p}$ is derived:

$$\tau_{\max,p} = \tau_0 \left[\frac{1}{2\pi} \left(\frac{K_{3\rho,e}}{\tau_0} \right)^2 \frac{2}{\rho} \right]^{1/(n+1)} = \left(\tau_{\max,e}^2 \tau_0^{n-1} \right)^{1/(n+1)} \tag{2.256}$$

Here, larger stresses and strains than with the original Neuber rule are found, in contrast to the tendency in Glinka's experimental results, after conversion of the tensile stresses there to shear stresses here.

A second investigation is devoted exclusively to the Neuber rule, using the Neuber nonlinear material law (Zappalorto and Lazzarin 2009). Pointed and rounded V-notches are considered, subjected to out-of-plane shear loading. The basic plastic and elastic NSIF relationships are stated in Sect. 2.5.7: $K_{3\rho,p}$, $K_{3\rho,p}^{(\gamma)}$, $K_{3\rho,e}$, $K_{3\rho,e}^{(\gamma)}$ and also $K_{3\rho,p} = f\,(K_{3\rho,e})$ according to Eqs. (2.227–2.229).

With the aim to check the Neuber rule, the following product is formulated:

$$K_{3\rho,p} K_{3\rho,p}^{(\gamma)} = 2\pi\gamma_0\tau_0\beta \left(\frac{K_{3\rho,e}}{\sqrt{2\pi}\tau_0} \right)^{\omega_1+1} \tag{2.257}$$

$$\beta = 2^{1-\omega_1}(1+\omega_1), \quad \omega_1 = \frac{\pi}{\pi - 2\alpha} \tag{2.258}$$

The plastic NSIFs in terms of the maximum stresses and strains read as follows:

$$K_{3\rho,p} = \sqrt{2\pi}\tau_{\max,p}, \quad K_{3\rho,p}^{(\gamma)} = \sqrt{2\pi}\gamma_{\max,p} r_0 \tag{2.259}$$

where $r_0 = \rho\,(q-1)/q$ with $(1 < q < 2)$ for hyperbolic notches and $q = 2$ for parabolic notches.

The elastic NSIF is given by the following expression (Zappalorto et al. 2008):

$$K_{3\rho,e} = \sqrt{2\pi}\tau_{\max,e} r_0^{1-\lambda_3} \tag{2.260}$$

Equation (2.257) written in the maximum stresses and strains according to Eqs. (2.25) and (2.260) reads as follows:

$$\tau_{\max,p}\,\gamma_{\max,p} = \tau_0\gamma_0\beta \left(\frac{\tau_{\max,e}}{\tau_0} \right)^{\omega_1+1} \tag{2.261}$$

where β and ω_1 are notch angle dependent parameters. Thus, the product of the stress and strain concentrations depends on the notch opening angle, contrary to the original Neuber rule.

In the special case of the parabolic notch ($2\alpha = 0$, $\omega_1 = 1$, $\beta = 2$), Eq. (2.261) results in:

$$\tau_{\max,\mathrm{p}}\,\gamma_{\max,\mathrm{p}} = \frac{2\tau^2_{\max,\mathrm{e}}}{G} \tag{2.262}$$

$$K_\tau\,K_\gamma = 2K_\mathrm{t}^2 \tag{2.263}$$

This result confirms Eq. (2.255) for $n \to \infty$, the condition, which brings the two different material laws more or less in correspondence (elastic perfectly-plastic behaviour).

The difference between Neuber's and Zappalorto–Lazzarin's final formulae, both derived for the same nonlinear material law, is discussed in detail by the second-mentioned authors. They uncover an inconsistency in Neuber's derivation, which expresses itself in the factor 1 instead of 2 on the nonlinear strains. But the removal of this deficiency does not solve the problem. Obviously, Neuber's original formula is applicable when approaching the limit case of purely elastic material behaviour. This is an indication that Neuber's original formula is appropriate in the range of small-scale yielding. Experimental and numerical (FE analysis) investigations have repeatedly demonstrated the applicability of the original formula with the reservation of a modification for mild notches. The modification has the effect that the resulting notch strains are slightly reduced. On the other hand, Zappalorto and Lazzarin's relationships, Eqs. (2.255) and (2.263), are appropriate for the extremely large plastic strains which occur close to pointed notch tips.

2.5.10 *Analytical Description of Elastic-Plastic Material Behaviour*

The analytical HRR and Neuber solutions for the stress and strain field at sharp notches under the condition of elastic-plastic material behaviour are actually nonlinear-elastic solutions. The solutions are bound to the condition of monotonic loading in every point of the field. Any unloading, globally or locally, is not allowed. The plastic strains are simply the nonlinear strain components, total strain minus linear-elastic strain. This condition applies to the analytical solutions and must be ascertained in comparative models using the FE method. The demanding mathematical formulations are easier to understand, if one considers them as referring to nonlinear-elastic material behaviour. Different types and variants of nonlinear material laws are in use.

Uniaxial Ramberg–Osgood Material Law

The relationship between stresses and strains in uniaxial monotonic loading, which is widely used by engineers, is the Ramberg–Osgood material law describing a single smooth curve without a distinct yield limit, Fig. 2.90:

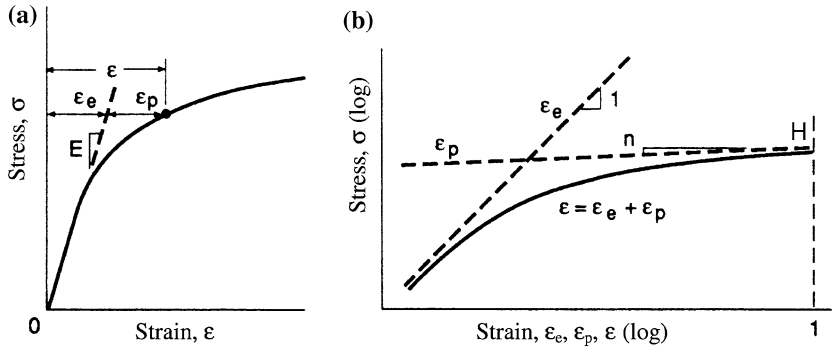

Fig. 2.90 Ramberg–Osgood material law: stress–strain curves drawn in linear (**a**) and logarithmic (**b**) coordinates; (Dowling 1993)

$$\varepsilon = \varepsilon_{\mathrm{e}} + \varepsilon_{\mathrm{p}} = \frac{\sigma}{E} + \left(\frac{\sigma}{H}\right)^{n} \tag{2.264}$$

with the elastic strain ε_{e}, the plastic strain ε_{p}, the modulus of elasticity E, the hardening (or strength) coefficient H and the hardening exponent n. The exponent n is determined from log σ over log ε plots. For the metallic engineering materials, $n = 2.5$–20.0 is found. In low-cycle fatigue assessments, a corresponding cyclic Ramberg–Osgood relationship is used. The cyclic material parameters may deviate substantially from the monotonic ones.

In engineering science, the offset yield limit $\sigma_{\mathrm{Y0.2}}$ is introduced, which denotes the stress where a plastic strain $\varepsilon_{\mathrm{Y0.2}} = 0.2\ \%$ occurs. Therefore, the following formula applies:

$$\frac{\varepsilon_{\mathrm{p}}}{\varepsilon_{\mathrm{Y0.2}}} = \left(\frac{\sigma}{\sigma_{\mathrm{Y0.2}}}\right)^{n} \quad (\varepsilon_{\mathrm{Y0.2}} = 0.002) \tag{2.265}$$

Equating ε_{p} from Eq. (2.264) and (2.265) gives:

$$\sigma_{\mathrm{Y0.2}} = \varepsilon_{\mathrm{Y0.2}}^{1/n} H \tag{2.266}$$

which means that $\sigma_{\mathrm{Y0.2}}$ depends on n and H for a defined $\varepsilon_{\mathrm{Y0.2}}$ and is not a third independent material parameter.

Multiaxial Ramberg–Osgood Material Law

The Ramberg–Osgood material law, generalised for multiaxial stress conditions, is usually presented in tensor form related to the stress and strain components, Eq. (2.183). Rather lengthy expressions for stresses, strains and strain energies result from it. A simplified procedure, preferred by engineers, is possible. The necessary conditions are monotonic loading, constant ratios of the stress

components and validity of the octahedral shear stress criterion (corresponding to the von Mises criterion). Then, according to Hencky's approach (Hencky 1924; Chakrabarty 2006), the components of the plastic strain tensor are set proportional to the components of the coaxial deviatoric stress tensor:

$$\varepsilon_{\mathrm{ij,p}} = \lambda s_{\mathrm{ij}} \tag{2.267}$$

For work-hardening materials, the coefficient λ depends on the von Mises equivalent stress σ_{eq}, which is considered to be a function of the equivalent plastic strain $\varepsilon_{\mathrm{p,eq}}$:

$$\sigma_{\mathrm{eq}} = \sqrt{\frac{3}{2} s_{\mathrm{ij}} s_{\mathrm{ij}}} \tag{2.268}$$

$$\varepsilon_{\mathrm{eq,p}} = \sqrt{\frac{2}{3} \varepsilon_{\mathrm{ij,p}} \varepsilon_{\mathrm{ij,p}}} \tag{2.269}$$

The relationship between σ_{eq} and $\varepsilon_{\mathrm{eq,p}}$ is given by the uniaxial stress versus plastic strain curve. The coefficient λ can be expressed by σ_{eq} and $\varepsilon_{\mathrm{eq,p}}$ or by the secant modulus E_{p} according to Eq. (2.270):

$$\lambda = \frac{3\varepsilon_{\mathrm{eq,p}}}{2\sigma_{\mathrm{eq}}} = \frac{3}{2E_{\mathrm{p}}} \tag{2.270}$$

It is a peculiarity of Hencky's approach that the coefficient λ is related to the stress–strain curve. In its original, more general definition, it is a constant factor which denotes the occurrence of plastic strain rates or strain increments as correlated with the deviatoric stress state.

The von Mises equivalent stress σ_{eq} expressed by the principal stresses σ_1, σ_2, σ_3 is related to the octahedral shear stress τ_{o}:

$$\sigma_{\mathrm{eq}} = \frac{1}{2}\sqrt{(\sigma_1 - \sigma_2)^2 + (\sigma_2 - \sigma_3)^2 + (\sigma_3 - \sigma_1)^2} = \frac{3}{\sqrt{2}}\tau_{\mathrm{o}} \tag{2.271}$$

The corresponding equivalent plastic strain $\varepsilon_{\mathrm{eq,p}}$ expressed by the principal plastic strains $\varepsilon_{1,\mathrm{p}}$, $\varepsilon_{2,\mathrm{p}}$, $\varepsilon_{3,\mathrm{p}}$ is related to the octahedral plastic shear strain $\gamma_{\mathrm{o,p}}$:

$$\varepsilon_{\mathrm{eq,p}} = \frac{\sqrt{2}}{3}\sqrt{(\varepsilon_{1,\mathrm{p}} - \varepsilon_{2,\mathrm{p}})^2 + (\varepsilon_{2,\mathrm{p}} - \varepsilon_{3,\mathrm{p}})^2 + (\varepsilon_{3,\mathrm{p}} - \varepsilon_{1,\mathrm{p}})^2} = \frac{1}{\sqrt{2}}\gamma_{\mathrm{o,p}} \tag{2.272}$$

The equivalent total strain $\varepsilon_{\mathrm{eq}}$ is the sum of its elastic and plastic components:

$$\varepsilon_{\mathrm{eq}} = \frac{\sigma_{\mathrm{eq}}}{E} + \varepsilon_{\mathrm{eq,p}} \tag{2.273}$$

The equivalent stress and strain, σ_{eq} and $\varepsilon_{\mathrm{eq,p}}$ or $\varepsilon_{\mathrm{eq}}$, is identical with the stress and strain, σ_1 and $\varepsilon_{1,\mathrm{p}}$ or ε_1, in the uniaxial tensile test case ($\sigma_{\mathrm{eq}} = \sigma_1$, $\sigma_2 = \sigma_3 = 0$, $\varepsilon_{\mathrm{eq,p}} = \varepsilon_{1,\mathrm{p}}$, $\varepsilon_{2,\mathrm{p}} = \varepsilon_{3,\mathrm{p}} = -0.5\varepsilon_{1,\mathrm{p}}$) so that any monotonic stress–strain curve is a sufficient basis for describing arbitrary stress and strain states. The

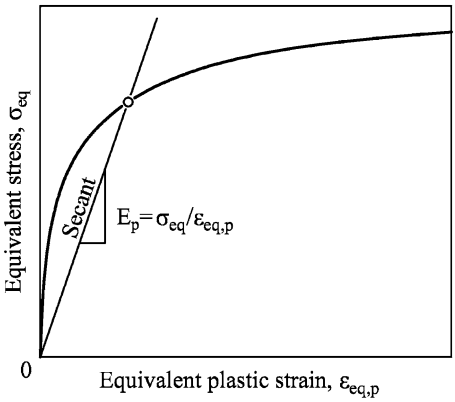

Fig. 2.91 Plastic modulus E_p defined as secant modulus of the equivalent stress over equivalent strain curve, identical with uniaxial stress σ_1 over strain ε_1 curve; (Dowling 1993)

plastic strain components are related to the stress components by equations which are structured analogous to the Hooke law equations, but with the elastic modulus E replaced by the plastic modulus E_p and with Poisson's ratio $\nu = 0.5$ related to the incompressibility condition for the plastic strains:

$$\begin{aligned}
\varepsilon_{x,p} &= \frac{1}{E_p}\left[\sigma_x - 0.5(\sigma_y + \sigma_z)\right], \quad \gamma_{xy,p} = \frac{3}{E_p}\tau_{xy} \\
\varepsilon_{y,p} &= \frac{1}{E_p}\left[\sigma_y - 0.5(\sigma_x + \sigma_z)\right], \quad \gamma_{yz,p} = \frac{3}{E_p}\tau_{yz} \\
\varepsilon_{z,p} &= \frac{1}{E_p}\left[\sigma_z - 0.5(\sigma_x + \sigma_y)\right], \quad \gamma_{zx,p} = \frac{3}{E_p}\tau_{zx}
\end{aligned} \tag{2.274}$$

The plastic tensile modulus E_p or alternatively the plastic shear modulus $G_p = E_p/3$ (with $\nu = 0.5$) is dependent on σ_{eq} and $\varepsilon_{eq,p}$ or on τ_o and $\gamma_{o,p}$:

$$E_p = \frac{\sigma_{eq}}{\varepsilon_{eq,p}}, \quad G_p = \frac{\tau_o}{\gamma_{o,p}}, \quad G_p = \frac{E_p}{3} \tag{2.275}$$

These plastic moduli are also named 'secant moduli' as illustrated by Fig. 2.91.

The multiaxial Ramberg–Osgood law has the general form:

$$\varepsilon_{eq} = \varepsilon_{eq,e} + \varepsilon_{eq,p} = \frac{\sigma_{eq}}{E} + \left(\frac{\sigma_{eq}}{H}\right)^{1/n} \tag{2.276}$$

The factor λ in Eq. (2.270) and the secant modulus E_p in Eq. (2.275), applied to the Ramberg–Osgood relationship, result in:

$$\lambda = \frac{3}{2}\frac{\sigma_{eq}^{n-1}}{H^n}, \quad E_p = \frac{H^n}{\sigma_{eq}^{n-1}} \tag{2.277}$$

Based on the equivalent stress and strain relationships, Eqs. (2.270–2.272), any arbitrary multiaxial stress state can be provided with the appertaining stress–strain relationship in terms of its characteristic stress and strain components.

Pure Shear Ramberg–Osgood Material Law

Most important is the application of the multiaxial Ramberg–Osgood material law to pure shear loading conditions, especially out-of-plane shear loading. The following relationship is thus gained (Dowling 1993):

$$\gamma = \frac{\tau}{G} + \sqrt{3}\left(\frac{\sqrt{3}\tau}{H}\right)^{1/n} \tag{2.278}$$

or alternatively:

$$\gamma = \frac{\tau}{G} + \left(\frac{\tau}{H_\tau}\right)^{1/n}, \quad H_\tau = \frac{H}{3^{(n+1)/2}} \tag{2.279}$$

This relationship is confirmed by the power law conversion from σ, ε to τ, γ components based on equated strain energy densities, Eq. (2.284).

In the case of out-of-plane shear loading, the resultant or equivalent stresses and plastic strains in the cross-sectional plane are:

$$\tau = \sqrt{\tau_{zx}^2 + \tau_{zy}^2}, \quad \gamma_\mathrm{p} = \sqrt{\gamma_{zx,\mathrm{p}}^2 + \gamma_{zy,\mathrm{p}}^2} \tag{2.280}$$

No simple relationship exists between the offset yield limit $\sigma_{\mathrm{Y0.2}}$ in the tensile test defined by $\varepsilon_{\mathrm{Y0.2}} = 0.2\ \%$, and the corresponding offset yield limit in the shear test, were γ_Y is initially undefined. The two shear test parameters may be determined by transfer from the equivalent stress–strain curve to the pure shear stress–strain curve. Alternatively, the parameters may be gained from equating the strain energy densities at the two yield limits. This has not yet been done.

Total Strain Power Law

Another way to describe elastic-plastic material behaviour in the considered theoretical solutions is to assume linear-elastic behaviour up to the reference values γ_0, τ_0 (or ε_0, σ_0) and a power law behaviour in terms of the total strains above the reference values, Figs. 2.92 and 2.93. This may be considered as the asymptotic form of the Ramberg–Osgood material law. The equations are given for out-of-plane shear loading in terms of γ, τ, but are transferable to tensile loading by introducing ε, σ instead of γ, τ [compare Eq. (2.176)]:

$$\begin{aligned} \frac{\gamma}{\gamma_0} &= \frac{\tau}{\tau_0} \quad (\gamma \le \gamma_0) \\ \frac{\gamma}{\gamma_0} &= \left(\frac{\tau}{\tau_0}\right)^n \quad (\gamma \ge \gamma_0) \end{aligned} \tag{2.281}$$

The reference values γ_0, τ_0 (or ε_0, σ_0) represent the linear-elastic stress and strain on the nonlinear $\tau{-}\gamma$ (or $\sigma{-}\varepsilon$) curve:

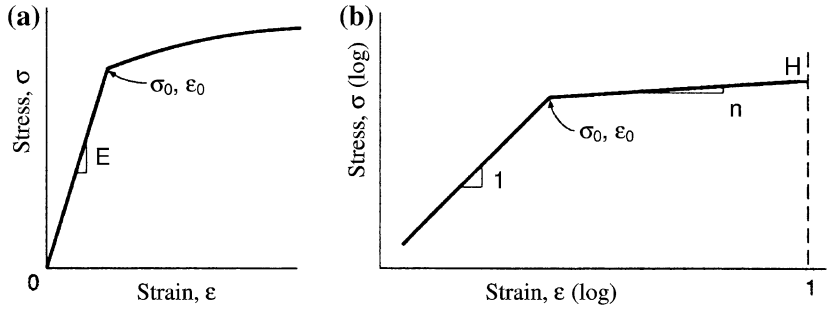

Fig. 2.92 Linear–elastic followed by total strain power law material behaviour: stress–strain curves drawn in linear (**a**) and logarithmic (**b**) coordinates; (Dowling 1993)

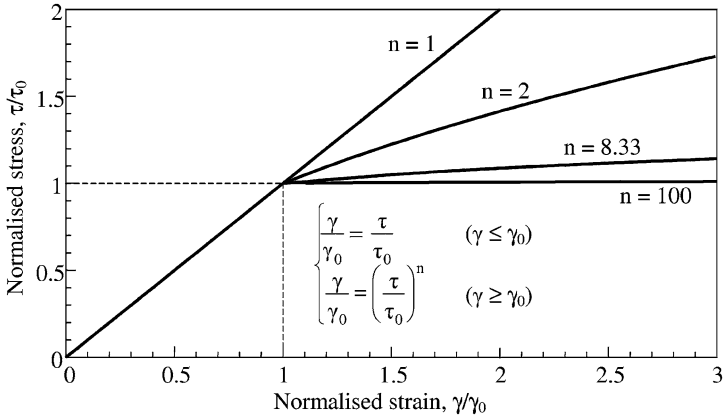

Fig. 2.93 Linear-elastic followed by total strain power law material behaviour: normalised stress–strain curves drawn in linear coordinates; (Lazzarin and Zappalorto 2008)

$$\gamma_0 = \frac{\tau_0}{G} = \left(\frac{\tau_0}{H_\tau}\right)^n, \quad \tau_0 = \left(\frac{H_\tau^n}{G}\right)^{1/(n-1)} \tag{2.282}$$

$$\varepsilon_0 = \frac{\sigma_0}{E} = \left(\frac{\sigma_0}{H}\right)^n, \quad \sigma_0 = \left(\frac{H^n}{E}\right)^{1/(n-1)} \tag{2.283}$$

There is no difference between the total strain power law and the Ramberg–Osgood relationship for very large strains, as they occur in the close vicinity of the notch tip, so that n and H_τ or H can be set equal, but there are major differences in the values of γ_0, τ_0 (or ε_0, σ_0) compared with those of γ_Y, τ_Y (or ε_Y, σ_Y), Fig. 2.94. The mentioned differences are relevant when considering the plastic zone size. One has to differentiate between the real size defined by ε_Y, σ_Y and the substitute size given by ε_0, σ_0.

In order to avoid confusion when comparing NSIF values from analytical expressions based on the total strain power law with those from FE analysis based

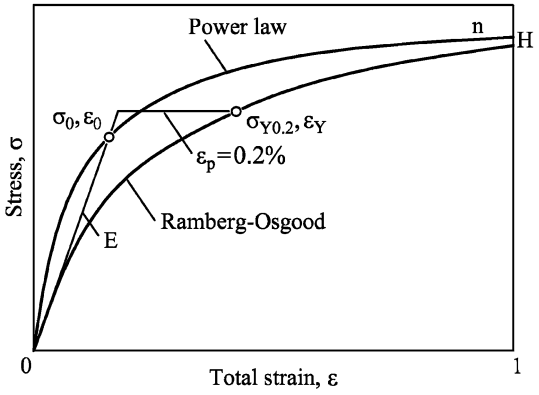

Fig. 2.94 Stress–strain curves, total strain power law in comparison to the Ramberg–Osgood law with characteristic material parameters; (Radaj, unpublished)

on the Ramberg–Osgood relationship, it should be kept in mind that identical values of H and n in the two producers are sufficient and that the reference values ε_0, σ_0 in the power law are a substitute for the real yield limit in the Ramberg–Osgood relationship, the substitute based on the elastic modulus E.

The power law in terms of ε, σ may be converted to the power law in terms of γ, τ based on the expressions for the equivalent stresses and strains, Eqs. (2.271–2.273), combined with the assumption of identical strain energy densities (Zappalorto and Lazzarin 2009). These are determined by integration of the power law curve starting at the origin, i.e. without the linear-elastic initial curve rise. They are termed W_{nl} ('nonlinear') instead of W_{p} ('plastic') as in the original publication above. Also, the derivation is formally modified; compare Eqs. (2.223) and (2.224):

$$W_{\mathrm{nl}} = \frac{n}{n+1}\frac{\sigma_{\mathrm{eq}}^{n+1}}{H^n} = \frac{n}{n+1}\frac{\tau^{n+1}}{H_\tau^n}, \quad H_\tau = \frac{H}{3^{(n+1)/2}} \tag{2.284}$$

$$W_{\mathrm{nl}} = \frac{n}{n+1}\frac{\sigma_{\mathrm{eq}}^{n+1}}{E\sigma_{\mathrm{eq},0}^{n-1}} = \frac{n}{n+1}\frac{\tau^{n+1}}{G\tau_0^{n-1}}, \quad \tau_0 = \sigma_{\mathrm{eq},0}\left(\frac{2(1+\nu)}{3^{(n+1)/2}}\right)^{1/(n-1)} \tag{2.285}$$

with $\sigma_{\mathrm{eq}} = \sqrt{3}\tau$ and $G = E/2(1+\nu)$. The hardening coefficient H_τ of the power law, Eq. (2.284), is identical with H_τ of the Ramberg–Osgood relationship, Eq. (2.279).

The total strain power law in Eq. (2.281) may alternatively be considered valid in the whole range of γ without the restriction $\gamma \geq \gamma_0$. Using γ_0, τ_0 as reference quantities for arbitrary values of γ, τ, a nonlinear-elastic material law is described, Fig. 2.95:

$$\frac{\gamma}{\gamma_0} = \left(\frac{\tau}{\tau_0}\right)^n \quad (1 < n < \infty) \tag{2.286}$$

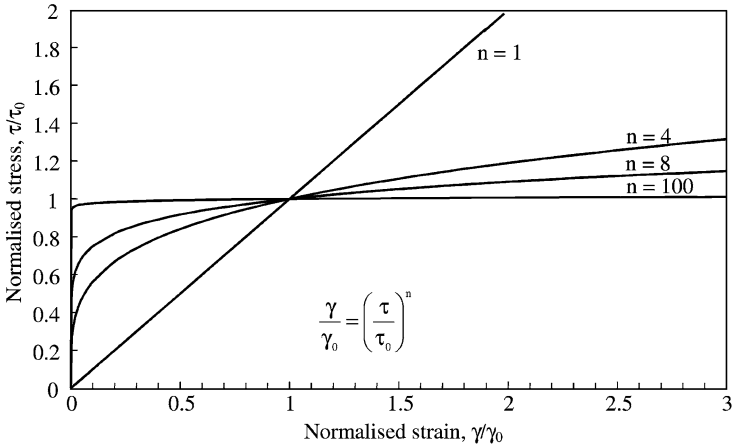

Fig. 2.95 Nonlinear-elastic total strain power law of material behaviour: normalised stress–strain curves drawn in linear coordinates; (Zappalorto and Lazzarin 2010)

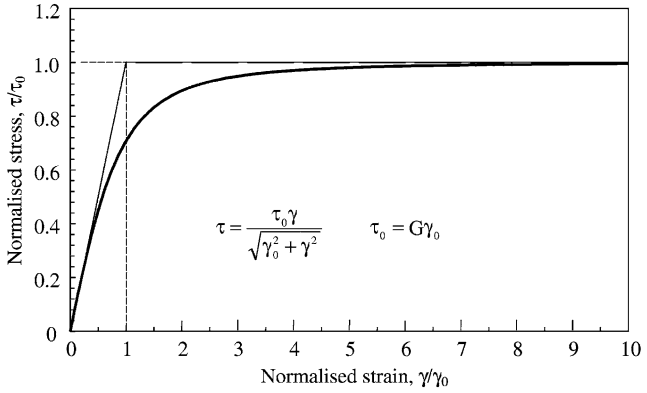

Fig. 2.96 Neuber nonlinear material law: normalised stress–strain curves drawn in linear coordinates; (Zappalorto and Lazzarin 2010)

Neuber's Nonlinear Material Law

Finally, the nonlinear stress–strain law used by Neuber is presented (Neuber 1958, 1961), Fig. 2.96:

$$\tau = \frac{\tau_0 \gamma}{\sqrt{\gamma_0^2 + \gamma^2}}, \quad \tau_0 = G\gamma_0 \tag{2.287}$$

where one of the two equations can also be substituted by the original Neuber version:

$$G\gamma = \frac{\tau}{\sqrt{1 - (\tau/\tau_0)^2}} \tag{2.288}$$

This material law has the following properties: $\tau \to \tau_0$ for $\gamma \to \infty$, $\tau \to G\gamma$ for $\gamma \to 0$ and a continuous strain hardening behaviour in the γ range between. Virtually no hardening occurs for values $\gamma/\gamma_0 \geq 5.0$. A stress singularity at pointed notches cannot be formed under these conditions, but a strain singularity very well.

The different material laws reviewed above will have an influence on the stress and strain fields at pointed or rounded notches. This influence manifests itself in different plastic NSIFs. Therefore, the plastic NSIFs depend on the material law. An exception is non-hardening material behaviour, where the plastic NSIFs are identical.

2.5.11 Conclusions

The elastic-plastic stress and strain fields at pointed or rounded notch tips can be uniformly described by plastic NSIFs as governing parameters. The plastic NSIFs are combined for that purpose with definite 'universal functions'. Both the stress and strain fields are handled within this analytical frame, differentiating between stress intensity factors and strain intensity factors. Definite relationships exist between elastic and plastic NSIFs, or, following the loading curve, between initial linear and final nonlinear NSIFs.

The available analytical solutions are derived for nonlinear-elastic material laws which may be interpreted as elastic-plastic behaviour under conditions of monotonic loading. Two different material laws are the basis of the analytical theory: the Ramberg–Osgood relationship asymptotically approximated by the total strain power law for strain-hardening materials (the HRR solutions) and Neuber's material law without hardening at large strains. These material laws allow closed form solutions for the antiplane fields and approximate solutions for the in-plane fields.

There remains the problem, how to interpret the derived analytical solutions in terms of the Ramberg–Osgood material law which is preferred by engineers and actually fits the real-world material behaviour better than the power material law or the Neuber material law does. There is no problem with the limit states of small elastic strains and large plastic strains at the notch tip, but there is a problem in the intermediate range, where the elastic-plastic boundary is established.

Valuable basic insights have been gained in respect of the following engineering issues, mainly under small-scale yielding conditions: plastic NSIFs for V-notches and parabolic notches, the size effect for V-notched specimens, expressions for the strain energy density and the *J*-integral, elastic-plastic stress and strain distributions in the bisector plane for various notch opening angles. The solutions for configurations with finite geometries are scaled by FE-analysis

results. The Neuber rule for extremely large strains is specified in terms of hardening exponent and notch opening angle for the extremely large strains at pointed notch tips.

2.6 Stress Intensity Factor Concept for Rigid Inclusions

2.6.1 Survey of Section Contents

Any geometrical or material discontinuity in an, apart from this, homogeneous elastic continuum produces local stress concentrations when the continuum or the discontinuity is subjected to any loadings. At the pointed edges of such discontinuities stress singularities occur. The stress singularities at crack tips, a geometrical discontinuity, are well known. When the crack is substituted by a rigid thin inclusion (also termed 'layer', 'lamella' or simply 'line'), the stresses at the pointed tip of the inclusion remain singular.

This is also the case if the thin inclusion is not rigid, but only stiffer or less stiff than the surrounding material. The thin inclusion can have membrane stiffness, bending stiffness or both. Rigid or elastic thin inclusions are of some application relevance in respect of coated or bonded members, lamella-reinforced composites and materials containing flat inclusions.

Despite a limited practical applicability of the thin inclusion models compared with crack models, a remarkable number of analytical solutions has been published (e.g. Sih 1965; Brussat and Westermann 1975; Wang et al. 1985, 1986; Chen 1986, 1991, 1992; Chen and Cheung 1987; Cheung and Chen 1989). Evaluation of these contributions shows that a sufficiently complete systematics of the basic loading modes (singular and non-singular) is not available, that the stress intensity factors are differently defined, and that the relevant limit value formulae are only partially given. The exposition below is based on a uniform redefinition of the basic models and their analytical treatment by the Kolosov–Muskhelishvili complex stress function theory (Radaj and Zhang 1993[(2)]).

The basic loading modes at rigid thin inclusion tips are defined in analogy to the basic loading modes at crack tips. The stresses and displacements in the close vicinity of these tips are described in a uniform format by stress intensity factors, angular functions and non-singular terms. The limit value formulae for the stress intensity factors are given. The flat and curved rigid thin inclusion is considered as an example of practical application.

The concept is open for extensions to wedge-shaped rigid inclusions without and with wedge tip rounding (Hasebe et al. 1990).

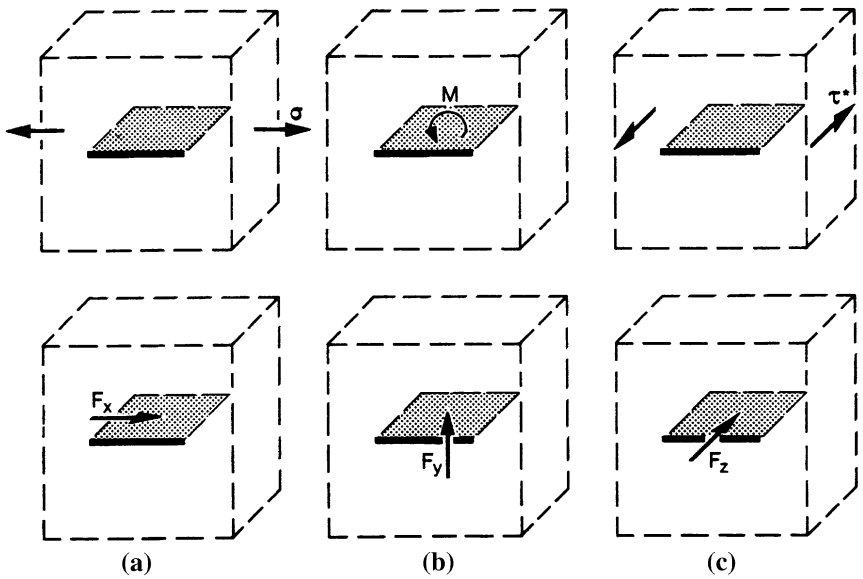

Fig. 2.97 Basic singular loading modes I*(**a**), II*(**b**) and III*(**c**) of rigid thin inclusion in infinite plate; plane and antiplane strain fields; arrows designate remote boundary stresses or resultant forces acting on the inclusion; (Radaj and Zhang 1993(2))

2.6.2 Basic Loading Modes at Rigid Thin Inclusion Tips

The basic loading modes at the tips of a rigid thin inclusion are defined in analogy to the basic loading modes at crack tips. The basic singular loading modes I*, II* and III* are shown in Fig. 2.97. A rigid thin inclusion strip permeates an infinite elastic body (or continuum). This configuration is substituted by a plate of finite thickness containing the inclusion. The multiaxiality condition with mode I* and mode II* loading is plane strain. Otherwise, out-of-plane singular effects will occur where the inclusion front line butts on the plate surface. The solutions below are also given for plane stress conditions, but this is only of academic interest. In mode III* loading, the out-of-plane deflections of the plate surfaces correspond to the condition in the out-of-plane shear loaded infinite body. Mode I* loading is characterised by longitudinal in-plane tensile (or compressive) basic stresses, mode II* loading by transverse in-plane basic shear stresses and mode III* loading by out-of-plane basic shear stresses. The basic stress state may be produced by a resultant force or moment (F_x, F_y, F_z, M), or by remote boundary stresses (σ, τ^*).

The basic non-singular loading modes 0I*, 0II* and 0III* are shown in Fig. 2.98. Mode 0I* loading is defined by triaxial tensile (or compressive) basic stresses (σ_{0x}, σ_{0y}, σ_{0z}) which suppress any displacement in the plane of the inclusion, $\varepsilon_{0x} = \varepsilon_{0z} = 0$, resulting in $\sigma_{0x} = \sigma_{0z} = \sigma_{0y}\nu/(1 - \nu)$. Mode 0II* loading is defined by in-plane basic shear stresses τ_0, which have no stress raising effect at the

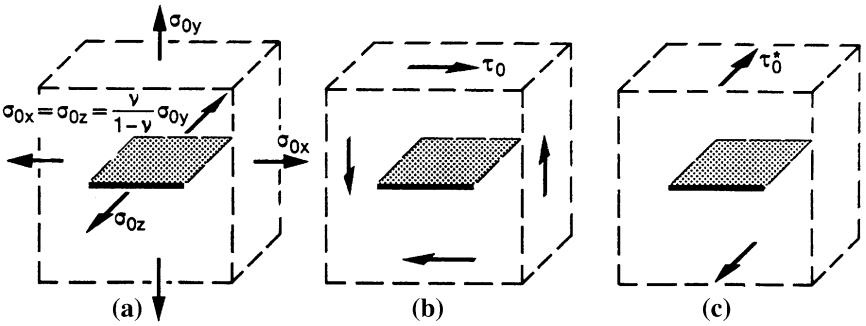

Fig. 2.98 Basic non-singular loading modes 0I*(**a**), 0II*(**b**) and 0III*(**c**) of rigid thin inclusion in infinite plate; plane and antiplane strain fields; arrows designate remote boundary stresses; (Radaj and Zhang 1993[(2)])

inclusion. The same applies to mode 0III* loading by out-of-plane basic shear stresses τ_0^*.

The analogy with the relevant crack models is obvious in respect of their number (three singular and three non-singular loading modes) and in respect of some basic characteristics, but the external or internal loading conditions are not the same.

2.6.3 Asymptotic Stress Field Close to Rigid Thin Inclusion Tips

The three basic loading modes with singular stresses at the rigid thin inclusion tip produce the following asymptotic stress distribution close to these tips. Actually, a crack with the flank sides rigidly supported is considered, Fig. 2.99:

$$\sigma_{ij} = \frac{1}{\sqrt{2\pi r}}\left[K_I^* f_{I,ij}^*(\theta) + K_{II}^* f_{II,ij}^*(\theta) + K_{III}^* f_{III,kz}^*(\theta)\right] \quad (2.289)$$
$$(i,j = x,y \text{ and } k = x,y \text{ or } i,j = r,\theta \text{ and } k = r,\theta)$$

The mode-related stress intensity factors K_I^*, K_{II}^* and K_{III}^* depend on the magnitude of the load, the length of the rigid thin inclusion and further geometrical parameters of the considered configuration. The mode-related functions $f_{I,ij}^*(\theta), f_{II,ij}^*(\theta)$ and $f_{I,ij}^*(\theta)$, describe the angular distribution of the stresses at the inclusion tip. The relationship above is strictly valid for $r \to 0$ and approximately valid for values of r which are small in relation to the inclusion length and other geometrical parameters of the configuration.

The three basic loading modes with non-singular stresses at the rigid thin inclusion tip are simply identical with the basic tensile and shear stresses in Cartesian format shown in Fig. 2.98. Their conversion into the polar coordinate system is elementary.

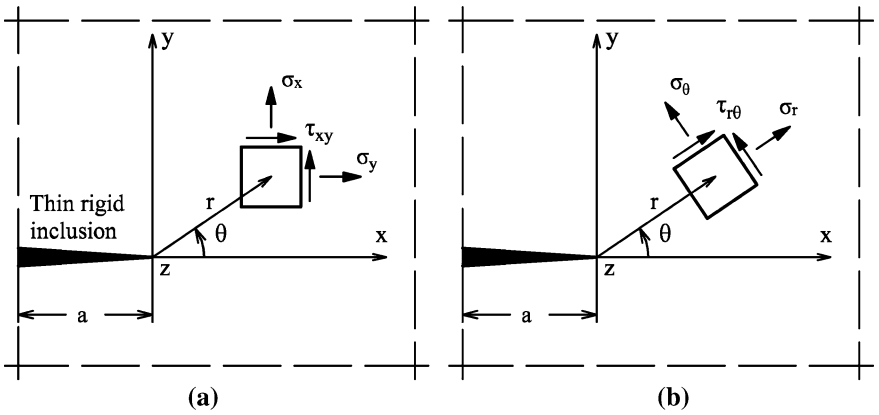

Fig. 2.99 Cartesian (**a**) and polar (**b**) coordinate system with correspondingly defined stresses at the tip of rigid thin inclusion; (Lazzarin and Tovo 1998)

The expressions for the stresses and displacements at the rigid thin inclusion tips are gained based on the Kolosov–Muskhelishvili complex stress function theory. The equations for in-plane loading (mode I* and II*) are derived from the stress functions $\varphi(\zeta)$ and $\psi(\zeta)$ for the infinite elastic plate containing a rigid elliptical inclusion (Muskhelishvili 1963, ibid. pp. 355–358). The equations for out-of-plane shear loading (mode III*) are derived from the Westergaard–type stress function $\varphi^*(z)$ for the infinite elastic plate containing a rigid thin inclusion (method according to Tada et al. 1999). Reference is also made to the author's relevant work (Radaj and Zhang 1993[(2)]).

The rigid thin inclusion of length $2a$ is considered as the geometrical limit case of a rigid elliptical inclusion with the semiaxis b reduced to zero. The function which maps the line $(-a \le x \le a)$ in the z-plane $(z = x + \mathrm{i}y)$ onto the unit circle in the ζ-plane $(\zeta = \rho \mathrm{e}^{\mathrm{i}\theta})$ reads:

$$z(\zeta) = \frac{a}{2}\left(\zeta + \frac{1}{\zeta}\right) \tag{2.290}$$

The inverse function $\zeta(z)$ is used to retransform the stress and displacement functions from the ζ-plane into the z-plane, thereby establishing bipolar coordinates in the z-plane represented by the radii r_0, r_1, r_2 and the angles θ_0, θ_1, θ_2, Fig. 2.100:

$$\zeta(z) = \frac{1}{a}(z \pm \sqrt{z^2 - a^2}) \tag{2.291}$$

Such bipolar coordinates have originally been used when solving the corresponding crack problem (Hahn 1976, ibid. pp. 77–78).

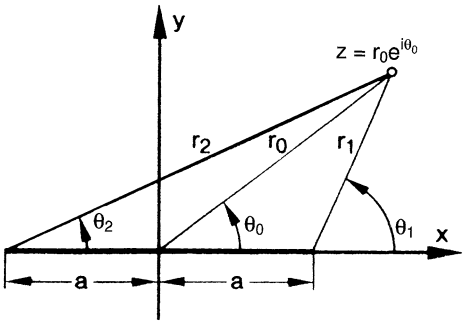

Fig. 2.100 Bipolar coordinates at rigid thin inclusion of length $2a$ in infinite plate (Radaj and Zhang 1993[2])

The stress and displacement equations for in-plane loading conditions (mode I* and II*) are valid both for plane strain ($\varepsilon_z = 0$) and plane stress ($\sigma_z = 0$) conditions, using different expressions for the parameter κ:

$$\kappa = 3 - 4\nu \quad (\varepsilon_z = 0) \tag{2.292}$$

$$\kappa = \frac{3-\nu}{1+\nu} \quad (\sigma_z = 0) \tag{2.293}$$

where $0 \leq \nu \leq 0.5$ is the Poisson's ratio, resulting in $1 \leq \kappa \leq 3$ for plane strain or $5/3 \leq \kappa \leq 3$ for plane stress. For structural steels with $\nu = 0.28$–0.30, the plane strain condition results in $\kappa = 1.8$–1.9.

The mode I* loading condition (longitudinal tension or compression) at the rigid thin inclusion is considered by the examples of remote longitudinal tension σ and of a longitudinal force F_x applied to the inclusion, Fig. 2.97a. The complete equations of the stress functions, the stresses (σ_x, σ_y, τ_{xy}) and the displacements (u, v) are reduced to the following relationships in the close vicinity of the inclusion tip ($r = r_1$, $\theta = \theta_1$, $r \ll a$), neglecting terms which are small of higher order (Radaj and Zhang 1993[2]):

$$\begin{Bmatrix} \sigma_x \\ \sigma_y \\ \tau_{xy} \end{Bmatrix} = \frac{K_\mathrm{I}^*}{\sqrt{2\pi r}} \begin{Bmatrix} \cos\theta/2\ (3+\kappa-2\sin\theta/2\ \sin 3\theta/2) \\ \cos\theta/2\ (1-\kappa+2\sin\theta/2\ \sin 3\theta/2) \\ \sin\theta/2\ (1+\kappa+2\cos\theta/2\ \cos 3\theta/2) \end{Bmatrix} \tag{2.294}$$

$$\begin{Bmatrix} u \\ v \end{Bmatrix} = \frac{K_\mathrm{I}^*}{\pi G}\sqrt{2\pi r} \begin{Bmatrix} \cos\theta/2\ (\kappa+\sin^2\theta/2) \\ -\sin\theta/2\ \cos^2\theta/2 \end{Bmatrix} \tag{2.295}$$

where G is the shear modulus which may be expressed in terms of the elastic modulus E by $G = E/2(1+\nu)$.

The stress intensity factors in the two considered loading cases are:

$$K_\mathrm{I}^* = \frac{1+\kappa}{8\kappa}\sigma\sqrt{\pi a} \tag{2.296}$$

$$K_{\mathrm{I}}^{*} = \frac{1}{2(1+\kappa)} \frac{F_x}{\sqrt{\pi a}} \tag{2.297}$$

These SIFs at the inclusion tip are smaller than the SIFs in the comparable crack loading cases ($K_{\mathrm{I}} = \sigma(\pi a)^{1/2}$, $K_{\mathrm{I}} = F_x/(\pi a)^{1/2}$). Similar definitions of the SIFs are found in the literature (Sih 1965; Wang et al. 1985).

Some further phenomena are worth to be mentioned. In the loading case of longitudinal tension σ, a constant transverse tensile stress $\sigma_{\mathrm{y}} = \sigma(\kappa - 1/\kappa)/8$ is acting on both sides of the rigid inclusion (non-reduced equations, $-a \le x \le a$), equilibrated by transverse compressive stress singularities ahead of the inclusion tips. The tensile force T_{x} in the rigid inclusion (per unit of plate thickness) is determined from τ_{xy} at $\theta = \pi$ and $\theta = -\pi$, adding up the two values and integrating them starting at the inclusion tip ($r = 0$):

$$T_x = 4(1+\kappa) K_{\mathrm{I}}^{*} \sqrt{\frac{r}{2\pi}} \quad (r \ll a) \tag{2.298}$$

The mode II* loading condition (transverse shear loading) at the rigid thin inclusion is considered by the examples of a turning moment M and of a transverse force F_y applied to the inclusion, Fig. 2.97b. The complete equations of the stress functions, the stresses (σ_x, σ_y, τ_{xy}) and the displacements (u, v) are reduced to the following relationships in the close vicinity of the inclusion tip ($r = r_1$, $\theta = \theta_1$, $r \ll a$), neglecting terms which are small of higher order (Radaj and Zhang 1993[(2)]):

$$\begin{Bmatrix} \sigma_x \\ \sigma_y \\ \tau_{xy} \end{Bmatrix} = \frac{K_{\mathrm{II}}^{*}}{\sqrt{2\pi r}} \begin{Bmatrix} \sin\theta/2\ (-3 + \kappa - 2\cos\theta/2\ \cos 3\theta/2) \\ \sin\theta/2\ (-1 - \kappa + 2\cos\theta/2\ \cos 3\theta/2) \\ \cos\theta/2\ (1 - \kappa - 2\sin\theta/2\ \sin 3\theta/2) \end{Bmatrix} \tag{2.299}$$

$$\begin{Bmatrix} u \\ v \end{Bmatrix} = \frac{K_{\mathrm{II}}^{*}}{\pi G} \sqrt{2\pi r} \begin{Bmatrix} \sin\theta/2\ \cos^2\theta/2) \\ -\cos\theta/2\ (\kappa - \sin^2\theta/2 \end{Bmatrix} \tag{2.300}$$

The stress intensity factors in the two considered loading cases are:

$$K_{\mathrm{II}}^{*} = \frac{1}{(1+\kappa)} \frac{M}{a\sqrt{\pi a}} \tag{2.301}$$

$$K_{\mathrm{II}}^{*} = \frac{1}{2(1+\kappa)} \frac{F_y}{\sqrt{\pi a}} \tag{2.302}$$

The transverse force T_y in the rigid inclusion (per unit of plate thickness) is determined from σ_y at $\theta = \pi$ and $\theta = -\pi$, adding up the two values and integrating them proceeding from the inclusion tip ($r = 0$):

$$T_y = -4(1+\kappa)K_{\mathrm{II}}^{*}\sqrt{\frac{r}{2\pi}} \quad (r \ll a) \tag{2.303}$$

The mode III* loading condition (out-of-plane shear loading) at the rigid thin inclusion is considered by the examples of remote out-of-plane shear stress $\tau^{*}$and of an out-of-plane force F_z applied to the inclusion, Fig. 2.97c. The Westergaard-type stress function $\varphi^{*}(z)$ for the two loading cases has been defined based on more general equations (Tada et al. 1973, p. 1.23). The stresses (τ_{xz}, τ_{yz}) and displacements w are derived therefrom in bipolar coordinates. The reduction to the stresses and displacements in the close vicinity of the inclusion tip is then performed (Radaj and Zhang 1993[(2)]). A solution available from the literature is based on Poisson's potential equation for the displacement function (Wang et al. 1986). The reduced equations for $r \ll a$ read:

$$\left\{ \begin{matrix} \tau_{xz} \\ \tau_{yz} \end{matrix} \right\} = \frac{K_{\mathrm{III}}^{*}}{\sqrt{2\pi r}} \left\{ \begin{matrix} \cos\theta/2 \\ \sin\theta/2 \end{matrix} \right\} \tag{2.304}$$

$$w = \frac{K_{\mathrm{III}}^{*}}{\pi G}\sqrt{2\pi r}\cos\theta/2 \tag{2.305}$$

The stress intensity factors in the two considered loading cases are:

$$K_{\mathrm{III}}^{*} = \tau^{*}\sqrt{\pi a} \tag{2.306}$$

$$K_{\mathrm{III}}^{*} = \frac{F_z}{2\sqrt{\pi a}} \tag{2.307}$$

The out-of-plane shear force T_z in the rigid inclusion (per unit of plate thickness) is determined from τ_{yz} at $\theta = \pi$ and $\theta = -\pi$, adding up the two values and integrating them proceeding from the inclusion tip ($r = 0$):

$$T_z = 4K_{\mathrm{III}}^{*}\sqrt{\frac{r}{2\pi}} \quad (r \ll a) \tag{2.308}$$

2.6.4 *Limit Value Formulae for Stress Intensity Factors at Rigid Thin Inclusion Tips*

The stress intensity factors K_{I}^{*}, K_{II}^{*}, K_{III}^{*} at rigid thin inclusion tips can be determined from any of the stress and displacement equations for mode I*, II*, III* loading in any polar plane, but the ligament plane ($\theta = 0$) is best suited for that purpose because of the characteristic stresses in that plane and because the stresses from different modes acting simultaneously can be separated here. The following limit value formulae are applicable evaluating the stresses in the ligament plane ($\theta = 0$), Eqs. (2.294), (2.299) and (2.304):

$$K_{\mathrm{I}}^{*} = \lim_{r\to 0} \frac{\sigma_x \sqrt{2\pi r}}{3+\kappa} \tag{2.309}$$

$$K_{\mathrm{II}}^{*} = \lim_{r\to 0} \frac{\tau_{xy} \sqrt{2\pi r}}{1-\kappa} \tag{2.310}$$

$$K_{\mathrm{III}}^{*} = \lim_{r\to 0} \tau_{xz} \sqrt{2\pi r} \tag{2.311}$$

Evaluation of the displacements in the ligament plane, Eqs. (2.295), (2.300) and (2.305) gives:

$$K_{\mathrm{I}}^{*} = \lim_{r\to 0} \frac{\pi G}{\kappa} \frac{u}{\sqrt{2\pi r}} \tag{2.312}$$

$$K_{\mathrm{II}}^{*} = \lim_{r\to 0} \frac{-\pi G}{\kappa} \frac{v}{\sqrt{2\pi r}} \tag{2.313}$$

$$K_{\mathrm{III}}^{*} = \lim_{r\to 0} \pi G \frac{w}{\sqrt{2\pi r}} \tag{2.314}$$

Evaluation of the forces in the inclusion Eqs. (2.298), (2.303) and (2.308), results in:

$$K_{\mathrm{I}}^{*} = \lim_{r\to 0} \frac{\pi}{2(1+\kappa)} \frac{T_x}{\sqrt{2\pi r}} \tag{2.315}$$

$$K_{\mathrm{II}}^{*} = \lim_{r\to 0} \frac{-\pi}{2(1+\kappa)} \frac{T_y}{\sqrt{2\pi r}} \tag{2.316}$$

$$K_{\mathrm{III}}^{*} = \lim_{r\to 0} \frac{\pi}{2} \frac{T_z}{\sqrt{2\pi r}} \tag{2.317}$$

Another limit value procedure for determining the stress intensity factor at the rigid inclusion tip is based on the notch stress concentration in the principal plane ($\theta = 0$) of the comparable rigid elliptical inclusion. Evaluating formulae for the loading cases of remote tension loading (mode I*), transverse shear loading (mode II*) and out-of-plane shear loading (mode III*), the following limit values for the notch radius $\rho \to 0$ are found (Radaj 1971; Radaj and Schilberth 1977; Mura 1987; Radaj and Zhang 1993[(2)]):

$$K_{\mathrm{I}}^{*} = \lim_{\rho\to 0} \frac{1}{1+\kappa} \sigma_{x\max} \sqrt{\pi\rho} \tag{2.318}$$

$$K_{\mathrm{II}}^{*} = \lim_{\rho\to 0} \frac{-1}{1+\kappa} \tau_{xy\max} \sqrt{\pi\rho} \tag{2.319}$$

$$K_{\mathrm{III}}^{*} = \lim_{\rho\to 0} \tau_{xz\max} \sqrt{\pi\rho} \tag{2.320}$$

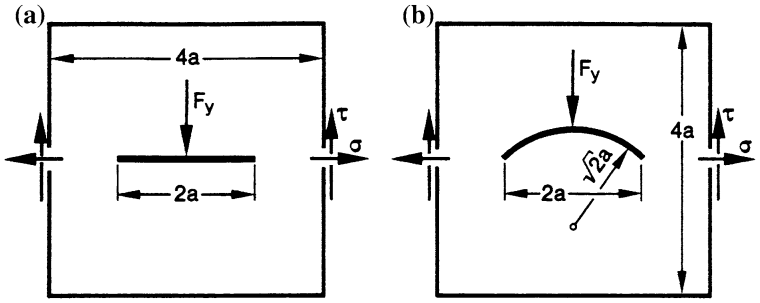

Fig. 2.101 Flat rigid thin inclusion (**a**) and curved rigid thin inclusion (**b**) in quadratic plate subjected to inclusion-parallel tensile loading (σ) or transverse shear loading (F_y, τ); (Radaj and Zhang 1993[(2)])

2.6.5 Example of Stress Intensity Factor Evaluation

The limit value formulae, Eqs. (2.309–2.317) allow to determine unknown stress intensity factors at rigid thin inclusion tips based on a FE or boundary element analysis of the stresses and displacements in the ligament plane ($\theta = 0$). As an example of application, a boundary element analysis has been performed for a flat and a curved (quarter-circular) rigid thin inclusion in a quadratic plate subjected to tensile or transverse shear loading, Fig. 2.101. The plate width is two times the crack length. The tensile stress σ has a constant value, the shear stress τ is variable according to a triangular shape, with a zero value at the corners of the quadratic plate and a maximum value in the midpoint of the loaded plate edge.

The stresses σ_x or τ_{xy} and the displacements $u = u_x$ or $v = u_y$ (with the coordinate x brought into line with the local direction of the inclusion at its tip) are determined at small distances from the inclusion tip ($r/a < 1.0$), placing the substructure boundary into the ligament plane ($\theta = 0$). These stress and displacement values are inserted into Eqs. (2.309), (2.310), (2.312) and (2.313) without the limit, resulting in $K_I^*(r)$ and $K_{II}^*(r)$, the medium values of the stress and displacement evaluation then being extrapolated to the inclusion tip applying a least square fit, Fig. 2.102. The values for the quadratic plate, K_I^* and K_{II}^*, are normalised by the values for the infinite plate, K_{I0}^* and K_{II0}^*. In the tensile loading case, K_I^* related to K_{I0}^* is slightly reduced. In the transverse shear loading case, K_{II}^* related to K_{II0}^* meets exactly the value 1.5 which results from the parabolic shear stress distribution in a comparable transverse-shear-loaded beam.

An evaluation has also been performed for the stress intensity factor ratios at flat and curved rigid thin inclusions in comparison, both in the tensile and transverse shear loading case, Table 2.8. The resultant stress intensity factor is determined according to $K^{*2} = K_I^{*2} + K_{II}^{*2}$. In the case of the curved rigid inclusion, non-singular stresses may occur at the inclusion tip which have not been evaluated.

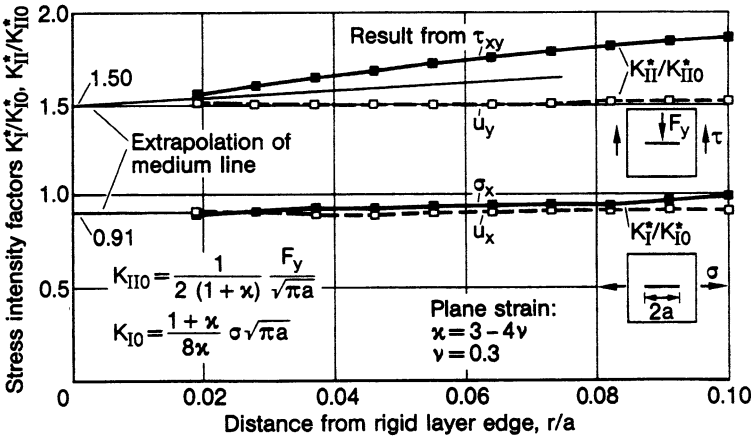

Fig. 2.102 Stress intensity factors for flat rigid thin inclusion subjected to tensile loading and transverse shear loading determined from ligament stresses (σ_x or τ_{xy}) and displacements ($u = u_x$, $v = u_y$), quadratic plate values K_I^* and K_{II}^* normalised by infinite plate values K_{I0}^* and K_{II0}^*; (Radaj and Zhang 1993[(2)])

Table 2.8 Stress intensity factor ratios for flat and curved rigid thin inclusion in quadratic plate subjected to tensile or transverse shear loading; (Radaj and Zhang 1993[(2)])

	Tensile loading			Transverse shear loading		
Inclusion type	K_I^*/K_{I0}^*	K_{II}^*/K_{I0}^*	K_{res}^*/K_{I0}^*	K_I^*/K_{II0}^*	K_{II}^*/K_{II0}^*	K_{res}^*/K_{II0}^*
Flat rigid	0.91	0.00	0.91	0.00	1.50	1.50
Curved rigid	0.58	0.77	0.96	0.75	0.93	1.19

2.6.6 Outlook to Wedge-Shaped Rigid Inclusion

Just as the SIF concept at crack tips has been extended to the NSIF concept at V-shaped notches, the SIF concept at rigid thin inclusion tips can be extended to an NSIF concept of rigid wedge-shaped inclusion tips. The crack or inclusion tips can either be pointed or rounded. A rigid wedge-shaped inclusion is identical with a V-shaped notch with its flanks rigidly fixed. This problem has early been solved for tensile and in-plane shear loading (modes 1^* and 2^*); (Hasebe et al. 1990).

The eigenvalue equations under the considered rigidly fixed notch flank condition read as follows:

$$\kappa \sin \lambda_1^* q\pi - \lambda_1^* \sin q\pi = 0 \tag{2.321}$$

$$\kappa \sin \lambda_2^* q\pi + \lambda_2^* \sin q\pi = 0 \tag{2.322}$$

Compared with the corresponding equations representing the free notch flank condition, Eqs. (2.66) and (2.67), the factor κ modifies the first term and the sign between the two terms is inverted.

The corresponding eigenvalue equation for out-of-plane loading is identical with the V-notch equation, Eq. (2.68):

$$\sin \lambda_3^*(2\pi - 2\alpha) = 0 \tag{2.323}$$

Comparing the published values of $\lambda_1^* = m_1 + 1$ and $\lambda_2^* = m_2 + 1$ for $\kappa = 2$ (Hasebe et al. 1990) with the values of λ_1 and λ_2, considering values for $2\alpha = 90°$, the degree of the singularity is diminished in tensile loading ($\lambda_1^* = 0.748$ compared with $\lambda_1 = 0.545$), but enlarged in transverse shear loading ($\lambda_2^* = 0.602$ compared with $\lambda_2 = 0.909$).

The maximum stress at the notch root in the bisector plane in the case of tensile loading and transverse shear loading, respectively, are given as a power series expansion (Hasebe et al. 1990):

$$\sigma_{r\max} = h_r \rho^{\lambda_1 - 1} + h_{r,2} \rho^{\lambda_{1,2} - 1} + h_{r,3} \rho^{\lambda_{1,3} - 1} + \ \ldots \tag{2.324}$$

$$\tau_{r\theta\max} = h_{r\theta} \rho^{\lambda_2 - 1} + h_{r\theta,2} \rho^{\lambda_{2,2} - 1} + h_{r\theta,3} \rho^{\lambda_{2,3} - 1} + \ \ldots \tag{2.325}$$

Since the series expansions in Eqs. (2.324) and (2.325) converge fast, two or three terms are sufficient in general to provide acceptable accuracy. When two or three SCFs for different values of ρ are known, e.g. by a FE analysis, then the full functional dependency is defined which is valid in the close vicinity of the inclusion tip.

Just as reference is made to the rhombic cutouts in Sect. 2.4.5 dealing with the SCFs of rounded V-notches, the corresponding rhombic inclusion problem may be addressed (Radaj and Schilberth 1977).

2.6.7 Conclusions

The SIF and NSIF concepts describing the stress, strain and displacement fields in the close vicinity of crack or notch tips can be transferred to the corresponding rigid inclusion tips. The basic singular and non-singular loading modes are defined in an analogous manner.

The asymptotic stress, strain and displacement fields close to the rigid inclusion tip are characterised by stress intensity factors linked with trigonometric function expressions. Based on these equations, limit value ($r \to 0$) formulae are derived which allow to determine the SIFs or NSIFs (not yet accomplished) from FE or boundary element analysis models. Other limit value ($\rho \to 0$) formulae relate the maximum notch stresses of comparable elliptical inclusions to the SIFs of flat thin inclusions.

A boundary element analysis of a flat and a curved rigid thin inclusion in a quadratic plate subjected to tensile or transverse shear loading is performed, demonstrating the application of the SIF concept. Finally, a wedge-shaped rigid inclusion without and with notch rounding is considered, providing an outlook to the more general NSIF concept.

In conclusion, it is shown that the rigid inclusion problems can be solved within the same analytical frame as has been developed for the open notch problems.

List of Symbols

A	Parameter relating K_{1p} to K_1
A_{11}, A_{22}, A_{33}	Coefficients in K_{eq} formula
A_k	Coefficient in K–N relationship
a	Elliptic crack depth, notch depth, crack length
a, b	Axes of ellipse
a, b, c	Coefficients in complex stress function
a_i, a_{cr}	Initiated and critical crack length
a_0	Microstructural length parameter
a_1, a_2	Parameters substituting K_1, K_2
$a_{2\tau}$, $a_{2\sigma}$	Factors in K_2 formulae
B_J, B_W	Parameters of J and $\overline{W}_p$, mode 3
b	Notch depth, semiwidth of net cross-section
C	Hardening coefficient ($C = H$)
C_1	Strain level parameter in $K_{3\rho}$
c	Elliptic crack semilength
d	Mesh width, element size
d, e, f	Coefficients in complex stress function
E, E'	Modulus of elasticity, original and substitute
e_{d1}, e_{d2}	Distortional strain energy density coefficients
F	Tensile force
$\tilde{F}$	Angle-dependent function of antiplane shear stress
F_x, F_y, F_z	Resultant forces acting on inclusion
f_T	Angle-dependent function of T-stress
f_1, f_2, f_3	Angle-dependent function of mode 1, 2, 3 stress
f_I, f_{II}, f_{III}	Angle-dependent function of mode I, II, III stress
G_{res}, G_{max}	Energy release rate, resultant and maximum value
G	Shear modulus
g_1, g_2, g_3, g_n	Coefficients in expression for σ_θ in bisector
H	Complex stress function
H, H_τ	Hardening coefficient, tensile and shear loading

h	Plate semithickness
h_1, h_2, h_3	Coefficients in expression for $\tau_{r\theta}$ in bisector
h_r, $h_{r\theta}$	Leading term factors of $\sigma_{r\ \max}$ and $\tau_{r\theta\ \max}$ at rigid wedge
I, I_e, I_p	Integral in HRR field equation, total, elastic, plastic
J	J-integral
J_2, J_K, J_T	J-integrals for kinking crack
$J_{3\mathrm{p}}$	J-integral related to $K_{3\mathrm{p}}$
J_I, J_II, J_III	J-integral, mode I, II, III
J_V, J_L	J-integrals of V-notches
K_t	Theoretical stress concentration factor
K_σ, K_ε	Stress and strain concentration factor, nonlinear
K_τ, K_γ	Shear stress and strain concentration factor, nonlinear
$K_{\mathrm{W,e}}$, $K_{\mathrm{W,p}}$	Strain energy concentration factor, elastic, plastic
K_I, K_II, K_III	Stress intensity factor, mode I, II, III
K_Ic, $K_\mathrm{I,c}$	Fracture toughness, critical stress intensity factor
K_I^*, K_II^*, K_III^*	Stress intensity factor, mode I*, II*, III*, rigid inclusion
K_I0^*, K_II0^*	Reference values of K_I^*, K_II^* in infinite plate
K_res, K_eq	Resultant and equivalent stress intensity factor
K_th	Threshold stress intensity factor
K_0, K_0^*	Threshold stress intensity factor, coplanar and kinking crack
K_1cr	Critical notch stress intensity factor
K_l, K_2, K_3	Notch stress intensity factor, mode 1, 2, 3
$K_{\mathrm{l}\rho}$, $K_{2\rho}$, $K_{3\rho}$	Generalised notch stress intensity factor, mode 1, 2, 3
$K_{1\rho}^*$	Generalised NSIF, T-stress-corrected
$K_{3\rho,\mathrm{e}}^{(\gamma)}$, $K_{3\rho,\mathrm{p}}^{(\gamma)}$	Notch strain intensity factor, mode 3, elastic, plastic
$\overline{K}_{\mathrm{i}\rho}$	Average NSIF, mode i = 1, 2, 3
K_O	Stress intensity factor, transverse singular mode O
$K_{2,\mathrm{n}}$	Nominal NSIF, mode 2
k	Inverse slope exponent, S–N curve
k_1, k_2, k_3	Geometry coefficients on K_1, K_2, K_3
k_1, k_{10}	Factors in $K_{1\rho}$ formula
M	Turning moment acting on the inclusion
M_t	Torsional moment
M_km, M_kb	Magnification factor on K_I, membrane, bending
m	Elastic-plastic antiplane shear exponent
N, N_E, N_C	Number of cycles, endurable values
n	Hardening exponent
P_f	Failure probability
q	Factor on $\pi/2$ for notch internal angle
R	Ratio of lower to upper load
R, R_0	Radius of integration path, of control volume

R_g, R_n	Radius of gross and net cross-section
R_p	Radius of plastic zone
r	Polar coordinate, radial distance
r^*	Radius of core region
r_0	Notch root distance
r_0, r_1, r_2	Radial distances in bipolar coordinate system
r_2	V-notch radius at rhombic cut-out
r_p	Radius of plastic zone
S	S-stress, non-singular
S_{min}, S_{max}	Strain energy density factors
s	Elastic-plastic eigenvalue exponent
s_{ij}	Deviatoric stress tensor
$s_{\gamma,p}$	Elastic-plastic strain eigenvalue exponent
T	T-stress, non-singular
T_x, T_y, T_z	Forces acting on rigid inclusion
T_σ, T_N	Scatter range indices related to σ and N
t, t_u, t_l	Plate thickness, upper and lower
u, v, w	Displacements in Cartesian coordinates
u_0, v_0	Remote boundary displacements
u_x, u_y, u_z	Displacements in Cartesian coordinates
u_i, $\tilde{u}_i$	Displacement vector, its angle-dependent term
W, W_e, W_p	Strain energy density, total, elastic, plastic
$\overline{W}$, $\overline{W}_e$, $\overline{W}_p$	Locally averaged strain energy densities
$W_{n,n}$	Strain energy density of nominal stress in net cross-section
w	Complex coordinate
x, y, z	Cartesian coordinates
x_p	Extension of plastic zone
Y_1, Y_2, Y_3	Geometry factors on K_I, K_{II}, K_{III}
Y_m, Y_b	Geometry factors on K_I, membrane, bending
z	Complex coordinate
z	Elastic-plastic eigenvalue exponent
α	Factor in normalised Ramberg–Osgood material law
α, α_{02}	Notch opening semi-angle
β	Angle of inclination against bar axis
β	Notch angle dependent parameter in Neuber rule for V-notch
γ	Internal semi-angle of V-notch
γ, γ_e, γ_p	Total, elastic and plastic shear strain
γ_0	Substitute or reference yield shear strain
$\gamma_{max,p}$	Maximal notch shear strain, nonlinear
$\gamma_{p,eq}$	Equivalent plastic shear strain
γ_Y	Yield limit shear strain, marked and offset
Δ	Relative deviation
δ	Thickness ratio

δ	Factor in reduced Ramberg–Osgood material law
δ_{ij}	Kronecker delta
ε, ε_e, ε_p	Total, elastic and plastic strain
ε_{ij}, $\tilde{\varepsilon}_{ij}$	Strain tensor, its angle-dependent term
ε_k, ε_{kH}	Maximum notch strain, nonlinear and Hooke
ε_n, ε_{nH}	Nominal strain, nonlinear and Hooke
$\varepsilon_{p,\,eq}$	Equivalent plastic strain
ε_0	Substitute or reference yield strain
ε_Y, $\varepsilon_{Y0.2}$	Yield limit strain, marked and 0.2 % offset
ζ	Complex coordinate
η	Factor on ρ for averaging $K_{i\rho}$
θ, $\bar{\theta}$	Polar angle, crack propagation angle
θ_0, θ_1, θ_2	Polar angles in bipolar coordinate system
κ	Stiffness parameter in plate theory
κ	In-plane multiaxiality parameter
λ_1, λ_2, λ_3	Eigenvalues at V-notch, mode 1, 2, 3
λ_1^*, λ_2^*, λ_3^*	Eigenvalues at rigid wedge, mode 1^*, 2^*, 3^*
λ_a, λ_s	Eigenvalues, antimetric and symmetric, antiplane shear
λ_O	Eigenvalue of transverse singular mode
μ	Exponent in complex stress function
ν	Poisson's ratio
ρ	Radius of notch curvature, notch radius
ρ^*	Microstructural support length
σ, σ_0, $\sigma_{x\infty}$	Remote tensile stress
σ_0	Substitute or reference yield stress
σ_0^*	Normal stress parallel to crack front
σ_{0x}, σ_{0y}, σ_{0z}	Remote boundary stresses, mode $0I^*$ loading
σ_1	First principal stress
σ_{cb}, σ_{tb}	Counter-bending and tensile-bending stress
σ_E, $\overline{\sigma}_E$	Endurance limit stress, original and averaged
σ_e, σ_{eq}	Effective and equivalent stress, von Mises
$\tilde{\sigma}_e$	Angle-dependent term of σ_e
σ_h	Hydrostatic stress
σ_{ij}, $\tilde{\sigma}_{ij}$	Stress tensor, its angle-dependent term
σ_k, σ_{kH}	Maximum notch stress, nonlinear and Hooke
σ_m, σ_b	Membrane and bending stress
σ_{max}, $\sigma_{\theta\,max}$	Maximum notch stress
σ_n, $\sigma_{n,g}$, $\sigma_{n,n}$	Nominal stress, in gross and net cross-section
σ_{n1}, σ_{n2}	Endurable nominal stress
σ_{nE}	Endurance limit nominal stress
σ_p	Peak stress
σ_r, σ_θ	Normal stresses in polar coordinates
σ_t, $\sigma_{t\,max}$	Tangential stress, its maximum value

σ_{th}	Threshold stress of crack propagation
σ_u, σ_l	Stress in upper and lower plate
σ_x, σ_y, σ_z	Normal stresses in Cartesian coordinates
σ_Y, $\sigma_{Y0.2}$	Yield limit, marked and 0.2 % offset
σ_I, σ_{II}, τ_{III}	Stresses related to mode I, II, III
$\sigma_\parallel$	Slit-parallel stress
τ	Resultant shear stress, antiplane
τ_0	Substitute or reference yield shear stress
τ_0, τ_0^*	Remote shear stress, in-plane and out-of-plane
τ_1	Principal shear stress
τ_E, $\bar{\tau}_E$	Endurance limit shear stress, original and averaged
τ_{eq}	Equivalent or resultant shear stress
τ_{max}, τ_{max}^*	Maximum notch shear stress, in-plane and out-of-plane
$\tau_{max,p}$	Maximum notch shear stress, nonlinear or plastic
τ_n, τ_n^*	Nominal shear stress, in-plane and out-of-plane
$\tau_{n,g}$, $\tau_{n,n}$	Nominal shear stress, gross and net cross-section
$\tau_{n,g}^*$	Nominal torsional stress, gross cross-section
$\tau_{r\theta}$	Shear stress in polar coordinates
τ_{rz}, $\tau_{\theta z}$	Out-of-plane shear stresses
τ_Y	Shear yield limit, marked or offset
$\tau_\perp$, $\tau_\parallel$	Shear stresses, transverse and longitudinal to edge
Φ	Elliptical integral, stress resultant function
φ, φ^*	Complex stress function
χ	Trigonometric eigenvalue coefficient
ψ	Complex stress or harmonic displacement function
ω, ω_1	Notch angle dependent parameter in $K_{3\rho}$
$\tilde{\omega}_1$, $\tilde{\omega}_2$	Auxiliary parameter in $K_{1\rho}$, $K_{2\rho}$
FE	Finite element
FEM	Finite element method
HRR	Hutchinson–Rice–Rosengren
NSIF	Notch stress intensity factor
SCF	Stress concentration factor
SIF	Stress intensity factor

References

Akin JE (1976) The generation of elements with singularities. Int J Numer Meth Engng 10:1249–1259

Anderson TL ([2]1995) Fracture mechanics – Fundamentals and applications. CRC-Press, Boca Raton Fla

Atzori B (1985) Fracture mechanics or notch effect for fatigue design (in Italian). In: Proc 13th AIAS Conf, Bergamo, pp 294–307

Atzori B, Meneghetti G (2001) Fatigue strength of fillet welded structural steels – finite elements, strain gauges and reality. Int J Fatigue 23:713–721
Atzori B, Lazzarin P, Tovo R (1997) Stress distribution for V-shaped notches under tensile and bending loads. Fatigue Fract Engng Mater Struct 20:1083–1092
Atzori B, Lazzarin P, Tovo R (1999(1)) From a local stress approach to fracture mechanics: a comprehensive evaluation of the fatigue strength of welded joints. Fatigue Fract Engng Mater Struct 22:369–381
Atzori B, Lazzarin P, Tovo R (1999(2)) Stress field parameters to predict the fatigue strength of notched components. J Strain Analysis 34:437–453
Atzori B, Lazzarin P, Filippi S (2001) Crack and notches: analogies and differences of the relevant stress distributions and practical consequences in fatigue limit predictions. Int J Fatigue 23:355–362
Ayatollahi MR, Dehghany M (2010) On *T*-stresses and V-notches. Int J Fract 165:1–126
Ayatollahi MR, Nejati M (2011) Determination of NSIFs and coefficients of higher order terms for sharp notches using finite element method. Int J Mech Sciences 53:64–177
Benthem JP (1977) State of stress at the vertex of a quarter-infinite plate in a half space. Int J Solids Struct 13:479–492
Benthem JP (1987) Stresses in the region of rounded corners. Int J Solids Struct 23:239–252
Berto F, Lazzarin P (2010) On higher order terms in the crack tip stress field. Int J Fract 161:221–226
Berto F, Lazzarin P, Kotousov A, Harding S (2011) Out-of-plane singular stress fields in V-notched plates and welded lap joints induced by in-plane shear load conditions. Fatigue Fract Engng Mater Struct 34:291–304
Bogy DB (1971) Two edge-bonded elastic wedges of different materials and wedge angles under surface tractions. J Appl Mech 38:377–386
Boukharouba T, Tamine T, Nui L, Chehimi C, Pluvinage G (1995) The use of notch intensity factor as a fatigue crack initiation parameter. Engng Fract Mech 52:503–512
Brussat TB, Westermann RA (1975) A Westergaard-type stress function for line inclusion problems. Int J Solids Struct 11:665–667
Carpenter WC (1984) Calculation of fracture mechanics parameters for a general corner. Int J Fract 24:45–58
Chakrabarty J (^{3}2006) Theory of plasticity. Oxford, Elsevier
Chen DH (1995) Stress intensity factors for V-notched strip under tension or in-plane bending. Int J Fract 70:81–97
Chen DH, Ushijima K (2000) Elastic-plastic stress singularity near the tip of V-notch. Int J Fract 106:117–134
Chen YZ (1986) Singular behaviour at fixed line tip in plane elasticity. Engng Fract Mech 25:11–16
Chen YZ (1991) Investigation of stress singularity coefficient for a finite plate containing rigid line. Engng Fract Mech 40:17–24
Chen YZ (1992) Evaluation of stress singularity coefficient from the solution of the notch problem. Comput Struct 42:563–567
Chen YZ, Cheung YK (1987) Stress singularity coefficients in an infinite plate containing rigid line and applied by concentrated forces. Engng Fract Mech 26:729–739
Cheng YZ (1988) Evaluation of K_2 values from the solution of notch problem. Int J Fract 38:R61–R64
Cheung YK, Chen YZ (1989) Multiple rigid line problems in an infinite plate. Engng Fract Mech 34:379–391
Cottrell B, Rice JR (1980) Slightly curved or kinked cracks. Int J Fract 16:155–169
Creager M, Paris PC (1967) Elastic field equations for blunt cracks with reference to stress corrosion cracking. Int J Fract Mech 3:247–252
Dini D, Hills DA (2004) Asymptotic characterisation of nearly sharp notch root stress fields. Int J Fatigue 130:651–666.

Dowling NE (1993) Mechanical behaviour of materials. Prentice Hall, New Jersey
Dunn ML, Suwito W, Cunningham S (1997(1)) Stress intensities at notch singularities. Engng Fract Mech 57:417–430
Dunn ML, Suwito W, Cunningham S (1997(2)) Fracture initiation at sharp notches: correlation using critical stress intensities. Int J Solid Struct 34:3873–3883
El Haddad MH, Topper TH, Smith KN (1979) Prediction of non-propagating cracks. Engng Fract Mech 11:573–584
Elber W (1970) Fatigue crack closure under cyclic tension. Engng Fract Mech 2:37–45
Elber W (1971) The significance of fatigue crack closure. ASTM STP 486, Philadelphia Pa, pp 230–242
Erdogan F, Sih GC (1963) On the crack extension in plates under plane loading and transverse shear. J Basic Engng 85:519–527
Eurocode 3 (2005) Design of steel structures, Part 1-9, Fatigue, EN 1993-1-9, Brussels, CEN
Filippi S, Lazzarin P (2004) Distributions of the elastic principal stress due to notches in finite size plates and rounded bars uniaxially loaded. Int J Fatigue 26:377–391
Filippi S, Ciavarella M, Lazzarin P (2002(1)) An approximate, analytical approach to the 'HRR'-solution for sharp V-notches. Int J Fract 117:269–286
Filippi S, Lazzarin P, Tovo R (2002(2)) Developments of some explicit formulas useful to describe elastic stress fields ahead of notches in plates. Int J Solids Struct 39:4543–4565
Gdoutos EE (1990) Fracture mechanics criteria and applications. Kluwer Acad Publ, Dordrecht
Glinka G (1985) Energy density approach to calculation of inelastic strain–stress near notches and cracks. Engng Fract Mech 22:485–508
Glinka G, Molski K (1981) A method of elastic-plastic stress and strain calculation at a notch root. Mater Sci Engng 50:93–100
Glinka G, Newport A (1987) Universal features of elastic notch tip stress fields. Int J Fatigue 9:143–150
Gough HJ (1950) Engineering steels under combined cyclic and static stresses. J Appl Mech 50:113–125
Gough HJ, Pollard HV (1935) The strength of metals under combined alternating stresses. In: Proc Inst Mech Eng 131:3–103
Gough HJ, Pollard HV (1937) Properties of some materials for cast crankshafts with special reference to combined stresses. In: Proc Inst Automob Eng 31:821
Gross R, Mendelson A (1972) Plane elastostatic analysis of V-notched plates. Int J Fract Mech 8:267–276
Gross D, Seelig T (32001) Bruchmechanik. Springer Verlag, Berlin
Haefele PM, Lee JD (1995) The constant stress term. Engng Fract Mech 50:869–882
Hahn HG (1976) Bruchmechanik. Teubner, Stuttgart
Harding S, Kotousov A, Lazzarin P, Berto F (2010) Transverse singular effects in V-shaped notches stressed in mode II. Int J Fract 164:1–14
Hasebe N, Kutanda Y (1978) Calculation of stress intensity factors from stress concentration factors. Engng Fract Mech 10:215–221
Hasebe N, Nakamura T, Iida J (1990) Notch mechanics for plane and thin-plate bending problems. Engng Fract Mech 37:87–99
Hein VL, Erdogan F (1971) Stress singularities in a two-material wedge. Int J Fract Mech 7:317–330
Hencky H (1924) Zur Theorie plastischer Deformationen und der hierdurch im Material hervorgerufenen Nachspannungen. Z Angew Math Mech 4:323–334
Hilton PD (1973) Plastic intensity factors for cracked plates subjected to biaxial loading. Int J Fract 9:149–156
Hilton PD, Hutchinson JW (1971) Plastic intensity factors for cracked plates. Engng Fract Mech 3:435–451
Hobbacher A (ed) (2009) Fatigue design of welded joints and components. IIW-Doc XIII-2151-07/XV-1254-07. Welding Research Council, Bulletin 520, New York

Hui CY, Ruina A (1995) Why *K*? Higher order singularities and small-scale yielding. Int J Fract 72:97–120
Hult JA, McClintock FA (1956) Elastic-plastic stress and strain distribution around sharp notches under repeated shear. In: 9th Int Congress Appl Mech, 8, Brussels
Hussain MA, Pu SL, Underwood J (1974) Strain energy release rate for a crack under combined mode I and mode II. In: Fracture analysis, ASTM STP 560, Philadelphia Pa, pp 2–28
Hutchinson JW (1968) Singular behaviour at the end of a tensile crack tip in a hardening material. J Mech Phys Solids 16:13–31
Irwin GR (1957) Analysis of stresses and strains near the end of a crack traversing a plate. J Appl Mech 24:361–364
Irwin GR (1958) Fracture. In: Handbuch der Physik, Vol 4, pp 551–590. Springer, Berlin
Kane TR, Mindlin RD (1956) High frequency extensional vibrations of plates. J Appl Mech 23:277–283
Kirsch G (1898) Die Theorie der Elasitzität und die Bedürfnisse der Festigkeitslehre. Z VDI 42:797–807
Koibuchi K, To K, Iida M, Hosomi T (1999) Fatigue strength assessment of welded toes and defects of structures based on cyclic plastic zone size. In: Engng Against Fatigue. Rotterdam, Balkema, pp 373–380
Kotousov A (2005) On stress singularities at angular corners of plates of arbitrary thickness under tension. Int J Fract 132:L29–L36
Kotousov A (2007) Fracture in plates of finite thickness. Int J Solids Struct 44:8259–8273
Kotousov A, Lew YT (2006) Stress singularities resulting from various boundary conditions in angular corners of plates of arbitrary thickness in extension. Int J Solids Struct 43:5100–5109
Kotousov A, Wang CH (2002) Three-dimensional solutions for transversally isotropic composite plates with a notch. Compos Struct 57:443–450
Kuang ZB, Xu XP (1987) Stress and strain fields at the tip of a V-notch in a power law hardening material. Int J Fract 35:39–53
Kullmer G (1992) Elastic stress fields in the vicinity of a narrow notch with circular root. In: Proc Eur Conf on Reliability and Structural Integrity of Advanced Materials, ECF9, pp 905–910
Kurath P (1992) Multiaxiality fatigue criteria for spot welds. SAE Techn Paper 920668, SAE. Warrendale Pa
Larsson SG, Carlsson AJ (1973) Influence of non-singular stress terms and specimen geometry on small-scale yielding at crack tips in elastic-plastic materials. J Mech Phys Solids 21:263–277
Lazzarin P (1986) Influence of welded joint geometry on stress fields in the highly stressed zones (in Italian). Riv Ital Saldatura 2:107–115
Lazzarin P, Filippi S (2006) A generalized stress intensity factor to be applied to rounded V-shaped notches. Int J Solids Struct 43:2461–2478
Lazzarin P, Livieri P (2000) Plastic zone size at the weld toe in welded joints made of steel and light metals (in Italian). Rev Ital Della Saldatura 52:421–437
Lazzarin P, Livieri P (2001) Notch stress intensity factors and fatigue strength of aluminium and steel welded joints. Int J Fatigue 23:225–232
Lazzarin P, Tovo R (1996) A unified approach to the evaluation of linear-elastic stress fields in the neighbourhood of cracks and notches. Int J Fract 78:3–19
Lazzarin P, Tovo R (1998) A notch stress intensity factor approach to the stress analysis of welds. Fatigue Fract Engng Mater Struct 21:1089–1103
Lazzarin P, Zambardi R (2002) The equivalent strain energy density approach reformulated and applied to sharp V-shaped notches under localized and generalized plasticity. Fatigue Fract Engng Mater Struct 25:917–928
Lazzarin P, Zappalorto M (2008) Plastic notch stress intensity factors for pointed V-notches under antiplane shear loading. Int J Fract 152:1–25
Lazzarin P, Tovo R, Meneghetti G (1997) Fatigue crack initiation and propagation phases near notches in metals with low notch sensitivity. Int J Fatigue 19:647–657
Lazzarin P, Tovo R, Filippi S (1998) Elastic stress distributions in finite size plates with edge notches. Int J Fract 91:269–282

Lazzarin P, Zambardi R, Livieri P (2001) Plastic notch stress intensity factors for large V-shaped notches under mixed mode load conditions. Int J Fract 107:361–377

Lazzarin P, Livieri P, Zambardi R (2002) A *J*-integral based approach to predict the fatigue strength of components weakened by sharp V-shaped notches. Int J Comp Appl Techn 15:202–210

Lazzarin P, Sonsino CM, Zambardi R (2004) A notch stress intensity approach to assess the multiaxial fatigue strength of welded tube-to-flange joints subjected to combined loadings. Fatigue Fract Engng Mater Struct 27:127–140

Lazzarin P, Berto F, Radaj D (2006) Uniform fatigue strength of butt and fillet welded joints in terms of local strain energy density. In: Proc 9th Int Fatigue Congress. Oxford, Elsevier Science, pp 1–10

Lazzarin P, Zappalorto M, Yates JR (2007) Analytical study of stress distributions due to semi-elliptic notches in shafts under torsion loading. Int J Engng Sci 45:308–328

Lazzarin P, Berto F, Radaj D (2009) Fatigue-relevant stress field parameters of welded lap joints – Pointed slit tip compared with keyhole notch. Fatigue Fract Engng Mat Struct 32:713–735

Lazzarin P, Zappalorto M, Berto F (2011) Generalized stress intensity factors for rounded notches in plates under in-plane shear loading. Int J Fract 170:123–144

Lee H, Kim N (2004) Fatigue life prediction of multi-spot welded panel structures using an equivalent stress intensity factor. Int J Fatigue 26:403–412

Lin KY, Tong P (1980) Singular finite elements for the fracture analysis of V-notched plate. Int J Numer Meth Engng 15:1343–1354

Linder J, Melander A, Larsson M, Bergengren Y (1998) Fatigue design of spot-welded austenitic and duplex stainless sheet steels. Fatigue Fract Engng Mater Struct 21:673–686

Livieri P, Tovo R (2009) The use of the J_V parameter in welded joints – Stress analysis and fatigue assessment. Int J Fatigue 31:153–163

Meneghetti G, Lazzarin P (2007) Significance of the elastic peak stress evaluated by FE analyses at the point of singularity of sharp V-notched components. Fatigue Fract Engng Mater Struct 30:95–106

Mizui M, Sekine T, Tsujimura A, Takishima T, Shimazaki Y (1988) An evaluation of fatigue strength for various kinds of spot-welded specimens. SAE Techn Paper 880375, SAE, Warrendale Pa

Mura T (1987) Micromechanics of defects in solids. Nijhoff, Dordrecht

Murakami Y (ed) (1987) Stress intensity factors handbook. Pergamon Press, Oxford

Mushkelishvili NI (1963) Some basic problems of the mathematical theory of elasticity. Noordhoff, Groningen.

Nakamura T, Parks DM (1989) Antisymmetrical 3d stress field near the crack front of a thin elastic plate. Int J Solids Struct 25:1411–1426

Neuber H ([2]1958, [3]1985) Kerbspannungslehre. Springer Verlag, Berlin

Neuber H (1961) Theory of stress concentration for shear-strained prismatical bodies with arbitrary nonlinear stress–strain law. J Appl Mech 28:544–550

Neuber H (1968[(1)]) A physically nonlinear notch and crack model. J Mech Phys Solids 16:289–294

Neuber H (1968[(2)]) Über die Berücksichtigung der Spannungskonzentration bei Festigkeitsberechnungen. Konstruktion 20:245–251

Noda NA, Nisitani H, Harada S, Takase Y (1995) Fatigue strength of notched specimens having nearly equal sizes of ferrite. Int J Fatigue 17:237–244

Noda NA, Oda K, Inoue T (1996) Analysis of newly defined stress intensity factors for angular corners using singular integral equations of the body force method. Int J Fract 76:243–261

Noda NA, Takase Y (2003) Generalised stress intensity factors for V-shaped notch in a round bar under torsion, tension and bending. Engng Fract Mech 70:1447–1466

Nui LS, Chehimi C, Pluvinage G (1994) Stress field near a large blunted tip V-notch and application of the concept of the critical notch stress intensity factor (NSIF) to the fracture toughness of very brittle materials. Engng Fract Mech 49: 235–335

Pook LP (1989) The significance of mode I branch cracks for mixed mode fatigue crack growth threshold behaviour. In: Brown MW, Miller KJ (eds) Biaxial and multiaxial fatigue. Mech Engng Publ, London, pp 247–263
Quian J, Hasebe N (1997) Property of eigenvalues and eigenfunctions for an interface V-notch in antiplane elasticity. Engng Fract Mech 56:729–734
Radaj D (1971) Kerbspannungen an Öffnungen und starren Kernen. Habilitation thesis, TU Braunschweig, self-publishing
Radaj D (1989) Stress singularity, notch stress and structural stress at spot-welded joints. Engng Fract Mech 34:495–506
Radaj D (2010) *T*-stress corrected notch stress intensity factors with application to welded lap joints. Fatigue Fract Engng Mater Struct 33:378–389
Radaj D, Giering A (1994) Spot-welded H-specimen – The local stress parameters. Materialprüf 36:275–281
Radaj D, Giering A (1995) Spot-welded double-cup specimen – The local stress parameters. Materialprüf 37:458–462; emendation 39:430
Radaj D, Heib M (1978) Energy density fracture criteria for cracks under mixed-mode loading. Materialprüf 20:256–262
Radaj D, Schilberth G (1977) Kerbspannungen an Ausschnitten und Einschlüssen. DVS-Verlag, Düsseldorf
Radaj D, Vormwald M (^{3}2007) Ermüdungsfestigkeit – Grundlagen für Ingenieure. Springer Verlag, Berlin
Radaj D, Zhang S (1991$^{(1)}$) Stress intensity factors for spot welds between plates of unequal thickness. Engng Fract Mech 39:391–413
Radaj D, Zhang S (1991$^{(2)}$) Simplified formulae for stress intensity factors of spot welds. Engng Fract Mech 40:233–236
Radaj D, Zhang S (1992) Stress intensity factors for spot welds between plates of dissimilar materials. Engng Fract Mech 42:407–426
Radaj D, Zhang S (1993$^{(1)}$) Analogies between crack tip and rigid line tip stresses and displacements. Engng Fract Mech 44:913–919
Radaj D, Zhang S (1993$^{(2)}$) Loading modes and stress intensity factors at rigid layer edges. Engng Fract Mech 46:199–208
Radaj D, Zhang S (1993$^{(3)}$) On the relations between notch stress and crack stress intensity in plane shear and mixed-mode loading. Engng Fract Mech 44:691–704
Radaj D, Zhang S (1994). Stress distribution at bimaterial crack tips. Engng Fract Mech 47:613–617
Radaj D, Zhang S (1995$^{(1)}$). Process zone fracture criteria for crack tips. Engng Fract Mech 50:111–120
Radaj D, Zhang S (1995$^{(2)}$) Punktgeschweißte Doppelhutprofilprobe unter Torsionsbelastung – lokale Beanspruchungsparameter und Schwingfestigkeit. Materialprüf 37:458–462; emendation 39:426
Radaj D, Zheng Z, Möhrmann W (1990) Local stress parameters at the weld spot of various specimens. Engng Fract Mech 37:933–951
Radaj D, Lehrke HP, Greuling S (2001) Theoretical fatigue-effective notch stresses at spot welds. Fatigue Fract Engng Mater Struct 24:293–308
Radaj D, Sonsino CM, Fricke W (^{2}2006) Fatigue assessment of welded joints by local approaches. Woodhead Publ, Cambridge and CRC Press, Boca Raton Fla
Radaj D, Berto F, Lazzarin P (2009) Local fatigue strength parameters for welded joints based on strain energy density with inclusion of small-size notches. Engng Fract Mech 76:1109–1130
Rice JR (1967) Stresses due to a sharp notch in a work-hardening elastic-plastic material loaded by longitudinal shear. J Appl Mech 34:287–298
Rice JR (1968) A path-independent integral and the approximate analysis of strain concentration by notches and cracks. J Appl Mech 35:379–386
Rice JR, Rosengren GF (1968) Plane strain deformation near a crack tip in a power-law hardening material. J Mech Phys Solids 16:1–12

Rooke DP, Cartwright DJ (1976) Compendium of stress intensity factors. Her Majesty's Stationary Office, London
Sanford RJ (2003) Principles of fracture mechanics. Pearson Education, Upper Saddle River, NJ
Sator C (2010) Asymptotische Nahfeldanalyse ebener Multi-Materialverbindungsstellen mit der Methode der komplexen Potentiale. TU Darmstadt, Forschungsbericht Mechanik, Bd. 21
Savruk MP, Kazberuk A (2006) Relationship between the stress intensity and stress concentration factors for sharp and rounded notches. Mater Sci 42:725–738
Savruk MP, Kazberuk A (2007) A unified approach to problems of stress concentration near V-shaped notches with sharp and rounded tip. Int J Appl Mech 43:182–197
Savruk MP, Kazberuk A (2010) Two-dimenstional fracture mechanics problems for solids with sharp and rounded V-notches. Int J Fract 161:79–95
Seeger T, Greuling S, Brüning J, Leis P, Radaj D, Sonsino CM (2005) Bewertung lokaler Berechnungskonzepte zur Ermüdungsfestigkeit von Punktschweißverbindungen. FAT-Schriftenreihe 196, Frankfurt
Seweryn A (2002) Modeling of singular stress fields using the finite element method. Int J Solids Struct 39:4787–4804
Seweryn A, Molski K (1996) Elastic stress singularities and corresponding generalised stress intensity factors for angular corners under various boundary conditions. Engng Fract Mech 55:529–556
Seweryn A, Mróz Z (1995) A non-local stress failure condition for structural elements under multiaxial loading. Engng Fract Mech 51:855–973
Seweryn A, Zwolinski J (1993) Solution for the stress and displacement fields in the vicinity of a V-notch of negative wedge angles in plane problems of elasticity. Engng Fract Mech 44:275–281
Sherry AH, France CC, Goldthorpe MR (1995) Compendium of *T*-stress solutions for two- and three-dimensional cracked geometries. Fatigue Fract Engng Mater Struct 18:141–155
Shlyannikov VN, Boychenko NV, Tartygasheva AM (2011) In-plane and out-of-plane crack tip constraint effects under biaxial nonlinear deformation. Engng Fract Mech 78:1771–1783
Sih GC (1965) Plane extension of rigidly embedded line inclusions. In: Huang TC, Johnson MW (eds) Developments in mechanics, vol 3. John Wiley, London, pp 61–79
Sih GC (1973) Handbook of stress intensity factors. Lehigh Univ, Bethlehem Pa
Sih GC (1974) Strain energy density factor applied to mixed-mode crack problems. Int J Fract 10:305–321
Sih GC (1975) A three-dimensional strain energy density factor theory of crack propagation. In: Three-dimensional crack problems. Leyden, Noordhoff, pp 15–80
Sih GC, Liebowitz H (1968) Mathematical theories of brittle fracture. In: Fracture, vol. 2, Mathematical fundamentals. Academic Press
Smith E (2004) The elastic stress distribution near the root of an elliptically cylindrical notch subjected to mode III loadings. Int J Engng Sci 42:1831–1839
Smith E (2006) The mode III elastic stress distribution near the root of an intrusion-type notch and of a keyhole notch. Int J Engng Sci 44:340–344
Sneddon IN (1946) The distribution of stress in the neighbourhood of a crack in an elastic solid. Proc Roy Soc, Ser A 187:229–260
Susmel L, Tovo R (2004) Multiaxial fatigue life prediction of two welded details subjected to local complex stress states. In: Proc 7th Int Conf on Biaxial/Multiaxial Fatigue and Fracture. Berlin, DVM, pp 447–452
Tada HP, Paris C, Irwin GR (1973) The stress analysis of cracks handbook. Del Res Corp, Hellertown Pa
Tada HP, Paris C, Irwin GR (^{3}1999) The stress analysis of cracks handbook. ASME Press, New York
Tanaka K, Okajima H, Koibuchi K (2002) Fatigue strength CAE system for three-dimensional welded structures. Fatigue Fract Engng Mater Struct 25:275–282
Theocaris PS, Ioakimidis NT (1979) The V-notched elastic half plane problem. Acta Mech 32:125–140

Tovo R, Lazzarin P (1999) Relationships between local and structural stress in the evaluation of the weld toe stress distribution. Int J Fatigue 21:1063–1078
Unger DJ (2001) Analytical fracture mechanics. Dover Publ, Mineola, NY
Unger DJ (2005) A plane stress perfectly plastic mode I crack solution with continuous stress field. J Appl Mech 72:62–67
Unger DJ (2007) A complete perfectly plastic solution for the mode I crack problem under plane stress loading conditions. J Appl Mech 74:586–589
Verreman Y, Nie B (1996) Early development of fatigue cracking at manual fillet welds. Fatigue Fract Engng Mater Struct 19:669–681
Verreman Y, Nie B (1997) Short crack fatigue propagation at fillet welds. In: Proc Int Conf on Performance of Dynamically Loaded Welded Structures. New York, WRC, pp 240–253
Wang TJ, Kuang ZB (1999) Higher order aymptotic solutions of V-notch tip fields for damaged nonlinear materials under antiplane shear loading. Int J Fract 96:303–329
Wang ZY, Zhang HT, Chou YT (1985) Characteristics of the elastic field of a rigid line inhomogeneity. J Appl Mech 52:818–822
Wang ZY, Zhang HT, Chou YT (1986) Stress singularity at the tip of a rigid line inhomogeneity under antiplane shear loading. J Appl Mech 53:459–461
Westergaard HM (1939) Bearing pressures and cracks. J Appl Mech 6:A49–A53
Williams ML (1952) Stress singularities resulting from various boundary conditions in angular corners of plates in tension. J Appl Mech 19:526–528
Williams ML (1957) On the stress distribution at the base of a stationary crack. J Appl Mech 24:109–114
Williams JG, Ewing PD (1972) Fracture under complex stress – The angled crack problem. Int J Fract Mech 8:441–446
Yao W, Xia K, Gu Y (1995) On the fatigue notch factor K_f. Int J Fatigue 17:245–251
Yang W, Freund LB (1985) Transverse shear effects for through-cracks in an elastic plate. Int J Solids Struct 21:977–994
Yang S, Yuan FG, Cai X (1996) Higher order asymptotic elastic-plastic crack tip fields under antiplane shear. Engng Fract Mech 54:405–422
Yuan FG, Yang S (1994/95) Analytical solutions of fully plastic crack tip higher order fields under antiplane shear. Int J Fract 69:1–26
Yuuki R, Ohira T (1986) Fracture mechanics analysis of the fatigue strength of various spot-welded joints. Seisan Kenyu 38:475–478
Yuuki R, Ohira T (1989) Development of the method to evaluate the fatigue life of spot-welded structures by fracture mechanics. IIW Doc III-928-89/XIII-1358-89
Yuuki R, Ohira T, Kishi N, Mori N (1985[(1)]) Fracture mechanics evaluating of the fatigue strength of spot-welded joints and structures. JSAE Paper 852096, pp 501–506
Yuuki R, Ohira T, Nakatsukasa H, Li W (1985[(2)]) Fracture mechanics analysis and evaluation of the fatigue strength of spot-welded joints (in Japanese). Trans JSME 51:1772–1779
Zappalorto M, Lazzarin P (2007) Analytical study of the elastic-plastic stress fields ahead of parabolic notches under antiplane shear loading. Int J Fract 148:139–154
Zappalorto M, Lazzarin P (2009) A new version of the Neuber rule accounting for the influence of the notch opening angle for out-of-plane shear loads. Int J Solids Struct 46:1901–1910
Zappalorto M, Lazzarin P (2010) A unified approach to the analysis of nonlinear stress and strain fields ahead of mode III loaded notches and cracks. Int J Solids Struct 47:851–864
Zappalorto M, Lazzarin P (2011[(1)]) In-plane and out-of-plane stress field solutions for V-notches with end holes. Int J Fract 168:167–180
Zappalorto M, Lazzarin P (2011[(2)]) Strain energy based evaluations of plastic notch stress intensity factors at pointed V-notches under tension. Engng Fract Mech 78:2691–2706
Zappalorto M, Lazzarin P (2011[(3)]) Stress fields due to inclined notches and shoulder fillets in shafts under torsion. J Strain Analysis 46:187–199
Zappalorto M, Lazzarin P (2011[(4)]) On the intensity of linear-elastic high order singularities ahead of cracks and re-entrant corners. Int J Solids Struct 48:953–961

Zappalorto M, Lazzarin P, Yates JR (2008) Elastic stress distributions resulting from hyperbolic and parabolic notches in round shafts under torsion and uniform antiplane shear loadings. Int J Solid Struct 45:4879–4901

Zappalorto M, Lazzarin P, Berto F (2009) Elastic notch stress intensity factors for sharply V-notched rounded bars under torsion. Engng Fract Mech 76:439–453

Zappalorto M, Lazzarin P, Filippi S (2010) Stress field equations for U and blunt V-shaped notches in axisymmetric shafts under torsion. Int J Fract 164:253–269

Zhang S (1999) Recovery of notch stress and stress intensity factors. In: NAFEMS World Congress '99, Effective engineering analysis, vol. 2:1103–1114

http://www.springer.com/978-3-642-30739-3

Advanced Methods of Fatigue Assessment

Radaj, D.; Vormwald, M.

2013, XIV, 490 p., Hardcover
ISBN: 978-3-642-30739-3